MEMS Micromirrors For Imaging Applications

Li Li

Department of Electronic and Electrical Engineering

Centre for Microsystems and Photonics

A thesis submitted to the Department of Electronic and Electrical Engineering of the

University of Strathclyde for the degree of Doctor of Philosophy

April 2013

This thesis is the result of the author's original research. It has been composed by the author and has not been previously submitted for examination which has lead to the award of a degree.

Signed: Li Li Date: April 2013

Acknowledgements

First of all, I would like to express my gratefulness to my supervisor, Professor Deepak Uttamchandani, who is a very kind, generous and understanding person and an earnest, experienced, respectful academic. From him, I have learned about how to be a scientific researcher; also, I have been inspired by his passionate, dedication and wisdom which I will definitely benefit for the rest of my life.

I would like to thank all the members in my research group, Center of Microsystems and Photonics, who has brought pure encouragement, cheerfulness and happiness to me in such generous way that working is one of the most enjoyable things during my three-year PhD study. Everyone is so hardworking, caring, helpful and inspiring. It is my happy experience with them which makes Glasgow my second home town.

As for who have helped me greatly on this work, I feel grateful about the patient guidance from Dr Walter Lubeigt on my academic and scientific writing skills and his PhD student, Mr Ran Li, who is hard-working research student and pleasant to work with. Also, I want to thank Dr Ian Armstrong, who kindly volunteered himself to proof read my writing and provided helpful suggestions.

Finally, I would like to thank my lovely parents. It is their unconditional love and supports that make me feel that I am spiritually rich and problems of mine could be simply undone with a thought of them.

Abstract

Optical MEMS (microelectromechanical systems) are widely used in various applications. In this thesis, the design, simulation and characterisation of two optical MEMS devices for imaging applications, a varifocal micromirror and a 2D scanning micromirror, are introduced. Both devices have been fabricated using the commercial Silicon-on-Insulator multi-users MEMS processes (SOIMUMPs), in the 10 μm thick Silicon-on-Insulator (SOI) wafer.

Optical MEMS device with variable focal length is a critical component for imaging system miniaturisation. In this thesis, a thermally-actuated varifocal micromirror (VFM) with 1-mm-diameter aperture is introduced. The electrothermal actuation through Joule heating of the micromirror suspensions and the optothermal actuation using incident laser power absorption have been demonstrated as well as finite element method (FEM) simulation comparisons. Especially, the optical aberrations produced by this VFM have been statistically quantified to be negligible throughout the actuation range. A compact imaging system incorporating this VFM has been demonstrated with high quality imaging results.

MEMS 2D scanners, or scanning micromirrors, are another type of optical MEMS which have been widely investigated for applications such as biomedical microscope imaging, projection, retinal display and optical switches for telecommunication network, etc. For large and fast scanning motions, the actuation scheme to scan a micromirror in two axes, the structural connections and arrangement are fundamental. The microscanner introduced utilises two types of actuators, electrothermal actuators and electrostatic comb-drives, to scan a 1.2-mm-diameter gold coated silicon micromirror in two orthogonal axes. With assistance of FEM software, CoventorWare, the structure optimisation of actuators and flexure connections are presented. The maximum optical scan angles in two axes by each type of actuator individually and by actuating the two at the same time have been characterised experimentally. By programming actuation signals, the microscanner has achieved a rectangular scan pattern with $7^{o} \times 10^{o}$ angular-scan-field at a line-scan rate of around 1656 Hz.

Contents

Chapter 1

Introduction

1.1 Historical Background

Microelectromechanical systems (MEMS) refer to devices or systems fabricated by micromachining technology with scales in micrometer or even nanometre range. The development of MEMS is driven by and still dependent on its fabrication technology which is originally employed for the manufacture of integrated circuits (ICs). The IC fabrication technology has been developed since early 1960's for the increasing requirements for miniaturisation of transistors of complex circuits. Both IC and MEMS are largely based on the silicon material whose fabrication technology allows integration and highly accurate alignment of large number of microscale structures on a common substrate. In turn, MEMS extended the fabrication technologies to combine electrical and mechanical components. During this time, the development of batch-fabrication process has achieved the production of multiple microscale devices at the same time which significantly reduced the cost and improved the reliability of semiconductor devices. In 1967, the research work on an electrostatically actuated silicon cantilever structure, called 'resonant gate transistor', developed by Nathanson has demonstrated batch fabrication of MEMS devices [1]. Around 1960-1970's, much research work was focused on developing pressure sensors [2] that successfully

promoted the initial MEMS device commercialisation. During 1970s and 1980s, several companies based on MEMS products have been established. In 1982, Kurt Petersen has published a paper 'silicon as a mechanical material' in which he reviewed the silicon properties, fabrication technologies to create silicon based structure and silicon based cantilever structure as transducers [3]. In 1992, the Multi-User MEMS Processes (MUMPs) were developed to allow multiple designs by different users to be fabricated using the same standard fabrication processes which is now commercially available from the foundry. Since 1990s, there has been tremendous increasing in the number of MEMS devices, technologies and applications. Examples of successful MEMS products are inkjet heads in printers, accelerometers in consumer electronics devices (game console WII and Iphone), gyroscopes used in modern cars and other applications to detect yaw, microphones in portable devices (mobile phones and laptop) [4], fluidic pumps and flow sensor for microfluid control, medical related biosensing and chemical sensing and various optical MEMS devices for displays and projection (e.g. Digital Micromirror Devices chip [5] in a projector based on DLP technology [6]), optical switching for data communication, variable attenuators, optical scanners, micromirror arrays, grating light modulators and optical filters.

1.2 Motivation of the research

MEMS technologies have shown great potential in reducing the scale of system with improved performance and efficiency in various applications and fields. Many novel MEMS based devices and applications have been exploited to challenge the conventional solutions and eventually benefited the development of an area. Generally, due to its manufacture, microscale sizes, 3D structure complexity and nature of multiphysics, there are potentials on reducing the costs, improving efficiency and performance, and even exploiting novel applications by attempting different materials, fabrication processes, accurate simulation and structure design. Besides, most of the MEMS devices are application dependent. A systematic design flow of the MEMS device with considerations of the structural design and application requirements is

required. In the imaging application area, MEMS optics has promoted the development of medical endoscopes and fibre optical transmission. These MEMS optics, combining the actuation function within a micrometer-range structure, can provide accurate optical tuning within a compact area. The actuation scheme using electrothermal, electrostatic forces have been widely applied and intensively researched. Although each individual actuation scheme has been well developed, it only provides background knowledge about its functionalities. When an actuation scheme is applied within a MEMS device, its performance needs to be re-evaluated with considerations of its interaction with the other parts of the MEMS device, desired and undesired effects on the optical performance.

1.3 Scope and Objectives

1.3.1 Scope

This thesis focuses on introducing the structural design, performance characterisation, and motion simulation of single-crystal-silicon MEMS micromirror designs aimed for imaging applications. All the devices presented here have been fabricated by MEMSCAP Inc. using Silicon-on-Insulator Multi-User MEMS Process (SOIMUMPs) and have been simulated using FEM based simulation software, CoventorWare, both of which are briefly reviewed in Chapter 2.

1.3.2 Objectives

The first objective of this research work is to design micromirrors meeting the requirements of an imaging application, such as high reflectivity and low aberration. Secondly, the MEMS micromirror designs are required to comply with the design rules of SOIMUMPs which provides a single structural layer made of single-crystal-silicon. Thirdly, FEM based simulation software, CoventorWare, to estimate the static

mechanical deformation of the MEMS micromirror models which is comparable with measurement results. Fourthly, the optimisation of the structure design needs to be carried out to improve the performance of MEMS micromirror using CoventorWare.

1.4 Original Contribution

- The optical aberrations produced by the electrothermally and the optothermally actuated varifocal micromirror, such astigmatism, trefoil, coma and spherical aberrations, were characterised to be ranging from a few micrometers to nanometers and thereby negligible by calculating the Zernike coefficients has been demonstrated.

- The optothermal actuation method for the varifocal micromirror has the maximum achievable variation range from 23.2 mm to 33.8 mm actuated by absorbing 25.8 mW from 488 nm wavelength normally incident laser source and proven to be at least 194% efficient than the 33 mW electrothermally actuated varifocal micromirror.

- A varifocal imaging system made up of 1-mm-diameter varifocal micromirror, beam splitter and a CMOS imaging sensor, has been assembled and produced shapely focused imaging results within object tracking range of around 176 mm when driven varifocal micromirror by either electrothermally or optothermally. The micromirror and the beam splitter of the imaging system can be assembled into a compact space of $20\times5\times5$ mm^3 according to the optical design layout, which is 7.4% smaller than an equivalent imaging system in one dimension reported in [7]

- A novel single-layer silicon MEMS scanning micromirror with 1.2 mm diameter, that can be hybrid actuated using electrothermal actuators and electrostatic comb-drives, has been designed for the single-pixel imaging application. A rectangular raster scan pattern of angle of field-of-view 10^o-by-7^o was achieved

by synchronising the actuation signal for two types of actuators and the line scan rate of which is no less than 1656 Hz.

1.5 Thesis Organisation

The organisation of this thesis is as follows:

Chapter 2 first briefly introduces the concept of MEMS and optical MEMS. Then, the design flow for MEMS devices has been described. The common techniques used during each step of designing the silicon based MEMS have been reviewed. Specifically, the techniques applied for designing MEMS devices, such as the SOIMUMPs fabrication, material properties characterisation and finite element simulation using CoventorWare, are described. Next, the state-of-the-art of structure design of electrothermal and electrostatic actuators are reviewed. Finally, two types of optical MEMS devices for imaging applications reported in the literature: the varifocal MEMS devices and MEMS scanning micromirrors, have been reviewed.

Chapter 3 and 4 introduces the structure design, performance characterisation, behaviour simulation and imaging application of a varifocal micromirror (VFM). Two thermal actuation methods, the electrothermal and the optothermal actuation, are described. The behaviour simulation in mechanical and thermal domains using both actuation methods is presented. The characterisation of surface curvature tuning range and optical aberration of this varifocal micromirror are described. A compact imaging system utilising such varifocal micromirror is demonstrated together with the imaging results. This results presented in this chapter have been published by the Journal of Microelectromechancial Systems in 2012.

The design, simulation, characterisation of a novel 2D scanning micromirror hybrid-actuated using electrothermal actuators and electrostatic comb-drives has been demonstrated in Chapter 5 and 6. First in Chapter 5, the case study of a 2D microscanner, using the same hybrid actuation scheme and fabricated using the

same processes, designed as a concept trial is presented. During the description of this case study, the maximum optical scan angles and 2D scanning pattern have been measured, and the limitations of this tentative design are analysed using FEM simulation. Learnt from this case, an improved hybrid-actuated microscanner is then presented in Chapter 6 with the description of its structure functionalities and optimisation. The FEM simulation of its static motion by electrothermal actuators and the dynamic motion at resonance are demonstrated. Then, characterisation of the fabricated device in terms of the maximum scan angles about two axes, its dynamic scanning rate and linearity has been performed. Finally, a 2D raster scan pattern by driving the micromirror with programmed synchronized signals for the two actuators are displayed. To summarise the results, the limitation, advantage, the potential optimisation and possible applications of this hybrid actuated 2D micromirror design are discussed. The work in this chapter has been presented as poster presentation in International Conference Optical MEMS and Nanophotonics from 6th to 9th August, 2012 in Banff, Canada.

Chapter 7 summarizes the main results of the thesis and suggests possible future work for improving the hybrid-actuated scanning micromirror.

References

[1] H. Nathanson, W. Newell, R. Wickstrom, and J. Davis, J.R., "The resonant gate transistor," *IEEE Transactions on Electron Devices*, vol. 14, pp. 117 – 133, Mar 1967.

[2] W. P. Eaton and J. H. Smith, "Micromachined pressure sensors: review and recent developments," *Smart Materials and Structures*, vol. 6, no. 5, p. 530, 1997.

[3] K. Petersen, "Silicon as a mechanical material," *Proceedings of the IEEE*, vol. 70, pp. 420 – 457, May 1982.

[4] P. Scheeper, A. Vanderdonk, W. Olthuis, and P. Bergveld, "A review of silicon microphones," *Sensors and Actuators A-Physical*, vol. 44, pp. 1–11, Jul. 1994.

[5] M. Douglass, "Lifetime estimates and unique failure mechanisms of the Digital Micromirror Device (DMD)," in *Reliability Physics Symposium Proceedings, 1998. 36th Annual. 1998 IEEE International*, pp. 9 –16, 31 1998-april 2 1998.

[6] Texas Instruments Inc., "DLP Technology." http://www.dlp.com/.

[7] H.-T. Hsieh, H.-C. Wei, M.-H. Lin, W.-Y. Hsu, Y.-C. Cheng, and G.-D. J. Su, "Thin autofocus camera module by a large-stroke micromachined deformable mirror," *Optics Express*, vol. 18, pp. 11097–11104, May 2010.

Chapter 2

Literature Review and MEMS Design Methodologies

2.1 Overview

This chapter includes the literature review of all the related topics, the description of applied technologies and the characterisation results of material properties. First, the definition and background of MEMS (microelectromechanical systems) and optical MEMS are briefly introduced in the following section. Next, in Section 2.3, the general design process for a MEMS device is summarised and described. The current state-of-the-art of reported technologies for each MEMS design step, including fabrications, materials, characterisation and simulation, are reviewed in Section 2.4. Next, the specific technologies used for designing MEMS devices of this thesis are described in Section 2.5. Particularly, characterisation methods and results of material properties resulting from fabrication are presented in detail. Then, in Section 2.6, the two common actuation mechanisms which are related to functionality of MEMS micromirrors of this thesis, the electrothermal and the electrostatic actuation, are reviewed. Finally, the literature of two types of optical MEMS devices related to this thesis are reviewed: the reported optical MEMS devices with tunable focal length

are reviewed and compared in Section 2.7; the reported MEMS scanning mirrors are reviewed in Section 2.8 with focuses on their actuation schemes and scanning performances.

2.2 MEMS and Optical MEMS

MEMS, short for micro-electro-mechanical system, is a system of micrometer-scale electronic components and mechanical structures fabricated using micromachining technology to measure and/or change non-electrical parameter(s) of the components or of the surrounding environment through electrical signal(s). MEMS devices are usually categorised into sensors and actuators based on the conversion between non-electrical and electrical signals. Due to their scales, MEMS are prone to be high volume production, low unit cost and low power consumption. Despite their micro- and even nano-metre sizes, the actuating and sensing performance of MEMS devices is an improvement in terms of sensitivity and accuracy compared to devices designed using macro-structures. With growing interest in miniaturized systems, MEMS are designed for diverse applications, such as radio frequency communication, imaging and projecting system, motion transducer, micro-power generation [1, 2], energy harvesting [3], chemical [4] and biomedical [5, 6, 7] systems.

Many MEMS have been designed for optical applications with tunable optical properties, such as focal plane, beam steering and beam shaping [8, 9, 10]. So far, optical MEMS devices, such as diffractive and refractive microlenses, micromirrors, beam splitters and beam combiners, are reported, which can be used in optical fibre communication [11], projection, display, imaging and lasers [12] in military, biomedical and consumer electronic fields. These optical MEMS devices can even enable applications which conventional optical components cannot achieve, such as a single MEMS optics with variable focal length. Besides, using MEMS fabrication technology, integrated optical MEMS components could be fabricated at the same time or even monolithically to achieve integrated micro-optical bench on a chip. Driven by

the increasing demand of the optical MEMS market globally [13], there are successful commercial optical MEMS products, such as digital micromirror devices (DMD), handhold projectors and fibre optical switches. Due to economical advantages and potentials, many optical MEMS devices have been designed and optical MEMS are also referred as micro-opto-electro-mechanical system (MOEMS).

2.3 MEMS Device Design Flow

Designing a MEMS device is to design and fabricate a 3D structure within micro- or even nano-scale using available materials to achieve certain actuating or sensing function. Therefore, the first step is to be aware of what to be achieved with the application or what is the functionality of MEMS device is to be designed. As an example, the requirements for a MEMS mirror used for imaging application are listed in the top box of flow chart in Figure 2.1. With the guidelines of design requirements, 3D structure of MEMS device are designed and verified through the processes flow circulated at the bottom of Figure 2.1 with **available materials** using steps of **fabrication processes**.

Design processes of a MEMS device include structure design, performance estimation and measurement. First, designing a MEMS device starts from preliminary drawing the **2D** (two dimensional) **layout**, which is the view of device from the top. This requires the user to keep in mind of the design rules of fabrication processes to be used. The 2D layout drawing of a MEMS design usually contains several layers which appear to be overlapped; each layer could define the shape formed using certain material or even the adding/removing of a material. A common computer-aid software used to draw the 2D layout design is L-Edit [14]. After drawing the 2D layout design, it is sent to the foundry where it will be fabricated into the 3D structure. This 2D layout drawing can also be used by the designer to build a 3D model together with the database of materials in order to simulate behaviour of device.

Before fabrication, designer uses either analytical or computer-aided method to

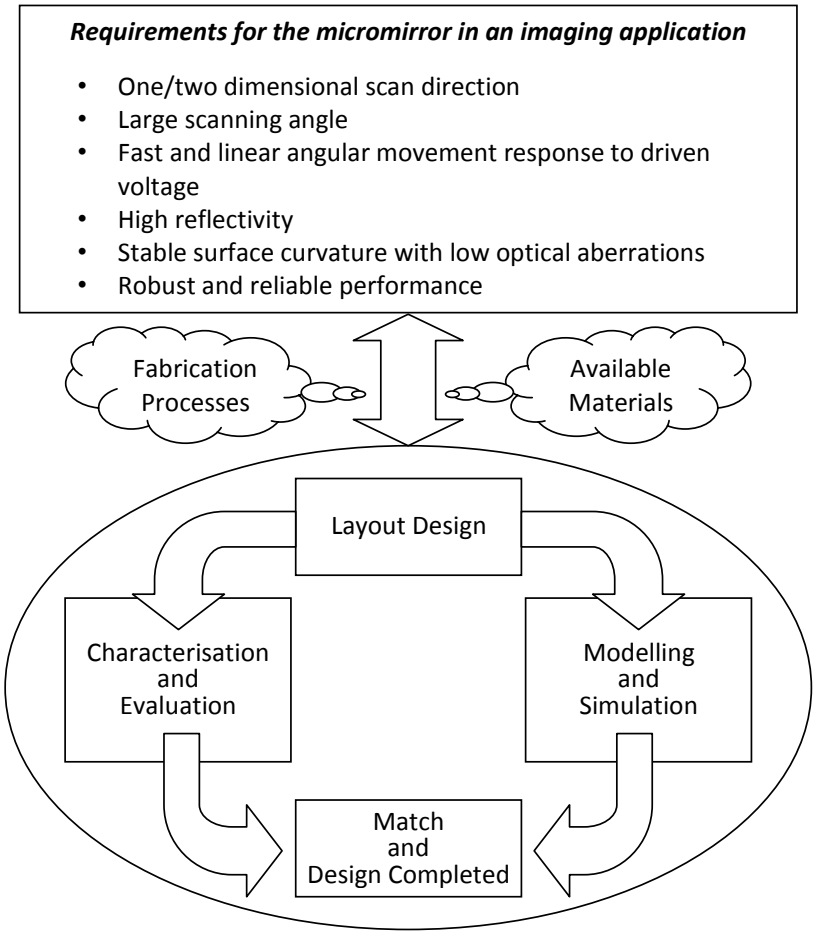

Figure 2.1: MEMS device design flow chart.

estimate the performance of MEMS design. The modelling and simulation of a MEMS device is usually a multiphysics problem; commonly, the analysis can be classified according to the physical transformation that occurs during operation, for example: electro-thermal, electro-mechanical, thermo-mechanical, electro-thermo-mechanical, magnet-mechanical or piezoelectric analysis. During this **modelling and simulation** process, not only agreement between the performances and the requirements can be verified, but also problems or limitations of design can be located and even be corrected before the final design submission and fabrication. Next, the state-of-the-art of MEMS device modelling and simulation methods are briefly reviewed in Section 2.4.4; and FEM (Finite Element Method) simulation and computer-aid software, CoventorWare, used to predict the performance of micromirror designs of this thesis are introduced in

Section 2.5.3.

After 2D layout drawing and performance estimation, MEMS device is fabricated using its 2D layout drawing. For the silicon micromirror designs in this thesis, the design is sent to foundry, MEMSCAP Inc., to be fabricated using commercial SOIMUMPs (Silicon-on-Insulator Multi-users MEMS processes). MEMSCAP Inc. runs MUMPs every three months. For this reason, the investigation timeline of a novel MEMS device using this SOIMUMPs is no less than three months. This once more indicates that, the effort to obtain an accurate performance is important for enhancing the output of a MEMS design with desired requirements. For the general overviews of concept and common technologies of MEMS fabrications are briefly described in Section 2.4.1; then in Section 2.5.1, detailed steps of SOIMUMPs used to fabricate the micromirror designs in this thesis are introduced.

Next, performance of the fabricated MEMS device is characterised in laboratory. The parameters of MEMS device to be measured are dependent on its functionality and application. Take MEMS actuators for example, its operation range, maximum mechanical deformation, deformation range and μm/mW or μm/V sensitivity need to be measured. After device characterisation, experimentally quantified performances of MEMS device are compared with the simulated results. Finally, MEMS device design flow is considered to be completed when the two agree with each other as well as with the design requirements.

In the following section, the current state-of-the-art of reported techniques for each step of MEMS device design is reviewed.

2.4 MEMS Technologies

2.4.1 Fabrication

The micromachining technology to fabricate MEMS devices is initially inherited from the one for integrated circuits (IC). There are two micromachining methods generally: the bulk and the surface micromachining. Bulk micromachining is achieved by anisotropic etching the bulk silicon substrate. Surface micromachining is depositing thin films of materials on top of silicon substrate in sequence and then selectively removing areas within thin films to create the 3D structure [15]. It is precise and can produce high surface-to-volume ratio (aspect ratio) 3D structures though the minimum feature size by which is material dependent, sub-micrometer and even nanometre features can be achieved at present [16, 17, 18]. The sequential fabrication steps to create microstructures of MEMS devices using surface and bulk micromachinings allow batch (i.e. multiple devices at the same time) and monolithic [1] fabrications of MEMS devices. However, due to the material deposition step, residual stress may be introduced and the resulting structure could buckle under constraints. Such micromachining introduced material properties have significant impact on the performance of MEMS devices. Nowadays, a lot of unique fabrication processes have been developed for specific MEMS device designs.

2.4.2 Materials

During the design flow of MEMS devices, it is important to obtain the precise properties of MEMS materials in order to perform accurate estimation of the devices behaviour and the performance. However, when a fabricated structure is scaled down to micrometer or nanometre range, its material properties are often significantly different from its bulk or microscale form. In the fabricated microscale structures, the assumption of homogeneous material properties is no longer reliable as for the

[1] microstructures integrated with driving, controlling and signal processing electronics [19].

bulk structure. Thus, localised properties variations of MEMS materials could alter the performance of devices fabricated together or from different batches [20]. One advantage of microscaling is that the defect density of a material is low which makes simple structures, such as microcantilevers, more reliable [21]. Besides, as mentioned above, this disparity of material properties between the bulk and the microscaled forms also results from the fabrication processes [22]. For example, during MEMS fabrication, materials usually experience high temperature, chemical reactions, doping and polishing which can change their mechanical, electrical, thermal properties. To distinguish them from the bulk form, the properties of a fabricated material are usually referred as the thin film properties.

Because of the flexibility of MEMS fabrication processes, it is convenient to generate dedicated test structures to measure MEMS material properties [23]. Generally, important material properties to be characterised include: density, elastic modulus, Poisson's ratio, thermal expansion coefficient, fracture stress, yield stress, in-plane residual stress and through-thickness stress gradient, electrical and thermal conductivity, etc. The material properties characterisation using microcantilever test structures will be described in Section 2.5.2.

2.4.3 Characterisation

Apart from the material properties characterisation using test structures mentioned in the last subsection, every fabricated MEMS device is required to be characterised in order to qualify its actual performance and compare with the simulated performance of its model; the methods used during characterisation of a MEMS device are dependent on its application. In this thesis, the MEMS characterisation methods are divided into static and dynamic ones. One of the most commonly used static methods is to measure the static surface profile of a device using microscopic white light interferometer (such as WYKO NT1100 surface profiling system). For dynamic motion measurements, one example is to measure the velocity or the displacement of a point on MEMS device accurately using a laser probe of the microscope coupled laser vibrometer. Other

performance quantification could be achieved by converting the device properties of interest to measurable parameters using available instruments; for example, measuring the wavefront of a light source reflected or refracted by a MEMS optics using Shack-Hartmann wavefront sensor, or quantifying the optical scan angle of a MEMS scanning mirror by measuring the scan length of a laser spot reflected by it. Detailed MEMS device characterisation methods will be described within the chapter for each device.

2.4.4 Modelling and simulation

Theoretical description of static or dynamic behaviour of a MEMS structure or device along its 3D dimensions is represented by a single or group of partial differential equations. Most of MEMS devices incorporate signals of multiple physics domains, such as thermal, mechanical and electrical parameters. Therefore, the equations for representing MEMS device behaviour can be coupled between heat, motion and electrostatic equation instead of a single differential equation in individual physical domain. The MEMS modelling and simulation is unavoidably an important step during MEMS design flow. It can assist MEMS designer to estimate the behaviour of structure in detail and also help a user to correct or improve the design before fabrication. Therefore, an accurate and efficient simulation could improve the output of a MEMS design.

There is no universal simulation technology covering all MEMS devices with various applications and structures currently. The fundamental of MEMS device behaviour modelling and simulation is to solve its partial differential equations along its 3D structure dimensions and about operation time. For simple or simplified microstructures and static problem, its partial differential equations can be converted to ordinary differential equation and be numerically solved. However, a lot of MEMS devices have complex 3D structure where numerical analysis cannot be applied due to invalid simplification and assumptions. In this case, the Finite Element Method (FEM) using computer-aided software becomes prevalent.

FEM is a branch of applied mathematics for numerical modelling physical behaviour to find the approximate solution of ordinary or partial differential equations describing physical problems of complicated structure or system. Generally, FEM is the discretisation of a complicated 3D structure into discretised simple tetrahedron or hexahedron elements (also described as meshing); the differential equation is applied to each element rather than to the whole MEMS structure to solve its nodes degree-of-freedom (DOF). The overall behaviour of MEMS device is presented by assembling nodes of all the elements. FEM solves problem through the following steps: discretisation of a continuous domain into a set of discrete sub-domains (called elements), derivation of element matrix, assembly of element matrices, derivation of system equations and then numerical solving of the system equations [24]. One challenge of performing FEM simulation is the computational resource efficiency especially for problems with coupling of multiple physics domains and nonlinear analysis (i.e. materials and geometry). Theoretically, a converged result can be achieved by increasing the number of meshing elements. However, the number of differential equations is proportional to the number of nodes generated from meshing. The nonlinear simulation time of a finely meshed 3D MEMS structure (i.e. $\sim$100,000 nodes) through its functional range could take up more than one day if a 2 GHz microprocessor and 5 GB RAM PC is used. On the other hand, a coarse meshing could result in inaccurate simulated results. Thus, trade-off between the overall meshing quality and computation resources is crucial.

Apart from FEM, model order reduction (MOR) is another method for MEMS device modelling and behaviour simulation, which shows advantage over FEM [2]. As the name of MOR implies, it can reduce the computation complexity by several orders of magnitude. The goal of MOR is to transform a high-dimensional system of differential equations to low-dimensional equivalent electrical component by fitting experimental or analytical data results of the device using compact modelling [25]. Compact modelling is a technique developed in electrical engineering to create an equivalent circuit network of resistors, capacitors and inductors for accurately describing the

[2]MOR, though is not within scope of this thesis, is worth to be briefly reviewed.

dynamic behaviour of a device. For a complex 3D MEMS device, each functional structure could be presented by a low-complexity electrical component; an equivalent circuit of the device could be assembled and simulated in a circuit simulator, such as SPICE. Such circuitry simulation can even be used to achieve system-level simulation which simulates the interaction between MEMS device function and its actual driving and controlling electrical circuit. The performance of MOR requires the designer to choose an accurate topology of circuit network intuitively, without strict guidelines, which could be time-consuming as well [25]. Presently, several algorithms and techniques for automatically generated MEMS compact models (macromodels) from FEM model of devices have been developed [26, 27]. Because macromodels of complicated MEMS 3D structures are generated from FEM models, they preserve the original characteristics for most operation conditions [27]. The macromodels can then be converted into circuit components for circuit simulator. Therefore, macromodels extraction based MOR has proven to be fast, flexible and preserving accuracy even for MEMS devices with complicated shape, compared to other MOR techniques (i.e. lumped element modelling) [26]. Figure 2.2 briefly illustrates steps of MOR.

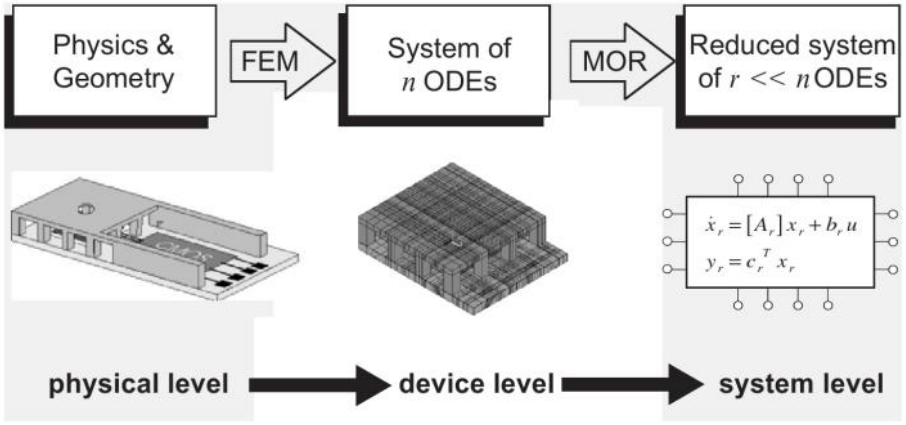

Figure 2.2: Schematic flow diagram of Model order reduction (MOR) from device to system-level simulation [25].

Despite the advantage of MOR over FEM, FEM is still commonly used because of large availability of software libraries, such as CoventorWare, COMSOL, ANSYS, IntelliCAD etc. Besides, FEM provides necessary results for constructing macromodels [28]. The performance simulation of MEMS devices[3] presented in this

[3]Apart from modelling the performance of MEMS device, MEMS modelling and simulation also

thesis using FEM based software CoventorWare [29] which will be introduced in Section 2.5.3.

2.5 Applied MEMS Technologies

After reviewing the reported technologies for each MEMS design process, the specific technologies (the SOIMUMPs fabrication process, the residual stress characterisation methods, the finite element simulation method and software) which are used for design single-crystal-silicon based MEMS mirrors of this thesis are introduced in detail in this section.

2.5.1 Fabrication — SOIMUMPs

The micromirrors described in this thesis are all fabricated in the 10 μm-thick SOI (Silicon-On-Insulator) wafer using SOIMUMPs® (Silicon-on-Insulator Multi-Users MEMS Processes) [30] run by MEMSCAPs Inc. [31]. The SOI wafer consists a stack of 400 μm thick handling wafer (or substrate), 1 μm thick buried silicon oxide and 10 μm thick single-crystal-silicon layer (or referred as SOI layer) as shown in Figure 2.3.

The SOIMUMPs start with a n-typed SOI wafer (Figure 2.3a). First, the top 10 μm thick SOI layer of the wafer is doped with Phosphorous dopant by depositing phosphosilicate glass (PSG) layer in a 1050^{o}C Argon environment for one hour (Figure 2.3b). After the doping process, PadMetal layer made up of 20-nm-thick chrome and 500-nm-thick gold is deposited on the top of SOI layer through the liftoff process (Figure 2.3c); its root mean square surface roughness is around 4 nm [32] due to being exposed to high temperature during the subsequent processes. The thin layer of chrome between gold and silicon enhances the adhesion of the gold. This

includes modelling the fabrication processes to create the MEMS 3D structure which is the main focus for the microfabrication process developing.

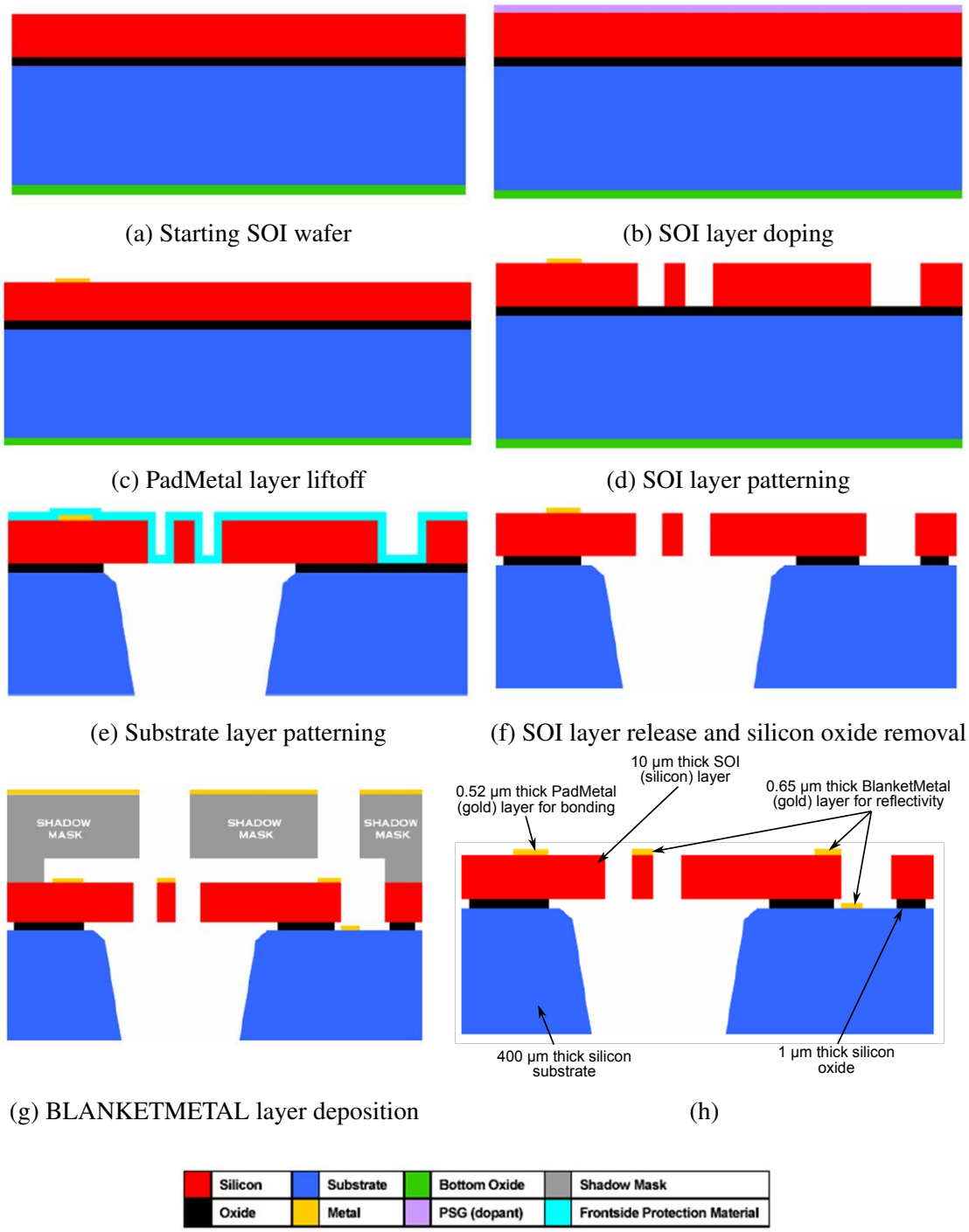

(a) Starting SOI wafer

(b) SOI layer doping

(c) PadMetal layer liftoff

(d) SOI layer patterning

(e) Substrate layer patterning

(f) SOI layer release and silicon oxide removal

(g) BLANKETMETAL layer deposition

(h)

Figure 2.3: Cross section view of SOI wafer during each process of SOIMUMPs [30].

PadMetal layer is usually used to provide electric pathways. Then, the structure in SOI layer is lithographically patterned and Deep-RIE (Reactive Ion Etched) using ICP (Inductively Coupled Plasma) technology (Figure 2.3d). Main functional structure of the device is usually patterned within this layer. The trench shape designed under part of the device is formed by etching the substrate layer using RIE process and etching

the oxide layer using wet oxide etch process (Figure 2.3e). After the release of device structure in SOI layer, the exposed oxide layer is etched by vapour HF process to minimize stiction (Figure 2.3f). The remained buried oxide layer can provide electrical isolation between SOI and substrate layer. Besides, an undercut which is the distance between edge of SOI layer and edge of buried oxide layer is also formed. Finally, a BlanketMetal layer consisting of 50-nm-thick Chrome and 600-nm-thick gold are evaporated on top of SOI layer using E-beam tool (Figure 2.3g). This gold layer is usually used as reflective surface over PadMetal layer due to its surface smoothness. The detailed steps of fabrication processes and design rules can be found in the users' guide in [30].

The benefit of using SOIMUMPs is that it allows the mass production of MEMS designs by multiple users within one flow of standard processes; also it has reliable and consistent design output and material properties. The patterning of SOI layer, which is usually used for functional structures, allows the minimum feature to be as small as 3 μm. Besides, it produces consistent designed dimension outputs: the thickness of SOI layer is characterised to be 9.5$\pm$0.4 μm; the undersize or oversize of designed in-plane features varies by only 0.14$\pm$0.03 μm [32]. Silicon material of SOI layer, is robust mechanical material with direction dependent Young's Modulus but close to steel (180 GPa), Knoop hardness twice of iron [33], and 1.97 GPa fracture strength with associated Weibull moduli of 8.9 [32]. Silicon oxide is mostly used as sacrificial layer in surface micromachining which can be removed and free the structure deposited above. Moreover, SOIMUMPs allow the etching at both sides of the wafer so that the suspended structure can be created over a through-hole (trench).

One drawback of SOIMUMPs is the limited number of structural layers. Different functional parts of the device fabricated in SOI layer using SOIMUMPs have uniform thickness, the same electrical, mechanical and thermal properties. Therefore, the parts of a MEMS device are interacting with each other mechanically and have limited thermal or electrical isolation.

2.5.2 Materials — properties characterisation

As reviewed in above sections, accurately quantified material properties are essential for the performance estimation of MEMS devices during the design process. MEMS material properties can be influenced by the scaling effect as well as by the fabrication processes. There are two mechanical properties that are originated from fabrication processes of SOIMUMPs and are relating to the performance of MEMS devices of this thesis: stress gradient along the thickness of SOI layer and residual stress within BlanketMetal layer.

First, SOIMUMPs fabricated silicon, referred as SOI layer, experienced a well studied through-thickness stress gradient caused from polishing, deposition and doping processes [32]. Because of this stress gradient, the structure patterned will deform: the cantilever-like structure curves out-of-plane, and the plate structure presents a concave surface curvature. The benefit of this property is that SOI electrothermal actuator, to be introduced in this thesis, cannot function without this stress gradient. The disadvantage is that it is impossible to fabricate a large and flat micromirror in the 10-μm-thick SOI layer. Therefore, it is important to quantify the stress gradient of SOI layer in order to estimate the mechanical performance and the optical limitation of micromirror designs. The stress gradient of SOI layer can be obtained using a cantilever test structure fabricated in this layer.

Another material property playing an important role for micromirror designs is the residual stress of BlanketMetal layer. To increase reflectivity, a layer of BlanketMetal gold can be deposited on top of silicon micromirror. Due to the evaporation method during the depositing process, the formed BlanketMetal layer has high tensile residual stress ($>$200 MPa). As a result, the stack of BlanketMetal gold layer of tensile residual stress and SOI layer of compressive residual stress results in a concave surface curvature. This residual stress within BlanketMetal layer can be characterised using a SOI cantilever test structure coated on top with BlanketMetal layer of interest.

The details of test structures and characterisation methods to quantify these values

will be described in the following subsections. Furthermore, other material properties of the doped silicon and the gold reported in the literature, which are applied in the models of micromirrors for behaviour simulation, are summarised at the end of this section together with the characterised ones.

2.5.2.1 Stress gradient in 10 μm thick SOI layer

As briefly mentioned above, the SOI layer of SOIMUMPs is compressively stressed[4] from polishing, high temperature deposition cooling and doping processes before the releasing step. Due to the non-uniformity, the bottom of SOI layer is more compressive than the top before release; the average stress σ_{ave} is in the middle of layer thickness as shown in Figure 2.4a. After release from the substrate, the mid-plane stress σ_{ave} is relieved to zero and the stress gradient still remains; the resulting top surface is tensile stressed and bottom surface is compressively stressed. This remaining stress gradient is equivalent to a bending moment about the structure's edges as shown in the Figure 2.4b. After bending, the stress is relieved and surface deformed into a concave curvature (Figure 2.4c).

To measure this stress gradient, series of 50-μm-wide cantilevers with 600 μm, 700 μm and 800 μm lengths were fabricated in the 10-μm-thick SOI layer using SOIMUMPs. The surface deformations of these cantilevers were measured using white light interferometer as demonstrated in Figure 2.5. The curvature κ of each cantilever can be calculated from its tip deflection δ and length L using the following equation:

$$\kappa = \frac{2\delta}{\delta^2 + L^2} \tag{2.5.1}$$

Assuming that the stress is distributed linearly through SOI layer thickness, the average stress σ_{ave} in the mid-plane can be calculated from the cantilever surface curvature by

[4]If a material has compressive stress within, its structure desires to compress, but the contraction is prevented. In the conventional declaration, compressive stress has a negative sign.

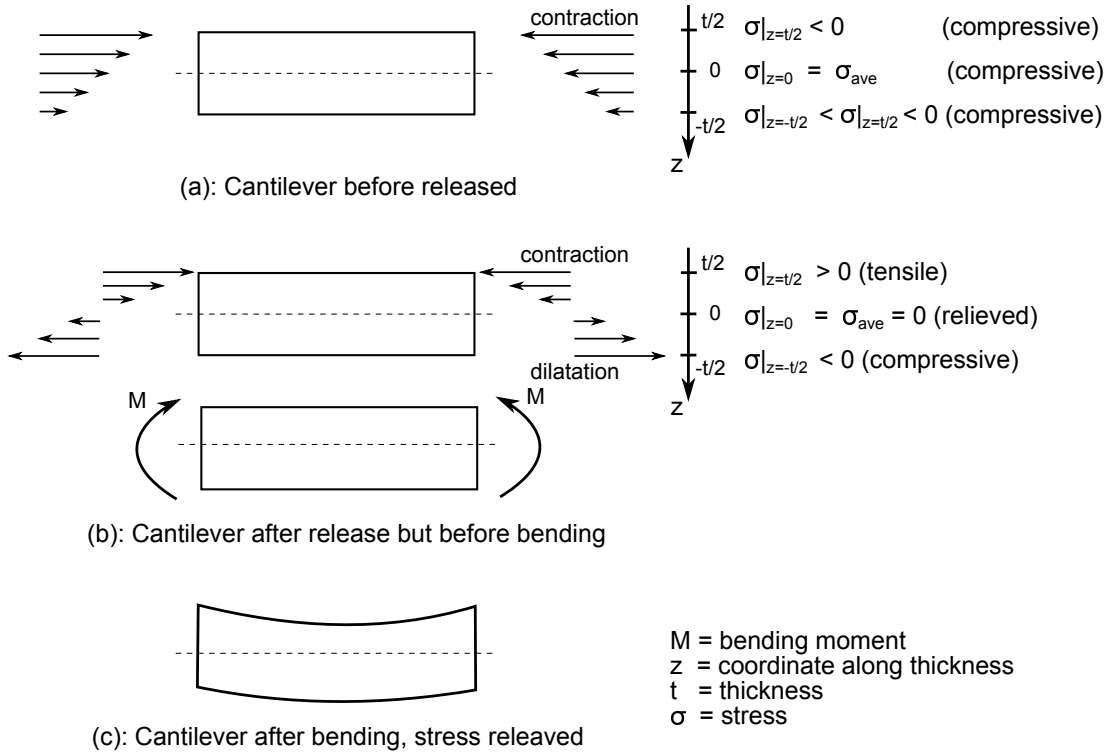

Figure 2.4: Cross sectional view of SOI layer of SOIMUMPs deformed by stress gradient.

using the following equation [32].

$$\sigma_{ave} = -E\kappa\frac{t}{2} \tag{2.5.2}$$

where,

E is the elastic modulus of SOI layer,

κ is the surface curvature of cantilever,

t is the thickness of cantilever.

Alternatively, for a linear stress gradient $\Delta\sigma$, the stress $\sigma(z)$ along the thickness of SOI layer before bending is [34, page 34]:

$$\sigma(z) = \Delta\sigma z \tag{2.5.3}$$

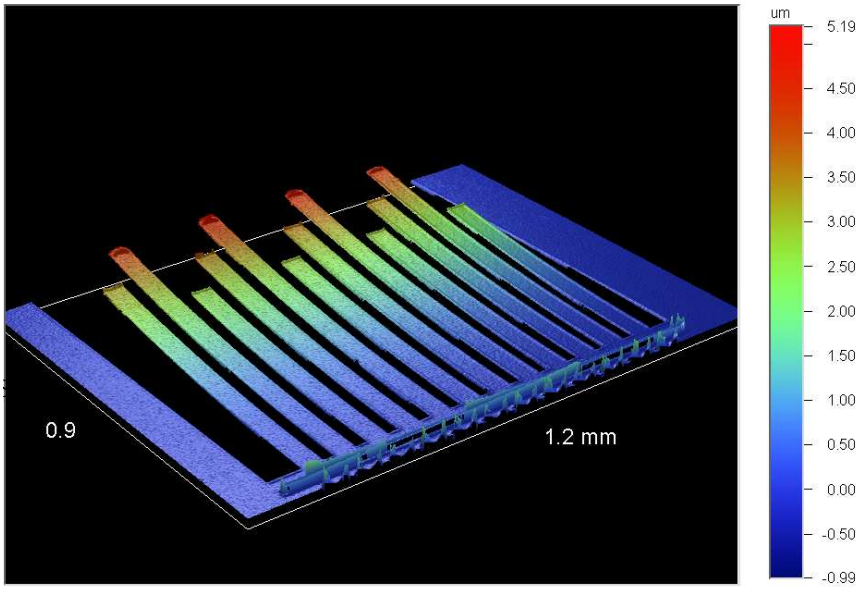

Figure 2.5: The test structures of cantilevers fabricated using SOIMUMPs for measuring stress gradient in the 10-μm-thick SOI layer.

The bending moment M of a cantilever (width w) due to a stress gradient is:

$$\begin{aligned} M &= \int_{-t/2}^{t/2} wz\sigma(z)\mathrm{d}z \\ &= \frac{1}{12}wt^3\Delta\sigma \\ &= \Delta\sigma I \end{aligned} \tag{2.5.4}$$

where, I is the moment of inertia of a rectangular cantilever and $I = \frac{wt^3}{12}$. The deformation of an elastic cantilever of length of L under the bending moment M could be expressed as its surface curvature κ [35, page 295]:

$$\frac{M}{EI} = \kappa = \frac{2\delta}{\delta^2 + L^2} \tag{2.5.5}$$

where, δ is the tip deflection of bending cantilever.

Therefore, from (2.5.4) and (2.5.5), the stress gradient $\Delta\sigma$ of the 10-μm-thick SOI layer can be expressed as:

$$\Delta\sigma = \frac{2E\delta}{\delta^2 + L^2} = E\kappa \tag{2.5.6}$$

From the measured tip deflections of test cantilevers listed in Table 2.1, the averaged stress gradient of 10-μm-thick SOI layer calculated from deformed cantilever samples using (2.5.6) is $\sim$2.4$\pm$0.1 MPa/μm. This value is used throughout this thesis for simulating mechanical deformation of micromirror devices; the application of which in CoventorWare built FEM model is described in [36, page R4, 103-105].

Table 2.1: Measured tip displacements of test cantilevers and calculated stress gradient of SOI layer.

Cantilever	Length (L) [μm]	Tip Deflection (δ) [μm]	Curvature (κ) [m^{-1}]	Young's Modulous (E) [GPa]	Thickness (d) [μm]	Average Stress (σ_{ave}) [MPa]	Stress Gradient ($\Delta\sigma$) [MPa/μm]	Average Stress Gradient [MPa/μm]
1	700	3.3	13.4	168	10	-11.2	2.2	2.4 $\pm$ 0.1
2	800	4.2	13.1			-11.0	2.2	
3	600	2.6	14.7			-12.4	2.5	
4	700	3.5	14.4			-12.1	2.4	
5	800	4.4	13.7			-11.5	2.3	
6	600	2.8	15.4			-12.9	2.6	
7	700	3.6	14.8			-12.4	2.5	
8	800	4.4	13.7			-11.5	2.3	
9	600	2.7	15.1			-12.7	2.5	
10	700	3.5	14.4			-12.1	2.4	
11	800	4.3	13.4			-11.3	2.3	
12	600	2.6	14.6			-12.2	2.4	

2.5.2.2 Residual stress in the 0.65 μm thick gold layer

Conventionally, the residual stress of a thin film metal deposited on a thicker (at least ten times) substrate can be calculated using the Stoney Equation [37]. In order to measure the residual stress of the BlanketMetal layer of SOIMUMPs, the test structure of a 10-μm-thick SOI cantilever fully coated with BlanketMetal gold layer on the top surface was also designed and fabricated using SOIMUMPs as shown in Figure 2.6a. However, SOI layer does not satisfy the assumption of being homogeneous and isotropic due to the existence of stress gradient. The Stoney equation is derived into the form shown in equation (2.5.7) with consideration of the underlying SOI layer deformation caused by stress gradient [38]. As marked in Figure 2.6b, the surface shape of the test cantilever for the characterisation was measured using white light interferometer.

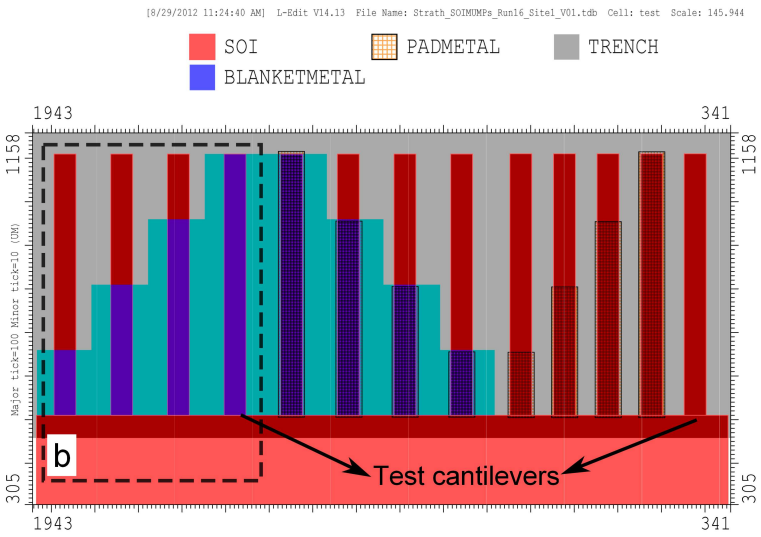

(a) 2D top view of a group of cantilevers in L-Edit

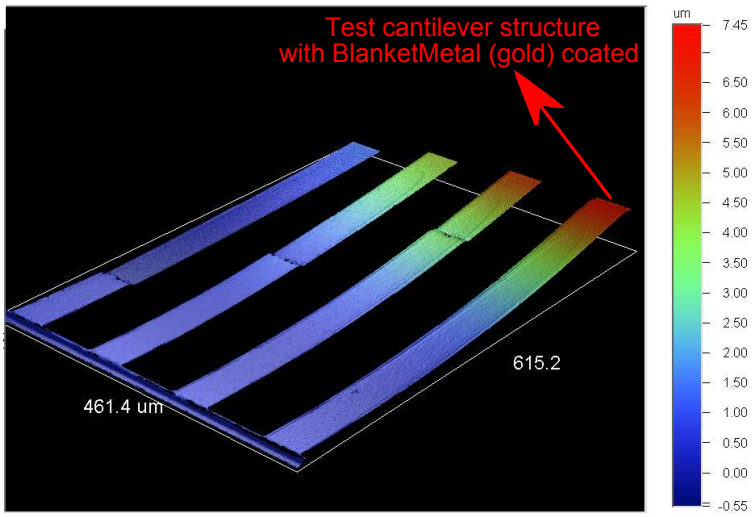

(b) surface profile measurement by white light interferometer

Figure 2.6: Test structures of SOI cantilevers coated with BlanketMetal layer.

$$\sigma_{go} = \frac{E_{si}(\kappa_{si,go} - \kappa_{si})t_{si}^2}{6t_{go}(1 - \upsilon_{si})} \tag{2.5.7}$$

where,

σ_{go} is the residual stress within BlanketMetal layer,

E_{si} is the elastic modulus of SOI layer,

t_{si} is the thickness of SOI layer,

$\kappa_{si,go}$ is the curvature of bimorph cantilever made of SOI and BlanketMetal layers,

t_{go} is the thickness of BlanketMetal gold layer,

υ_{si} is the Poisson ratio of SOI layer.

In Table 2.2, the curvature (κ_{si}, $\kappa_{si,go}$) of both SOI cantilever and gold coated SOI cantilever on five samples are summarised; the averaged residual stress within BlanketMetal layer is calculated to be $\sim$274.7$\pm$11 MPa using Equation (2.5.7). The positive sign of σ_{go} indicates that the residual stress within BlanketMetal layer is tensile. Similar to the illustration in Figure 2.4b, when tensile stressed metal is coated on compressive stress silicon layer, the resulting structure has a concave surface curvature.

Table 2.2: The measurements of test cantilevers and calculated residual stress within BlanketMetal layer using modified Stoney equation [38].

Chip Number	Cantilever	Tip Deflection (δ) [μm]	Length (L) [μm]	Curvature (κ) [m^{-1}]	E_{si} [GPa]	υ_{si}	t_{si} [μm]	t_{go} [μm]	σ_{go} [MPa]
1	SOI	2.7	600	13.7	168	0.28	10	0.65	269.8
	SOI + BlanketMetal	9.5		58.8					
2	SOI	2.7		13.7					263.3
	SOI + BlanketMetal	9.4		57.7					
3	SOI	2.8		13.9					268.6
	SOI + BlanketMetal	9.3		58.8					
4	SOI	2.1		13.8					281.7
	SOI + BlanketMetal	9.4		60.9					
5	SOI	2.2		15.0					290.2
	SOI + BlanketMetal	22		63.5					
The averaged residual stress of BlanketMetal gold layer									274.7 $\pm$ 11

E_{si} is the elastic modulus of SOI layer,
υ_{si} is the Poisson ratio of SOI layer,
d_{si} is the thickness of SOI layer,
d_{go} is the thickness of BlanketMetal layer,
σ_{go} is the residual stress in BlanketMetal layer.

2.5.2.3 Other material properties of SOI and BlanketMetal layers

Apart from the characterised stress gradient of SOI layer and residual stress of BlanketMetal layer, values of other material properties of these two materials quoted from literature, such as electrical, thermal, mechanical material properties, are summarised in Table 2.3.

Notice that material properties of SOI and BlanketMetal layers display two sources of nonlinearity. First, coefficient of thermal expansion (CTE), thermal conductivity, specific heat and electrical conductivity of SOI are temperature dependent. Second, modulus and stress of SOI layer is direction dependent. In FEM simulation, analysis of models with such nonlinearities is computational expensive which consumes computation memory and time.

2.5.3 Modelling and simulation software — CoventorWare

The FEM simulation software used for estimating the performances of micromirror designs in this thesis is CoventorWare [29] which is very useful and specialised for MEMS device simulation. First of all, CoventorWare can build FEM 3D models using 2D layout design file of MEMS device together with the built-in fabrication process simulator ('Foundry design kit') and material properties database. The fabrication process simulator allows users to model the fabrication steps provided by a foundry or self designed. It creates 3D model together with features resulting from fabrications, such as the undercut offset and the sidewall angle, in an automatic 3D model creation step. Therefore, by setting the simulator following fabrication design rules, the generated model could have geometric structure close to the actual MEMS device. The commercial SOIMUMPs [30] are included in Foundry design kit of CoventorWare. Moreover, the material properties database contains forty common materials used for MEMS fabrication; this database provides a good guideline for an initial investigation or simulation. The user can choose to create or modify properties for a more accurate simulation.

CoventorWare provides several physics solvers, such as electrostatic, thermal, mechanical and piezoelectric, to analysis either steady-state or transient behaviour of a MEMS model in individual or coupled physics domains. The main solvers used to simulate micromirror designs introduced in this thesis are modal analysis and electro-thermo-mechanical analysis.

Table 2.3: Material properties of SOI and BlanketMetal layers used for FEM simulation of MEMS micromirror models.

	Unit	Silicon	Gold
Density	Kg/m^3	2331 [39]	19300 [39]
Elastic Modulus	GPa	$E_{x[100]}$=$E_{y[010]}$=$E_{z[001]}$=130 G_{yz}=G_{zx}=G_{xy}=0.796 [41]	57 [40]
Poisson		ν_{yz} = ν_{zy} = ν_{xy} = 0.28 [41]	0.42 [40]
CTE	1/K	2.432x10^{-6} at 280 K 2.616$\times$10^{-6} at 300 K 3.253$\times$10^{-6} at 400 K 3.614$\times$10^{-6} at 500 K 3.842$\times$10^{-6} at 600 K [43] 4.016$\times$10^{-6} at 700 K 4.151$\times$10^{-6} at 800 K 4.185$\times$10^{-6} at 900 K 4.258$\times$10^{-6} at 1000 K 4.384$\times$10^{-6} at 1200 K	1.4x10^{-5} [42]
Thermal Conductivity	W/mK	150 at 300K 111 at 345 K 100 at 402 K 73.4 at 493 K 59.0 at 595 K [44] 42.3 at 800 K 32.1 at 1000 K 24.3 at 1200 K 23.0 at 1413 K 20.5 at 1606 K	317 [39]
Specific Heat	J/kgK	5 at 300K 755 at 345K 789 at 400K [44] 831 at 493 K 856 at 595 K 856 at 1606 K	129 [39]
Electric Resistivity	Ω*μm	56.2 at 200K 60.6 at 300K 64.9 at 400K [45] 70.0 at 500 K 80.0 at 600 K 91.7 at 700 K	0.023 at 300K 0.031 at 400K [39]
Surface Emissivity		0.6 [46]	0.02 [47]
Stress Gradient	MPa/μm	2.4 [48]	-
Residual Stress	MPa	-3.9 [32]	$\sim$275 [38]

In order to perform an efficient (accurate and fast) FEM simulation using CoventorWare, first, the targeted physics domain and the associated solver need to be identified. Then, based on the choice of solver, the shape and the order of meshing element can be selected accordingly. In theory, the results of FEM simulations should converge to the same level when applied meshing elements are sufficient small

regardless of their shapes. However, due to the limited computation resources during presented research work, the meshing density is limited and, therefore, essential for the results accuracy level. For the analysis to be presented, the best achievable meshing size or density is used. Next, general description of two types of meshing elements used is presented and guidelines for the meshing quality are introduced.

2.5.3.1 Meshing elements

In Figure 2.7, two shapes of volume elements are used to mesh micromirror designs in this thesis: hexahedron and tetrahedron. Both element shapes have options of linear and parabolic orders. Parabolic elements have extra nodes in the centre and in the middle of each edge. A linear tetrahedron has 4 nodes and a parabolic tetrahedron has 11 nodes; a linear hexahedron has 8 nodes and a parabolic hexahedron has 27 nodes. A meshed FEM model with more nodes requires more computation resources. Thus, considering a structure meshed using all four types of elements respectively with the same density. The model with linear tetrahedrons requires the least computation cost while the one with parabolic hexahedrons are the most computational expensive. The relative comparison of computation cost of the four meshing elements can be expressed as following:

$$\text{linear tetrahedron} < \text{linear hexahedron} < \text{parabolic tetrahedron} < \text{parabolic hexahedron}.$$

It is claimed in Section 4.3.3 of CoventorWare reference handbook [36] that, first, the linear tetrahedron is too stiff to be useful; secondly, it is recommended that the linear hexahedron meshing element is the most cost efficient among four meshing shapes; thirdly, parabolic elements provide the best resolution for complicated stress state (residual stress and stress gradient of SOIMUMPs materials) at low cost. Also, according to Section 2.1.1 and Section 4.3.1 of the handbook [36], the hexahedron element is recommended as the ”best practice” for a mechanical simulation. Combining these guidelines with the author’s experience, parabolic elements (including parabolic tetrahedron and hexahedron) are preferred over the

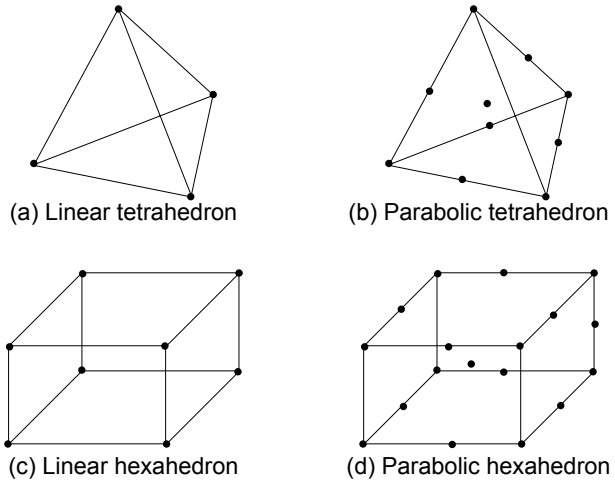

Figure 2.7: The linear and parabolic meshing elements in CoventorWare.

linear ones for simulation performed in this thesis.

2.5.3.2 Meshing quality

The impact of meshing quality on FEM simulation results depends on several factors. For example, solving the mechanical deflection of a uniform rectangular cantilever with linear material properties is fairly simple and has been widely presented as example in many text books. The meshing of such simple structure could be coarse and uniform without crucially affect on its simulation accuracy. However, in order to be able to solve FEM model of a complicated device with non-uniform geometries of largely different aspect ratios (overall 100 times different) and nonlinear material properties under high loads (i.e. the deformation is over 10% of the longest dimension), it is difficult to generate high quality meshing all over the structure without creating a large amount of nodes (i.e. over 100,000). The MEMS micromirrors to be presented in this thesis satisfy the conditions described. Therefore, the meshing quality is critical for an accurate behaviour estimation of such complex model especially with a limited computational resources.

In order to improve the simulation efficiency and preserve the accuracy level at the same time, one solution is to trade-off the meshing density on low stressed locations with important locations of high stresses: locally refined meshing can be defined for

high stressed and largely deformed parts (the maximum deflection is more than 10% of the maximum geometric dimension [36]); coarse meshing for less stressed and lightly deformed parts. In such way, the meshing density is non-uniform across the model structure.

Meshing of 3D model controlled by users has a direct impact on the accuracy of FEM simulation results. If a FEM model is badly meshed, for example, considerable percentage of elements has excessive small or large interior angles or excessive large aspect ratios comparing to suggested value, especially located on the stressed parts, FEM simulation could fail to complete with an error of excessive distorted elements. As listed in Section 2.2.2 of CoventorWare reference handbook [36], the general acceptance for a good meshing quality can refer to the following standards:

- Small range of values for edge lengths of meshing elements.
- Corner angles that are close to 90^{o} for quadrilateral and hexahedral meshing elements and 60^{o} for triangular and tetrahedral elements.
- Low elements aspect ratios [5].

2.5.3.3 Computation Resources

The FEM simulation presented is carried out with the following computation resources:

- 2 GB RAM
- 3 GB Disk Swap Space
- 2 GHz Intel® Core™ 2 Duo CPU

[5]The aspect ratio of the meshing element is defined as $R = A^{3/2}/V$, in which A is the area of the face perpendicular to the shell normal, and V is the layer volume[36].

2.6 MEMS Actuation Mechanisms

Actuators designed using MEMS fabrication technology in micrometer scale are to convert electrical signals to mechanical force, displacement or structure deformation. These MEMS actuators, or microactuators, are applied in various applications, such as microfluidics systems [49], biomedical systems [50], optical systems [51, 52] and consumers' electronics [53, 54, 55]. Currently reported actuation mechanisms are: electrothermal, electrostatic, electromagnetic, piezoelectric, pneumatic, hydraulic [56], photostrictive [57] and magnetrostrictive [58].

Electrothermal and electrostatic actuation schemes are two most popular options in MEMS, because they can be both fabricated in multi-users MEMS processes and compatible with IC. Generally, electrostatic actuation requires applications of high voltage (from tens of up to hundreds of volts). However, due to the capacitive circuit, low current is generated during actuation which results in low power consumption. Electrostatic actuation could be designed to produce static displacement as well as to excite resonant mode of structure. At high frequencies (at least hundreds of Hertz), nonlinearity dynamic response of the electrostatic actuated MEMS device could be observed. Moreover, since the capacitance is also dependent on relative permittivity of the media material (air or gas), application of electrostatic actuation is limited to the relative humidity and environment gas, for example, the level of relative humidity can effect the surface charge magnitude, charging decay time and adhesive/stiction between electrodes which can shorten the lifetime of electrostatic MEMS devices, such as MEMS optical switches [59]. On the other hand, electrothermal actuation requires less driving voltage (i.e. up to around 20 V) but high power consumption (i.e. hundreds of milliwatts). The electrothermal actuation could produce large static displacement up to hundreds of micrometers. Opposite to electrostatic actuation, the electrothermal actuators are usually operated at DC voltage levels rather than at structural resonant frequencies, because the response of electrothermal actuation is limited by thermal response time, typically several tens of milliseconds. In this section, the geometric design of such electrothermal and electrostatic actuation mechanisms

which are relating to devices in this thesis are reviewed in detail.

2.6.1 Electrothermal actuation

The microactuator deformed by thermal expansion energy converted from the electrical signal was reported as early as 1988 [60] which used the bimorph structure with layers of different materials of different thermal expansion coefficients [61]. The bimorph actuators were intensively studied by the research group led by H. K. Xie, whose recent work on a curved multimorph electrothermal actuator was published in [62]. With the development of surface fabrication technology, J. H. Comtois and V. M. Bright have fabricated an in-plane electrothermal actuator from a single layer of polysilicon [63] in 1997. This in-plane electrothermal actuator consists of two beams of different widths jointed connected at free ends and fixed to substrate at the other side; the wider beam is fixed to substrate through a thin beam connection. By applying an electrical current through the actuator, the thinner beam flexes due to temperature rise from Joule heating while the wider beam with less resistance as well as high stiffness experiences less thermal expansion. At the fixed end of the wider beam, the thin connection also bends at the temperature rise. The resulting motion is that the free end of this thermal actuator bends towards the wider beam side. Such design was used either in pairs as a micro-gripper or micro-twister [50] or in an array where several such electrothermal actuators are cascaded connected to a long beam structure at the free ends to provide higher in-plane displacement than a single actuator [63]. Right after the publication of such a successful design, many research groups started to investigate designing electrothermal actuators based on such a structure. Q. A. Huang and N. Lee developed a mathematical analysis method on geometric design and optimisation of such in-plane electrothermal actuators [64, 65] in 1999. N. D. Mankanme, G. K. Ananthasuresh [66] and R. Hickey et al. [67] have both developed thermal analysis or modelling in order to optimise the structure design of such in-plane two-beam electrothermal actuator in 2001 and 2002. L. Que et al have designed a V-shape in-plane electrothermal actuator formed by two joint-connected equal width beams [68]. This in-plane two-beam

V-shape actuator can also be cascaded into an array to produce higher displacement [69].

Apart from the in-plane structure made out from a single layer of boron doped silicon, W. C. Chen et al. have developed an out-of-plane electrothermal actuator made up of four parallel, 240 μm-long cantilevers connected at the free ends by a joint beam [70] in 2003. The two inner cantilevers of this microactuator design had lower level than the outer two in vertical direction. Each of two inner cantilevers are connected to the joint beam through a step structure. Thus, the expansions between inner and outer cantilevers have a vertical difference due to the step structure when a current flowing through either two inner or two outer cantilevers. And this step-shape feature of the four-beam out-of-plane electrothermal actuator allows its tip to displace at 7 and -6 μm in up and down directions when applied 5 V to two inner and outer cantilevers respectively. Later in 2008, W. C. Chen et al. utilised this step feature again to fabricate a bridge-structure out-of-plane electrothermal actuator capable of 13 μm upwards vertical displacement at 54 mW [71]. In 2009, C, Elbuken et al. have analysed and fabricated a similar four-parallel-beam out-of-plane electrothermal actuator of 200 μm long which achieved not only 8.2 μm up vertical displacement but also 2.5 μm left and -2.4 μm right lateral displacement at 10 V [72]. In 2006, A. Atre has analysed the performance of a 126 μm-long three-parallel-beam out-of-plane electrothermal actuator made up of two alternative layers of polysilicon which achieved out-of-plane tip deflection of 9 μm at 6 V and 145 mW [73]. In 2007, D. Girbau et al designed a V-shape out-of-plane electrothermal actuator of various pre-bend angles whose upwards vertical displacements were estimated to be around 4.5 μm at maximum when driven by 4 V [74]. In 2009, Lijie Li et al. have designed a 1800-μm-long three-parallel-beam out-of-plane electrothermal actuator made of single layer of silicon provided a 32 μm upwards vertical displacement at 10 V [75]. Table 2.4 summaries the performance of the above-mentioned out-of-plane MEMS electrothermal actuators.

Table 2.4: Summary and comparison of out-of-plane electrothermal actuators in the literature.

Electrothermal actuator	Length [μm]	Thickness [μm]	Voltage [V]	Power [mW]	Static Vertical Displacement [μm]
2003 [70]	240	2	5	–	7, -6
2006 [73]	126	2/1.5	6	$\sim$145	9
2007 [74]	165	2/1.5	4	$<$2.5	1.5
2008 [71]	600	2.2	–	54	13
2009 [72]	200	2/1.5	10	$<$154	8.2
2009 [75]	1800	10	10	–	32

2.6.2 Electrostatic actuation

The microfabricated electrostatic actuator is essentially a capacitor whose capacitance varies either by changing distance or by changing overlapping area between electrode pair to provide lateral or vertical displacement during actuation; and the generated electrostatic force (F_e) converted from applied voltage can be expressed as:

$$F_e = \frac{1}{2}\epsilon \Delta A \frac{V^2}{d^2} \tag{2.6.1}$$

or,

$$F_e = \frac{1}{2}\epsilon A \frac{V^2}{\Delta d^2} \tag{2.6.2}$$

where,

ϵ is the dielectric constant of the medium in the gap between electrode pair;

A is the overlapping area between electrode pair;

V is the applied voltage level;

d is the distance between electrode pair.

Area-tuning electrostatic actuators could also produce out-of-plane rotation with the torque generated (T_e) can be expressed as (2.6.3).

$$T_e(\theta) = \frac{1}{2}V^2 \frac{\partial C}{\partial \theta} \tag{2.6.3}$$

where,

C is the capacitance of the actuator;

θ is the rotational angle.

Electrostatic actuation is the most popular technique among the microscale actuation schemes in MEMS. This is mainly because of the efficiency caused by the scaling effect: if all dimensions of a parallel-plates capacitor are scaled by single variation represented by symbol s ($0<s\leq1$), the electrostatic force generated gives higher acceleration (by 1/s for the constant electric field or by $1/s^2$ for $s^{-0.5}$ times electric field) [76, 77]. Apart from efficiency, electrostatic actuators have advantages of low power consumption, fast response and IC compatible as well. Electrostatic actuation has been applied for applications such as, micromotors [78], microgrippers [79], switches, [80], acoustic sensing [81], optical deformable mirror [82] and optical microscanner [83]. Besides, electrostatic sensing could be equally efficient as its actuation function using the same structure [84]. To apply electrostatic forces, the electrodes could be arranged into paralleled electrode pair and interdigitated comb-finger structures as shown in Figure 2.8.

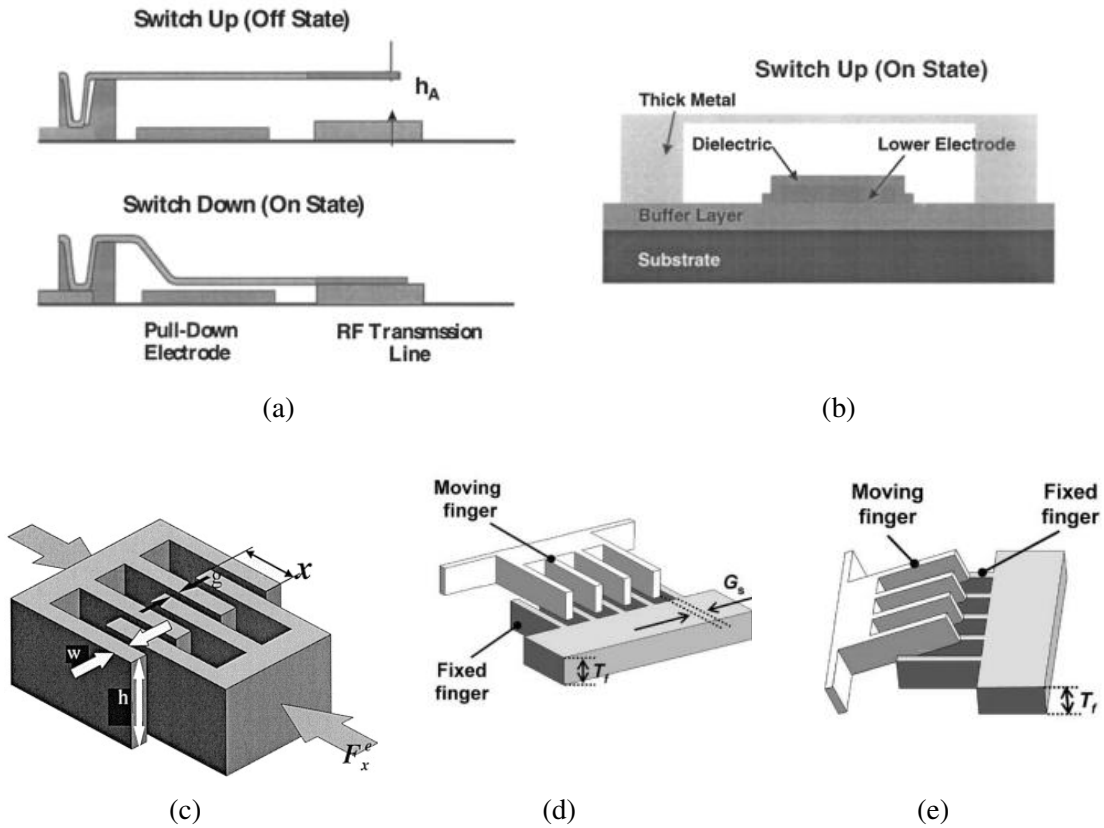

Figure 2.8: Functional diagram of MEMS electrostatic actuators: (a) cantilever; (b) bridge [80]; (c) lateral comb-drives [85]; (d) staggered vertical comb-drives; (e) angular vertical comb-drives [86].

The report of electrostatic actuation in micrometer scale can be dated as early as 1990s. In 1994, C. W. Storment et al reported series of all-aluminium electrostatic cantilevers and torsional actuators whose displacement ranges were limited by electrodes' gap [87]. In 1998, Texas Instruments Inc. reported a digital micromirror device (DMD), implementing electrostatic actuation based on parallel-plate structure [88]. This DMD was successfully applied into a commercialized DLP (Digital Light Processing) projector [89]. Such parallel-plate electrostatic actuator was also widely adopted in RF switches for their fast switch time (i.e. only a few microseconds) [80]. Compared to the parallel-plate electrostatic actuators, comb-drives structure have no theoretical tuning limitation but can be practically limited by the elastic range of the support spring and the length of comb fingers [90]. In 1991, L. E. Larson et al first reported a MEMS area tuning capacitor based on interdigitated comb structures with capacitance tunable range from 35 fF to 100 fF and 225 μm in-plane (lateral) displacement at up to 200 V [91]. In 2004, H. D. Nguyen et al have reported 25 μm thick silicon comb-drives structure with electrodes aligned with an initial angular offset [92]. These angular vertical comb-drives (AVC) generated 15^{o} rotational angle at $\sim$22 V DC and had a continuous capacitance tuning range from 0.27 pF to 8.6 pF. Later in 2005, two pairs of these comb-drives were used to drive a 1 mm diameter microscanner to tilt in two directions by 6^{o} and 3 ^{o} at around 50 V (dc) respectively [93]. Electrostatic comb-drives are currently widely investigated and adopted for applications requiring large and fast dynamic motion, such as fast (i.e. hundreds to kilohertz) scanning micromirrors with large rotational angle (up several tens of degree). Moreover, these interdigitated combs cannot only be used for actuation, but also operated at dynamic motion for frequency tuning.

Currently, a lot of effort has been made to accurately model and predict the dynamic behaviour of electrostatic actuated microstructures. The difficulty is the assumption on the operational conditions (such as damping) and nonlinearity of dynamic behaviour (such as hysteresis, structural stiffening and softening). Besides, the structural designs of electrostatic actuated devices (i.e. flexure and supporting structures) are various and are application dependent. Due to these limitations, there is no universal analysis

method to model the dynamic behaviour of an electrostatic actuated device. Some analysis methods have to depend on parameters (i.e. damping ratio) measured from the fabricated device [94]. In this thesis, the application of comb-drives structure is focused rather than the accurate dynamic behaviour modelling.

In the next sections, two types of optical MEMS devices, the varifocal micromirrors and scanning micromirrors, which are subjects of the rest of this thesis are reviewed.

2.7 Varifocal Micromirrors

Optical MEMS devices with tunable focal length (or referred as varifocal) contributes greatly on miniaturisation of imaging system. Conventional imaging systems tune the focal plane by changing the distance between lenses using motors which require bulk volume and excess power. On the other hand, MEMS optics, which couple electrical and mechanical signals in one structure, can not only reduce the scale of varifocal imaging system by one order of magnitude but also reduce the power consumption. There are two types of varifocal MEMS optics, microlenses and micromirrors. Varifocal microlens is a refractive optics system that usually adopts two layers of membranes enclosing liquid within. Microlenses can change its focal length by mechanically changing the surface pressure so as to vary curvature or by changing the surface tension of liquid droplet using electro-wetting. However, liquid microlenses could suffer physical difficulties, such as sensitivity to ambient temperature, shaking and tilt of module. Varifocal micromirror (VFM) is a reflective optics system which can mechanically deform its surface radius of curvature (ROC) to change the focal length. Different from the astrophysical deformable mirror, which has very fine local surface deformation of less than the tenth of wavelength ($\sim$10 nm) for the entire aperture, VFM focuses on producing tunable focal length without aberrations [95].

Varifocal MEMS mirror can be used for range finder, confocal microscope [96] coherence tomography (OCT) [97, 98] and auto-focusing imaging system [99]. There

are many reported VFM in literature. For example, in 1997, G. Vdovin reported a 1-cm-diameter silicon nitride VFM with focal length varied from infinite to 0.25 m when driven at 200 V [100]. In 2001, P. Himmer designed a 1-mm-diameter and 1-μm-thick silicon nitride VFM which achieved variable focal length from 36 mm to 360 mm when driven at 100 V [101]. In 2003, W. Liu and J. Talghader reported an electrothermally actuated gold-coated polysilicon VFM of 1.5 μm thickness and 0.1 mm diameter. It was reported to have ROC variation from 2.5 mm to 8.2 mm when electrical current of 11 mA was applied [102]. In 2005, W. Greger et al presented a 20-mm-diameter polymer VFM varing focal length from 1 m to 0.1 m at electro-magneto actuating voltage of 12 V and 110 mA [103]. In 2006, U. Mescheder et al have demonstrated a very thin and large SOI membrane of 0.5 μm thickness and over $>$5 mm diameter which achieved 900 mm focal length variation range when electrostatically driven at 150 V [104]. In 2008, A. Alzaydi et al reported a 950-μm-diameter polyester VFM with focal length varying from 100 mm to 3 mm when driven at 22.5 KPa hydraulic pressure [105]. In 2009, R. Hokari and K. Hane fabricated an electrostatically-actuated SOI VFM with dimension of 10 μm thickness and 500 μm diameter. This VFM achieved a focal length change from infinity to 24 mm at 215 V driven voltage [106]. In 2011, T. Sasaki and K. Hane have reported an electrostatically-actuated 1-μm-thick and 400-μm-diameter SOI VFM capable of focal length changing from -28 mm (convex) to 21 mm (concave) when drived at 22 V [95]. Later in 2012, they presented another electrostatically-actuated SOI VFM with focal length variation from -128 mm to 93 mm at 50 V [107].

These reported VFM mentioned above have various sizes, materials and actuation schemes. Generally, reflective VFM with thin and large (i.e. thickness $\leq$ 5 μm and diameter $\geq$ 1 mm) mirror structure could produced at least hundreds of millimeter focal length variation range as summarised in Table 2.5. Though many efforts have been made to produce VFM with large tunable range, these reported VFM referenced above did not present a statistical characterisation of their optical aberrations.

Table 2.5: Summary and comparison of some reported VFM in the literature.

VFM	Thick-ness [μm]	Aperture Diameter [mm]	Rest ROC [mm]	Actuated ROC [mm]	Focal Length Tuning Range [mm]	Optical Power Tuning Range [m^{-1}]	Actuation Method	Max. Voltage [V]	Max. Current [mA]	Response Time [ms]	Optical Aberration
1997 [100]	0.5 – 1	10	∞	500	∞ – 250	4	ES	200	–	10	ASG
2001 [101]	1	1	720	72	324	50	ES	100	–		
2003 [102]	1.5	0.1	2.5	8.2	3	556	ET		11	2	
2005 [103]	-	20	2000	200	900	9	EM	12	110		
2006 [104]	5.02	>5	∞	200	∞–100	10	ES	150	–		none*
2008 [105]	0.5	0.95	200	5	97	323	HP	(22.5 kPa)		33	
2009 [106]	10	0.5	∞	48	∞ – 24	42	ES	215	–		none*
2011 [95]	1	0.4	-56	42	49	167	ES	22			
2012 [99, 108]	$\sim$4	4.5	∞	100	∞ – 50	20	ES	$\sim$150		0.4	ASG&DIST
2012 [107]	1	0.3	-256	186	221	18.6	ES	50		$\sim$2.5	

* = Quantified by fitting surface shape with parabolic curve shape.
ES = Electrostatic ET = Electrothermal EM = Electromagnetic
HP = Hydraulic pressure ASG = Astigmatism DIST = Distorsion

2.8 Scanning Micromirror

MEMS-based scanning micromirrors are another important category of optical MEMS. They are widely used in various applications, such as optical switches in telecommunication networks [109], high-definition image projection and retinal displays [110, 111, 112], bar-code scanning for inventory monitoring, range-finding systems for safe-vehicular navigation, and free-space laser communications [113]. Specifically, scanning micromirrors enable the miniaturization of imaging systems such as endoscopic [5, 7, 114, 115], confocal [116, 117], and coherent tomography (OCT) [6, 97, 118] imaging systems. For example, the research group lead by H. Urey have focused on developing electromagnetically driven 2D microscanner [53] for projecting, retinal display and imaging applications since 2000; their 2D electromagnetic microscanners have been successfully implemented into the handhold projectors which are commercially available from Microvision Inc. [54]. In 2010, an in-vivo skin imaging system using this electromagnetic 2D microscanner was presented by C. L. Arrasmith and co-authors [52]. In 2008, both Y. Xu et al [119] and J. Sing et al [120] have developed and implemented two axes scanning micromirrors actuated using bimorph electrothermal actuators for OCT probe in bioimaging. Research group lead by H. K. Xie also developed electrothermally-actuated 2D micromirrors [121] and implemented them into an endoscopic OCT biomedical imaging system. Moreover, H. Miyajima et al proposed and compared the electrostatic

and the electromagnetic 2D scanning micromirrors for the miniaturized confocal microscope application in 2004 [122]. In 2007, the electrostatic comb-drives actuated 2D scanning micromirror has also been demonstrated with the application of superresolution digital imaging system by K. Yu and co-authors [123]. Y. M. Wang et al and H. Ra et al demonstrated the use of electrostatic comb-drives actuated 2D microscanner for biomedical hyperspectral imaging system [124] and for biomedical in-vivo microscopic imaging [125] respectively. In 2012, Y. Bai et al have developed an electrostatically-actuated 2D MEMS scanner using sidewall electrodes for biomedical imaging [126].

Generally, structure of a scanning micromirror consists of a mirror plate, actuators and flexure connections. The scanning motion of a micromirror is provided by actuators. Scanners that produce tilt or rotation about one axis are referred as one-dimensional (1D) scanners. If scanners can produce tilt or rotation motion in two orthogonal axes, they are referred as 2D scanners. The actuation scheme and the flexure connections are essentials for scanning micromirrors, they define optical scanning angles — their major functionality. Therefore, the scanning micromirror design is to utilise efficient actuation scheme, produce large scan angles and fast scanning speed or frame rate to meet its application requirements. Currently, popular actuation schemes are electromagnetic, electrostatic and electrothermal actuations. In the next paragraph, MEMS-based scanning micromirrors with actuation schemes and scanning abilities are reviewed.

Around 1996 to 1998, M. H Kiang, O. Solgaard et al demonstrated three 1D microscanners out of polysilicon for bar-code reading system which were capable of 11^o - 28^o optical scan angles resonantly at 2 - 4 kHz [83]. In 2003, U. Krishnamoorthy, D. Lee and O. Solgaard fabricated a 300×100 μm^2 micromirror which was driven by electrostatic combs and was capable of resonantly rotating by 40^o optical scan angle at 5.8 kHz [127]. In 2004, D. Hah and co-authors further demonstrated the analysis of maximum rotational angle and pull-in condition of an AVC (angular vertical comb-drives) actuated 1-mm-diameter scanning micromirror and presented its advantage over the SVC (staggered vertical comb-drives) actuated micromirror

[128]. A. Jain et al demonstrated a 2D scanning micromirror achieved the maximum static scan angles of $40^o \times 25^o$ by driving bimorph electrothermal actuators at total 230 mW [114]. In 2005, J. Kim et al fabricated a 0.65 mm $\times$ 0.65 mm rectangular 2D scanning micromirror out of 50-μm-thick SOI [129]. It was capable of resonantly scanned at $27^o \times 20^o$ optical angles excited by two groups of orthogonally connected AVC. In order to produce large scan angle, the micromirror and the four AVC took up around 1.7 mm $\times$ 2 mm in total. In the same year, W. Piyawattanametha et al presented a 1-mm-diameter 2D scanning micromirror with similar arrangement of four AVC where the whole device took up around 2.7 mm $\times$ 2.9 mm area [93]. Their microscanner was fabricated from 35-μm-thick polysilicon and was capable of $12^o \times 8^o$ maximum optical scan angles at DC voltage level. Later in 2006, W. Piyawattanametha et al have introduced a two-photon fluorescence imaging system using a 0.75 mm × 0.75 mm rectangular micromirror with comb-drives arrange around within and outside micromirror frame [130]. It was capable of scanning resonantly at 16^o (1.76 kHz) and 6^o (1.02 kHz) in two directions respectively. In 2007, L. J. Li et al presented an SOI scanning micromirror achieved tilting at 5^o when driven the electrothermal actuator at DC power of 18 V and 23 mA and achieved also resonantly scanning at 2.2 kHz by 8^o optical scan angle [131]. In 2008, H. Urey et al presented an electromagnetically-actuated scanning micromirror [132]. When driven at 250 mA ac current signal, the microscanner achieved the maximum optical scan angles 10^o and 140^o at resonant frequencies of 647 and 414 Hz respectively. In 2011, Y. Watanabe and co-authors presented electromagnetically-actuated scanning micromirror achieved 2.95 and 3.68 deg/mA scan resolution for OCT imaging application [133]. Table 2.6 summaries the performance of abovementioned 2D microscanners.

Overall, most of the electrostatic actuators designed for MEMS scanners are actuated at resonant frequencies to produced optical scan angles up to around several tens of degrees; however, this actuation scheme have problems such as nonlinear dynamic response and pull-in failure which is short circuit of capacitance caused by attraction force between electrodes. Besides, it could end up with large device area in several square millimetres. Electromagnetic actuation requires external magnet which limiting

system miniaturisation. Electrothermally-actuated 2D scanning micromirror can generate static tilt position but limited to be operated at high frequencies due to thermal response time. Furthermore, these reported 2D scanning micromirrors all utilised the same actuation mechanism for both scan axes.

Table 2.6: Summary and comparison of 2D scanning micromirror in the literature.

2D scanning micromirror	micromirror size		Actuation Method	Max. Voltage	Max. Current	Max. Optical Scan Angles	Resonant Frequency	Scan Patten
	Thickness [μm]	Area [mm]		[V]	[mA]	[°]	[Hz]	
2004 [114]	∼45	1^2	ET	15, 17 V_{dc}	6.3, 8	40°×25°	445, 259	–
2005 [129]	50	0.65^2	ES	$20V_{dc}$+$15V_{pp}$, $30V_{dc}$+$25V_{pp}$	–	27°×20°	10.65, 1540	Lissajous
2005 [93]	35	$1^2\pi$	ES	55, 50 V_{dc}	–	12°×8°	315, 144	–
2006 [130]	30	0.75^2	ES	45,58 V_{pp}	–	16°, 6°	1760, 1020	–
2008 [132]	230	5^2	EM	–	250(dc)	10°, 140°	647, 414	Lissajous
2012 [134]	∼450	1.5×1	ET&EM	$10V_{dc}$, $1V_{ac}$	12,1.26	±1.5°,±10°	74,202	Lissajous

ES = Electrostatic ET = Electrothermal EM = Electromagnetic

References

[1] "Review on microfabricated micro-solid oxide fuel cell membranes," *Journal of Power Sources*, vol. 194, no. 1, pp. 119 – 129, 2009.

[2] D. C. Walther and J. Ahn, "Advances and challenges in the development of power-generation systems at small scales," *Progress in Energy and Combustion Science*, vol. 37, pp. 583–610, Sep. 2011.

[3] S. Kerzenmacher, J. Ducre, R. Zengerle, and F. von Stetten, "Energy harvesting by implantable abiotically catalyzed glucose fuel cells," *Journal of Power Sources*, vol. 182, no. 1, pp. 1 – 17, 2008.

[4] R. Srinivasan, S. Firebaugh, I.-M. Hsing, J. Ryley, M. Harold, K. Jensen, and M. Schmidt, "Chemical performance and high temperature characterization of micromachined chemical reactors," in *Solid State Sensors and Actuators, 1997. TRANSDUCERS '97 Chicago., 1997 International Conference on*, vol. 1, pp. 163 –166 vol.1, Jun. 1997.

[5] S. R. Chamot and C. Depeursinge, "MEMS for enhanced optical diagnostics in endoscopy," *Minimally Invasive Therapy & Allied Technologies*, vol. 16, no. 2, pp. 101–108, 2007.

[6] J. Walther, M. Gaertner, P. Cimalla, A. Burkhardt, L. Kirsten, S. Meissner, and E. Koch, "Optical coherence tomography in biomedical research," *Analytical and Bioanalytical Chemistry*, vol. 400, pp. 2721–2743, Jul. 2011.

[7] S. F. Elahi and T. D. Wang, "Future and advances in endoscopy," *Journal of Biophotonics*, vol. 4, pp. 471–481, Aug. 2011.

[8] S. Mias and H. Camon, "A review of active optical devices: I. amplitude modulation," *Journal of Micromechanics and Microengineering*, vol. 18, no. 8, p. 083001, 2008.

[9] S. Mias and H. Camon, "A review of active optical devices: II. phase modulation," *Journal of Micromechanics and Microengineering*, vol. 18, no. 8, p. 083002, 2008.

[10] C. Friese, A. Werber, F. Krogmann, W. Mnch, and H. Zappe, "Materials, effects and components for tunable micro-optics," *IEEJ Transactions on Electrical and Electronic Engineering*, vol. 2, no. 3, pp. 232–248, 2007.

[11] M. C. Wu, O. Solgaard, and J. E. Ford, "Optical MEMS for lightwave communication," *Journal of Lightwave Technology*, vol. 24, pp. 4433 –4454, Dec. 2006.

[12] A. Q. Liu and X. M. Zhang, "A review of MEMS external-cavity tunable lasers," *Journal of Micromechanics and Microengineering*, vol. 17, pp. R1–R13, Jan. 2007.

[13] E. Mounier and L. Robin, "Analyst corner: MEMS market will continue double digit growth, to double by 2017," *MEMS Trends*, vol. 10, pp. 18–20, Apr. 2012. http://www.i-micronews.com/newsletter/download/April-2012,1300412.pdf.

[14] Tanner EDA ®, "Industry-leading productivity for analog, mixed signal and MEMS layout from Tanner EDA." http://www.tannereda.com/products/l-edit-pro.

[15] W. Lang, "Silicon microstructuring technology," *Materials Science and Engineering: R: Reports*, vol. 17, no. 1, pp. 1 – 55, 1996.

[16] S. Choi, C. Kim, W. Kim, I. Sohn, and H. Lee, "Micromachining on the chrome stainless mold steel using the femtosecond laser," *Advanced Science Letters*, vol. 4, pp. 3113–3118, Aug.-Oct. 2011.

[17] L. Ressier, E. Palleau, and S. Behar, "Electrical nano-imprint lithography," *Nanotechnology*, vol. 23, no. 25, p. 255302, 2012.

[18] J. Bustillo, R. Howe, and R. Muller, "Surface micromachining for microelectromechanical systems," *Proceedings of the IEEE*, vol. 86, pp. 1552–1574, Aug. 1998.

[19] J. Smith, S. Montague, J. Sniegowski, J. Murray, and P. McWhorter, "Embedded micromechanical devices for the monolithic integration of MEMS with CMOS," in *Electron Devices Meeting, 1995. IEDM '95., International*, pp. 609–612, 1995.

[20] J. Judy, "Microelectromechanical systems (MEMS): fabrication, design and applications," *Smart Materials & Structures*, vol. 10, pp. 1115–1134, Dec. 2001.

[21] W. Van Arsdell and S. Brown, "Subcritical crack growth in silicon MEMS," *Journal of Microelectromechanical Systems*, vol. 8, pp. 319 –327, Sep. 1999.

[22] S. Spearing, "Materials issues in microelectromechanical systems (MEMS)," *Acta Materialia*, vol. 48, no. 1, pp. 179 – 196, 2000.

[23] S. V. Kamat, "Experimental techniques for the measurement of mechanical properties of materials used in microelectromechanical systems," *Defence Science Journal*, vol. 59, pp. 605–615, Nov. 2009.

[24] S. S. RAO, *The Finite Element Method in Engineering*. Elsevier Science: Butterworth-Heinemann, 4th ed. ed., 2011.

[25] T. Bechtold, E. Rudnyi, and J. Korvink, *Fast Simulation of Electro-Thermal MEMS: Efficient Dynamic Compact Models*. Microtechnology and MEMS, Springer London, Limited, 2007.

[26] E. Hung and S. Senturia, "Generating efficient dynamical models for microelectromechanical systems from a few finite-element simulation runs," *Journal of Microelectromechanical Systems*, vol. 8, pp. 280 –289, Sep. 1999.

[27] Y.-J. Yang and C.-C. Yu, "Extraction of heat-transfer macromodels for MEMS devices," *Journal of Micromechanics and Microengineering*, vol. 14, no. 4, p. 587, 2004.

[28] C. Leondes, *MEMS/NEMS: handbook techniques and applications*. MEMS/NEMS: Handbook Techniques and Applications, Springer, 2006.

[29] Coventor Inc., "CoventorWare integrated suite of design simulation software." http://www.coventor.com/products/coventorware/.

[30] A. Cowen, G. Hames, D. Monk, S. Wilcenski, and B. Hardy, *SOIMUMPs Design Handbook*. MEMSCAP Inc., Revison 8.0 ed. http://www.memscap.com/products/mumps/soimumps/reference-material.

[31] MEMSCAPs Inc., 2011-2012. 3021 E. Cornwallis Rd, PO Box 14486, Research Triangle Park, Durham, NC 27709, USA .

[32] D. C. Miller, B. L. Boyce, M. T. Dugger, T. E. Buchheit, and K. Gall, "Characteristics of a commercially available silicon-on-insulator MEMS material," *Sensors and Actuators A: Physical*, vol. 138, no. 1, pp. 130 – 144, 2007.

[33] K. Petersen, "Silicon as a mechanical material," *Proceedings of the IEEE*, vol. 70, pp. 420 – 457, May 1982.

[34] G. M. Rebeiz, *RF MEMS: Theory, Design, and Technology*. John Wiley and Sons, 2003.

[35] A. C. John Case and C. T. F. Ross, *Strength of Materials and Structures*. Oxford : Butterworth-Heinemann, 4th ed. ed., 1999.

[36] CoventorWare, *ANALYZER Reference: Standard Capabilities*. CoventorWare Inc., version 2012 ed., 2012.

[37] G. G. Stoney, "The tension of metallic films deposited by electrolysis," *Proceedings of The Royal Society A*, vol. 82, no. 11, pp. 172 – 175, 1909.

[38] D. C. Miller, C. F. Herrmann, H. J. Maier, S. M. George, C. R. Stoldt, and K. Gall, "Thermomechanical evolution of multilayer thin films: Part I. mechanical behavior of Au/Cr/Si microcantilevers," *Thin Solid Films*, vol. 515, pp. 3208–3223, 2007.

[39] D. R. Lide, *Handbook of chemistry and physic*. CRC Press, 2004.

[40] T. P. Weihs, S. Hong, J. C. Bravman, and W. D. Nix, "Mechanical deflection of cantilever microbeams: a new technique for testing the mechanical properties of thin films," *Journal of Materials Research*, vol. 3, pp. 931–942, 1988.

[41] M. Hopcroft, W. Nix, and T. Kenny, "What is the Young's modulus of silicon?," *Journal of Microelectromechanical Systems*, vol. 19, pp. 229 –238, Apr. 2010.

[42] J.-H. Jou, C.-N. Liao, and K.-W. Jou, "A method for the determination of gold thin film's mechanical properties," *Thin Solid Films*, vol. 238, no. 1, pp. 70 – 72, 1994.

[43] Y. Okada and Y. Tokumaru, "Precise determination of lattice parameter and thermal expansion coefficient of silicon between 300 and 1500 K," *Journal of Applied Physics*, vol. 56, no. 2, pp. 314–320, 1984.

[44] Y. S. Yang, Y. H. Lin, Y. C. Hu, and C. H. Liu, "A large-displacement thermal

actuator designed for MEMS pitch-tunable grating," *Journal of Micromechanics and Microengineering*, vol. 19, p. 12pp, 2009.

[45] P. W. Chapman, O. N. Tufte, J. D. Zook, and D. Long, "Electrical properties of heavily doped silicon," *Journal of Applied Physics*, vol. 34, pp. 3291 –3295, Nov. 1963.

[46] P. J. Timans, "Emissivity of silicon at elevated temperatures," *Journal of Applied Physics*, vol. 74, pp. 6353 –6364, Nov. 1993.

[47] L. N. Aksyutov, "Normal spectral emissivity of gold, platinum, and tungsten," *Journal of Engineering Physics and Thermophysics*, vol. 27, pp. 913–917.

[48] L. Li, V. Stankovic, L. Stankovic, L. Li, S. Cheng, and D. Uttamchandani, "Single pixel optical imaging using a scanning MEMS mirror," *Journal of Micromechanics and Microengineering*, vol. 21, no. 2, p. 025022, 2011.

[49] A. Nisar, N. Afzulpurkar, B. Mahaisavariya, and A. Tuantranont, "MEMS-based micropumps in drug delivery and biomedical applications," *Sensors and Actuators B: Chemical*, vol. 130, no. 2, pp. 917 – 942, 2008.

[50] N. Chronis and L. Lee, "Electrothermally activated SU-8 microgripper for single cell manipulation in solution," *Journal of Microelectromechanical Systems*, vol. 14, pp. 857 – 863, Aug. 2005.

[51] M. C. Wu, O. Solgaard, and J. E. Ford, "Optical MEMS for lightwave communication," *Lightwave Technology, Journal of*, vol. 24, pp. 4433 –4454, Dec. 2006.

[52] C. L. Arrasmith, D. L. Dickensheets, and A. Mahadevan-Jansen, "MEMS-based handheld confocal microscope for in-vivo skin imaging," *Optics Express*, vol. 18, pp. 3805–3819, Feb. 2010.

[53] A. D. Yalcinkaya, H. Urey, D. Brown, T. Montague, and R. Sprague,

"Two-axis electromagnetic microscanner for high resolution displays," *Journal of Microelectromechanical Systems*, vol. 15, pp. 786–794, Aug. 2006.

[54] Microvision, Inc., "Microvision.com." http://www.microvision.com/.

[55] S. Fuller, E. Wilhelm, and J. Jacobson, "Ink-jet printed nanoparticle microelectromechanical systems," *Journal of Microelectromechanical Systems*, vol. 11, pp. 54 –60, Feb. 2002.

[56] M. De Volder and D. Reynaerts, "Pneumatic and hydraulic microactuators: a review," *Journal of Micromechanics and Microengineering*, vol. 20, Apr. 2010.

[57] P. Poosanaas, K. Tonooka, and K. Uchino, "Photostrictive actuators," *Mechatronics*, vol. 10, no. 45, pp. 467 – 487, 2000.

[58] K. Hashimoto, M. Yamaguchi, H. Kogo, and M. Naoe, "Magnetostrictive properties of sputtered Co-Cr film on surface acoustic wave," *IEEE Transactions on Magnetics*, vol. 17, no. 6, pp. 3181–3183, 1981.

[59] U. Zaghloul, G. Papaioannou, B. Bhushan, F. Coccetti, P. Pons, and R. Plana, "On the reliability of electrostatic NEMS/MEMS devices: Review of present knowledge on the dielectric charging and stiction failure mechanisms and novel characterization methodologies," *Microelectronics Reliability*, vol. 51, no. 911, pp. 1810 – 1818, 2011.

[60] W. Riethmuller and W. Benecke, "Thermally excited silicon microactuators," *IEEE Transactions on Electron Devices,*, vol. 35, pp. 758 –763, Jun. 1988.

[61] S. Timoshenko, "Analysis of bi-metal thermostats," *Journal of the Optical Society of America*, vol. 11, pp. 233–255, Sep. 1925.

[62] S. Pal and H. Xie, "A curved multimorph based electrothermal micromirror with large scan range and low drive voltage," *Sensors and Actuators A: Physical*, vol. 170, no. 12, pp. 156 – 163, 2011.

[63] J. H. Comtois and V. M. Bright, "Applications for surface-micromachined polysilicon thermal actuators and arrays," *Sensors and Actuators A: Physical*, vol. 58, no. 1, pp. 19 – 25, 1997.

[64] Q.-A. Huang and N. K. S. Lee, "Analysis and design of polysilicon thermal flexure actuator," *Journal of Micromechanics and Microengineering*, vol. 9, no. 1, p. 64, 1999.

[65] Q.-A. Huang and N. K. S. Lee, "Analytical modeling and optimization for a laterally-driven polysilicon thermal actuator," *Microsystem Technologies*, vol. 5, pp. 133–137, 1999.

[66] N. D. Mankame and G. K. Ananthasuresh, "Comprehensive thermal modelling and characterization of an electro-thermal-compliant microactuator," *Journal of Micromechanics and Microengineering*, vol. 11, no. 5, p. 452, 2001.

[67] R. Hickey, M. Kujath, and T. Hubbard, "Heat transfer analysis and optimization of two-beam microelectromechanical thermal actuators," vol. 20, pp. 971–974, AVS, 2002.

[68] L. Que, J.-S. Park, M.-H. Li, and Y. Gianchandani, "Reliability studies of bent-beam electro-thermal actuators," in *Reliability Physics Symposium, 2000. Proceedings. 38th Annual 2000 IEEE International*, pp. 118 –122, 2000.

[69] J. M. Maloney, D. S. Schreiber, and D. L. DeVoe, "Large-force electrothermal linear micromotors," *Journal of Micromechanics and Microengineering*, vol. 14, no. 2, p. 226, 2004.

[70] W.-C. Chen, C.-C. Chu, J. Hsieh, and W. Fang, "A reliable single-layer out-of-plane micromachined thermal actuator," *Sensors and Actuators A: Physical*, vol. 103, no. 12, pp. 48 – 58, 2003.

[71] W.-C. Chen, P.-I. Yeh, C.-F. Hu, and W. Fang, "Design and characterization of single-layer step-bridge structure for out-of-plane thermal actuator," *Journal of Microelectromechanical Systems*, vol. 17, pp. 70 –77, Feb. 2008.

[72] C. Elbuken, N. Topaloglu, P. Nieva, M. Yavuz, and J. Huissoon, "Modeling and analysis of a 2-DOF bidirectional electro-thermal microactuator," *Microsystem Technologies*, vol. 15, pp. 713–722, 2009.

[73] A. Atre, "Analysis of out-of-plane thermal microactuators," *Journal of Micromechanics and Microengineering*, vol. 16, no. 2, p. 205, 2006.

[74] D. Girbau, M. Llamas, J. Casals-Terre, X. Simo-Selvas, L. Pradell, and A. Lazaro, "A low-power-consumption out-of-plane electrothermal actuator," *Journal of Microelectromechanical Systems*, vol. 16, pp. 719 –727, Jun. 2007.

[75] L. Li and D. Uttamchandani, "Dynamic response modelling and characterization of a vertical electrothermal actuator," *Journal of Micromechanics and Microengineering*, vol. 19, no. 7, p. 075014, 2009.

[76] W. Trimmer, "Microrobots and micromechanical systems," *Sensors and Actuators*, vol. 19, pp. 267–287, Sep. 1 1989.

[77] W.-M. Zhang, G. Meng, and D. Chen, "Stability, nonlinearity and reliability of electrostatically actuated MEMS devices," *Sensors*, vol. 7, pp. 760–796, May 2007.

[78] P. Favrat, L. Paratte, H. Ballan, M. Declercq, and N. deRooij, "A 1.5-V-supplied CMOS ASIC for the actuation of an electrostatic micromotor," *IEEE-ASME Transactions on Mechatronics*, vol. 2, pp. 153–160, Sep. 1997.

[79] F. Beyeler, A. Neild, S. Oberti, D. J. Bell, Y. Sun, J. Dual, and B. J. Nelson, "Monolithically Fabricated Microgripper With Integrated Force Sensor for Manipulating Microobjects and Biological Cells Aligned in an Ultrasonic Field," *Journal of Microelectromechanical Systems*, vol. 16, pp. 7 –15, Feb. 2007.

[80] E. Brown, "RF-MEMS switches for reconfigurable integrated circuits," *Microwave Theory and Techniques, IEEE Transactions on*, vol. 46, pp. 1868 –1880, Nov. 1998.

[81] W. Pan, P. Soussan, B. Nauwelaers, and H. A. Tilmans, "A surface micromachined electrostatically tunable film bulk acoustic resonator," *Sensors and Actuators A: Physical*, vol. 126, no. 2, pp. 436 – 446, 2006.

[82] R. Krishnamoorthy, T. Bifano, and G. Sandri, "Statistical performance evaluation of electrostatic micro actuators for a deformable mirror," in *Microelectronics Structures and MEMS for Optical Processing II* (Motamedi, ME and Bailey, W, ed.), vol. 2881 of *Proceedings of The Society of Photo-Optical Instrumentation Engineers (SPIE)*, pp. 35–44, 1996.

[83] M.-H. Kiang, O. Solgaard, K. Lau, and R. Muller, "Electrostatic combdrive-actuated micromirrors for laser-beam scanning and positioning," *Journal of Microelectromechanical Systems*, vol. 7, pp. 27 –37, Mar. 1998.

[84] K. Oda, H. Takao, K. Terao, T. Suzuki, F. Shimokawa, I. Ishimaru, and F. Oohira, "Vertical comb-drive MEMS mirror with sensing function for phase-shift device," *Sensors and Actuators A: Physical*, vol. 181, no. 0, pp. 61 – 69, 2012.

[85] H.-K. Chang and Y.-K. Kim, "UV-LIGA process for high aspect ratio structure using stress barrier and C-shaped etch hole," *Sensors and Actuators A: Physical*, vol. 84, no. 3, pp. 342 – 350, 2000.

[86] D. Hah, P. Patterson, H. Nguyen, H. Toshiyoshi, and M. Wu, "Theory and experiments of angular vertical comb-drive actuators for scanning micromirrors," *IEEE Journal of Selected Topics in Quantum Electronics*, vol. 10, pp. 505 – 513, May-Jun. 2004.

[87] C. Storment, D. Borkholder, V. Westerlind, J. Suh, N. Maluf, and G. Kovacs, "Flexible, dry-released process for aluminum electrostatic actuators," *Journal of Microelectromechanical Systems*, vol. 3, pp. 90 –96, Sep. 1994.

[88] M. Douglass, "Lifetime estimates and unique failure mechanisms of the Digital

Micromirror Device (DMD)," in *Reliability Physics Symposium Proceedings, 1998. 36th Annual. 1998 IEEE International*, pp. 9 –16, 31 1998-april 2 1998.

[89] Texas Instruments Inc., "DLP Technology." http://www.dlp.com/.

[90] J. Yao, "RF MEMS from a device perspective," *Journal of Micromechanics and Microengineering*, vol. 10, pp. R9–R38, Dec. 2000.

[91] L. Larson, R. Hackett, M. Melendes, and R. Lohr, "Micromachined microwave actuator (MIMAC) technology-a new tuning approach for microwave integrated circuits," in *Microwave and Millimeter-Wave Monolithic Circuits Symposium, 1991. Digest of Papers, IEEE 1991*, pp. 27 –30, Jun. 1991.

[92] H. Nguyen, D. Hah, P. Patterson, R. Chao, W. Piyawattanametha, E. Lau, and M. Wu, "Angular vertical comb-driven tunable capacitor with high-tuning capabilities," *Journal of Microelectromechanical Systems*, vol. 13, pp. 406 – 413, Jun. 2004.

[93] W. Piyawattanametha, P. Patterson, D. Hah, H. Toshiyoshi, and M. Wu, "Surface- and bulk- micromachined two-dimensional scanner driven by angular vertical comb actuators," *Journal of Microelectromechanical Systems*, vol. 14, pp. 1329 – 1338, Dec. 2005.

[94] Y. K. Hong and R. Syms, "Dynamic response modeling of MEMS micromirror corner cube reflectors with angular vertical combdrives," *Journal of Lightwave Technology*, vol. 25, pp. 472 –480, Feb. 2007.

[95] T. Sasaki and K. Hane, "Initial deflection of silicon-on-insulator thin membrane micro-mirror and fabrication of varifocal mirror," *Sensors and Actuators A: Physical*, vol. 172, no. 2, pp. 516 – 522, 2011.

[96] Y. Shao and D. L. Dickensheets, "MOEMS 3-D scan mirror for single-point control of beam deflection and focus," *Journal of Micro/Nanolithography, MEMS, and MOEMS*, vol. 4, no. 4, pp. 041502–041502–7, 2005.

[97] B. Qi, A. P. Himmer, L. M. Gordon, X. V. Yang, L. D. Dickensheets, and I. A. Vitkin, "Dynamic focus control in high-speed optical coherence tomography based on a microelectromechanical mirror," *Optics Communications*, vol. 232, no. 16, pp. 123 – 128, 2004.

[98] V. X. D. Yang, Y. Mao, B. A. Standish, N. R. Munce, S. Chiu, D. Burnes, B. C. Wilson, I. A. Vitkin, P. A. Himmer, and D. L. Dickensheets, "Doppler optical coherence tomography with a micro-electro-mechanical membrane mirror for high-speed dynamic focus tracking," *Optics Letters*, vol. 31, pp. 1262–1264, May 2006.

[99] H.-C. Wei, Y.-H. Chien, W.-Y. Hsu, Y.-C. Cheng, and G.-D. J. Su, "Controlling a MEMS deformable mirror in a miniature auto focusing imaging system," *IEEE Transactions on Control Systems Technology*, vol. 20, pp. 1592–1596, Nov. 2012.

[100] G. Vdovin, "Quick focusing of imaging optics using micromachined adaptive mirrors," *Optics Communications*, vol. 140, no. 46, pp. 187 – 190, 1997.

[101] P. A. Himmer, D. L. Dickensheets, and R. A. Friholm, "Micromachined silicon nitride deformable mirrors for focus control," *Optics Letters*, vol. 26, pp. 1280–1282, Aug. 2001.

[102] W. Liu and J. J. Talghader, "Current-controlled curvature of coated micromirrors," *Optics Letters*, vol. 28, pp. 932–934, Jun. 2003.

[103] W. Greger, D. Arnold, R. Jurischka, A. Schoth, C. Muller, J. Wilde, and H. Reinecke, "A new approach for focusing deformable mirrors fabricated in polymer technology," in *Optical MEMS and Their Applications Conference, 2005. IEEE/LEOS International Conference on*, pp. 45 –46, Aug. 2005.

[104] U. M. Mescheder, C. Esta, G. Somogyi, and M. Freudenreich, "Distortion optimized focusing mirror device with large aperture," *Sensors and Actuators A: Physical*, vol. 130131, no. 0, pp. 20 – 27, 2006.

[105] A. A. Alzaydi, J. T. Yeow, and S. L. Lee, "Hydraulic controlled polyester-based micro adaptive mirror with adjustable focal length," *Mechatronics*, vol. 18, no. 2, pp. 61 – 70, 2008.

[106] R. Hokari and K. Hane, "A varifocal convex micromirror driven by a bending moment," *IEEE Journal of Selected Topics in Quantum Electronics*, vol. 15, pp. 1310 –1316, Sep.-Oct. 2009.

[107] T. Sasaki and K. Hane, "Varifocal micromirror integrated with comb-drive scanner on silicon-on-insulator wafer," *Journal of Microelectromechanical Systems*, vol. 21, pp. 971 –980, Aug. 2012.

[108] J.-L. Wang, T.-Y. Chen, Y.-H. Chien, and G.-D. J. Su, "Miniature optical autofocus camera by micromachined fluoropolymer deformable mirror," *Optics Express*, vol. 17, pp. 6268–6274, Apr. 2009.

[109] M. Ward and F. Briarmonte, "Lucent's new all-optical router uses Bell labs microscopic mirrors," Nov. 1999. http://www.bell-labs.com/news/1999/november/10/1.html.

[110] H. Urey, "MEMS scanners for display and imaging applications," in *Optomechatronic Micro/Nano Components, Devices, and Systems* (Katagiri, Y, ed.), vol. 5604 of *Proceedings of The Society of Photo-Optical Instrumentation Engineers (SPIE)*, pp. 218–229, 2004.

[111] Y. Ko, J. Cho, Y. Mun, H. Jeong, W. Choi, J. Kim, Y. Park, J. Yoo, and J. Lee, "Eye-type scanning mirror with dual vertical combs for laser display," *Sensors and Actuators A: Physical*, vol. 126, pp. 218–226, Jan 26 2006.

[112] M. Yoda, K. Isamoto, C. Chong, H. Ito, A. Murata, S. Kamisuki, M. Atobe, and H. Toshiyoshi, "A MEMS 1D optical scanner for laser projection display using self-assembled vertical combs and scan-angle magnifying mechanism," in *Solid-State Sensors, Actuators and Microsystems, 2005. Digest of Technical*

Papers. TRANSDUCERS '05. The 13th International Conference on, vol. 1, pp. 968 – 971 Vol. 1, Jun. 2005.

[113] L. Zhou, M. Last, V. Milanovic, J. Kahn, and K. Pister, "Two-axis scanning mirror for free-space optical communication between uavs," in *Optical MEMS, 2003 IEEE/LEOS International Conference on*, pp. 157 – 158, Aug. 2003.

[114] A. Jain, A. Kopa, Y. Pan, G. Fedder, and H. Xie, "A two-axis electrothermal micromirror for endoscopic optical coherence tomography," *IEEE Journal of Selected Topics in Quantum Electronics*, vol. 10, pp. 636 – 642, May-Jun. 2004.

[115] Y. HAGA and M. ESASHI, "Biomedical microsystems for minimally invasive diagnosis and treatment," *Proceedings of the IEEE*, vol. 92, pp. 98 – 114, Jan. 2004.

[116] U. Hofmann, S. Muehlmann, M. Witt, K. Dorschel, R. Schutz, and B. Wagner, "Electrostatically driven micromirrors for a miniaturized confocal laser scanning microscope," in *Miniaturized Systems With Micro-Optics And MEMS* (Motomedi, ME and Goering, R, ed.), vol. 3878 of *Proceedings of The Society of Photo-Optical Instrumentation Engineers (SPIE)*, pp. 29–38, 1999.

[117] H. Miyajima, M. Nishio, Y. Kamiya, M. Ogata, Y. Sakai, and H. Inoue, "Development of two dimensional scanner-on-scanner for confocal laser scanning microscope "LEXT" series," in *Optical MEMS and Their Applications Conference, 2005. IEEE/LEOS International Conference on*, pp. 23 –24, Aug. 2005.

[118] K. Isamoto, K. Totsuka, T. Suzuki, T. Sakai, A. Morosawa, C. Chong, H. Fujita, and H. Toshiyoshi, "A high speed MEMS scanner for 140-kHz SS-OCT," in *Optical MEMS and Nanophotonics (OMN), 2011 International Conference on*, pp. 73 –74, Aug. 2011.

[119] Y. Xu, J. Singh, C. S. Premachandran, A. Khairyanto, K. W. S. Chen, N. Chen, C. J. R. Sheppard, and M. Olivo, "Design and development of a 3D

scanning MEMS OCT probe using a novel SiOB package assembly," *Journal of Micromechanics and Microengineering*, vol. 18, no. 12, p. 125005, 2008.

[120] J. Singh, J. H. S. Teo, Y. Xu, C. S. Premachandran, N. Chen, R. Kotlanka, M. Olivo, and C. J. R. Sheppard, "A two axes scanning SOI mems micromirror for endoscopic bioimaging," *Journal of Micromechanics and Microengineering*, vol. 18, no. 2, p. 025001, 2008.

[121] H. Xie, Y. Panc, and G. Fedder, "Endoscopic optical coherence tomographic imaging with a CMOS-MEMS micromirror," *Sensors and Actuators A: Physical*, vol. 103, pp. 237–241, Jan. 15 2003.

[122] H. Miyajima, K. Murakami, and M. Katashiro, "MEMS optical scanners for microscopes," *IEEE Journal of Selected Topics in Quantum Electronics*, vol. 10, pp. 514 – 527, May-Jun. 2004.

[123] K. Yu, N. Park, D. Lee, and O. Solgaard, "Superresolution digital image enhancement by subpixel image translation with a scanning micromirror," *IEEE Journal of Selected Topics in Quantum Electronics*, vol. 13, pp. 304 –311, Mar.-Apr. 2007.

[124] Y. Wang, S. Bish, J. W. Tunnell, and X. Zhang, "MEMS scanner enabled real-time depth sensitive hyperspectral imaging of biological tissue," *Optics Express*, vol. 18, pp. 24101–24108, Nov. 2010.

[125] H. Ra, W. Piyawattanametha, M. J. Mandella, P.-L. Hsiung, J. Hardy, T. D. Wang, C. H. Contag, G. S. Kino, and O. Solgaard, "Three-dimensional in vivo imaging by a handheld dual-axes confocal microscope," *Optics Express*, vol. 16, pp. 7224–7232, May 12 2008.

[126] Y. Bai, M. Pallapa, A. Chen, P. Constantinou, S. Damaskinos, B. C. Wilson, and J. T. Yeow, "A 2D MEMS mirror with sidewall electrodes applied for confocal MACROscope imaging," Feb. 2012.

[127] U. Krishnamoorthy, D. Lee, and O. Solgaard, "Self-aligned vertical electrostatic

combdrives for micromirror actuation," *Journal of Microelectromechanical Systems*, vol. 12, pp. 458 – 464, Aug. 2003.

[128] D. Hah, P. Patterson, H. Nguyen, H. Toshiyoshi, and M. Wu, "Theory and experiments of angular vertical comb-drive actuators for scanning micromirrors," *IEEE Journal of Selected Topics in Quantum Electronics*, vol. 10, pp. 505 – 513, May-Jun. 2004.

[129] J. Kim, D. Christensen, and L. Lin, "Monolithic 2-D scanning mirror using self-aligned angular vertical comb drives," *Photonics Technology Letters, IEEE*, vol. 17, pp. 2307 – 2309, Nov. 2005.

[130] W. Piyawattanametha, R. P. J. Barretto, T. H. Ko, B. A. Flusberg, E. D. Cocker, H. Ra, D. Lee, O. Solgaard, and M. J. Schnitzer, "Fast-scanning two-photon fluorescence imaging based on a microelectromechanical systems two- dimensional scanning mirror," *Optics Letters*, vol. 31, pp. 2018–2020, Jul. 2006.

[131] L. Li, M. Begbie, G. Brown, and D. Uttamchandani, "Design, simulation and characterization of a mems optical scanner," *Journal of Micromechanics and Microengineering*, vol. 17, no. 9, p. 1781, 2007.

[132] H. Urey, S. Holmstrom, and A. Yalcinkaya, "Electromagnetically actuated FR4 scanners," *Photonics Technology Letters, IEEE*, vol. 20, pp. 30 –32, Jan.1, 2008.

[133] Y. Watanabe, Y. Abe, S. Iwamatsu, S. Kobayashi, Y. Takahashi, and T. Sato, "Electromagnetically driven two-axis optical beam steering MEMS mirror and its dependence of actuation on magnetic field," *Electronics and Communications in Japan*, vol. 94, no. 11, pp. 24–31, 2011.

[134] K. Koh and C. Lee, "A two-dimensional MEMS scanning mirror using hybrid actuation mechanisms with low operation voltage," *Journal of Microelectromechanical Systems*, vol. 21, no. 5, pp. 1124–1135, 2012.

Chapter 3

Bimorph Varifocal Micromirror – Design And Analysis

3.1 Overview

MEMS varifocal devices can mechanically change their focal length. Those types of devices usually have much smaller scale (in millimeter or even in microns) comparing to conventional varifocal system using group of lenses. Common varifocal devices are usually fabricated into a microlens [1, 2] or micromirror [3]. Microlenses can change their refractive index by mechanically deforming their refractive surfaces [4] or changing optical refraction properties of the material [5]. Varifocal micromirrors (VFM) change their radius of curvature by mechanically deforming the reflective surface by using electrothermal [3], electrostatical [6, 7], piezoelectrical [8, 9] or pneumatic [10] actuation mechanisms.

Liu et al. [11] have incorporated an electrothermal VFM into a tunable optical cavity for sensing application. The 1.5 μm thick and 100 μm diameter circular polysilicon VFM can be gold coated to achieve a radius of curvature (ROC) variation from 2.5 mm to 8.2 mm. However, the rather small aperture size of their VFM significantly restricted

its use to tightly focused optical beams. Hsieh et al. [12] have demonstrated an autofocus system using a 3 mm diameter electrostatic actuated varifocal membrane. Their Z-shape optical imaging system is capable of focusing object at a distance of 160 mm and 78 mm by changing the focus power from 0 to 20 Dioptre at 0 V and 150 V respectively. However, their imaging results were not very sharp and the authors stated that this was possibly due to non coated lens surfaces and misalignment in their system.

In this chapter, the design and simulation of a 1.2 mm diameter, thermally-actuated, gold/single-crystal silicon bimorph VFM are described. This device is more than one order of magnitude bigger in diameter and about six times thicker compared to Liu's device in [3] and [11]. As opposed to the multi-electrostatic actuator driven deformable mirror used in [12], this thermally actuated VFM gives a uniformly-expanding mirror surface which exhibits very little higher-order optical aberrations. In the Section 3.2, the micromirror geometric design, fabrication and the actuation principle are described. In Section 3.3, the finite element model of the VFM built using CoventorWare is introduced and simulation results of static mechanical behaviour by electrothermal and optothermal actuation are presented. In section 3.4, the VFM performance dependence on its structural geometries is discussed.

3.2 Structure Design

3.2.1 Geometrical structure

The VFM is made up of a circular bimorph micromirror plate suspended by eight serpentine springs over a through-hole. The micromirror consists of a 1.2 mm diameter, 10 μm thick single crystal silicon layer with a 1 mm diameter, 0.65 μm thick gold layer stacked on top. The two circular layers are designed to be concentrically aligned. The gold layer on top functions as the reflective surface of the VFM. The surrounding eight serpentine springs are identically designed and are patterned in

the same 10 μm thick single crystal silicon layer as the bimorph micromirror. Each serpentine spring is 8 μm in width, and 1530.7 μm in length. They are arranged around the micromirror in an equally-spaced radial pattern. The outer ends of the suspension springs are anchored to the substrate. At each serpentine suspension anchor, a 592 μm x 392 μm rectangular gold pad is connected to provide an electrical connection. The springs provide the function of suspensions as well as electrical current pathways to the micromirror. Figure 3.1 displays the image of the VFM taken by the scanning electron microscope (SEM).

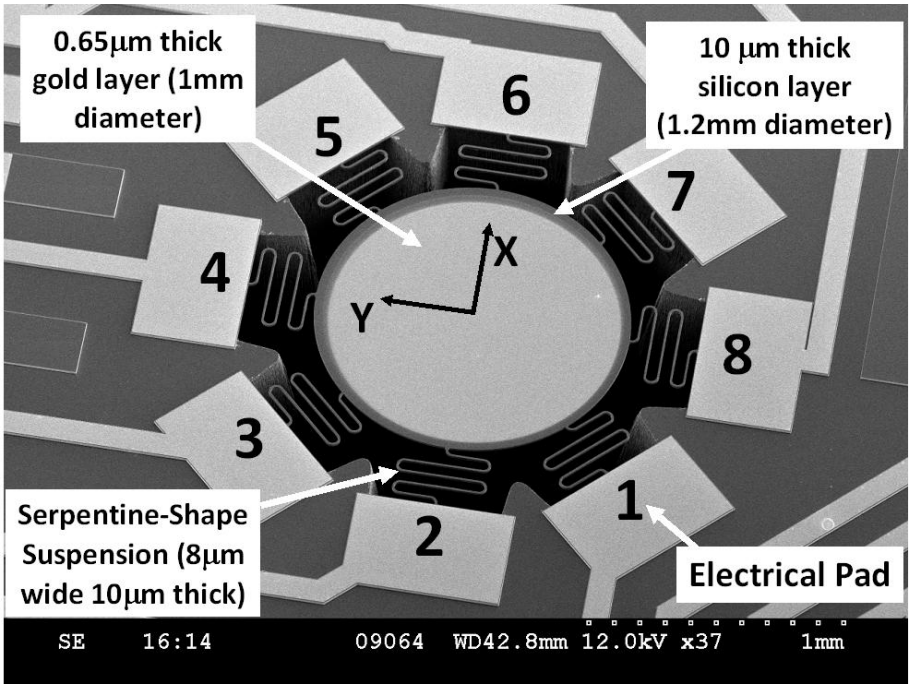

Figure 3.1: SEM image of the bimorph varifocal micromirror (VFM) fabricated using SOIMUMPs.

3.2.2 Fabrication

The VFMs were fabricated in silicon-on-insulator multi-users MEMS fabrication processes (SOIMUMPs) [13] performed by MEMSCAP Inc. using a 10 μm thick SOI (silicon-on-insulator) wafer. The SOI layer used in these fabrication proceses are known to present an in-plane compressive residual stress of -3.9 MPa [14] as well as a through thickness stress gradient of $\sim$2.4 MPa/μm [14, 15]. The 0.65 μm thickness gold layer evaporated on top of the silicon layer by the E-beam tool experiences an

in-plane tensile residual stress of around $\sim$274.7$\pm$11 MPa. The characterisation of the stress gradient of the SOI layer and the in-plane residual stress of the gold layer are detailed in Section 2.5.2. The combined stresses of these two stacked layers result in an initial concave curvature on the VFM surface after fabrication. Due to condition variation during the fabrication processes, different VFMs, even fabricated in the same process, have slightly different initial ROCs. The detailed characterisation of the initial surface shapes of VFM samples will be described in Section 4.3.1.

3.2.3 Actuation method

The bimorph structure of the micromirror of the VFM can change the surface curvature when the mirror body experiences a temperature change. Due to the mismatched coefficients of thermal expansion (CTE) between the gold and silicon layers of the VFM, the two layers expand or contract by different magnitudes when the temperature changes. During a temperature rise, the gold layer, with a higher CTE of $1.41\text{x}10^{-5}$ K^{-1} [16], expands more than the silicon layer, with a lower CTE of $2.5\text{x}10^{-6}$ K^{-1} [17] and the VFM surface becomes flatter from its initially concave shape. With a temperature drop, the gold layer will contract more than the silicon layer and the VFM surface becomes more concave.

A temperature rise can be provided either by electrothermal actuation or optothermal actuation. During the electrothermal actuation, a DC potential difference is introduced between any pair (or pairs) of two electrical pads of the VFM. The current flows through the gold pad(s) and the connecting serpentine spring(s), into the cross-section of the mirror body of VFM and exit through another serpentine spring(s) and the corresponding gold pad(s). A temperature rise occurs to the VFM as a result of Joule heating where the current is flowing. During optothermal actuation, a temperature rise is generated on the VFM by converting the absorbed optical power to heat when a laser beam is incident on the silicon surface on the bottom of the VFM.

The surface shape of the gold layer of VFM is quantified by the measured radius of

curvature (ROC). When the reflective surface of the gold layer is parallel to the X-Y plane in the coordinate system, the pointing away upwards from surface is noted as the vertical positive of the Z-axis in the coordinate system of VFM, the negative ROC indicates a concave gold surface shape and the positive ROC indicates a convex surface shape. Therefore, at a temperature rise, the VFM ROC will change to a higher value; and at the temperature drop, the VFM ROC will change to a lower value. Since the curvature of the VFM described does not change from concave to convex shape, the ROC value of the VFM are all described as positive for simplification.

3.3 Finite Element Simulation

To understand and visualize the static thermo-mechanical behaviour of the VFM, the computer-aid Finite Element Method (FEM) tool, CoventorWare [18], was used to build a solid model of the VFM and calculate the thermal and mechanical response during each actuation method, namely the electrothermal and optothermal actuation. Specifically, the temperature distribution over the device structure, such as the value and location of the maximum temperature on the device, is calculated and displayed as well as the average temperature of the gold surface. The mechanical deformation of the VFM can be obtained by calculating the curvature variation of the gold layer surface at each actuation power level.

3.3.1 FEM model

The VFM model was built directly from the 2D layout design file which is used for fabrication processes. Thus, the geometric error between the model and the fabricated device is due to either the assumption set in CoventorWare or the tolerance of the actual processes provided by MEMSCAP Inc foundry. Figure 3.2 shows the 3D model of VFM built in CoventorWare.

The model of VFM is made up of two stacked material layers. The top layer is a

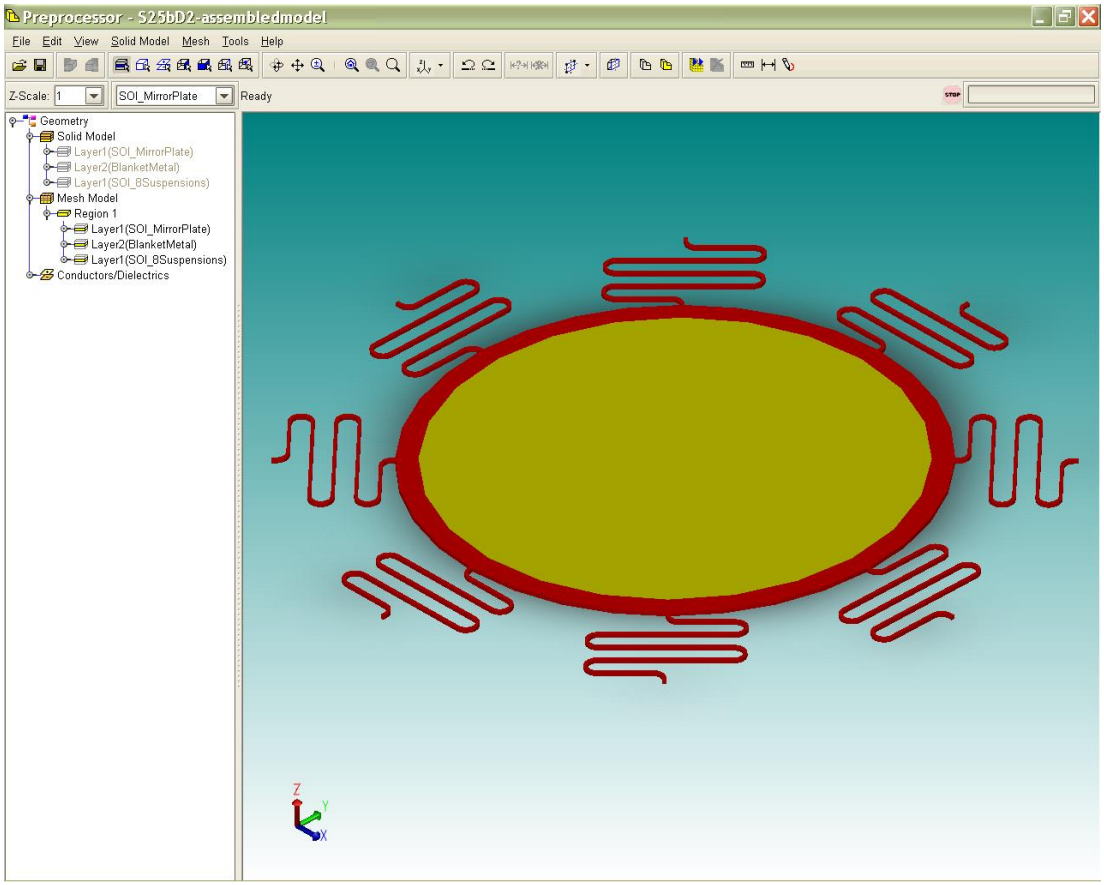

Figure 3.2: The solid model of VFM building in CoventorWare

0.65 μm thick layer of gold (concenterically coated on the silicon micromirror surface) which is the reflective part of the VFM, and the second layer is the 10 μm thick silicon material including the micromirror and eight suspensions. The material properties used for the gold layer and the single crystal silicon layer of VFM are described in Table 2.3 on page 29. From the geometric dimensions, the model can be considered to have three parts, the eight suspensions, the gold layer and silicon layer of the bimorph micromirror plate. As shown in Table 3.1, each suspension is identically designed to be thin and long with an aspect ratio[1] of 10 and the circular layers of silicon and the gold in the micromirror have aspect ratio of 33630 and 1500 respectively. Due to the fact of the very different aspect ratios between parts of the bimorph micromirror and suspensions, it is difficult to mesh the model with the same meshing element type and provide high meshing quality at the same time.

[1]The aspect ratio is defined as $A^{\frac{3}{2}}/V$, where A is the area of the surface parallel to the wafer top and V is the layer volume [19, section 2.3].

Table 3.1: The geometric summary for the VFM solid model of built in CoventorWare.

VFM Solid Model Parts	A [μm^2]	V [μm^3]	Aspect ratio ($A^{\frac{3}{2}}/V$)
Suspension	12216	122155	10
Silicon layer of micromirror	1130973	11309734	106
Gold layer of micromirror	950332	6177186	150

A is the area of the top surface on the structure parelleled with wafer plane (X and Y - axes), V is the volume of the parts.

3.3.2 Meshing of the model

According to the meshing guideline provided by CoventorWare Analyzer Reference [19, section 4.33] described in Section 2.5.3, due to stresses existing in the device layers after fabrication, parabolic shapes are stated to be suitable meshing elements. To demostrate and investigate the FEM simulation consistence using different shapes of parabolic meshing elements, the VFM solid model was first meshed with parabolic tetrahedrons of one element through the layer thickness and then meshed with parabolic hexahedrons of two elements through the layer thickness.

Tetrahedrons can be used for any 3D geometry in theory [19, section 2.3.4]. Ideally, an average corner angle of 60^o among all the tetrahedrons used to mesh the solid model indicates good quality meshing results. However, due to the aspect ratio difference among the parts of VFM model, the average corner angle of tetrahedrons of VFM is around 70^o even with a reduced mesh size. The eight suspensions were set to use tetrahedrons of an average element faces of 30. The bimorph micromirror plate was set to use tetrahedrons of an average element faces of 50. The illustration of the FEM meshing using tetrahedron and hexahedron elements are displayed in Figure 3.3. The meshing quality of the VFM FEM model using the parabolic tetrahedrons is summarised in Table 3.2. For comparison, the VFM model was also meshed with parabolic hexahedrons element as shown in Figure 3.4. Since there are 27 nodes per parabolic hexahedron shape, it is more computational expensive to simulate with parabolic hexahedrons. Therefore, a less dense meshing is set when using parabolic hexahedrons as summarised in Table 3.3.

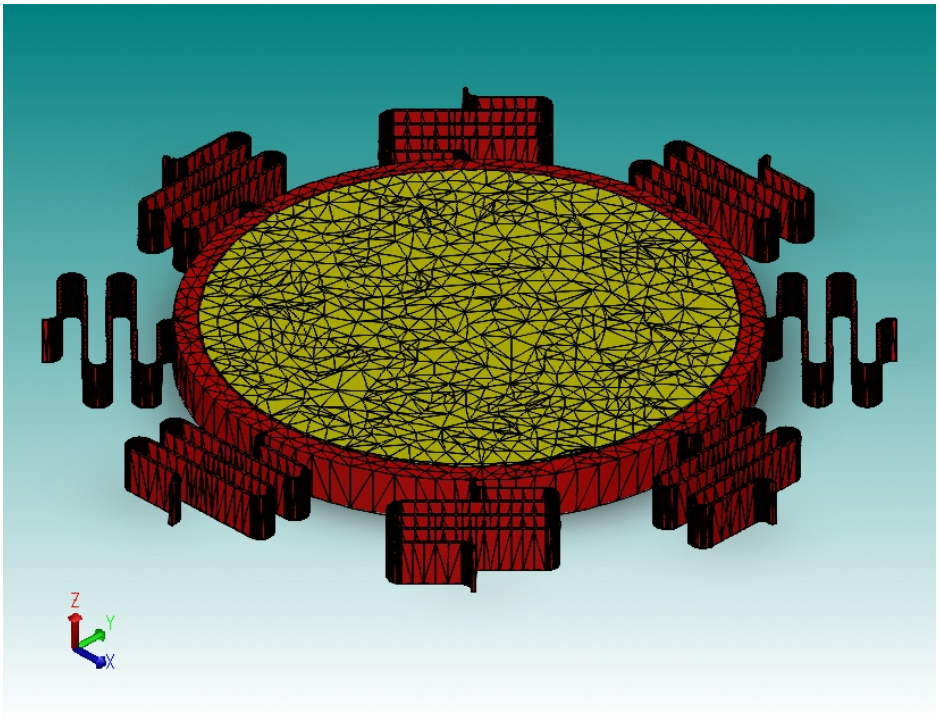

Figure 3.3: Parabolic tetrahedron element meshed VFM model.(The model is 10 times scaled in thickness direction for viewing clarity.)

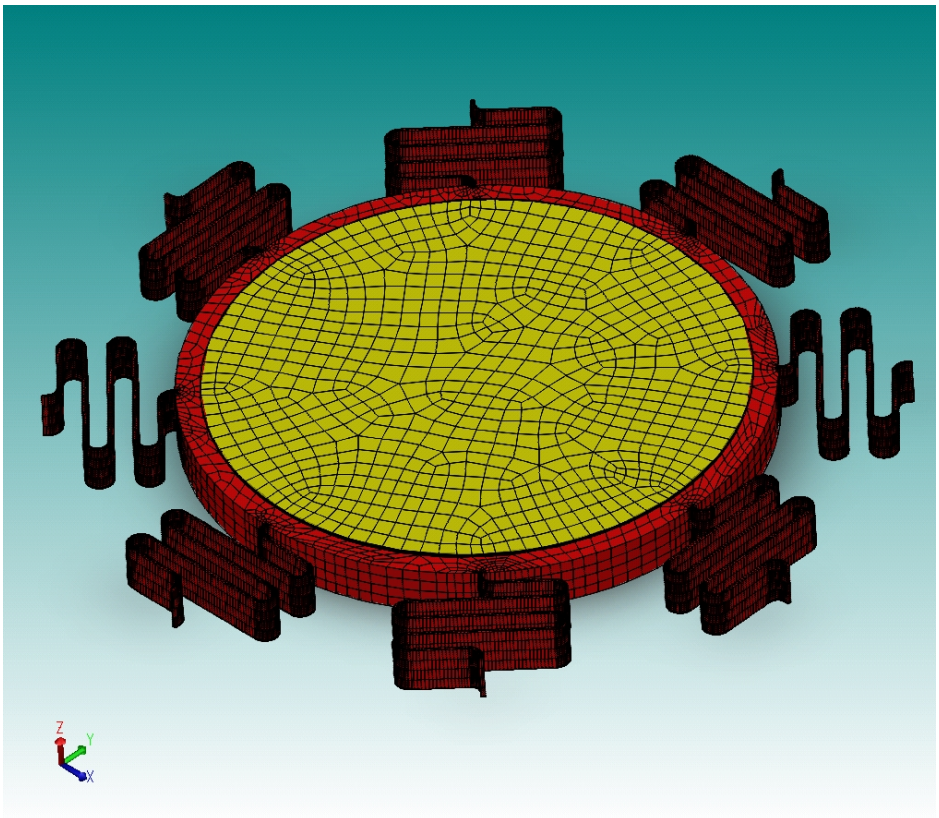

Figure 3.4: Linear shell hexahedron element meshed VFM model.(The model is 10 times scaled in thickness direction for viewing clarity.)

Table 3.2: Mesh setting and quality results of the varifocal micromirror by parabolic tetrahedrons meshing elements

Parts		Unit	Serpentine spring	Gold Coated Micromirror	
				Silicon layer	Gold layer
Meshing Element Shape			Parabolic Tetrahedrons		
Number of volume meshing elements			942	5090	4677
Number of volume meshing nodes			2618	10585	9513
Element Aspect Ratio	Min		1.1	1.2	10
	Max		9.0	31.4	157.0
	Average		2.1	4.7	70
Element Corner Angle	Min	°	9.4	2.1	0.4
	Max		144.7	161.1	177
	Average		70	70	70
Edge Length	Min	μm	1.2	1.9	0.65
	Max		31.4	104	102.8
	Average		11.9	37.0	36.1

Table 3.3: Mesh setting and quality results of the varifocal micromirror by parabolic hexahedron meshing elements

Parts		Unit	Serpentine spring	Gold Coated Micromirror	
				Silicon layer (*)	Gold layer
Meshing Element Shape			Parabolic Hexahedrons		
Number of volume meshing elements			1680	3233	13392
Number of volume meshing nodes			26454	39396	161691
Element Aspect Ratio	Min		1	1	7.3
	Max		4.0	4.1	18
	Average		1.7	2.5	32.6
Element Corner Angle	Min	°	3.6	39.5	44.3
	Max		176	143	143
	Average		89	90	90
Edge Length	Min	μm	0.6	4	0.65
	Max		22.5	33	16.7
	Average		9	17	6.9

(*): The compressive stress -3.9 MPa within the silicon layer of the VFM has to be ignored when simulating with the hexahedron meshing element, due to the limited computational resources. For accurrate simulation with hexahedrons and including the compressive stress of the silicon layer, much higher meshing density is required.

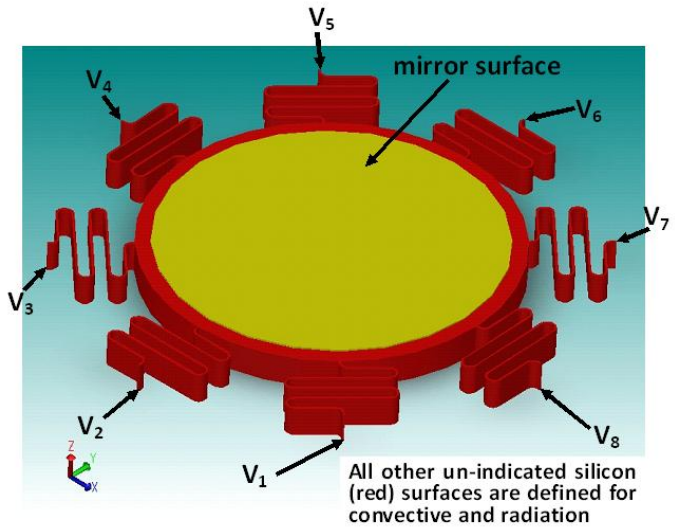

Figure 3.5: Surfaces named in the 3D VFM solid model. (The model is 10 times scaled in thickness direction for viewing clarity.)

3.3.3 Simulation results of electrothermally actuated VFM

The electro-thermo-mechanical (ETM) behaviour of an electrothermally actuated VFM is simulated by applying 11 voltage potential levels between 0 V and 10 V to the selected faces from V1 to V8 in Figure 3.5. The gold layer has an in-plane tensile residual stress of around 285 MPa [20] while the silicon layer has an in-plane compressive residual stress of around -3.9 MPa [14] and through thickness stress gradient of 2.4 MPa/μm [15]. Thermal losses such as heat conduction from the VFM device to the substrate, heat convection and radiation from the surfaces to the surrounding environment were included in the FEM. The ambient air temperature and the convection coefficient were assumed to be 20^{o}C and 25 W/m^{2}K respectively. The material properties of the structural silicon and the gold layers of the VFM used in the FEM are listed in Table 2.3.

Figure 3.6 plots the estimated ROC calculated from VFM models meshed by tetrahedrons and hexahedrons during electrothermal actuation. Mechanical simulations on the curvature variation as a function of the electrothermally actuation power, using tetrahedron and hexahedron meshing elements has an agreement of 96%. Table C.1 and Table C.2 list the simulated thermal and mechanical results of VFM

model using the two different meshing element shapes. FEM simulation results of the VFM model shown later in this chapter are made by the the solid model with tetrahedron meshing elements.

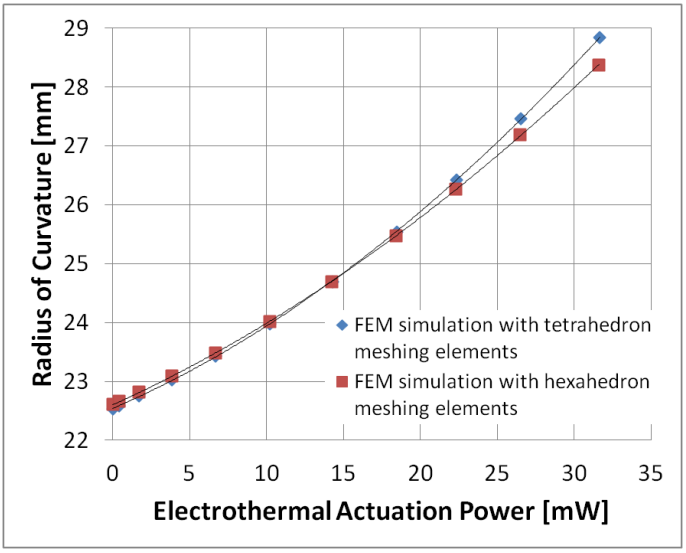

Figure 3.6: The estimated ROC of the electrothermally actuated VFM FEM model meshed by tetrahedron and hexahedron meshing elements.

Next, the temperature distribution when the VFM model is actuated through two opposite electrical pads, V1 and V5, (Figure 3.7) and through two adjacent electrical pads, V1 and V2 (Figure 3.8) was also simulated. As expected, when actuated electrothermally through the electric pads, the highest temperature is located in the middle of the serpentine-shape springs. In Figure 3.7b and Figure 3.8b, the maximum temperature (red) on the mirror edge is $\sim 12^{o}$ and $\sim 15^{o}$ higher than the minimum temperature (blue) on the rest of the micromirror when driven through two opposite and adjacent electrical pads respectively. However, the illustrations include the area of the 1.2 mm diameter circular silicon layer and the 1 mm diameter gold layer. This slightly smaller diameter gold layer is chosen to be deposited on the top of the silicon layer in order to avoid the over-heating on the gold layer edge due to the high temperature generated by the thin silicon supports during electrothermal actuation. Therefore, after hiding both the springs and the silicon layer of the micromirror as illustrated in Figure 3.7c and Figure 3.8c, the maximum temperature on the mirror edge is 5^{o}C and 7^{o}C higher than the rest of the micromirror at 33 mW when the electrothermal actuation power is applied through two opposite and adjacent supporting springs respectively.

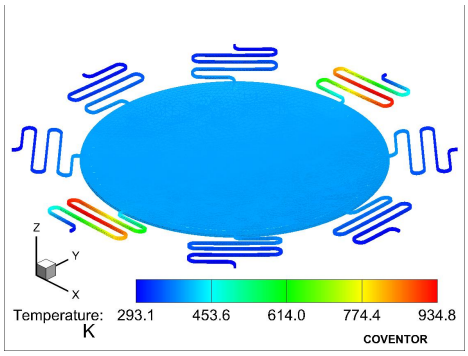

(a) Overview

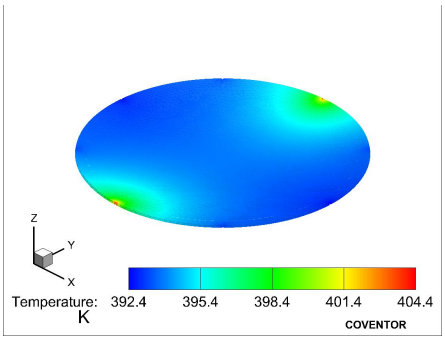

(b) Gold and silicon layers

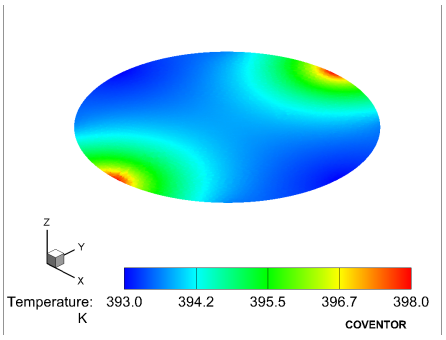

(c) Gold layer of micromirror

Figure 3.7: FEM simulation of the temperature distribution of the bimorph varifocal micromirror when driven a pair of opposite electric pads at 33 mW.

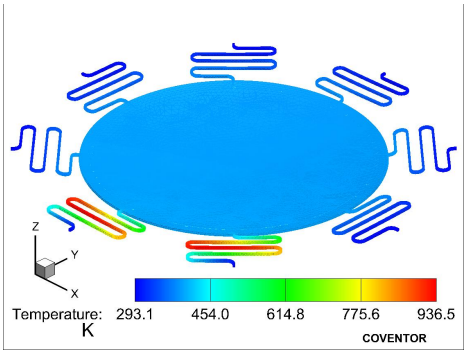

(a) Overview

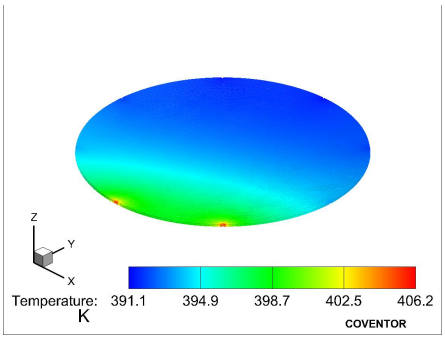

(b) Gold and silicon layers

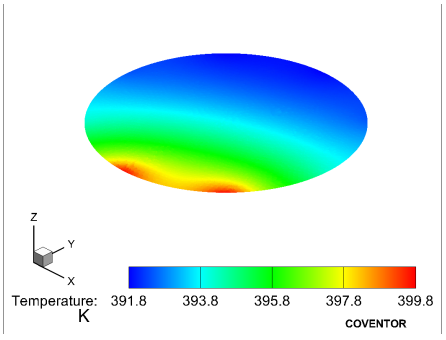

(c) Gold layer of micromirror

Figure 3.8: FEM simulation of the temperature distribution of the bimorph varifocal micromirror when driven pair ofadjacent electric pads at 33 mW.

Since the mechanical deformation of this VFM responds to the average temperature of the bimorph micromirror, the calculated average temperature rise on the micromirror surface as a function of electrothermal actuation power is plotted in Figure 3.9. The estimated averaged temperature of the VFM changes linearly with the actuating power. VFM surface reaches a static average temperature of around 120^oC at driving power of 33 mW.

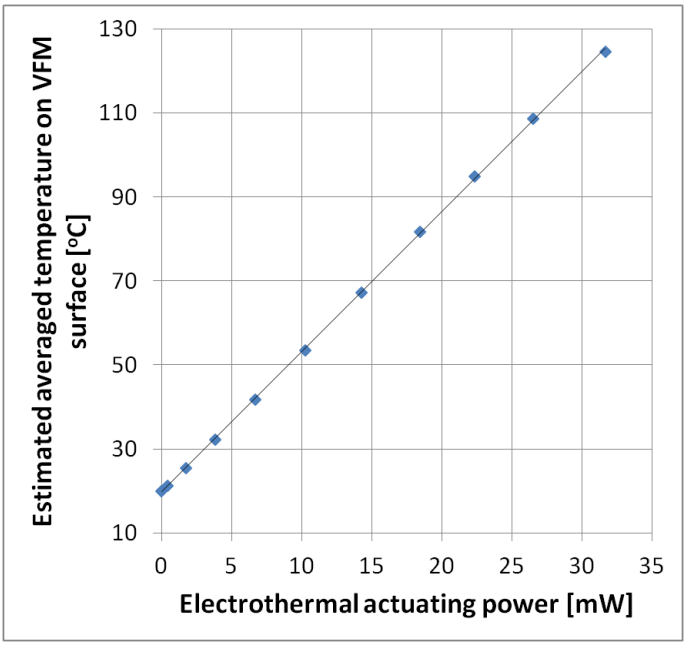

Figure 3.9: Estimated average temperature of the gold surface of the electrothermally actuated bimorph varifocal micromirror through opposite electric pads V1 and V5.

3.3.4 Simulation results of optothermally actuated VFM

During the optothermal actuation of VFM, a laser source will be normally incident on the silicon layer on the backside of the VFM. The power of the incident laser source is assumed to be absorbed through 10 μm thick silicon layer of the micromirror. The incident beam diameters of the three laser sources were measured to be 592 μm at 488 nm, 594 μm at 514 nm and 369 μm at 532 nm. So a cylinder with a cross section diameter the same size as the measured laser beam diameter was defined through the VFM silicon layer thickness in the FEM model as shown in Figure 3.10. The absorbed energy which was determined during experimental measurement is assumed

to be the heat generated within this cylinder volume. The same meshing density as the electrothermally actuated VFM model with the tetrahedron meshing elements was used for the optothermal actuation simulation. Also, the heat dissipation is assumed to be same as the electrothermally actuated VFM simulation.

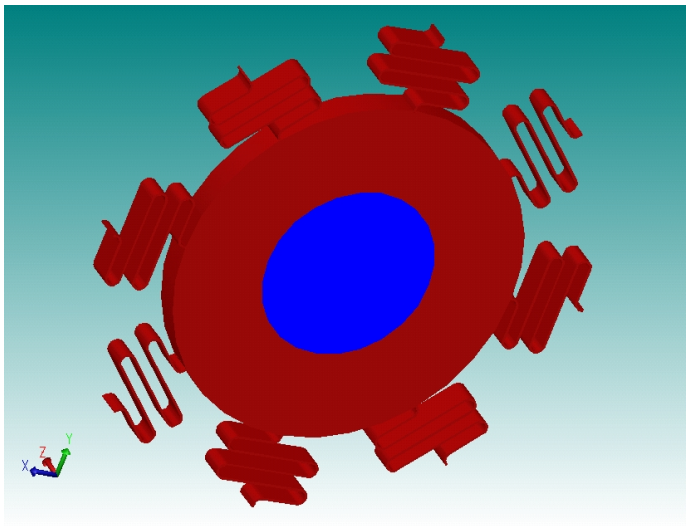

(a)

Figure 3.10: A volume (highlighted with colour blue) with the diametre of incident laser beam is defined through the thickness of silicon layer of the bimorph micromirror. The absorbed optical radiatiation is assumed to be generated within this volume. (The model is 10 times scaled in thickness direction for viewing clarity.)

Comparing the simulated temperature distribution of the electrothermally actuated VFM (Figure 3.7 and Figure 3.8) with the one of optothermally actuated VFM (Figure 3.11) shows the optothermal actuation generates the temperautre rise directly within the micromirror of the VFM where the laser was incident rather than heating the silicon from the edges. Therefore, the maximum temperature is in the center of the micromirror where the laser was simulated to be incident; whereas, the maximum temperature generated by the electrothermal actuation is located in the middle length of the serpentine-springs which the current was passing through. Besides, the average temperature on the mirror surface in Figure 3.11, generated by simulating the absorbed optothermal actuation power of 25.8 mW, is 204.6^{o}C which is higher than the calculated value generated by 33 mW electrothermal actuation power displayed in Figure 3.7. Figure 3.12 plots the estimated average gold layer surface temperature of VFM as a function of the absorbed laser power. In Table C.3 in page 234, the

simulated mechanical and thermal performance of the optothermally actuated VFM is summarised. And the ROC variation plots against the absorbed optothermal actuation power using the three laser sources are demonstrated together with the characterisation results in page 119.

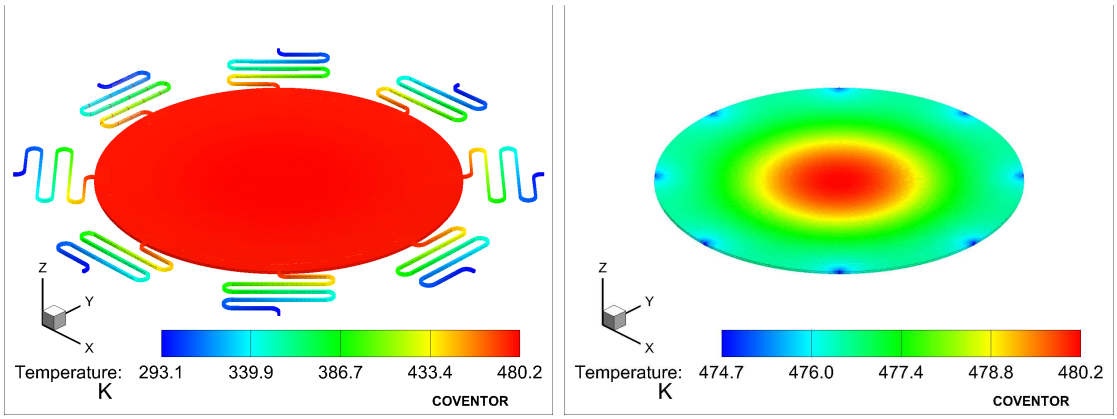

(a) (b)

Figure 3.11: The simulated temperature distribution on the VFM during the optothermal actuation of 25.8 mW absorbed within silicon volume of the micromirror.

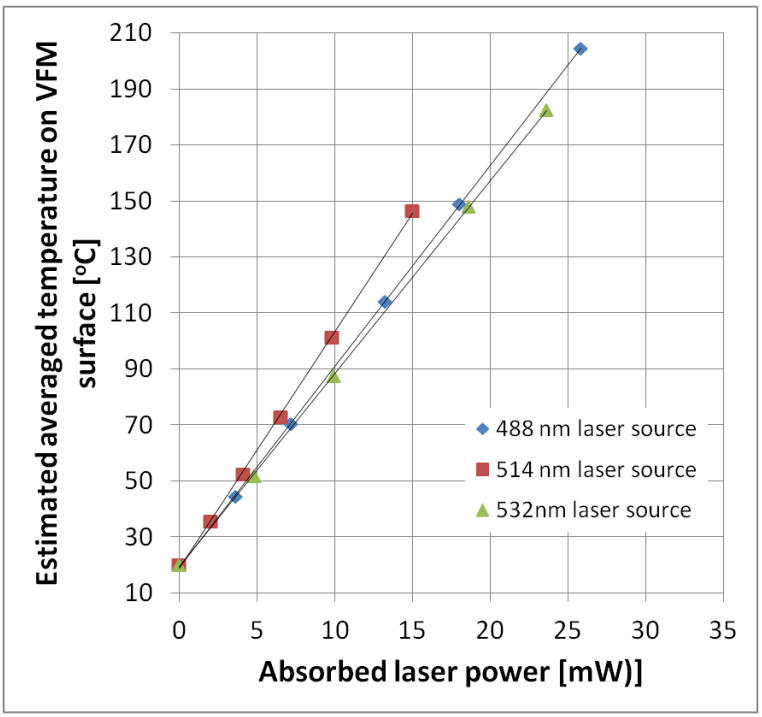

Figure 3.12: Estimated average temperature of the gold surface of the optothermally actuated bimorph varifocal micromirror using three laser sources.

3.4 Discussion

This chapter has demonstrated a 1.2 mm diameter bimorph gold-silicon varifocal micromirror fabricated using commercial fabrication process, SOIMUMPs, on a 10 μm thick SOI wafer. The focal length of the VFM can be repeatably tuned from 11 mm to 15 mm by electrothermal actuation power up to 33 mW or it can be actuated upto 5.3 mm variation by absorbed optical power of 25.8 mW from a 488 nm wavelength laser source. The optical aberrations of the VFM design, such as the astigmatism, trefoil, coma and spherical aberration, are measured to be in the nanometer range using Zernike analysis. In this section, the effects of the mechanical property variation, the geometry dimensions and the structural design of the VFM to the ROC tunable range performance improvement are discussed.

3.4.1 Initial ROC

The initial ROCs of the VFM samples, #1, #2 and #3, were measured to vary within range of 22.8$\pm$0.5 mm and are shown in Table 4.2. The initial ROC variation between devices was thought to be mainly due to uncontrolled condition variation during the gold layer evaporation process. One inconsistent sample, VFM #3, which has the initial ROC of around 35 mm and ROC variation range of around 20 mm at electrothermal actuation power of 33 mW was much higher than the other three VFM samples. Therefore, the impact of the initial curvature of the VFM on the ROC tunable range is estimated by applying different residual stresses to the gold layer of the FEM model.

When applying a 210 MPa residual stress to the gold layer of the VFM model with other properties unchanged, the initial ROC is calculated to be 25.5 mm. The ROC variation range versus the electrothermal actuation power of the VFM with initial ROC of 25.5 mm is plotted in Figure 3.13. As a comparison, the electrothermal actuation of a VFM model with initial ROC of 22.5 mm actuated at the same power is also plotted in the same figure. The comparison indicates that a VFM with an initially flatter surface ROC of 25.5 mm (13.3% flatter than the other VFM model), has a ROC

variation range of 13 mm which is 68.8% higher than the other VFM model with initial ROC of 22.5 mm over the same range of electrothermal actuation power.

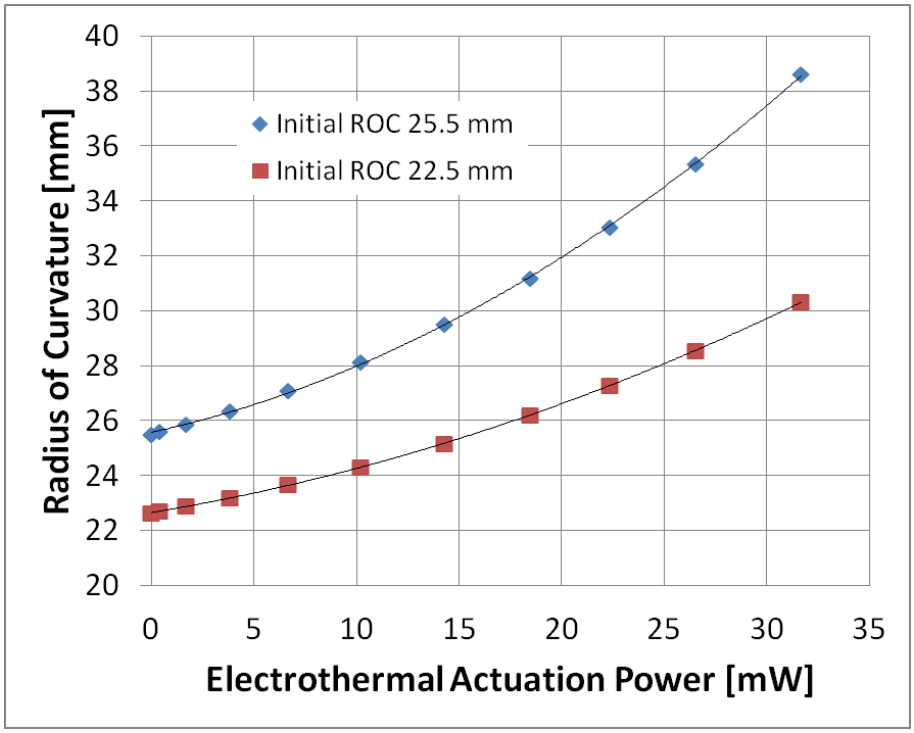

Figure 3.13: Simulated VFM ROC variation and corresponding polynomial fitting as function of the actuation power with different initial ROC.

3.4.2 Gold layer thickness

The ROC variation range of the VFM surface could also be theoretically improved by increasing the thickness of the gold layer on the micromirror surface. A geometry parametric study was performed on the VFM model by increasing the thickness of the gold layer deposited onto the silicon assuming that the residual stress within the gold layer varies accordingly to provide the same initial curvature. Figure 3.14 demonstrates the ROC variation range of of the VFM model with the thickness of the gold layer increased from the SOIMUMPs design value of 650 nm to 975 nm. The VFM model with gold layer thickness of 975 nm has a ROC variation range of 12.8 mm, increased by 110% over the design with the default gold layer thickness of 650 nm.

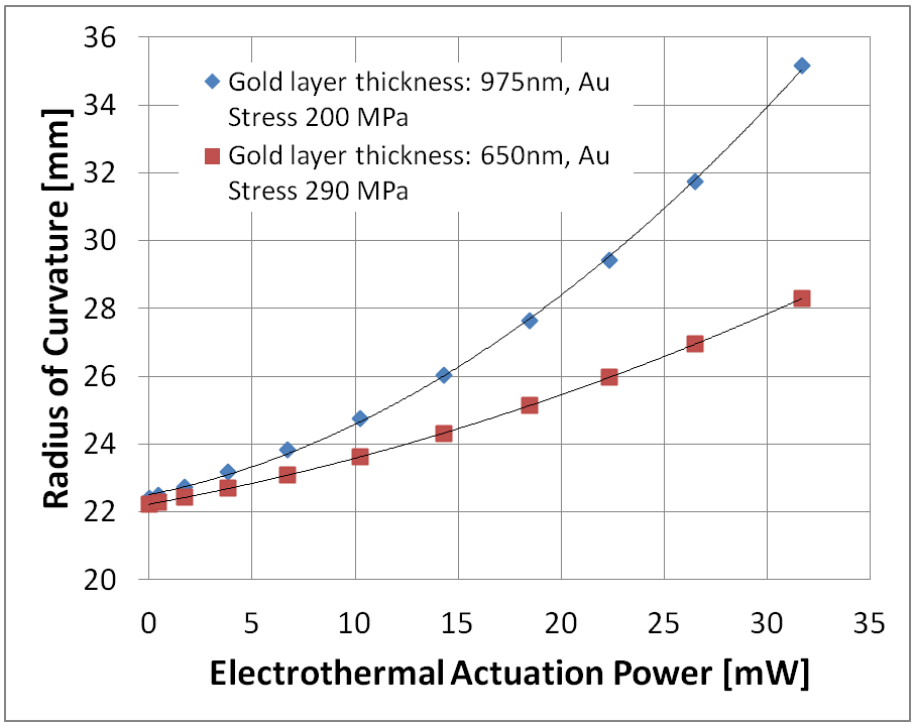

Figure 3.14: Simulated VFM ROC variation and corresponding polynomial fitting as function of the actuating power when gold layers with different thicknesses but the same residual stress are deposited.

3.4.3 Diameter of the VFM design

In practical imaging applications, the area of the reflecting micromirror is usually required to be increased so that more light could be used to produce high intensity images. Therefore, the bimorph micromirror diameter of VFM design is increased to 2 mm in the FEM model with other dimenions unchanged, and the mechanical performance of this 2 mm VFM model is estimated and compared with the FEM simulation made for original VFM design of 1.2 mm diameter micromirror.

In Figure 3.15, with the same material properties applied[2], the 2 mm VFM has a 77% flatter initial ROC of around 40 mm than the original 1.2 mm VFM design. The ROC variation range of the 2 mm VFM is 1.7 mm, reduced by 72% from the 1.2 mm VFM model. By linear estimation, the electrothermally actuated 2 mm diameter VFM model

[2]Due to the limited computational resource, the meshing density for the 2 mm VFM model can not maintain for resolving the material stresses. Therefore, the effective stress gradient of 13 MPa/μm is applied to the SOI layer of both the FEM models, instead of the applying the residual stresses of the gold and silicon layers and stress gradient of the silicon layer.

has a ROC variation sensitivity of around 0.05 mm/mW. Therefore, by only increasing the diameter of micromirror of the VFM design, the ROC variation sensitivity to the electrothermal actuation power will be reduced.

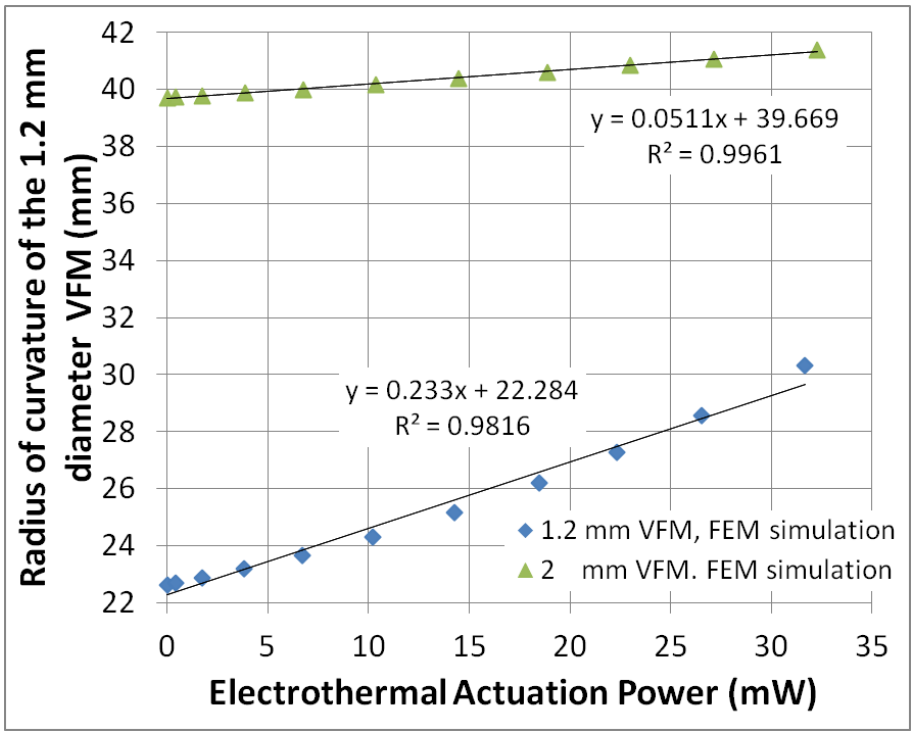

Figure 3.15: FEM simulation results of the varifocal micromirror design with diameter of the micromirror increased from 1.2 mm to 2 mm.

3.4.4 Performance limitation by external condition

In both simulation and characterisation sections, the electrothermal and optothermal actuations of the VFM are proven to provide a temperature rise from the initial temperature or from the ambient temperature of the VFM. Since the curvature of the VFM is determined by the micromirror temperature, the VFM can not only change its surface curvature when intentionally actuated; the initial ROC of the VFM at 0 mW is also sensitive to the ambient temperature. Moreover, the ROC tunable range of the VFM is different under an inconsistent ambient temperature. Therefore, performance stability and reliability of the temperature sensitive VFM is limited by the heat dissipation mechanism, such as radiation into the surrounding environment and heat conduction to the substrate, in the real application. Therefore, a further optical

Table 3.4: FEM simulation of the 2-mm-diameter electrothermally actuated VFM using tetrahedron meshing elements.

DC Voltage [V]	Current [mA]	Power [mW]	Radius of Curvature [mm]	Average Mirror Surface Temperature [^{O}C]	Maximum Temperature on VFM device [^{O}C]	Sensitivity [mm/mW]
0	0.00	0.00	39.7	20.0	20	0.04
1	0.43	0.43	39.7	20.7	24	0.04
2	0.87	1.73	39.8	22.6	35	0.04
3	1.29	3.86	39.9	25.8	56	0.04
4	1.69	6.75	40.0	30.2	88	0.05
5	2.07	10.34	40.2	35.5	133	0.05
6	2.41	14.48	40.4	41.7	193	0.05
7	2.70	18.87	40.6	48.2	275	0.05
8	2.87	23.00	40.8	54.2	372	0.06
9	3.01	27.12	41.1	60.1	483	0.06
10	3.23	32.27	41.4	67.2	622	0.06

imaging system utilising the VFM could implement a closed-loop controlled electric peltier cooler to maintain the substrate temperature of the VFM for a consistent heat conduction.

References

[1] S. T. Choi, J. Y. Lee, J. O. Kwon, S. Lee, and W. Kim, "Varifocal liquid-filled microlens operated by an electroactive polymer actuator," *Optics Letters*, vol. 36, pp. 1920–1922, May 2011.

[2] A. Mermillod-Blondin, E. McLeod, and C. B. Arnold, "High-speed varifocal imaging with a tunable acoustic gradient index of refraction lens," *Optics Letters*, vol. 33, pp. 2146–2148, Sep. 2008.

[3] W. Liu and J. J. Talghader, "Current-controlled curvature of coated micromirrors," *Optics Letters*, vol. 28, pp. 932–934, Jun. 2003.

[4] N. Binh-Khiem, K. Matsumoto, and I. Shimoyama, "Polymer thin film deposited on liquid for varifocal encapsulated liquid lenses," *Applied Physics Letters*, vol. 93, Sep. 22 2008.

[5] S. Suyama, M. Date, and H. Takada, "Three-dimensional display system with dual-frequency liquid-crystal varifocal lens," *Japanese of Applied Physics Part 1 - Regular Papers Short Notes Review Papers*, vol. 39, pp. 480–484, Feb. 2000.

[6] R. Hokari and K. Hane, "A varifocal convex micromirror driven by a bending moment," *IEEE Journal of Selected Topics in Quantum Electronics*, vol. 15, pp. 1310 –1316, Sep.-Oct. 2009.

[7] C. Knoernschild, C. Kim, B. Liu, F. P. Lu, and J. Kim, "MEMS-based optical beam steering system for quantum information processing in two-dimensional atomic systems," *Optics Letters*, vol. 33, pp. 273–275, Feb. 2008.

[8] A. Ishii and J. Mitsudo, "Constant-magnification varifocal mirror and its applications to measuring three-dimensional(3-D) shape of solder bump," *IEICE Transactions on Electronics*, vol. E90-C, pp. 6–11, 2007.

[9] M. Mescher, M. Vladimer, and J. Bernstein, "A novel high-speed piezoelectric deformable varifocal mirror for optical applications," in *Micro Electro Mechanical Systems, 2002. The Fifteenth IEEE International Conference on*, pp. 511 –515, 2002.

[10] A. A. Alzaydi, J. T. Yeow, and S. L. Lee, "Hydraulic controlled polyester-based micro adaptive mirror with adjustable focal length," *Mechatronics*, vol. 18, no. 2, pp. 61 – 70, 2008.

[11] W. Liu and J. Talghader, "Spatial-mode analysis of micromachined optical cavities using electrothermal mirror actuation," *Journal of Microelectromechanical Systems*, vol. 15, pp. 777 –785, Aug. 2006.

[12] H.-T. Hsieh, H.-C. Wei, M.-H. Lin, W.-Y. Hsu, Y.-C. Cheng, and G.-D. J. Su, "Thin autofocus camera module by a large-stroke micromachined deformable mirror," *Optics Express*, vol. 18, pp. 11097–11104, May 2010.

[13] A. Cowen, G. Hames, D. Monk, S. Wilcenski, and B. Hardy,

SOIMUMPs Design Handbook. MEMSCAP Inc., Revison 8.0 ed. http://www.memscap.com/products/mumps/soimumps/reference-material.

[14] D. C. Miller, B. L. Boyce, M. T. Dugger, T. E. Buchheit, and K. Gall, "Characteristics of a commercially available silicon-on-insulator MEMS material," *Sensors and Actuators A: Physical*, vol. 138, no. 1, pp. 130 – 144, 2007.

[15] L. Li, V. Stankovic, L. Stankovic, L. Li, S. Cheng, and D. Uttamchandani, "Single pixel optical imaging using a scanning MEMS mirror," *Journal of Micromechanics and Microengineering*, vol. 21, no. 2, p. 025022, 2011.

[16] J.-H. Jou, C.-N. Liao, and K.-W. Jou, "A method for the determination of gold thin film's mechanical properties," *Thin Solid Films*, vol. 238, no. 1, pp. 70 – 72, 1994.

[17] Y. Okada and Y. Tokumaru, "Precise determination of lattice parameter and thermal expansion coefficient of silicon between 300 and 1500 K," *Journal of Applied Physics*, vol. 56, no. 2, pp. 314–320, 1984.

[18] Coventor Inc., "CoventorWare integrated suite of design simulation software." http://www.coventor.com/products/coventorware/.

[19] CoventorWare, *ANALYZER Reference: Standard Capabilities*. CoventorWare Inc., version 2012 ed., 2012.

[20] D. C. Miller, C. F. Herrmann, H. J. Maier, S. M. George, C. R. Stoldt, and K. Gall, "Thermomechanical evolution of multilayer thin films: Part I. mechanical behavior of Au/Cr/Si microcantilevers," *Thin Solid Films*, vol. 515, pp. 3208–3223, 2007.

Chapter 4

Bimorph Varifocal Micromirror – Characterisation And Application

---

4.1 Overview

In conventional varifocal imaging systems the reflective and refractive optical components have fixed focal length. The mechanical moving parts are used to change the distances between optical elements of the system, so that the imaging system can focus at variable planes (as illustrated in Figure 4.1). However, the MEMS varifocal devices have variable focal length and have replaced the bulky mechanical moving parts in conventional varifocal imaging systems. Besides, due to the fabrication processes, the MEMS devices can be made with scales between millimeter to micrometer. In this way, the imaging system using a MEMS varifocal device can be assembled for a compact and portable requirement, such as in-vivo endoscopic imaging systems or mobile camera systems.

Generally, the main optical performance standards of a varifocal micromirror are the tunable range of its focal length and optical aberrations while actuated. Therefore, it is important to characterise these two parameters to check its agreement with the

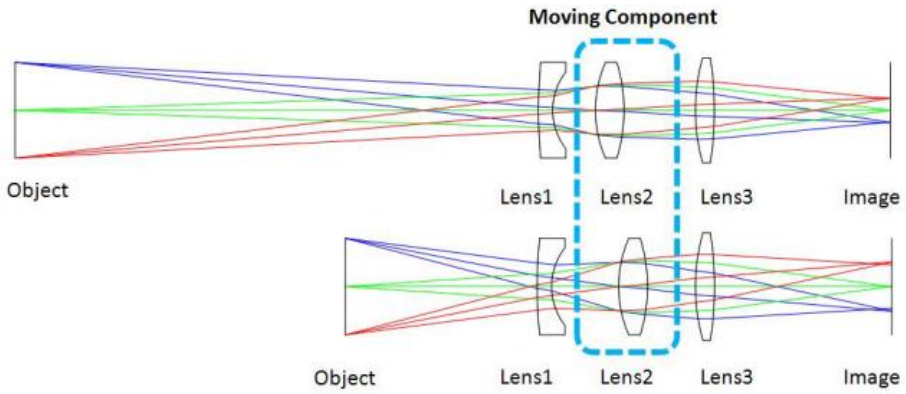

Figure 4.1: The conventional scheme of auto-focus system using moving lenses [1].

requirements of an imaging system. Most of characterisation methods used for the reported varifocal micromirrors are measuring the cross-sectional profiles to obtain the focal lengths and radii of curvature (ROC) [2, 3, 4, 5, 6, 7]. In [1, 8], MTF (modulation transfer function) was used to estimate the optical performance of a deformable mirror driven autofocus imaging system. ROC of the cross-section of a micromirror can be used to calculate its focal length when symmetric geometry mirror plate is assumed. MTF also utilises two orthogonal cross-sectional profiles to represent the micromirror. These two characterisation methods are limited by representing the micromirror using selected cross-sectional profiles with the rest of surface profiles on the micromirror ignored or assumed to be symmetric. In this chapter, the optical performance of the SOIMUMPs fabricated VFM were characterised using the full surface profile on micromirror as well as the ROC of cross-sectional profile. Furthermore, implementation of an active optical imaging system using VFM is described and the sharply focused imaging results are presented.

In this chapter, the characterisation of VFM, using two thermal actuation methods, the electrothermal and optothermal actuations, is described. During each actuation method, the static surface deformation and optical aberrations were characterised. The dynamic response speed of the electrothermally actuated VFM to an electrical voltage square waveform was measured.

First, in Section 4.2, the detailed characterisation methodologies to measure the ROC, optical aberrations and dynamic response time of thermally actuated VFM are

described. In Section 4.3, the results of surface deformations, ROC tunable range and optical aberrations of VFM using both electrothermal and optothermal actuations are presented. Section 4.4 demonstrates an optical imaging system and its imaging results when the VFM are driven by both actuation methods. Section 4.5 discusses the performance stability of the VFM in terms of hysteresis and comparison between a 2 mm diameter VFM with shortened suspension springs which fabricated using the same processes.

4.2 Characterisation Methodology

4.2.1 Surface shape characterisation

The surface shape of the VFM at each actuating level was scanned using a white light interferometer (VEECO NT1100) [9], and is illustrated in Figure 4.2. The radii of curvature (ROC) of the mirror along two orthogonal directions (noted as X-profile and Y-profile Figure 4.3), are calculated in the instrument software from each surface profile measurement. The ROC of each VFM surface profile was represented by averaging the ROC of X-profile and Y-profile, using the following equation:

$$ROC = \frac{ROC_x + ROC_y}{2} \tag{4.2.1}$$

where ROC_x and ROC_y are the radius of curvature of the two curves along X and Y profiles in Figure 4.3. Then, the ROC of VFM surface profile were measured for several times (i.e. 6) during each actuation power to obtain the standard deviation.

Furthermore, to characterise the shape of the curves, the two curves extracted from each VFM surface profile measurement were fitted with the conic section part of an aspherical shape equation [10]:

$$z = \frac{cr^2}{1 + \sqrt{1 - (1 + k)c^2r^2}} \tag{4.2.2}$$

where z is the sag of the surface, c is curvature of the VFM surface, r is the radial coordinate of the point on the curve, and k is conic constant. And the shape of the curve z is:

$$\begin{cases} \text{oblate elliptical} & \text{if } k > 0 \\ \text{spherical} & \text{if } k = 0 \\ \text{prolate elliptical} & \text{if } 0 > k > -1 \\ \text{parabolic} & \text{if } k = -1 \\ \text{hyperbolic} & \text{if } k < -1. \end{cases}$$

An analysis solver was used to find the minimum difference between the measurement and conic section (defined in (4.2.3)) by varying c, k and the offset of r and z using Excel. The resulting conic constant k obtained using this curve fitting method was used to identify the shapes of the measured curves on VFM. The quality of the fitting is quantified by the numerical difference between the measurements $z'(n)$ and fitted results $z(n)$ of (4.2.2) which is described in the following equation:

$$D = \text{difference} = \text{root mean squared error} = \sqrt{\frac{\sum_{i=1}^{n}(z'(i) - z(i))^2}{n}} \tag{4.2.3}$$

where n represents the point on measured curves of VFM surface and corresponding fitted point using conic section.

4.2.2 Optical aberrations - Zerinke coefficients

The optical performance of the VFM can be qualified by the optical aberrations which the VFM could produce during actuation. The wavefront formed by the reflective surface of the VFM can be orthogonally decomposed into the Zernike polynomials over the micromirror aperture size. The coefficients of the Zernike polynomials are used to quantify the value of optical aberrations. The mathematical description of the Zernike polynomials in polar coordinates are shown given by Equation 4.2.4 [11]:

$$Z_{n,m}(r,\theta) = \begin{cases} N_n^m R_n^{|m|}(r) cos(m\theta) & m \geq 0 \\ -N_n^m R_n^{|m|}(r) sin(m\theta) & m < 0 \end{cases} \tag{4.2.4}$$

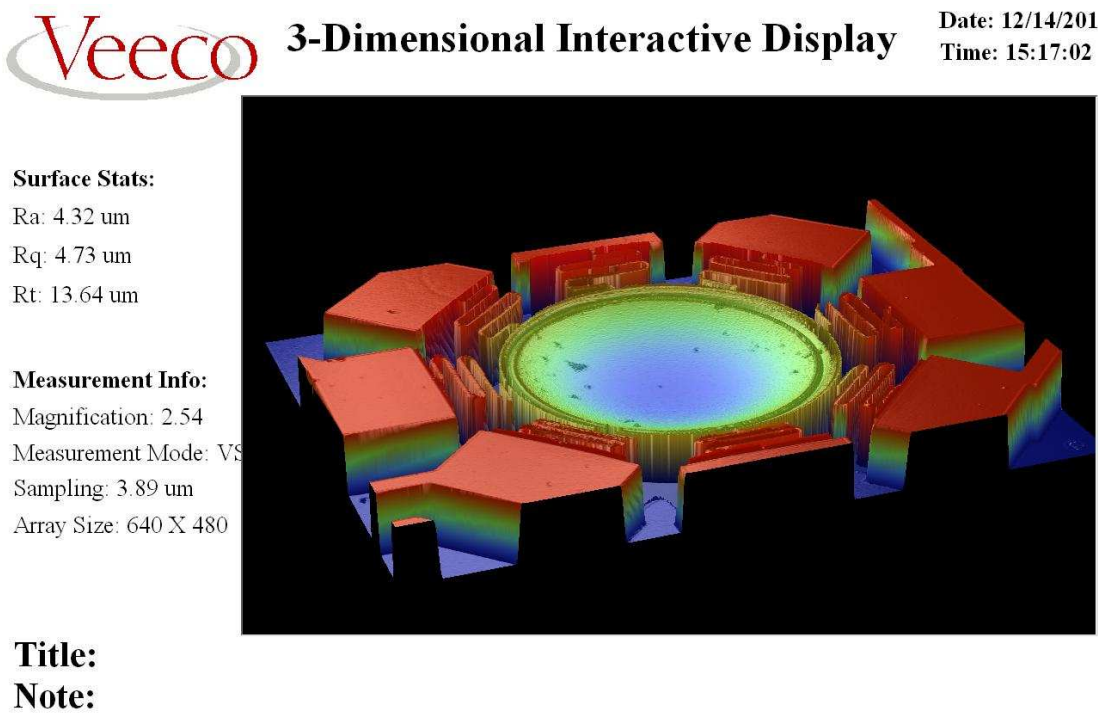

Figure 4.2: Surface scanning result of non-actuated VFM in 3D view using white light interferometer.

where,

r is the radial coordinate ranging from 0 to 1;

θ is the azimuthal component ranging from 0 to 2π;

n is the highest power (order) of the radial polynomial;

m is the azimuthal frequency of the sinusoidal component and can only take -n, -n+2, -n+4, ... , +n.

N_n^m is the nomalisation factor described as:

$$N_n^m = \sqrt{\frac{2(n+1)}{1+\delta_{m0}}} \tag{4.2.5}$$

where,

δ_{m0} is the kronecker delta function, which is δ_{m0} = 1, for m = 0 and δ_{m0} = 0, for m $\neq$ 0.

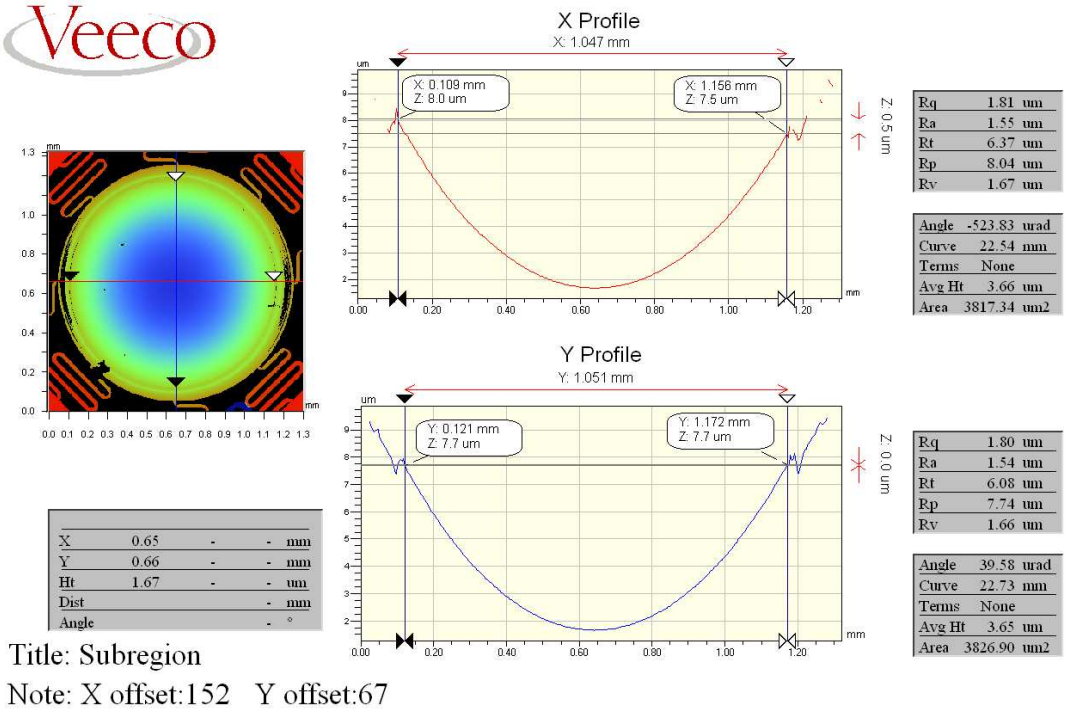

Figure 4.3: 2D view of two orthogonal curves extracted from surface profile result of non-actuated VFM using white light interferometer.

$R_n^{|m|}(r)$ is radial polynomial which is described as:

$$R_n^{|m|}(r) = \sum_{s=0}^{(n-|m|/2)} \frac{(-1)^s (n-s)!}{s![0.5(n+|m|)-s]![0.5(n-|m|)-s]!} r^{n-2s} \tag{4.2.6}$$

Table 4.1 summaries the Zernike coefficients in the polynomials and the names described in terms of optical aberration. The first three Zernike coefficients Z_1, Z_2 and Z_3 do not produce any optical aberrations and indicate the position where the image will be formed relative to the optical axis. Therefore, Z_1, Z_2 and Z_3, are not measurements of the optical aberrations. Figure B.1 illustrates the wavefront view of the first fifteen Zernike modes programed using Equation (4.2.4) in MATLAB.

To calculate the theoretical Zernike coefficients the VFM would produce during actuation, an M-file MATLAB program (Appendix D) was produced to import and process the VFM surface profile measurements by the white light interferometer and calculate the Zernike coefficients from it.

Table 4.1: The list of first fifteen Zernike coefficients.

Mode (Z_i)	Order (n)	Frequency (m)	Normlisation N_n^m	Radial Polynomial $R_n^{\|m\|}(r)cos(m\theta)$ or $R_n^{\|m\|}(r)sin(m\theta)$	Aberration Name
Z_1	0	0	1	1	piston
Z_2	1	-1	2	$rsin(\theta)$	tip(Y)
Z_3	1	1	2	$rcos(\theta)$	tilt (X)
Z_4	2	-2	$\sqrt{6}$	$r^2sin(2\theta)$	astigmatism $\pm45^o$
Z_5	2	0	$\sqrt{3}$	$2r^2-1$	defocus
Z_6	2	2	$\sqrt{6}$	$r^2cos(2\theta)$	astigmatism0/90^o
Z_7	3	-3	$2\sqrt{2}$	$r^3sin(3\theta)$	trefoil y
Z_8	3	-1	$2\sqrt{2}$	$3r^3*sin(\theta)-2r*sin(\theta)$	coma y
Z_9	3	1	$2\sqrt{2}$	$3r^3cos(\theta)-2rcos(\theta)$	coma x
Z_{10}	3	3	$2\sqrt{2}$	$r^3cos(3\theta)$	trefoil x
Z_{11}	4	-4	$\sqrt{10}$	$r^4sin(4\theta)$	tetrafoil y
Z_{12}	4	-2	$\sqrt{10}$	$4r^4sin(2\theta)-3r^2sin(2\theta)$	2nd astigmatism y
Z_{13}	4	0	$\sqrt{5}$	$6r^4-6r^2+1$	spherical
Z_{14}	4	2	$\sqrt{10}$	$4r^4cos(2\theta)-3r^2cos(2\theta)$	2nd astigmatism x
Z_{15}	4	4	$\sqrt{10}$	$r^4cos(4\theta)$	tetrafoil x

First, the surface profile measurements exported into a *.dat file. The raw data is required to be surface fitted to interpolate any null data caused by non-reflective areas on the micromirror surface of the VFM, such as those caused by dust. The surface fitting of the data is performed using the M-file generated by the GUI function **cftool** in MATLAB and the fitted result is demostrated in Figure 4.4.

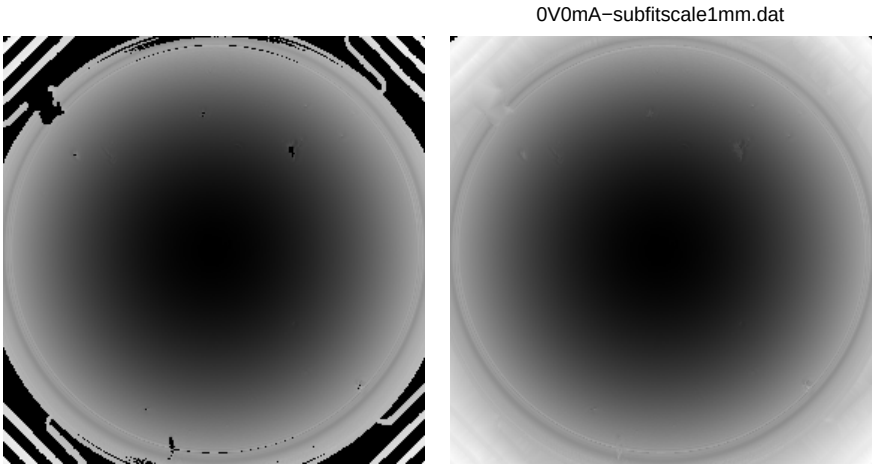

(a) (b)

Figure 4.4: The imported surface measurement data of the VFM at 0 V (a) and the processed data after the surface fitting by **cftool** in MATLAB.

The function, **ZernikeCalc.m** in line 40 and 43 of the codes in Appendix D, for calculating the Zernike coefficient are provided by [12]. This function is tested by

calculating the Zernike coefficients of a spherical surface defined in the Cartesian coordinate system and generated by using the equation of a sphere:

$$R^2 = (x - x_0)^2 + (y - y_0)^2 + (z - z_0)^2$$

and,

$$\begin{aligned} z &= f(x, y, R) \\ &= \sqrt{R^2 - (x - x_0)^2 - (y - y_0)^2} + z_0 \end{aligned}$$

where,

R is the radius of the sphere,

x_0, y_0 and z_0 are centroid point of the sphere.

Assuming the offset x_0 and y_0 are both zero, the surface profile z of a sphere with radius R of 1.5 mm, is generated for $x \in$ (-1 mm, 1 mm) and $y \in$ (-1 mm, 1 mm) (Figure 4.5a). Using **ZernikeCalc.m**, the best fitted Zernke mode is displayed, and is shown in Figure 4.5b. The first six Zernike coefficients, Z_1, Z_2, Z_3, Z_4, Z_5 and Z_6, calculated by using the **ZernikeCalc.m** function is 1.32 mm, 0 mm, 0 mm, 0 mm , -0.19 mm and 0 mm respectively, which is consistent with the theoretical values. The sign of the Zernike coefficients depends on deformation orientations.[1] Since the defocus term Z_5 (or Z_2^0) is defined as $\sqrt{3}(2r^2 - 1)$, the radius of curvature of the wavefront can be derived from this definition into the following relationship:

$$\begin{aligned} ROC_x &= 2\frac{-\phi^2}{16\sqrt{3}Z_{5x}} \\ ROC_y &= 2\frac{-\phi^2}{16\sqrt{3}Z_{5y}} \end{aligned} \tag{4.2.7}$$

where ϕ is the pupil diameter and Z_{5x}, Z_{5y} are expressed as:

$$\begin{aligned} Z_{5x} &= Z_5 + \frac{Z_6}{\sqrt{2}} \\ Z_{5y} &= Z_5 - \frac{Z_6}{\sqrt{2}} \end{aligned} \tag{4.2.8}$$

[1]Positive defocus indicates diverging rays from the optical axis. The negative defocus indicates converging rays from the optical axis

Using Equation (4.2.7) and (4.2.8), the ROC of the tested spherical surface is:

$$ROC = ROC_x = ROC_y = 2\frac{-2^2}{16\sqrt{3}(-0.19)} = 1.52 \text{ [mm]}$$

which is the defined radius of curvature for the tested spherical surface. Therefore, this m-file function is valid for characterisation of optical aberration of the thermally actuated VFM. Detailed results are presented in Section 4.3.2 and 4.3.3.

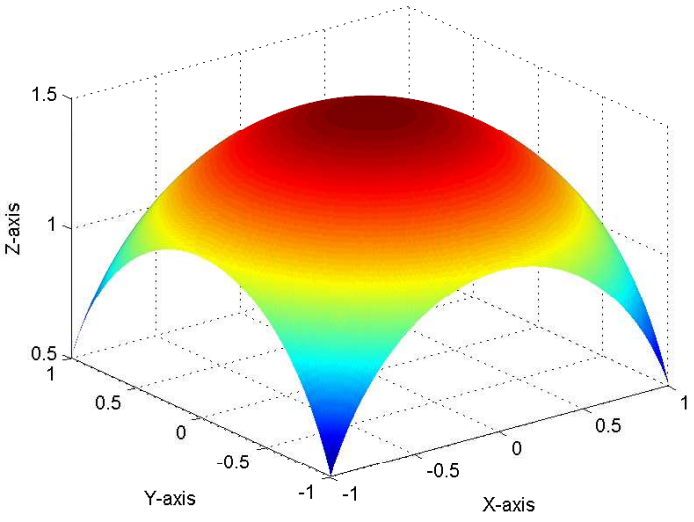

(a)

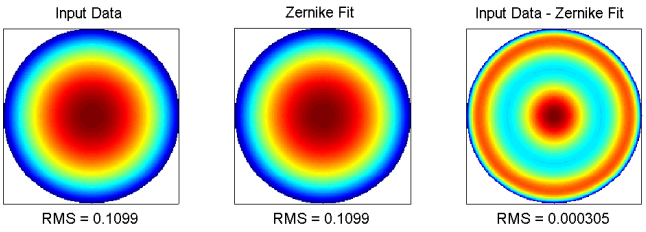

(b)

Figure 4.5: The spherical surface with ROC of 1.5 mm generated for area from$x$ $\in$(-1 mm, 1 mm) and y $\in$(-1 mm, 1 mm) (a). The Zernike mode fitted by using MATLAB function **ZernikeCalc.m** [12].

To experimentally measure the optical aberrations of the wavefront reflected by the VFM, the experimental setup was aligned as illustrated in Figure 4.6. A lower power ($<$1 mW) probe He-Ne laser beam was collimated by a lens group (lens 1 and lens 2) and normally incident onto the VFM surface via a beam splitter. The beam reflected

by the VFM was then directed towards the lenslet of the Shack-Hartmann wavefront sensor [13]. At the plane of the sensor lenslet, the wavefront of the beam is the 1:1 image of the VFM surface. In this way, the reflected laser beam wavefront formed by the curved surface of VFM can be measured; and the optical aberrations of this wavefront can be calculated by fitting the measured wavefront with Zernike polynomials in the wavefront sensor program.

Due to the aperture size of the measurement system be limited by the reflected surface size of VFM (1 mm diameter), only the first six Zernike coefficients can be evaluated accurately using this setup. Higher order (n $\geq$ 2) aberrations such as coma (Z_8 and Z_9), trefoil (Z_7 and Z_{10}) and spherical aberration (Z_{13}) cannot be directly measured in the setup.

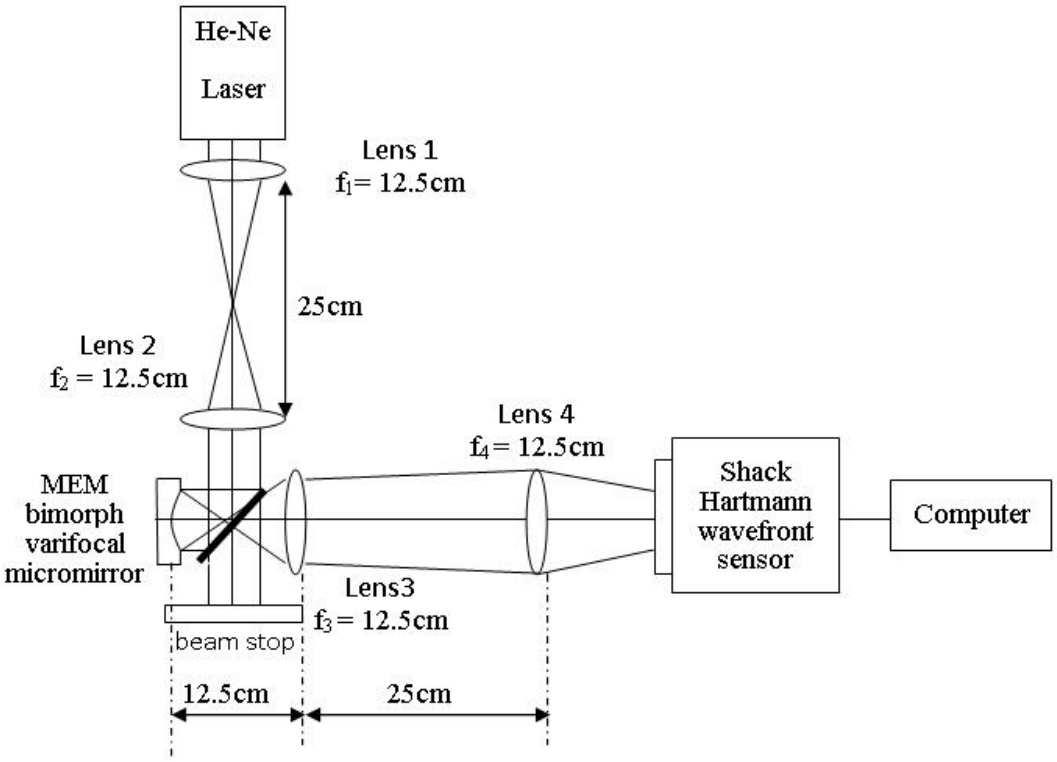

Figure 4.6: Interferometer measurement optical setup with Shack-Hartmann Wavefront sensor.

The defocus aberration of Z_5 and astigmatism Z_6 can be related to the ROC of the wavefront, where this wavefront ROC is half of the VFM ROC. Thus, the ROC of the VFM reflective surface in X-axis and Y-axis (ROC_x and ROC_y) can be calculated from wavefront Zernike coefficients using Equation (4.2.7) and (4.2.8).

4.2.3 Dynamic response

The dynamic response time of the electrothermally actuated VFM was measured using a scanning laser doppler vibrometer (Polytech OFC 3001). The vertical displacement of the centroid point of the micromirror when driven by an electrical voltage square wave was measured. Due to setup and equipment limitations, the dynamic response time was not performed for the optothermally actuated VFM.

4.3 Characterisation results

4.3.1 Initial ROC and resistances of four VFM samples

Before any thermal actuation, the four fabricated VFM samples were scanned under the white light interferometer at a controlled laboratory temperature of $\sim$20^{o}C to determine their initial ROC value. Although the VFMs are fabricated from the same design layout and the same process, one sample out of the four had an initial ROC of 35.5 mm, the other three samples had initial ROC in the range of 22.81 mm with standard deviation of 0.59. A possible reason for this difference could be due to uncontrollable factors during the process of evaporation of BLANKET gold layer causing temperature differences between dies arranged on the same wafer. The resistance of each VFM, measured between two of the eight electric pads are recorded and summarised in Table 4.2. The initial resistance of all four VFMs are consistent with an average value of 2.29 kΩ.

Table 4.2: Initial ROC and resistances of four VFM devices at 20^{o}C with no actuation.

	Surface shape			Resistance	
	ROC_x [mm]	ROC_y [mm]	ROC [mm]	Average [kΩ]	Std. Dev.
VFM #1	22.15	22.36	22.36	2.33	0.02
VFM #2	23.10	23.70	23.43	2.27	0.02
VFM #3	22.64	22.84	22.74	2.32	0.02
VFM #4	35.89	35.54	35.00	2.25	0.01

The Std. Dev. is the standard deviation of measured resistances of the eight combinaitons of the two selected pads of each VFM sample.

4.3.2 Electrothermal actuation method with joule heating

4.3.2.1 Electrothermal actuation threshold

To characterise the thermal damage threshold of the electrothermal actuation, an overdriven experiment was carried out on one of the VFM samples (VFM #4). During the initial overdriven experiment, a serie of increasing DC voltage levels with 1 V increment was applied to the two opposite electrical pads along the Y-profiles (Pads 4 and 8 in Figure 3.1) and the corresponding power was recorded as the actuation level. In Figure 4.7, the ROC of VFM #4 displayed a linearity of 0.54 mm/mW before 10 V (33 mW) and a nonlinearity when electrothermal actuation power was beyond 50 mW. The initial ROC of VFM #4 at room temperature, after the first time overdriven, and did not return to 35 mm but changed to 23.9 mm. The surface roughness also increased after this first application of the high voltage and current. Therefore, 50 mW was considered to be the thermal damage or electrothermal actuation threshold. The experiment was immediately repeated and the ROC of VFM #4 displayed a different linearity of 0.23 mm/mW and nonlinearity after 150 mW. Thus, the actuation threshold during the repeated experiment changed to 150 mW. These overdriven experiments on VFM #4 demonstrated that applying an actuation power higher than the measured threshold will result in permanent thermal damage to the VFM and inconsistent mechanical and electrical behaviour. To avoid overheating and maintain repeatable ROC changes during actuations, the electrothermal DC actuation voltage was limited to 10 V ($\sim 33 \pm 1$ mW) for all the VFM in this thesis.

4.3.2.2 Surface shape and radius of curvature

During electrothermal actuation, the VFMs were driven at 11 electrical DC voltage levels from 0 V to 10 V through two opposite pads along the Y-profile (Pads 4 and 8) and the corresponding power was used to present the actuation level. Figure 4.8 (a) and (b) show the contour images of VFM #3 surface profile measurements at 0 V and at 10 V (33 mW) with the same colour scale. The ROC of the VFM

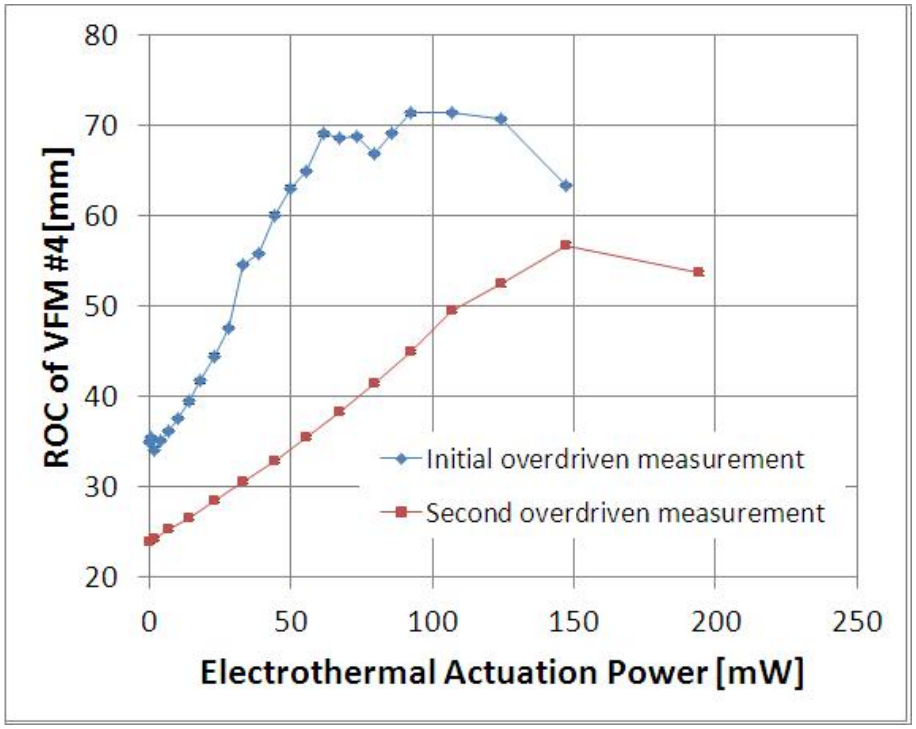

Figure 4.7: The ROC variation of the electrothermally overdriven VFM.

surface at each electrothermal actuation power level was firstly characterised by averaging from the ROC_x and ROC_y of the two curves along X and Y profiles using equation (4.2.1). Table 4.3 summarises the ROC results of the electrothermally actuated VFM, measured using the white light interferometer. The ROC variation sensitivity of the electrothermally actuated VFM was measured to be in the range between ∼0.14 and ∼0.23 mm/mW.

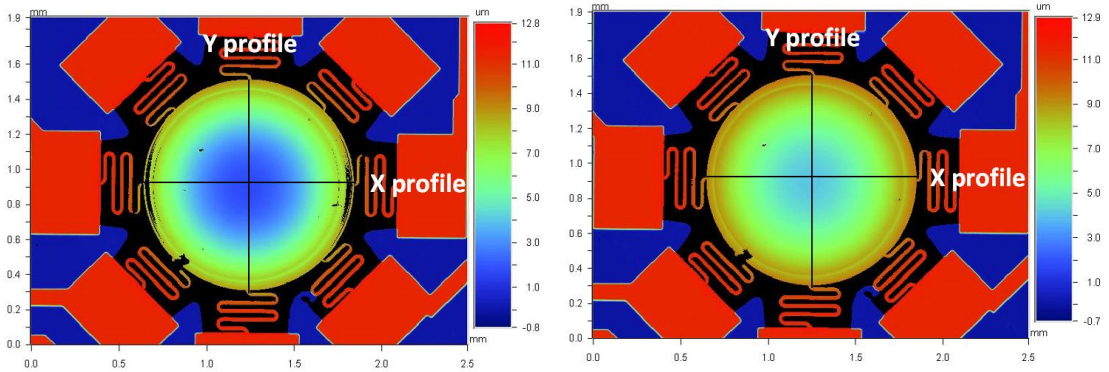

(a) (b)

Figure 4.8: Surface profile measurements of VFM #3 actuated at 0 V (a) and at 10 V (b).

Figure 4.9 shows the X and Y profiles extracted from the surface at 0 mW and at 33

Table 4.3: ROC along X- and Y- profiles the surface of electrothermal VFM.

Voltage [V]	Current [mA]	Power [mW]	ROC_x [mm]	ROC_y [mm]	ROC [mm]	Sensitivity [mm/mW]
0	0.00	0.00	22.57	22.76	22.67	
1	0.37	0.37	22.60	22.79	22.70	0.08
2	0.79	1.58	22.74	22.99	22.87	0.14
3	1.20	3.60	23.11	23.30	23.21	0.17
4	1.58	6.32	23.63	23.80	23.72	0.19
5	1.96	9.80	24.47	24.57	24.52	0.23
6	2.29	13.74	25.13	25.19	25.16	0.16
7	2.59	18.13	26.12	26.13	26.13	0.22
8	2.86	22.88	27.24	27.22	27.23	0.23
9	3.08	27.72	28.30	28.26	28.28	0.22
10	3.30	33.00	29.45	29.33	29.39	0.21

mW. The lower traces correspond to 0 mW applied to the VFM, representing the initial curvature of the VFM at laboratory temperature (20°C). The upper traces correspond to the application of 33 mW (10 V, 3.3 mA). Therefore, when the VFM is electrothermally actuated through the suspensions, the micromirror surface is not only becoming flatter but is also lifted up. From the plot in Figure 4.9, the lowest point of the micromirror was lifted by around 2.2 μm for 33 mW actuation power. The shape of the two curves are closely overlaid despite the electrical current only flowing through suspensions in the Y-profile.

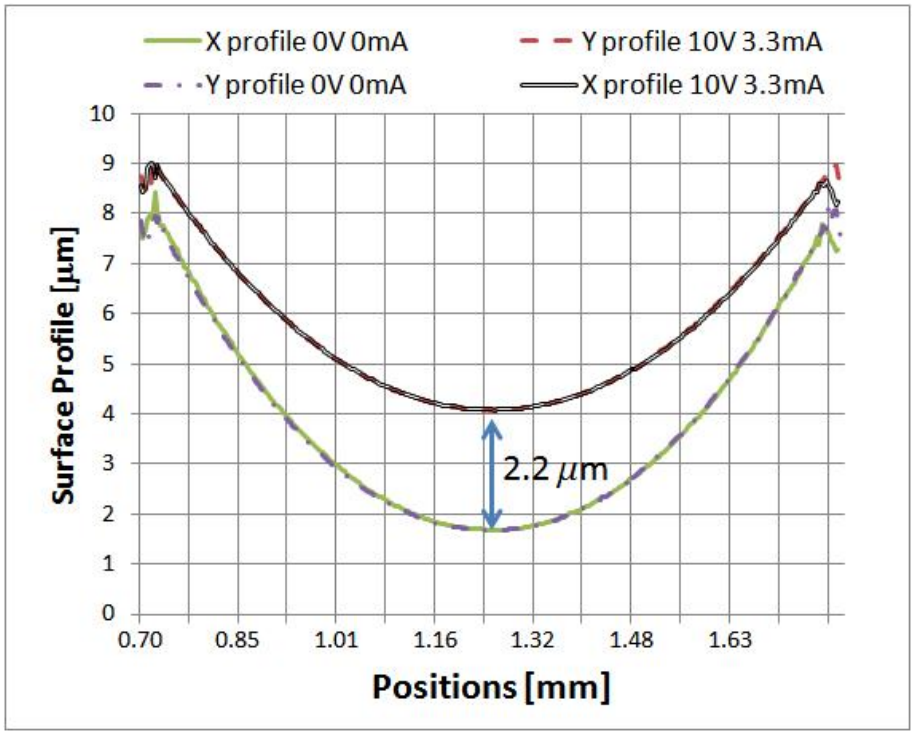

Figure 4.9: Surface profile along X and Y ordinations when actuated at 0 V and 10 V 3.3 mA.

To identify the shape of curves on the electrothermally actuated VFM, the measured curves (illustrated in Figure 4.9) were fitted with the conic section of the ashperical shape using Equation (4.2.2). Figure 4.10 plots the fitted and the measured curves on VFM Y-profiles. Table 4.4 summarises the curve fitting results. All the extracted curves can be closely fitted to the theoretical shape equation with small difference of less than 0.25 mm^2 (sum of squares of differences between fitted and raw data). At 0 mW, the curve profiles displayed were fitted to the equation with a conic constant of approximately zero (in range of -3.6×10^{-5}). At 33 mW, the surface curves were fitted to a conic section with a conic constant of around 23. As soon as the VFM was electrothermally actuated, the surface shape became an oblate ellipsoid shape. Besides, compared the results listed in Table 4.4 with the ones in Table 4.3, the ROC calculated from the conic section was consistent with the ROC measured using the white light interferometer.

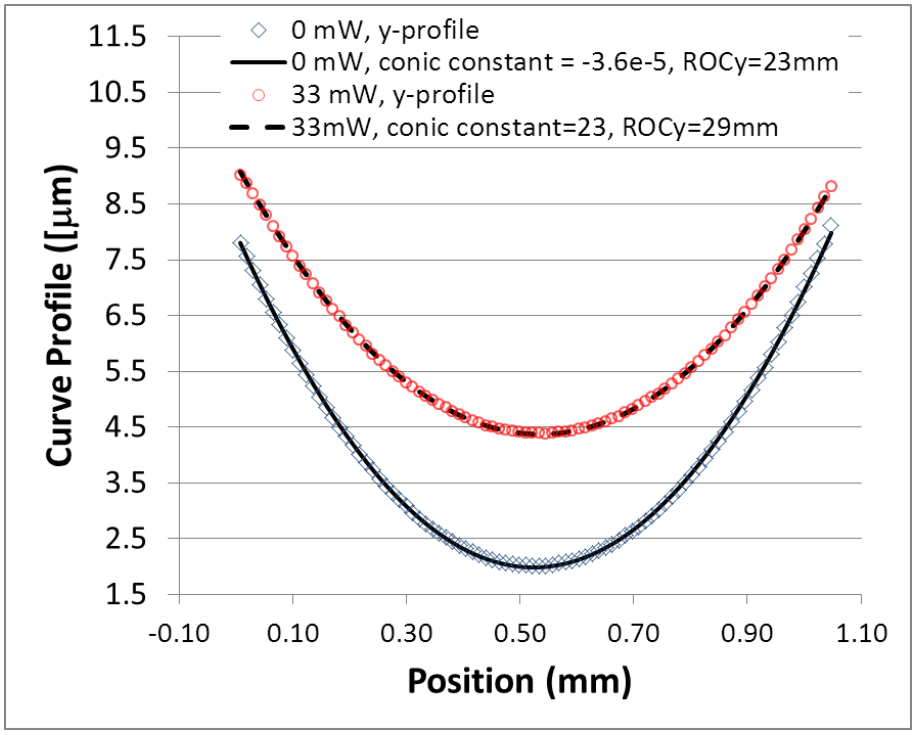

Figure 4.10: Surface profile along Y-axis profiles at 0 mW and 33 mW with curve fit using conic section.

To investigate the effect of the electrothermal actuation through different combinations of the eight suspensions, the ROC variations when driving through two opposite electric pads (pad number 4 and 8 in Figure 3.1 on page 62) and through two adjacent

Table 4.4: Curve fit between the measured curves on the surface of electrothermally actuated VFM and conic section of the fitted aspherical equation.

DC Voltage [V]	Current [mA]	Power [mW]	Fitted ROC [mm]		Cornic Constant		Differences(*)		Curve Shape	
			x-profile	y-profile	x-profile	y-profile	x-profile	y-profile	x-profile	y-profile
0	0.00	0.00	22.67	22.90	3.86E-06	-3.56E-05	0.03	0.03	spherical	
1	0.37	0.37	22.95	23.05	7.84	8.99	0.03	0.03		
2	0.79	1.58	22.99	23.15	17.41	16.55	0.03	0.02		
3	1.20	3.60	23.33	23.52	17.72	16.56	0.03	0.02		
4	1.58	6.32	23.87	24.01	14.70	13.80	0.03	0.02		
5	1.96	9.80	24.70	24.81	19.30	17.12	0.03	0.02	oblate elliptical	
6	2.29	13.74	25.35	25.42	19.43	17.97	0.02	0.02		
7	2.59	18.13	26.36	26.39	18.98	16.85	0.02	0.02		
8	2.86	22.88	27.52	27.53	19.50	19.66	0.02	0.02		
9	3.08	27.72	28.52	28.50	22.90	22.00	0.02	0.01		
10	3.30	33.00	29.74	29.60	25.19	22.79	0.01	0.01		

(*) calculated using equation (4.2.3).

pads (pad number 7 and 8) were measured. The results are presented in Figure 4.11 and show no measurable difference between the VFM ROC changes by delivering electric current through different pairs of electrical pads. Furthermore, actuation through more than one pair of pads was conducted. Three pairs of electric pads are connected in parallel to actuate the VFM. In Figure 4.12, the VFM surface deformation measured by ROC values through three pairs is identical to the measurement obtained through only one pair of electric pads at the same driving power. The long term repeatability of the VFMs was also investigated. In Figure 4.13, three measurements were taken of the same VFM #3 over the four-month period during which time the device had been in regular use for characterisation. Figure 4.14 shows the ROC variation of three VFM devices with the same electrothermal actuation voltage level. It can be seen that the ROC variation range and rate of three VFM devices are in agreement, however, there are slightly different initial ROC values most probably due to material and process variations occurring during device fabrication. During ROC measurements using white light interferometer, each VFM surface profile at a certain actuation level was measured for 6 times and the standard deviation for those measurements was 0.03 for low actuation power and increased to 0.3 at 10 V, 3.3 mA.

The estimated temperature distribution during simulation of electrothermal actuation in Figure 3.7c and Figure 3.8c displays high temperature areas on the mirror's edge next to the connection where the current flows into and out of the VFM. Therefore, the area on the micromirror edge to which the current flowing serpentine springs are connected

closely are inspected by the white light interferometer. No localised deformation was measured apart from the overall surface curvature variation. Furthermore, the optical quality degradation can be characterised by Zernike coefficients. The aberration due to the local deformation from the edge of the circular micromirror can be measured by Z_{11} and Z_{15} of the surface profile of the VFM gold layer. Detail characterisation using Zernike coefficients is described in the followed sub-section.

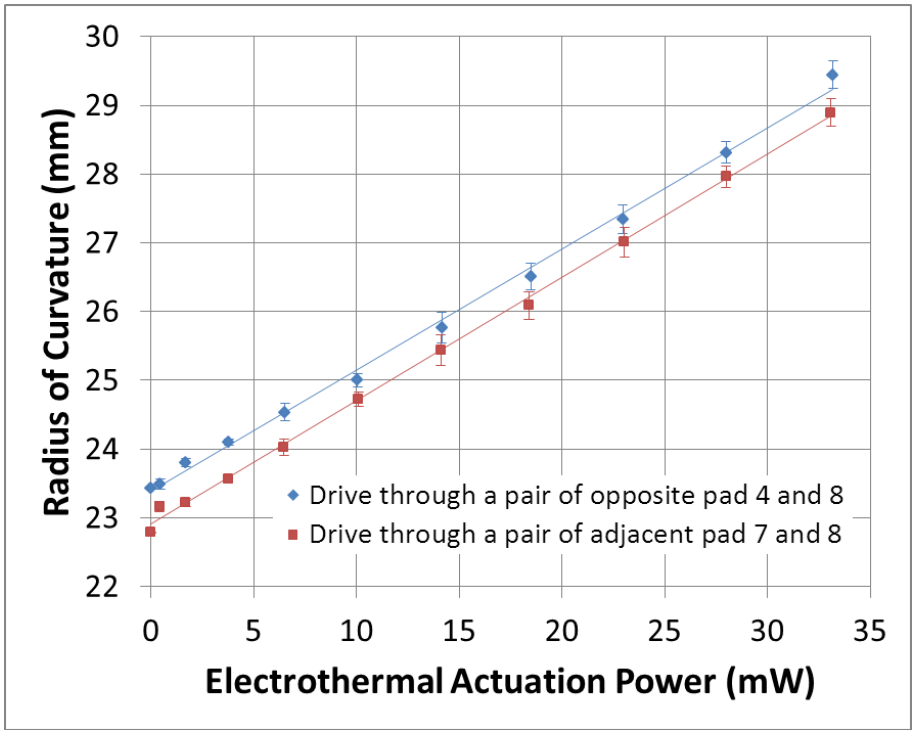

Figure 4.11: ROC changes of VFM by driving through two opposite and two adjacent electric pads.

4.3.2.3 Optical aberrations calculation and measurement

Optical aberrations, produced by the reflective gold surface of the VFM, are described in this sub-section. Using the Zernike polynomials [14], the reflected wavefront produced by the reflective surface of VFM is orthogonally decomposed over the aperture of the gold layer. Considering the surface profile of the VFM measured by the white light interferometer is the wavefront reflected by the VFM and inherited the 1:1 mirror image of the surface profile. Thus, optical aberrations produced by the VFM reflective surface such as the defocus and astigmatism etc., can be calculated from the

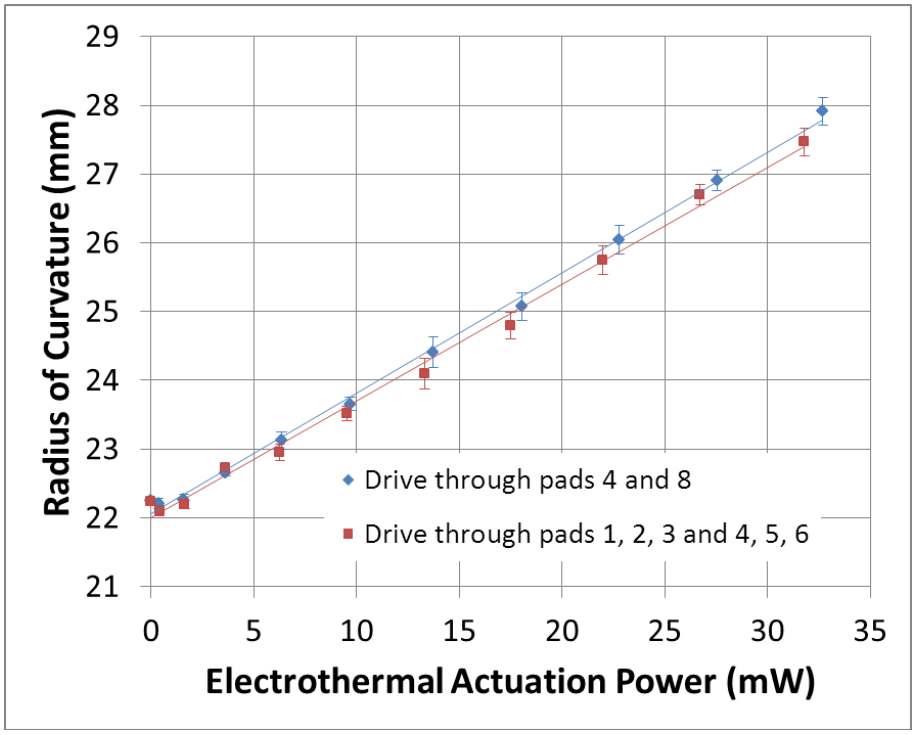

Figure 4.12: ROC changes of VFM by driving through three pairs and one pairs of electric pads.

VFM gold layer surface profile using Zernike coefficients.

As shown in Figure 4.15, the defocus Zernike mode was the best fitted shape with the VFM surface throughout the actuation range. Table C.4 summarises the first fifteen Zernike coefficients calculated from the surface profile measurements at 11 voltage levels. The bar diagram in Figure 4.16 plots the results at 0 V, 5 V and 10 V. The first three Zernike coefficients describe the alignment between the VFM and the white light interferometer measurement system and are not optical aberrations. Apart from the piston term (Z_1), tip term (Z_2) and tilt term (Z_3), the defocus aberration (Z_5), which dominate among the first fifteen calculated aberrations, was in several micrometers and was decreasing with the increased electrothermal actuation levels. Other higher order (n $\geq$ 2) aberrations such as astigmatism (Z_4 and Z_6), coma (Z_8 and Z_9), trefoil (Z_7 and Z_{10}) and spherical (Z_{13}) were in the nanometer range and were negligible. Overall, the standard deviations for all the Zernike coefficients calculated from the surface profiles are within several tens of nanometers. The calculated results of optical aberrations produced by the electrothermally actuated VFM indicate the VFM would

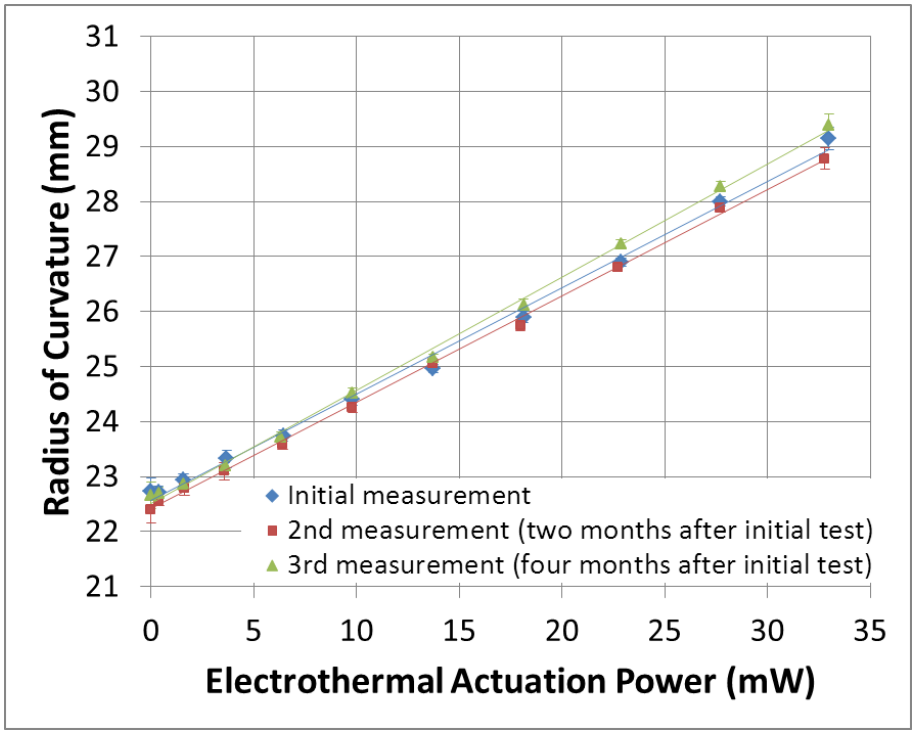

Figure 4.13: Repeat measurements of ROC of the same VFM as a function of driving power.

produce very small distortion and blurring for imaging applications.

Moreover, the astigmatism (Z_6) is in the range of several nanometers and are more than 100 to 1000 times smaller than the defocus term (Z_5). Thus, Z_{5x} and Z_{5y} in Equation (4.2.8) are approximately equal. Using Equation (4.2.7), the ROC calculated from the defocus aberration term (Z_5) with an aperture diameter (ϕ) of 1 mm during the electrothermal actuation are listed in the last row of Table C.4 and are consistent with the measured ROC.

To verify the optical aberrations calculated from the surface profiles of the electrothermal actuated VFM, the wavefront produced by the VFM was measured by the wavefront sensor using the experimental setup illustrated in Figure 4.6. A collimated low power probe He-Ne laser beam reflected by the VFM surface was measured during electrothermally actuation of the VFM. The Zernike coefficients of the wavefront were returned by the sensor software after fitting the measurement to Zernike polynomials. However, due to the small aperture size determined by the VFM diameter, only the first six Zernike coefficients can be measured. Table C.5

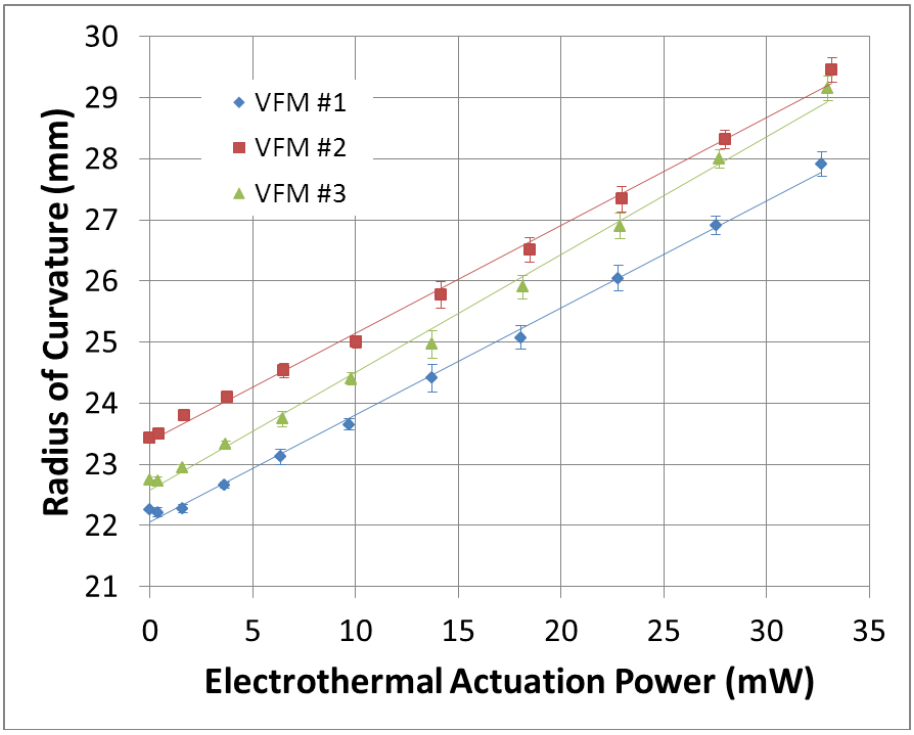

Figure 4.14: ROC variation of three VFM devices as a function of electrothermal actuation power.

summarises the measured results of the Zernike coefficients using the experimental setup. Figure 4.17 plots the Zernike coefficients at 0 V, 5 V and 10 V returned by the wavefront sensor and are similar to the estimated results calculated previously from VFM surface profile measurements using MATLAB, the dominant aberration was the defocus (Z_5) which has a small value in micrometer range and decreased with increasing electrothermal actuation power level. Also, the astigmatism terms (Z_4 and Z_6), which were 100 to 500 times smaller than the defocus aberration, were in nanometer range and negligible.

The first six calculated Zernike coefficients and those measured using the wavefront sensor are not equal because of the different aperture sizes measured in the two methods. In the wavefront sensor based measurement setup, the aperture diameter measured at the plane of the sensor lenslet was in the range between 0.37 mm and 0.41 mm, whereas in the white light interferometer, the aperture size is $\sim$1 mm (the same as the gold layer diameter) resulting from directly scanning the VFM surface. However, the two sets of Zernike coefficients obtained by different aperture size can

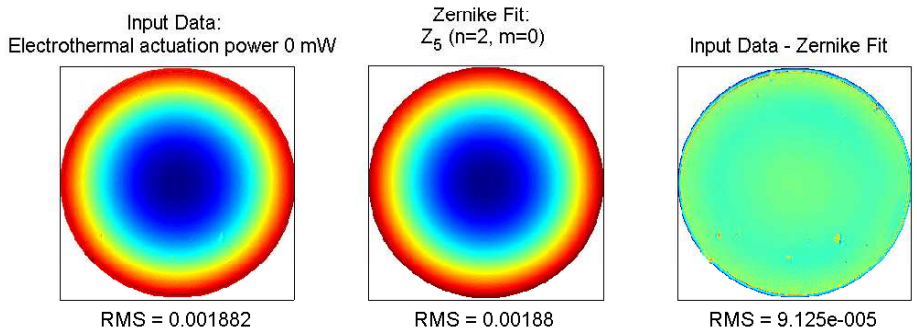

(a) VFM with no actuation

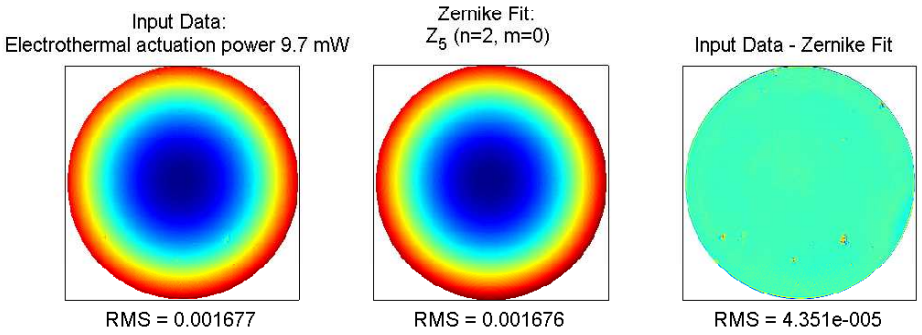

(b) VFM actuated electrothermally at 9.7 mW

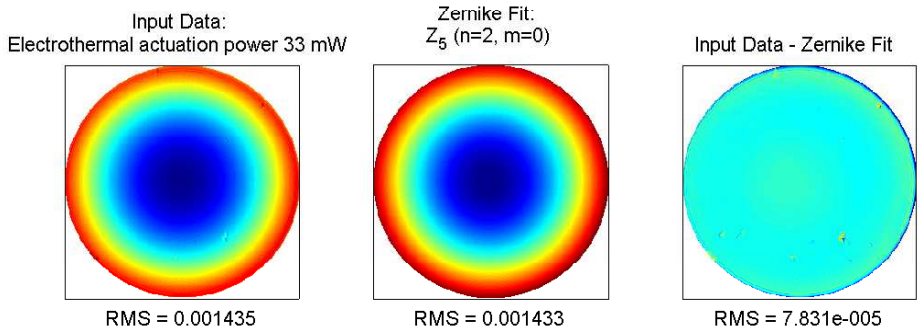

(c) VFM actuated electrothermally at 33 mW

Figure 4.15: The best Zernike mode fit of VFM surface profile at 0 V, 5 V and 10 V.

be compared using the scaling equation provided by [15].

$$b_{2m} = \frac{r_2^2}{r_1^2}(a_{2m} - a_{4m}\sqrt{15}(1 - \frac{r_2^2}{r_1^2}) + a_{6m}\sqrt{21}(2 - 5\frac{r_2^2}{r_1^2} + 3\frac{r_2^4}{r_1^4}) \tag{4.3.1}$$

Since, the higher order aberrations (n=4,=6 or terms a_{4m} and a_{6m} in the above equations) can not be measured using wavefront sensor and the estimated values calculated from the surface profiles are in the nanometer range (and are 100 to 500

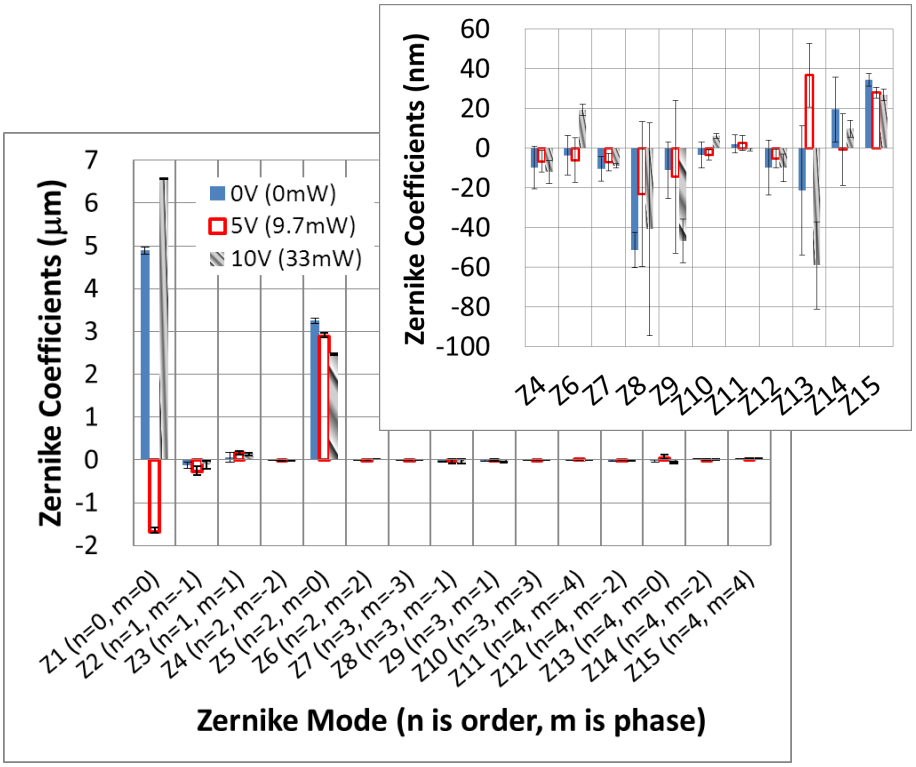

Figure 4.16: Zernike coefficients of the electrothermomechanically actuated VFM at 0 V, 5 V and 10 V; the inset shows the same data with a smaller scale.

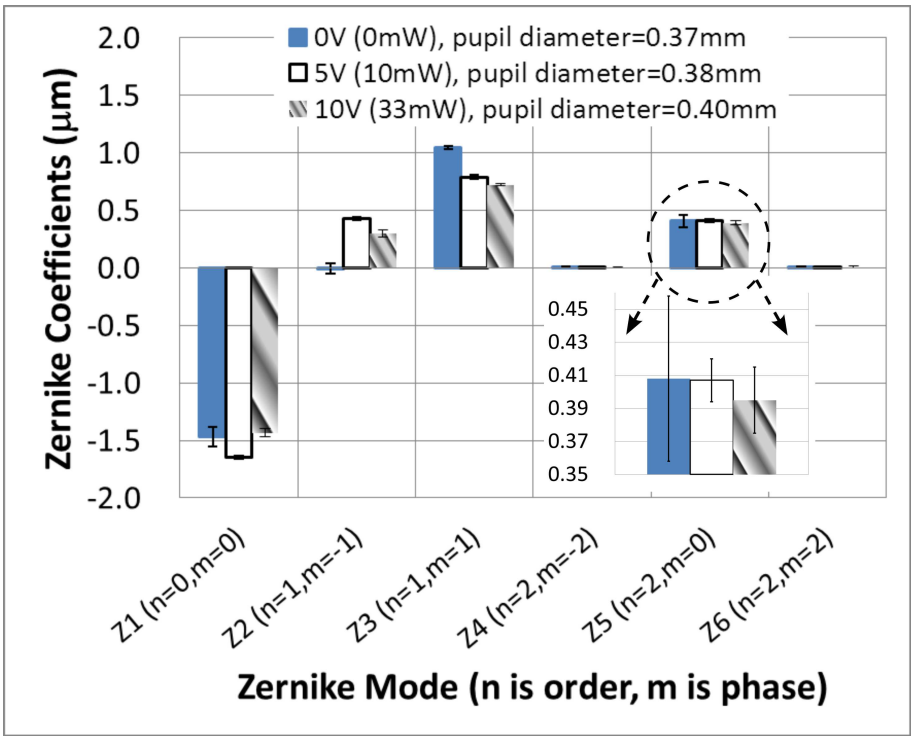

Figure 4.17: Astigmatism of the bimorph varifocal micromirror measured by Shack-Hartmann wavefront sensor.

times smaller than defocus aberration (n = 2, or the term a_{2m}) in the above equation)), the equation can be further simplified as:

$$b_{2m} = \frac{r_2^2}{r_1^2}(a_{2m}) \tag{4.3.2}$$

Therefore, the main aberration term defocus, Z_5, measured using the white light interferometer and wavefront sensor has at most 6% difference throughout the actuation power range. The first three Zernike terms, Z_1, Z_2 and Z_3, are distinguishably different due to the different alignment between the two characterisation setup. The astigmatism, Z_4 and Z_6, despite having differences over around 200%, still remain below 10 nm range.

In the last row of Table C.5, the ROC calculated from Z_5 by using Equation (4.2.7) when considering Z_{5x} and Z_{5y} in Equation (4.2.8) are approximately the same since astigmatism (Z_6) is negligible compared to the defocus term Z_5.

4.3.2.4 Comparison between measured and simulated ROC

The surface shape of an electrothermally actuated VFM was simulated and characterised in terms of ROC at 11 increasing actuation power levels. In Figure 4.18, the ROC measured by the white light interferometer and wavefront sensor has an agreement of at least 93% using (4.3.3). Both experimentally measured ROCs vary linearily with the electrothermal actuation power. The results from the wavefront sensor measured ROC starting at higher initial ROC than the white light interferometer measured equivalent. This could be explained by the VFM absorbing probe He-Ne laser power in addition to the electrothermal actuation power during the wavefront sensor measurement.

$$\text{difference between data A and B in percentage} = \frac{\text{A} - \text{B}}{\text{A}} \times 100, (A > B) \tag{4.3.3}$$

In Figure 4.18, the plot also includes the ROC simulated by FEM software CoventorWare. Compared to the experimentally measured ROC, the simulated results are less linear. The possible reasons might be due to the limited meshing density, the assumptions on the material properties and the surface boundary conditions, such as the constant value of thermal expansion coefficient and Young's Modulus of silicon layer, and heat losses through the air convection and radiation on the device surfaces. Despite this, the simulation and characterisation results have an agreement of at least $\sim 93\%$.

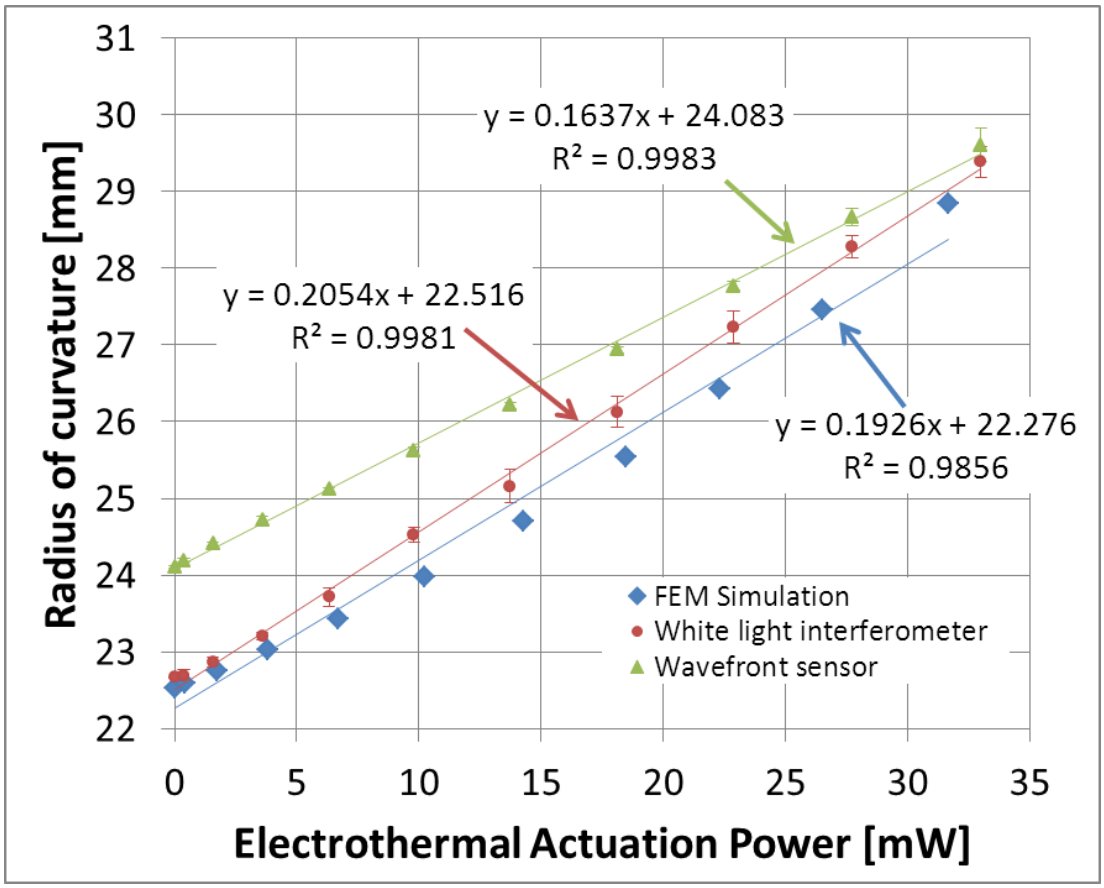

Figure 4.18: FEM simulated ROC and measured ROC as a function of driving power.

4.3.2.5 Dynamic response

The dynamic response of the VFM was obtained by measuring its mechanical rise and fall times at the center point when a electrical voltage step was applied. The values are used as a gauge of how fast the VFM can reach stability when the electrothermal

actuation power is switched on and off. During the experiment, a 1.2 Hz 50% duty cycle, square-wave voltage signal operating between 0 V and 10 V was applied to two opposite electrical pads (Pads 4 and 8) of the VFM. At the same time, the vertical displacement at the centre of the VFM was measured using a scanning laser Doppler vibrometer (Polytech OFC 3001). Figure 4.19 shows that the 0% - 90% rise time of the VFM was 130 ms and the 90% - 0% fall time was 121 ms, while the vertical displacement of the VFM centre is about 2.2 μm which is in line with the surface profile scanner measurements displayed in Figure 4.9 on page 95.

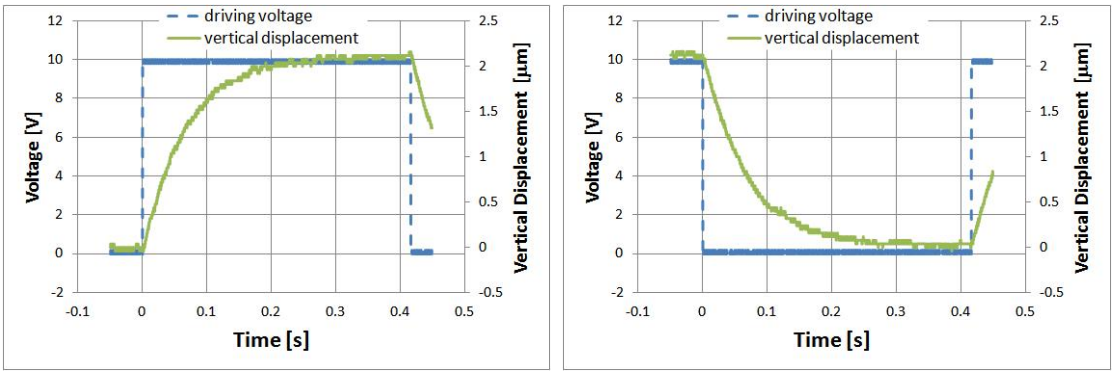

(a) (b)

Figure 4.19: The rise time (a) and fall time (b) of the vertical movement of the centre point of the varifocal micromirror to a 50% duty cycle square wave between 0 V and 10 V. (N.B. the displacement range setting was 0.5 μm/V)

4.3.3 Optothermal actuation method with laser beams

To achieve optothermal actuation, a different VFM device from the same fabrication batch bonded to a supporting PCB board with a 1.5 mm diameter circular opening under the VFM. During optothermal actuation, a laser beam was incident normally onto the center of the silicon surface at the bottom of VFM. Three laser sources with wavelengths of 488 nm, 514 nm and 532 nm were used during characterisation experiments. The 488 nm and 514 nm laser sources were provided by an argon ion laser. The 532 nm laser source was generated from a battery driven, frequency doubled, Nd:YAG laser.

Optothermal actuation uses the heat converted from the energy that the VFM absorbs

from the incident laser beam on the silicon layer. Therefore, the actuation level of the optothermal actuation is noted in the absorbed laser power rather than the incident laser power as the absorbed laser power is dependent on the incident angle of the incoming laser beam. During the experiments, the incident laser beam is kept normal to (or within $\sim 5^{o}$) to the silicon surface at the back of VFM. The absorbed laser power was obtained by subtracting the reflected and the transmitted laser power from the incident laser power. Thus, the laser power absorption of the VFM was measured to be 60% at 488 nm, is 65.4% at 514 nm and is 66.4% at 532 nm.

4.3.3.1 Surface shape and radius of curvature

The surface shape variation of the optothermally actuated VFM was first measured using the white light interferometer for different actuation powers. As the surface profile measurements demonstrated in Figure 4.20, the magnification had to be increased to five times (compared to Figure 4.8 in page 94) so that the field of view was small enough to avoid the transmitted, reflected and scattered actuating laser light saturating the image sensor of the white light interferometer. A drawback of having a smaller view is that the scanner could not scan any area which can be taken as a reference height and the relative vertical level of the micromirror could not be compared during actuation. Therefore the two images in Figure 4.20 have different scales.

Following the same characterisation procedure as for the electrothermally actuated VFM, the surface ROC of the optothermally actuated VFM at each actuation level was represented by averaging the ROC of the curves along two orthogonal axes, the X and Y profiles, using the equation (4.2.1). The results are summarised in Table 4.5.

In Figure 4.21a, the ROC variations caused by the three laser sources are plotted as functions of the absorbed optical power. By the linear fitting of the measurements, the VFM has a ROC variation sensitivity to the absorbed power of 0.47 mm/mW, 0.31 mm/mW and 0.52 mm/mW for optothermal actuation with 488 nm, 514 nm and 532 nm wavelength light respectively. In this Figure 4.21, the fitting of ROC

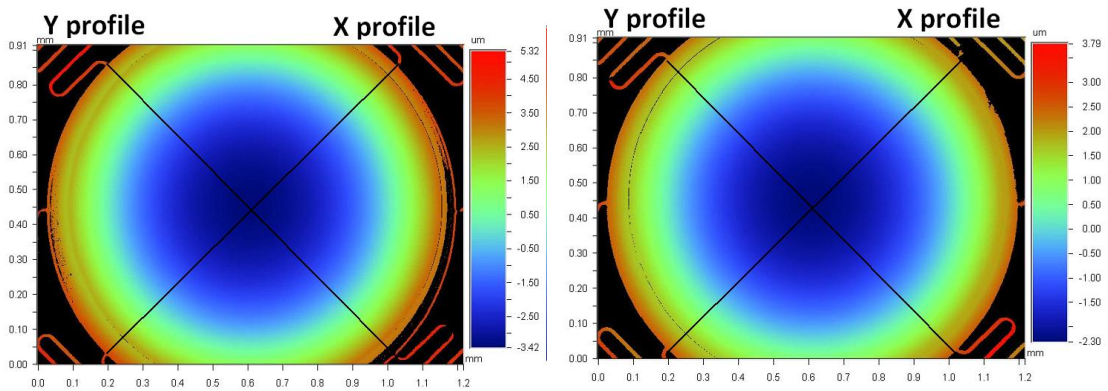

(a) (b)

Figure 4.20: Surface profile measurements of the VFM using the white light interferometer actuated at 0 mW (a) and at 43 mW (b) by an argon ion laser operating at 488 nm wavelength.

Table 4.5: The ROC of the optothermally actuated VFM measured by white light interferometer.

	Total Power [mW]	Absorbed Power [mW]	ROC_x[mm]	ROC_y[mm]	ROC [mm]	Sensitivity [mm/mW]
	6.0	3.6	23.27	23.21	23.24	
	12.0	7.2	24.68	24.66	24.67	0.40
488 nm	22.0	13.2	27.00	27.11	27.06	0.40
	30.0	18.0	29.53	29.49	29.51	0.51
	43.0	25.8	33.81	33.79	33.80	0.55
	3.0	2.0	22.51	22.47	22.49	
	6.2	4.1	23.19	23.18	23.19	0.33
514 nm	10.0	6.5	23.82	23.81	23.82	0.26
	15.0	9.8	24.86	24.87	24.87	0.32
	23.0	15.0	26.59	26.51	26.55	0.32
	7.7	4.8	21.58	21.60	21.59	
	15.0	9.9	24.51	24.50	24.51	0.55
532 nm	28.0	18.6	28.17	28.19	28.18	0.42
	35.5	23.6	31.82	31.84	31.83	0.72

variations when VFM was actuated by the 532 nm laser source has an intercept at 19.137 mm which is around 9.9% to 12.5% difference to the intercept of ROC variations actuated by 488 nm and 514 nm laser sources respectively. This could be caused by misalignment of the laser source and the optical components of the experimental setup when changing from the argon ion laser source (488 nm and 514 nm wavelengths) to the Nd:YAG laser source (532 nm wavelength).

In order to compare the electrothermal and optothermal actuation methods, measured ROC variations are plotted as functions of actuation power in Figure 4.21a. The ROC

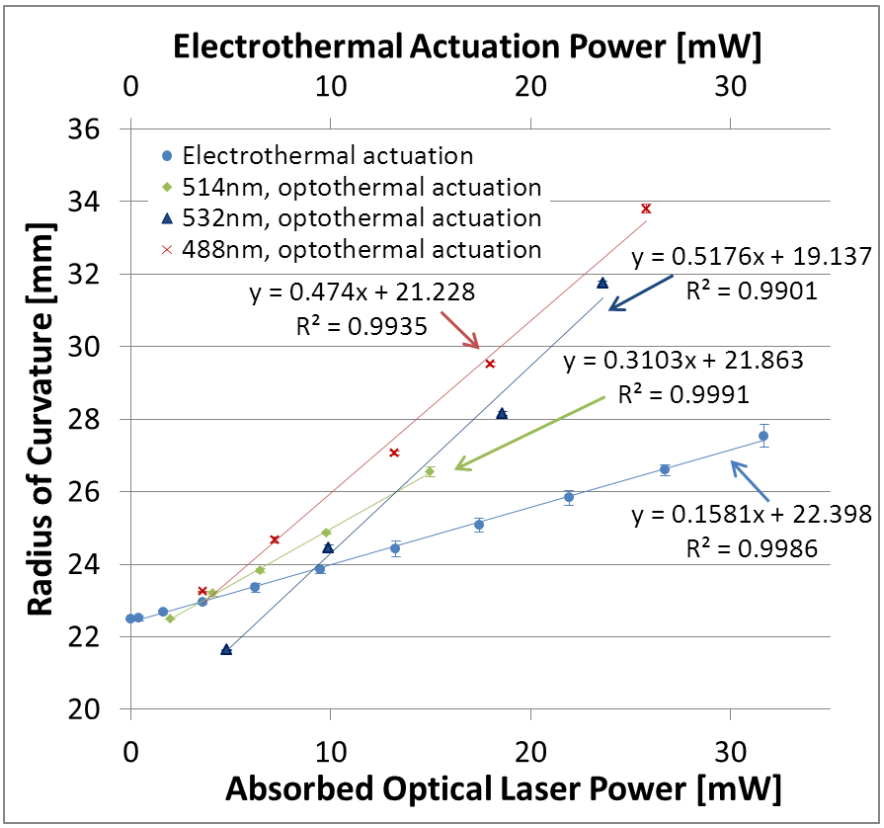

(a)

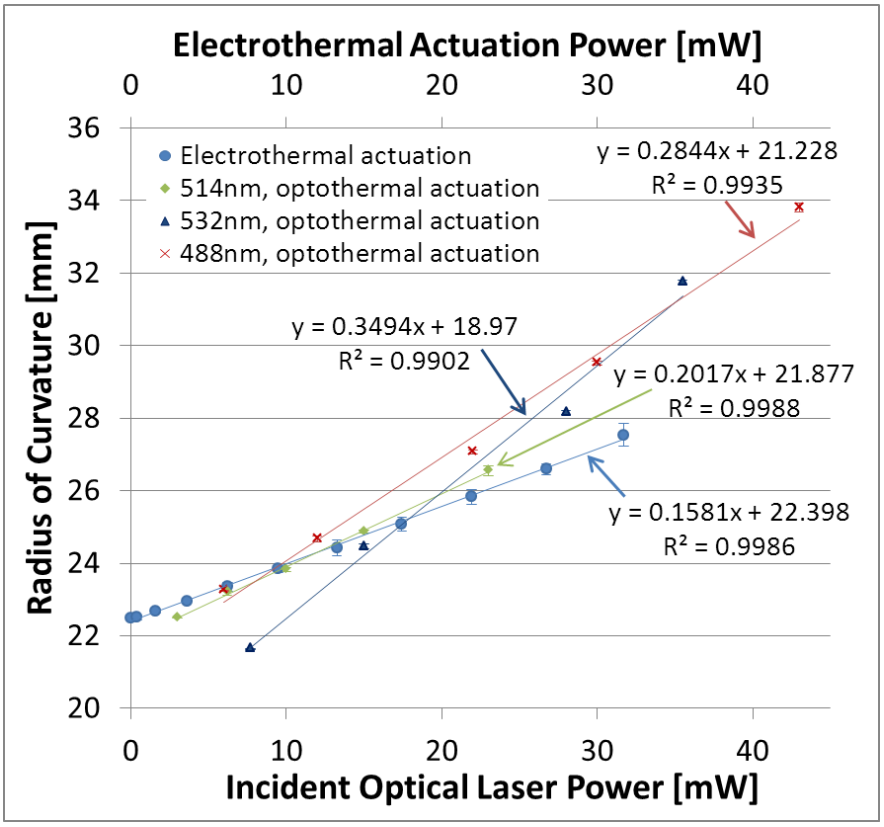

(b)

Figure 4.21: ROC of VFM by electrothermal and optothermal actuation methods.

of VFMs vary linearly with both electrothermal and optothermal actuation power. The electrothermally actuated VFM has a sensitivity of 0.16 mm/mW which is much lower than that of the optothermally actuated VFM. Note that even when the sensitivity was calculated using the total incident laser power as shown in Figure 4.21b, the sensitivity of the optothermally actuated VFM is 0.28 mm/mW, 0.20 mm/mW and 0.35 mm/mW for 488 nm, 514 nm and 532 nm respectively which is still higher than one of the electrothermally actuated VFM. The reason for this is that the optothermal actuation power was delivered directly to the micromirror plate while the electrothermal power was not only used to heat up the VFM but also the suspensions where the current was flowing. The results demonstrate that optothermal actuation is at least 194% more efficient than electrothermal actuation for this VFM structure design.

From the characterisation results between the electrothermal and optothermal actuation, the ROC variation sensitivity of optothermal actuation is higher than that of electrothermal actuation due to the fact that the electrothermal power heats up not only the micromirror but also the serpentine-shape springs which the current is passing through. To further analyse the efficiency differences between the electrothermally and optothermally actuated VFM, the relative resistances of the bimorph micromirror and the serpentine springs are considered. The resistance of the serpentine-shape spring is about 1.07 kΩ, calculated from the geometric shape and resistivity of the silicon material, and the resistance of the micromirror is 158 Ω after subtracting the resistances of two supports from the total resistance of $\sim$2.3kΩ measured between the two electrical pads as is illustrated in Figure 4.22. During the electrothermal actuation, the current passing through the two supports and the micromirror is the same. According to the Joule heating, the heat generated within one supporting spring is $\sim$6.8 times higher than the heat generated within the bimorph micromirror. Therefore, when the applied current is passing through two serpentine-shape springs, the generated heat within the two springs is $\sim$13.6 times higher than the heat generated with bimorph micromirror.

$$\frac{Q_{spring}}{Q_{mirror}} = \frac{I^2 R_{spring} t}{I^2 R_{mirror} t} = \frac{1070\Omega}{158\Omega} = 6.8$$

where,

Q_{spring} and Q_{mirror} are the heat generated within the serpentine-shape spring and the bimorph micromirror of VFM respectively,

R_{spring} and R_{mirror} are the resistance of the serpentine-shape spring and the bimorph micromirror of VFM respectively,

I is the serial current passing through both the two serpentine springs and the micromirror,

t is the duration of the Joule heating.

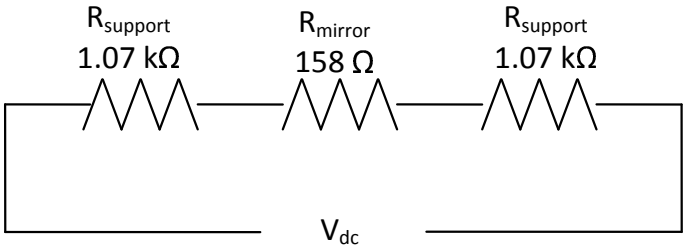

Figure 4.22: The resistance representives of the serpentine-shape springs and the micromirror when the electrothermal actuation power is driven through two out of the eight electrical pads.

Figure 4.23 illustrates the average temperature of the gold layer surface of the VFM model extracted from the FEM simulation of both the electrothermal actuation and optothermal actuation. At the same actuation power of either electrothermal or absorbed optothermal actuation, the average temperature of the gold layer of the VFM generated by the optothermal actuation power is higher than is generated by the electrothermal actuation power.

The X and Y profiles of the optothermally actuated VFM surface measurement at each actuation level were fitted using equation (4.2.2) and are listed in Table 4.6. Compared to the conic section fitted results of the electrothermally actuated VFM on page 97, the surfaces of the optothermally actuated VFM maintained the same conic constant through the actuation levels. One main reason could be that the eight suspensions of the optothermally actuated VFM stay relatively 'cold' and in similar temperature condition, since the heat is generated at center of the micromirror from the bottom surface of the silicon layer and the suspensions are functioning as heat conducting pathways to the substrate besides providing mechanical support. Therefore, the VFM

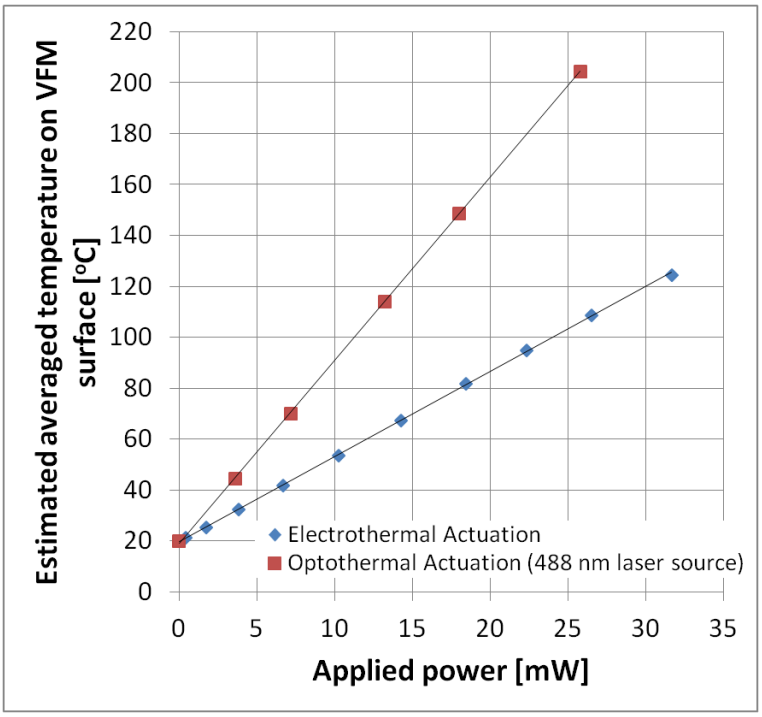

Figure 4.23: Estimated average temperature on the gold layer surface of the VFM FEM model as a function of the electrothermal and absorbed optothermal actuation power.

surface shape stayed oblate elliptical during the optothermal actuation. In contrast, for electrothermal actuation, the maximum temperature is simulated to be located in the middle sections of the thin and long suspensions which are selected to allow current flow through. Thus, during the electrothermal actuation, the suspensions which were used for electrical current pathways were heated up more than the others which were not. However, these unbalanced thermomechanical conditions among the eight suspensions affect VFM curve shapes in an insignificant way, since both the calculated and measured Zernike coefficients of electrothermally actuated VFM showed minor aberrations with values only in several micrometers range.

4.3.3.2 Optical aberration calculation and measurement

After characterising the curves on the surface of the optothermally actuated VFM, shapes of the curves display a constant conic constant during actuation and the curvature is more sensitive to optothermal thermal actuation power rather than electrothermal actuation power. Then, the optical aberrations of the optothermally

Table 4.6: The conic fit between the curves on the surface of the optothermally actuated VFM and conic section of the fitted aspherical equation.

Wavelength [nm]	Laser output power [mW]	Absorbed laser power [mW]	Fitted ROC [mm]		Conic Constant		Differences(*)		Curve Shape	
			X-profile	Y-profile	X-profile	Y-profile	X-profile	Y-profile	X-profile	Y-profile
488 nm	0	0	22.99	23.56	323.90	504.15	0.03	0.03	oblate elliptical	
	6.0	3.6	24.35	24.62	323.89	504.15	0.02	0.01		
	12.0	7.2	25.77	26.08	323.90	504.15	0.01	0.01		
	22.0	13.2	27.90	28.37	323.89	504.15	0.01	0.01		
	30.0	18.0	30.27	30.69	323.89	504.14	0.02	0.01		
	43.0	25.8	34.52	34.90	323.88	504.13	0.01	0.01		
514 nm	3.0	2.0	23.80	23.91	463.21	504.15	0.03	0.01		
	6.2	4.1	24.46	24.61	463.21	504.15	0.03	0.01		
	10.0	6.5	25.07	25.21	463.21	504.15	0.02	0.01		
	15.0	9.8	26.10	26.20	463.21	504.15	0.02	0.01		
	23.0	15.0	27.65	27.85	463.20	504.14	0.02	0.01		
532 nm	7.7	4.8	23.95	24.09	463.21	504.15	0.03	0.01		
	15.0	9.9	25.68	25.53	463.21	504.15	0.03	0.01		
	28.0	18.6	29.52	29.48	463.21	504.15	0.02	0.01		
	35.5	23.6	32.98	32.91	463.21	504.15	0.01	0.01		

(*) calculated using equation (4.2.3).

actuated VFM was calculated by performing the Zernike analysis over the VFM surface measurement at each actuation power level using the MATLAB codes in Appendex D on page 247.

As explained in the last subsection, the magnification of the white light interferometer was increased during the optothermal actuation to avoid scattered laser light saturate the image sensor during measurement. The view of the VFM used for measurements is therefore slightly smaller than the micromirror diameter, and the whole area of the VFM surface could not be scanned during measurement.

Figure 4.24 illustrates the Zernike mode Z_5 (defocus) fitting with the surface measurements of the optothermally actuated VFM actuated at the maximum available incident power using 488 nm, 514 nm and 532 nm wavelengths respectively. A mask of ellipse shape was used to calculate Zernike coeffients produced by optothermally actuated VFM rather than the circular mask, because a reduced aperture size of microscopic white light interferometer was need to avoid sensor saturation by the scatterred laser beam (Figure 4.20) compared to the one used for measuring electrothermally actuated VFM (Frigure 4.8). Therefore, the Zernike coefficients of surface measurements of the optothermally actuated VFM using the ellipse mask are scaled from (4.2.4) using equations in [16]. Table C.6 summaries the first fifteen Zernike coefficients calculated at each incident laser power using the

three wavelengths. Similar to the electrothermally actuated VFM (page 235), the optothermally actuated VFM has been dominated by a defocus aberration of several micrometers which decreases as the laser actuation power increase. Again, higher order aberrations (n $\geq$2), such as astigmatism (Z_4 and Z_6), coma (Z_8 and Z_9), trefoil (Z_7 and Z_{10}) and spherical (Z_{13}) are all in the nanometer range and are negligible, as the diagrams of Figure 4.25, Figure 4.26 and Figure 4.27 illustrated.

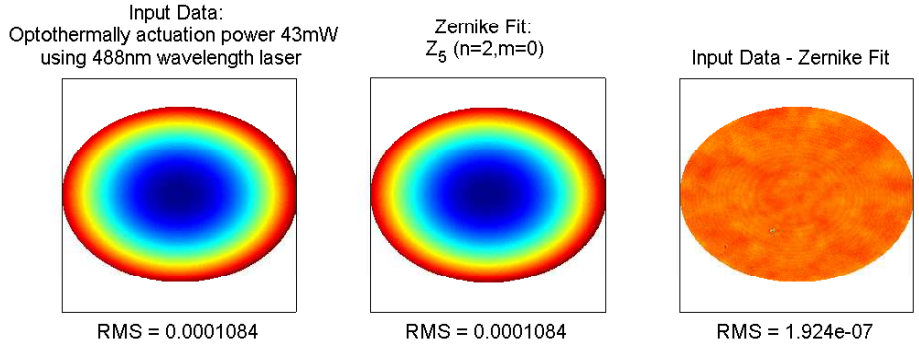

(a) VFM actuated at 43 mW using 488 nm wavelength laser beam

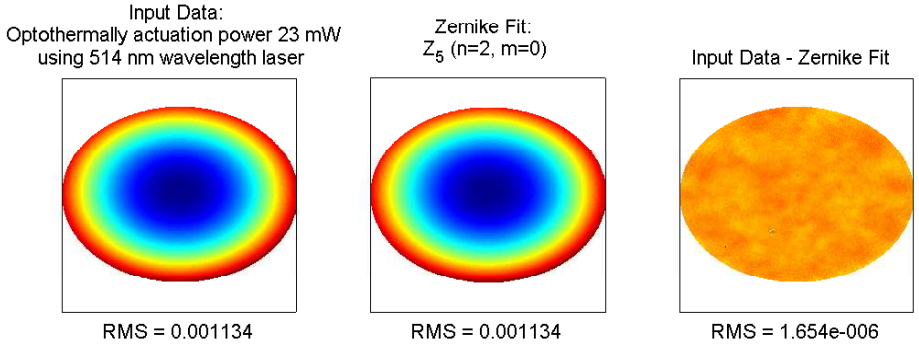

(b) VFM actuated at 23 mW using 514 nm wavelength laser beam

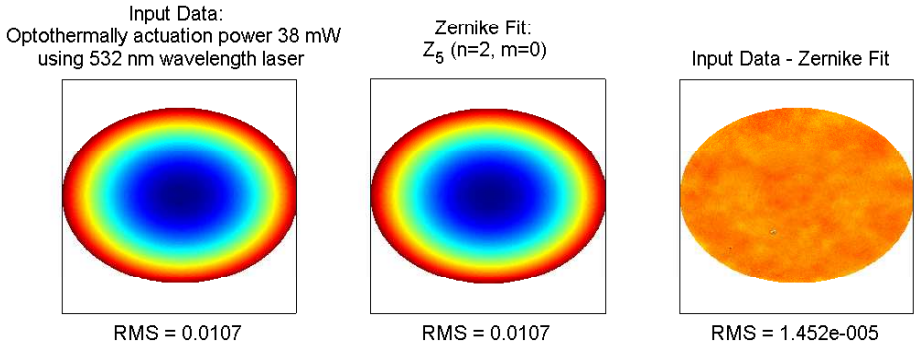

(c) VFM actuated at 7 mW using 532 nm wavelength laser beam

Figure 4.24: The best Zernike mode fit of optothermally actuated VFM surface profile.

The optical aberrations of the optothermally actuated VFM were then measured by the

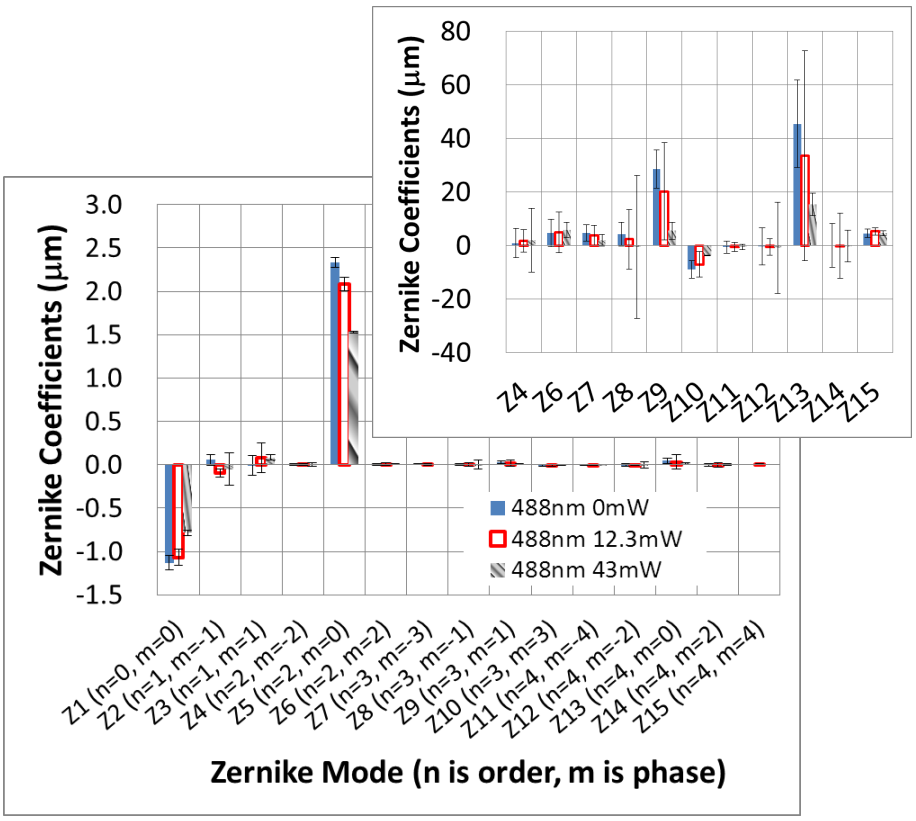

Figure 4.25: Calculated Zernike coefficients of optothermally-actuated VFM by 488nm laser.

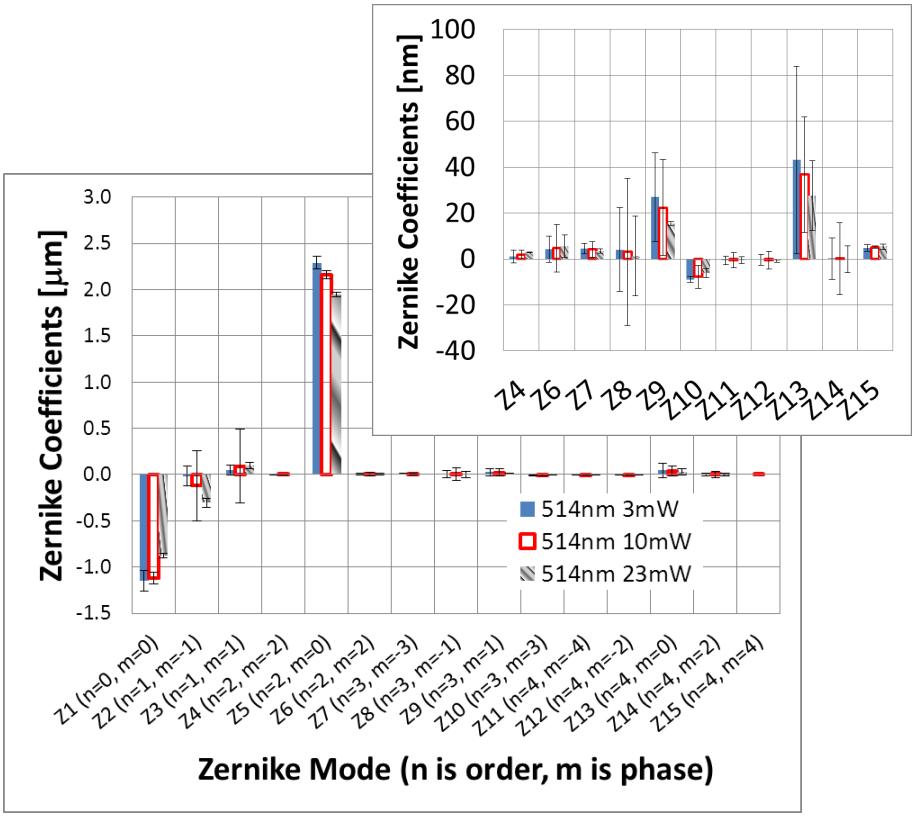

Figure 4.26: Calculated Zernike coefficients of optothermally-actuated VFM by 514nm laser.

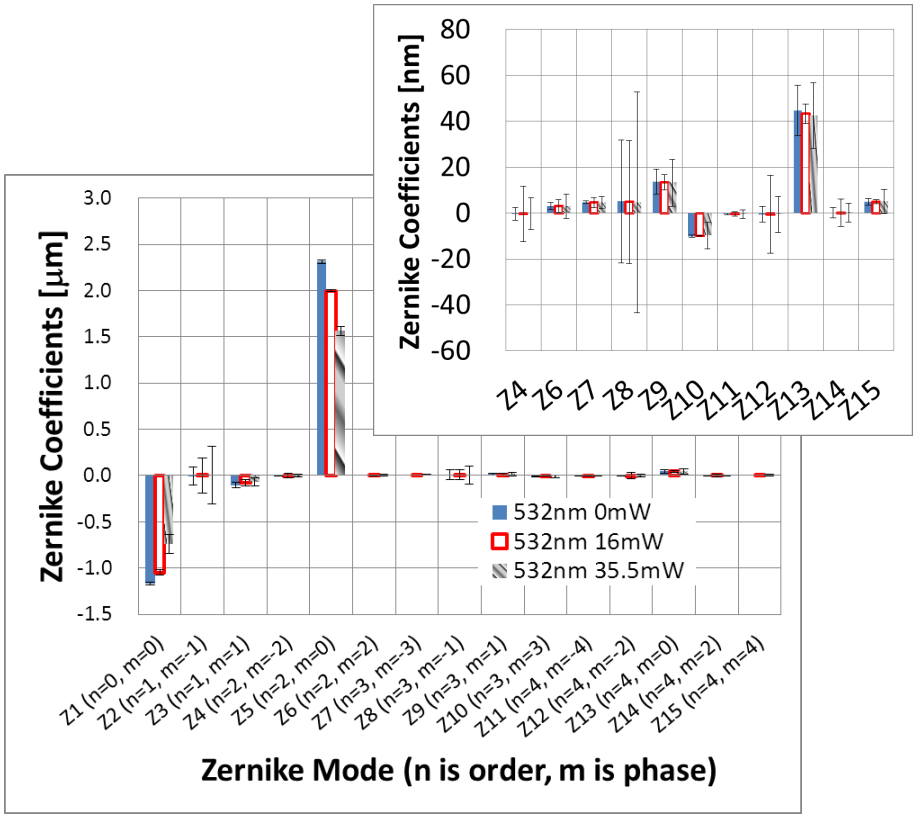

Figure 4.27: Calculated Zernike coefficients of optiothermally-actuated VFM by 532nm laser.

wavefront sensor using the setup of Figure 4.6. During the experiment, the actuation laser beam was incident onto the back surface of the VFM with a very small angle ($<5^{o}$) in order to avoid the transmitted laser beam disturbing the measurement of the probe He-Ne laser beam at the measuring plane wavefront sensor lenslet. Again, due to the aperture size of the optical measurement (setup determined by the 1 mm diameter of the reflective gold layer), only the first six Zernike coefficients can be stably and accurately measured. Table C.7 summaries the Zernike coefficients measured by the wavefront senor using three wavelength laser sources. Figure 4.28, Figure 4.29, and Figure 4.30 demonstrate the measured Zernike coefficients of the VFM during optothermal actuation using 488 nm, 514 nm and 532 nm wavelength laser sources. Since the Zernike coefficients calculated from the surface profile measurements used a non-circular mask, direct comparison to the values measured by wavefront sensor setup using Equation (4.3.2) can not be performed in this case.

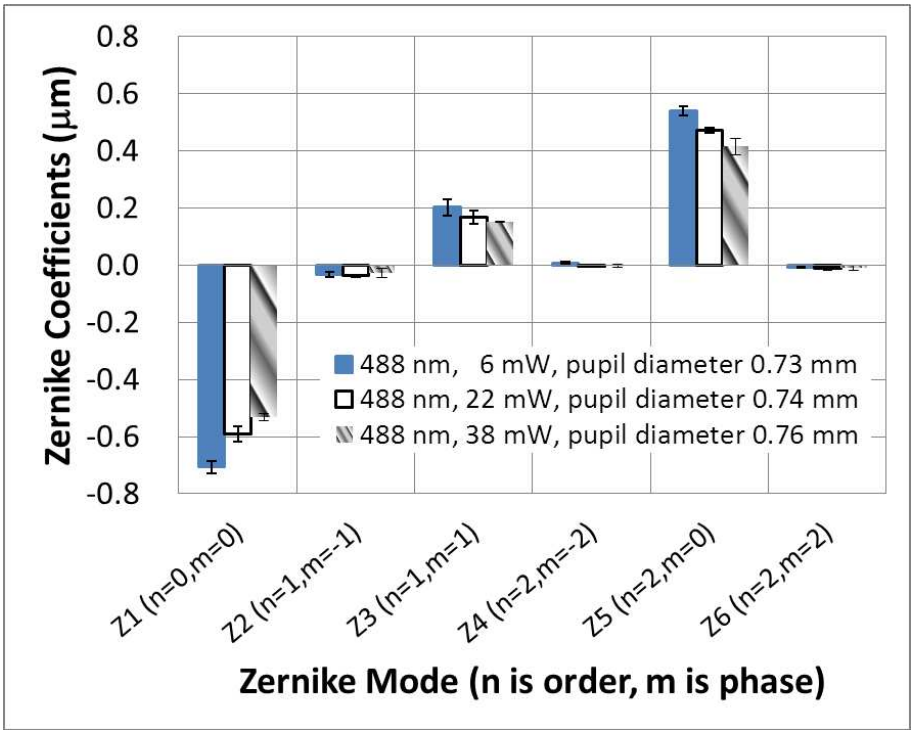

Figure 4.28: Zernike coefficients measured by the Shack-Hartmann wavefront sensor when actuated using 488 nm wavelength laser source (error range within several tens of nanometers).

4.3.3.3 Comparison between measured and simulated ROCs

The ROC of the VFM surface measured using white light interferometer and calculated from the wavefront sensor measurements are plotted as a function of the absorbed laser power in Figure 4.31, Figure 4.32 and Figure 4.33 for the 488 nm, 514 nm and 532 nm wavelengths respectively. The results show the ROC variation using both measurement methods change linearly with the absorbed actuation power and have an agreement of at least 99% for 488 nm and 514 nm wavelength laser and at least 96% for the 532 nm wavelength laser.

The simulation results of the optothermal actuation using the three laser sources described on page 234 are also plotted together with the measurements for comparison. Although the simulated ROC variations show non-linearity due to the absorbed actuation power, the results still show agreement with the measurements of at least 93% 96% and 94% for 488 nm, 514 nm and 532 nm wavelength laser respectively.

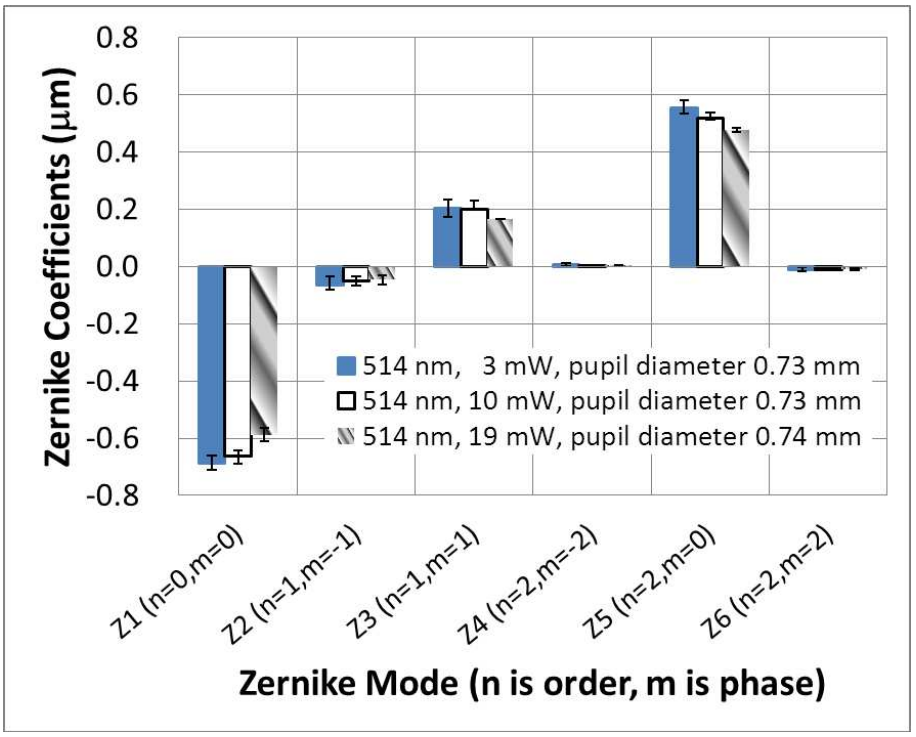

Figure 4.29: Zernike coefficients measured by the Shack-Hartmann wavefront sensor when actuated using 514 nm wavelength laser source (error range within several tens of nanometers).

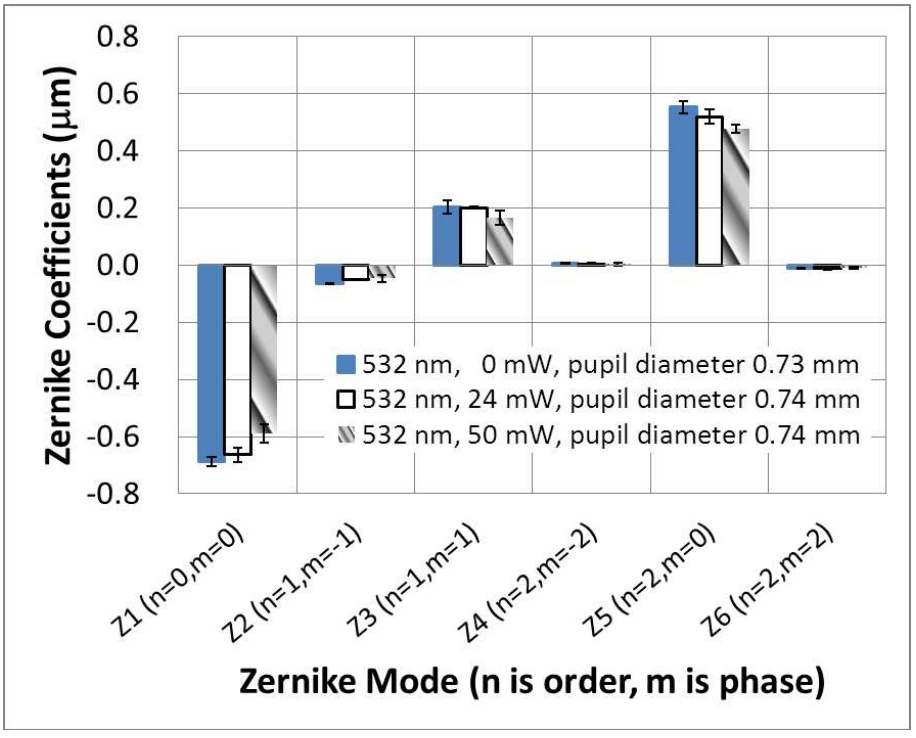

Figure 4.30: Zernike coefficients measured by the Shack-Hartmann wavefront sensor when actuated using 532 nm wavelength laser source (error range within several tens of nanometers).

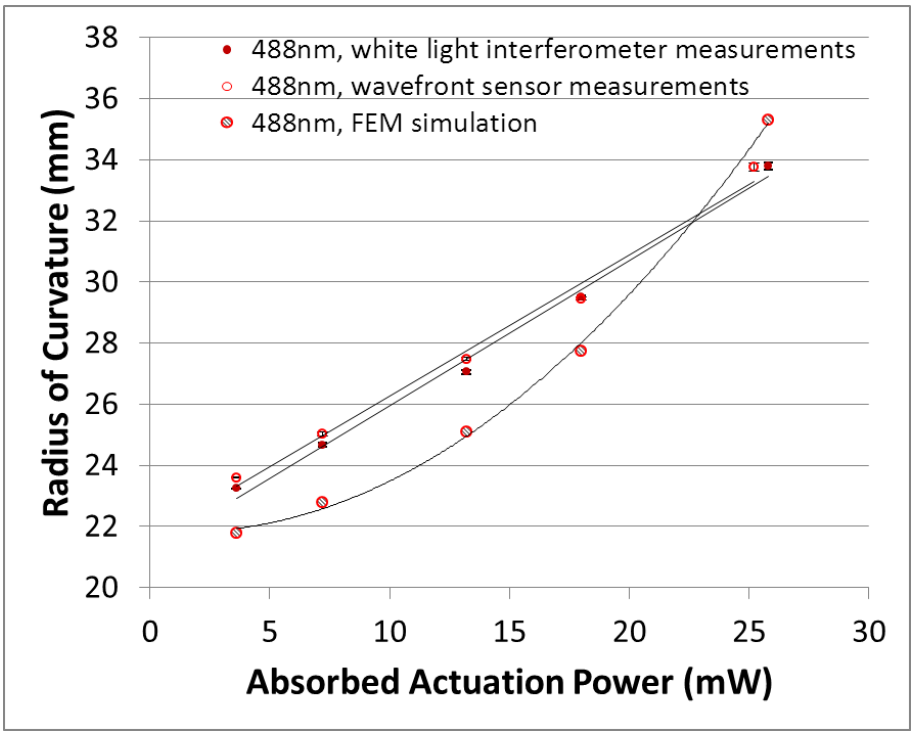

Figure 4.31: FEM simulated ROC and measured ROC as a function of absorbed 488 nm laser power.

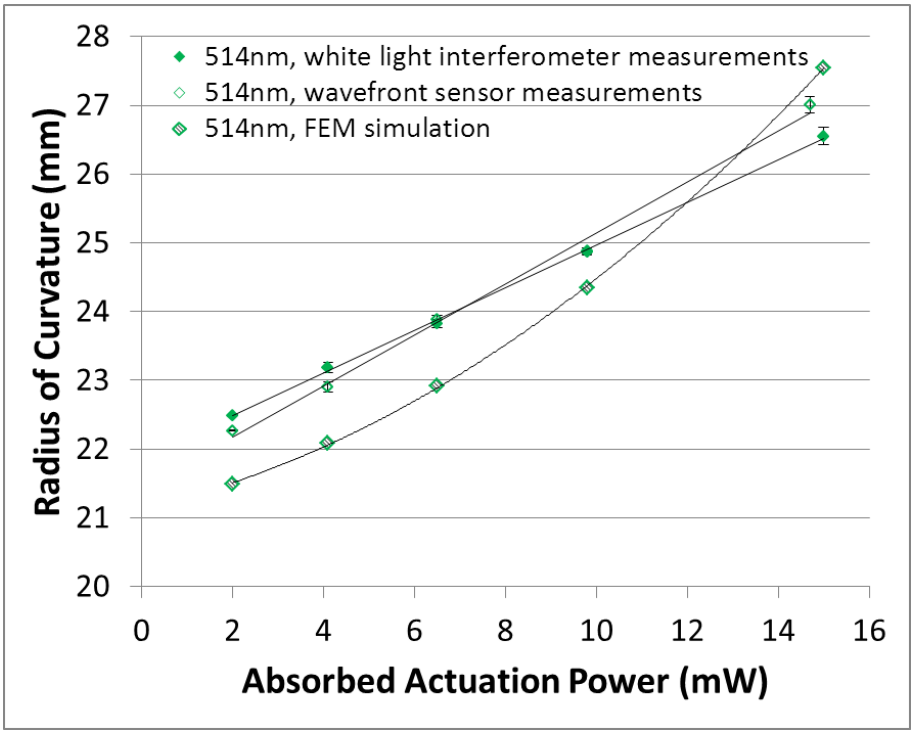

Figure 4.32: FEM simulated ROC and measured ROC as a function of absorbed 514 nm laser power.

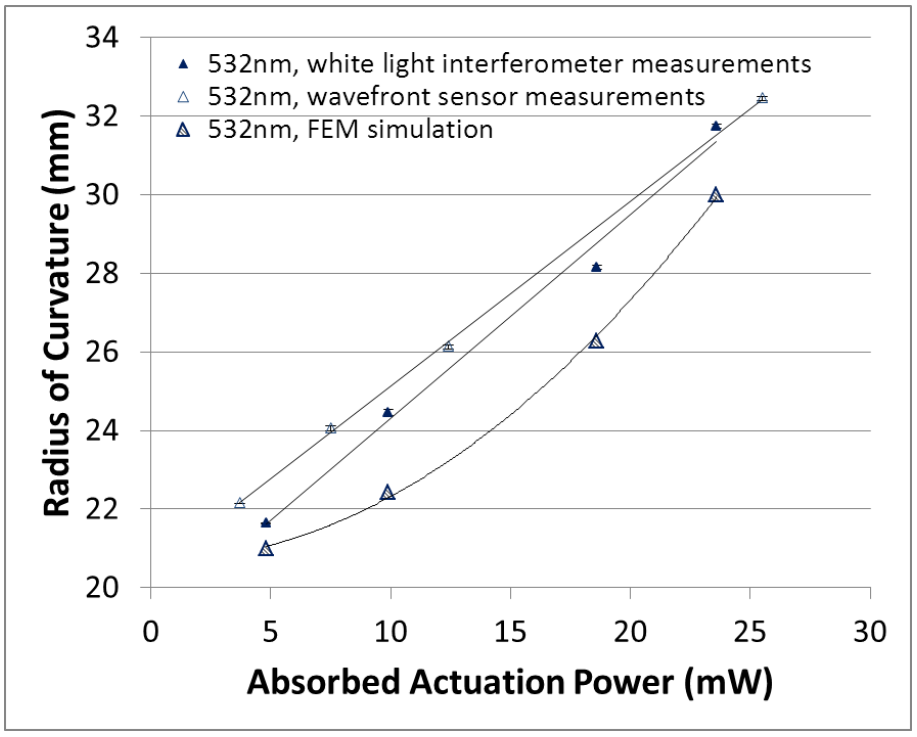

Figure 4.33: FEM simulated ROC and measured ROC as a function of absorbed 532 nm laser power.

4.4 Optical Imaging System

In order to demonstrate the performance of the VFM in an imaging application, the VFM was incorporated into an optical imaging system (Figure 4.34). Illuminated objects are placed on the optical axis of the imaging system with the object-to-VFM distance ranging from L_{omin} to L_{omax}. Light arriving from the object is directed to the VFM surface using a plate beam splitter. The light is then focussed by the VFM onto a CMOS image sensor located at a distance D_s away from the VFM.

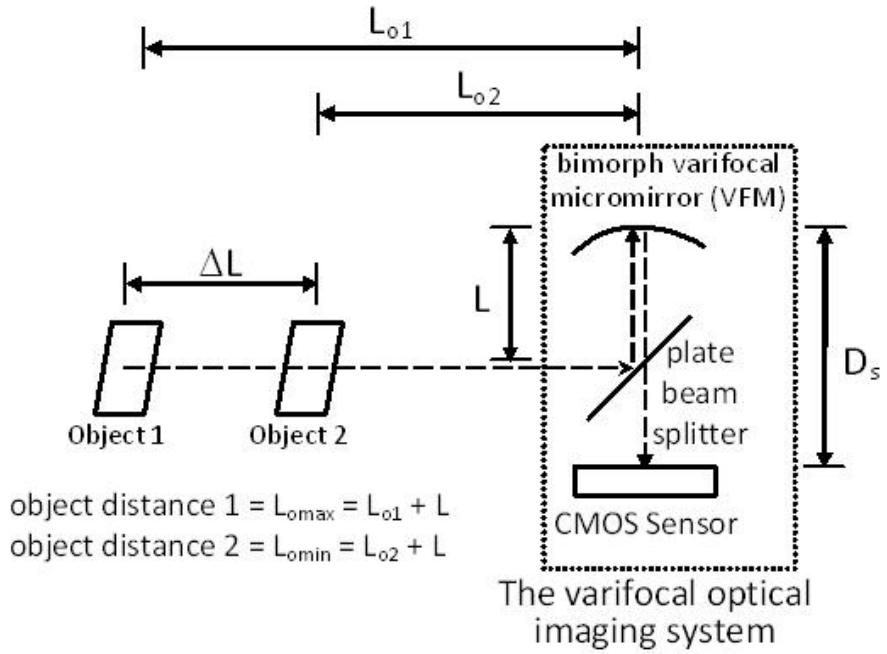

Figure 4.34: Diagram of the varifocal optical imaging system using the varifocal micromirror.

Applying the simple mirror equation [17, Chapter 36, page 1012], the minimum and maximum object distances (L_{omin} and L_{omax}) are related to the ROC_{min} and ROC_{max} of the VFM by the following equations:

$$L_{omin} = \frac{D_s ROC_{min}}{2D_s - ROC_{min}} \tag{4.4.1}$$

$$L_{omax} = \frac{D_s ROC_{max}}{2D_s - ROC_{max}} \tag{4.4.2}$$

where D_s is the distance between the CMOS image sensor and the VFM; ROC_{min} and ROC_{max} are the radii of curvature of the VFM at 0 mW and the maximum driving

power at 10 V (i.e 31mW for the VFM device used in the imaging system) respectively.

In the varifocal imaging system, two different objects were located at the nearest and the furthest object distance (i.e. L_{omin} and L_{omax}) to present the imaging system tracking range. Before the VFM was implemented in the varifocal imaging system, the minimum ROC was measured to be 22 mm and the maximum ROC was measured to be 27.8 mm at 31 mW. The CMOS sensor was fixed at the distance of 15 mm from the VFM. As seen in Figure 4.35, the left half of a 7 mm-by-7 mm letter A was sharply imaged at a distance of 41.5 mm at 0 mW, and the right half of a 30 mm-by-30 mm letter A was sharply imaged at 175.5 mm at 31 mW. In this case, the optical imaging system presents an object tracking range of 134 mm when D_s was fixed at 15 mm. Additionally, a repeat measurement was taken when D_s was increased to 16.5 mm. The resulting images are displayed in Figure 4.36 with L_{omin} of 32.5 mm and L_{omax} of 85 mm, giving an object tracking range of 52.5 mm. Finally, to demonstrate the system imaging coloured objects at D_s of 17.5 mm, a blue and a red colouring pencil were estimated to be sharply imaged at L_{omin} of 30.5 mm and at L_{omax} of 66.5 mm respectively (Figure 4.37).

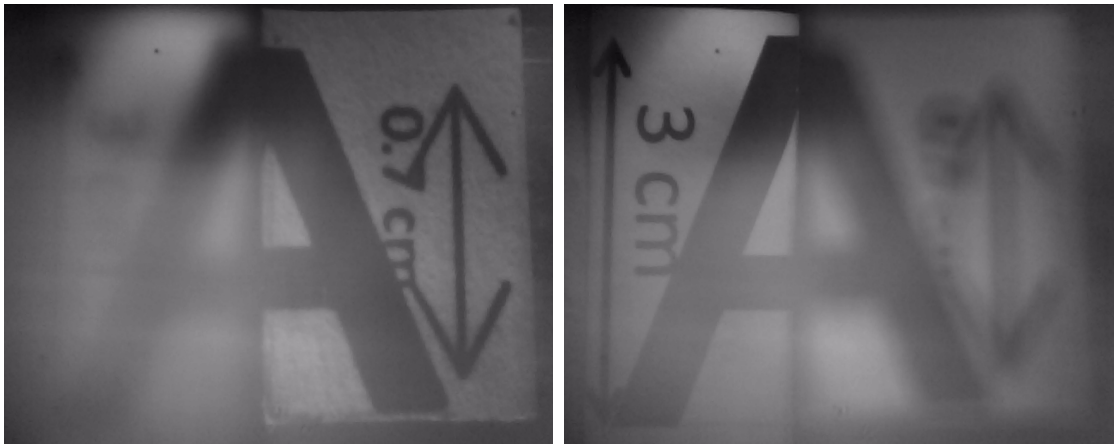

(a) (b)

Figure 4.35: Images of the 30x30mm letter A (left part) and 7x7mm letter A(right part) obtained by the varifocal imaging system (D_s=15mm, L_{omax}=175.5mm and L_{omin}= 41.5mm). The un-actuated mirror focuses on right part of letter A (a) while in (b), the mirror using 10V focuses on the left part of letter A.)

Focused imaging results using the optothermally-actuated VFM were also obtained when D_s was 15 mm. An example of this optothermal actuation is shown in

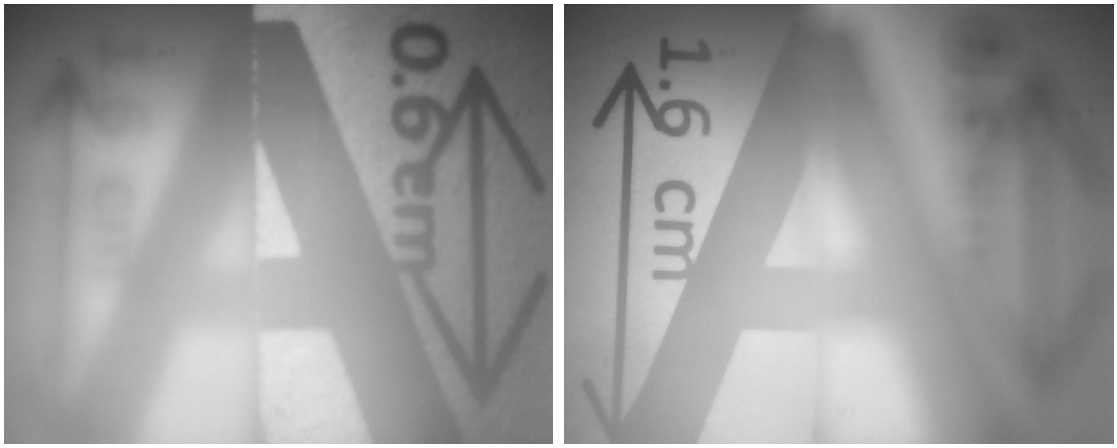

(a) (b)

Figure 4.36: Images of the 16x16mm letter A (left part) and 6x6mm letter A(right part) obtained by the varifocal imaging system (D_s=16.5mm, L_{omax}=85mm and L_{omin}=32.5mm). The un-actuated mirror focuses on right part of letter A (a) while in (b), the mirror using 10V focuses on the left part of letter A.

Figure 4.38 where the VFM was driven by 22.8 mW of laser output power (λ=488 nm, 60% VFM absorption) with the red and blue pencils located at L_{omax} of 209 mm and L_{omin} of 44 mm from the CMOS sensor respectively. With no actuation, the blue pencil was in focus while the red one was in focus with incident optothermal actuation of 22.8 mW.

Table C.8 summarises the sensor distance (D_s), the measured and calculated values (using Equation (4.4.1) and (4.4.2)) for L_{omin} and L_{omax}, and the object tracking range (ΔL) of the varifocal imaging system measured in the three experiments. In Equation (4.4.2), as D_s decreasing infinity close to the ROC_{max} of the VFM, L_{omax} becomes infinity which indicating the system will be able to focus on an image located infinite distance away from the VFM; therefore, the object tracking range, defined by ΔL = L_{omax}-L_{omin}, becomes infinite long in this case. Less than 3% discrepancy between the measured and calculated values was observed in the experiments and this difference is mainly due to the measurement error in D_s.

The last row of Table C.8 presents a 27% difference between the calculated and the measured object distances for the focused image. This is due to the depth of field (DOF) of the imaging system. Using the DOF equations (4.4.3) given in [18, chapter

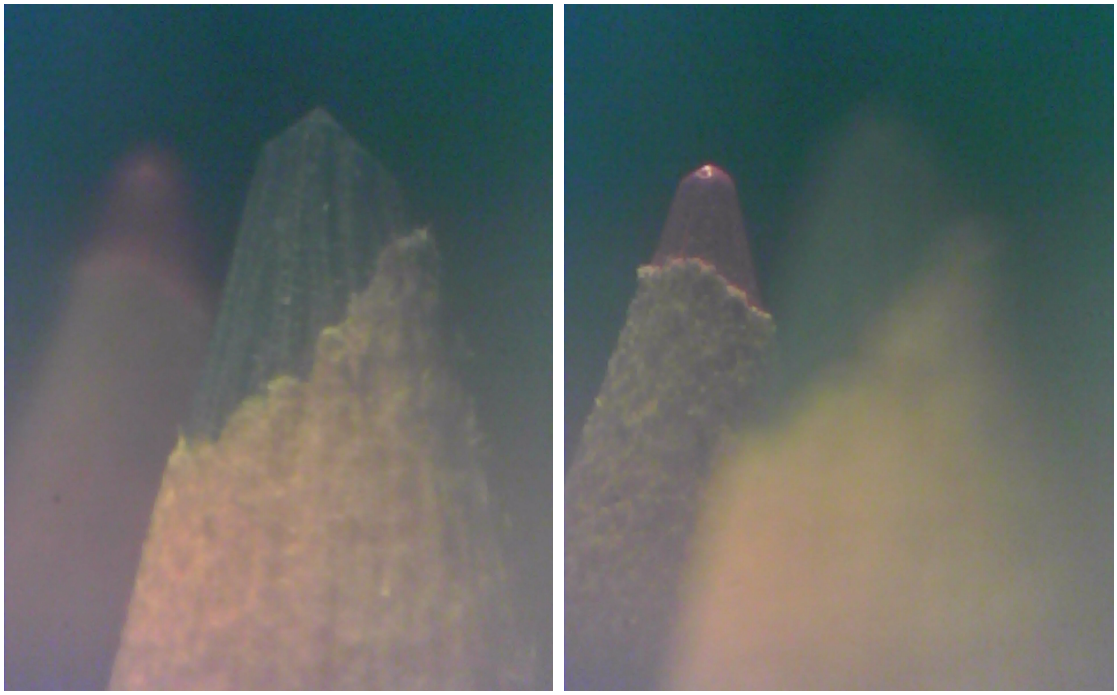

(a) (b)

Figure 4.37: Images of the blue and red pencils located 30mm and 66.5mm away from the VFM with D_s=17.5mm. The un-actuated mirror focuses on blue pencil (a) while in (b), the mirror using 10V focuses on the red pencil.

22, page 217-221] and taking the diameter of the aperture as 1 mm and the estimated circle of confusion for the CMOS sensor to be 0.02 mm, the near limit of the DOF of the varifocal imaging system at the VFM optothermal actuation power of 22.8 mW was calculated to be 133 mm while the far limit was 217 mm. It can be seen that the measured object distance lies between these two limits, thus explaining the origin of focusing uncertainty (error) which leads to the large difference of 27%. We calculated the near limit of DOF and far limit of DOF for all results in Table C.8, and in all cases the measured object distance lay between these limits. For a fixed aperture, the DOF increases when the VFM ROC is increased by the actuating power. Moreover, the judgement on the sharpness of the image results of Figure 4.38b is made more difficult by the small image size of the red pencil which is placed further away than the blue pencil and also by the speckle from the scattered actuating laser collected by the sensor.

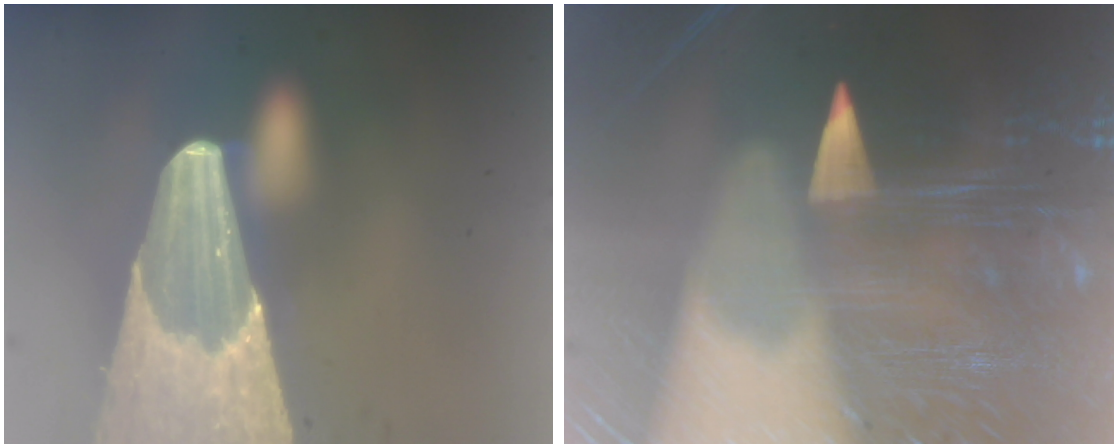

(a) (b)

Figure 4.38: Images of the blue and red pencils located 44 mm and 209 mm from the VFM with D_s of 15 mm. The un-actuated mirror focuses on the blue pencil (a); while in (b), the mirror driven by using 488 nm wavelength 22.8 mW laser power focuses on the red pencil.(b) also displays imaging of the scattered blue laser light leading to speckle over the target objects of the colour pencils.

$$\begin{aligned} D_n &= \frac{L_o(ROC/2)^2}{(ROC/2)^2 + NcL_o} \\ D_f &= \frac{L_o(ROC/2)^2}{(ROC/2)^2 - NcL_o} \\ N &= \frac{ROC/2}{\phi} \\ DOF &= D_f - D_n \end{aligned} \tag{4.4.3}$$

where,

ROC is the radius of curvature of the gold layer surface of VFM,

L_o is the object distance of the imaging system,

N is the f-number,

c is the circle of confusion in mm and is assumed to be 0.02 mm,

ϕ is the diameter of the gold layer surface of the VFM,

D_n is the near distance of the acceptable sharpness,

D_f is the far distance of the acceptable sharpness,

DOF is the depth of the field.

As the reflection of the gold coating of the micromirror is measured to be 50% using the low power HeNe laser and the refraction and reflection rate of the plate beam splitter is

50% and 50%, only 12.5% of the object light reaches the CMOS sensor in this optical imaging system.

4.5 Discussion

4.5.1 Hysteresis effect during electrothermal actuation

Hysteresis experiments of measuring the steady state ROC of VFM samples #1 and #3 by applying a DC voltage level, through electrical pads 4 and 8, were made: first increasing from 0 V to 10 V (33 mW) and then decreasing to 0 V with each voltage level applied for around 30 seconds to prevent temperature rise on the substrate of the VFM due to the heat conduction during experiment. As presented in Figure 4.39 and Figure 4.40, small offset of around -0.3 mm were observed for measurements of both VFM devices when the electrothermal actuation power was stepped down to 0 mW. Therefore, the hysteresis of ROC is negligible when actuation varies from different levels.

4.5.2 Length of the suspending springs

In the last subsection, the mechanical performance of an increased diameter of VFM micromirror is estimated by simulation of the electrothermal actuation. Despite the heat losses within the current passing springs during the electrothermal actuation, the Joule heating of the suspension springs contributes to the temperature rise of the micromirror along with the Joule heating of the micromirror itself. Continued from the geometric variation study of the last subsection, the impact of length of suspension spring on the electrothermal actuation performance of the VFM is estimated using FEM simulation in this subsection.

Previously, the geometric design of the original VFM described in this chapter is varied by first increasing the diameter of the micromirror from 1.2 mm to 2 mm.

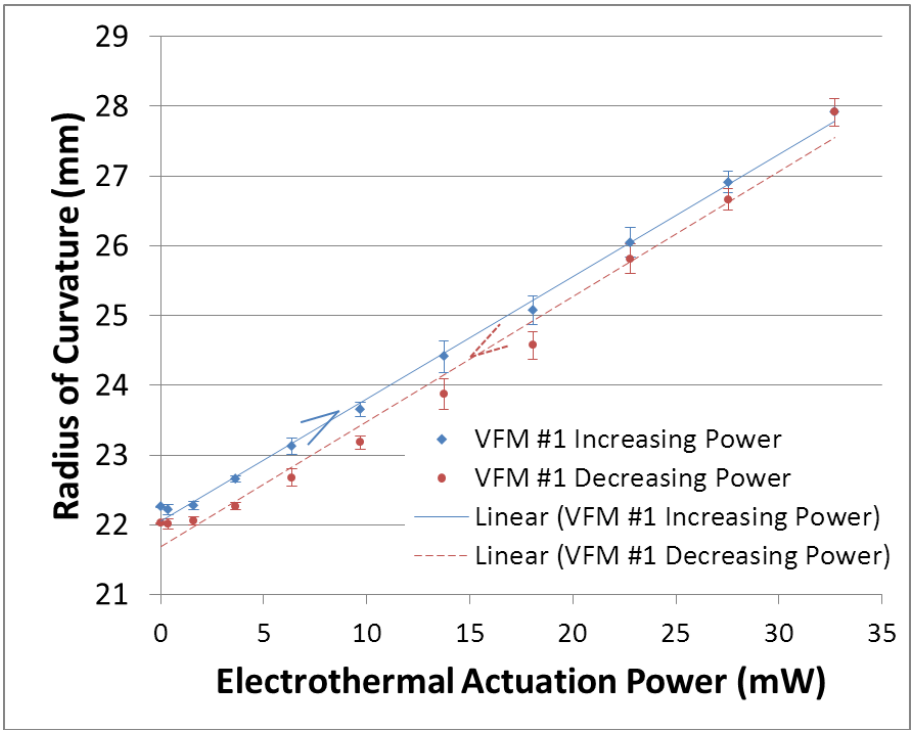

Figure 4.39: ROC variation of VFM sample #1 when the electrothermal actuation power increasing towards maximum values and then decreasing from maximum value to zero.

In this subsection, the length of the suspension spring of the 2 mm VFM design is reduced from 1531 μm to 787 μm, and the resistance of each spring is reduced from 1071 kΩ to 551 kΩ. The electrothermal actuation of this 2 mm diameter VFM with shorter suspending springs is simulated by applying voltage levels from 0 V to 10 V through two opposite springs. The radius of curvature of this modified VFM model is calculated and plotted together with both the original 1.2 mm diameter VFM and the 2 mm diameter VFM in Figure 4.41. The ROC variation sensitivity of the 2 mm diameter VFM is reduced by -41% compared to the original 1.2 mm diameter VFM under the same simulated voltage levels. When the VFM geometric modification is further changed by reduced the length of each spring to 787 μm, the ROC variation sensitivity of which is further reduced to 0.03 mm/mW, a reduction of 49% compared to the 2 mm VFM model. Therefore, by reducing the length of supporting springs their resistances can be reduced, but doing so reduces the mechanical ROC variation sensitivity of the VFM design instead of making an improvement.

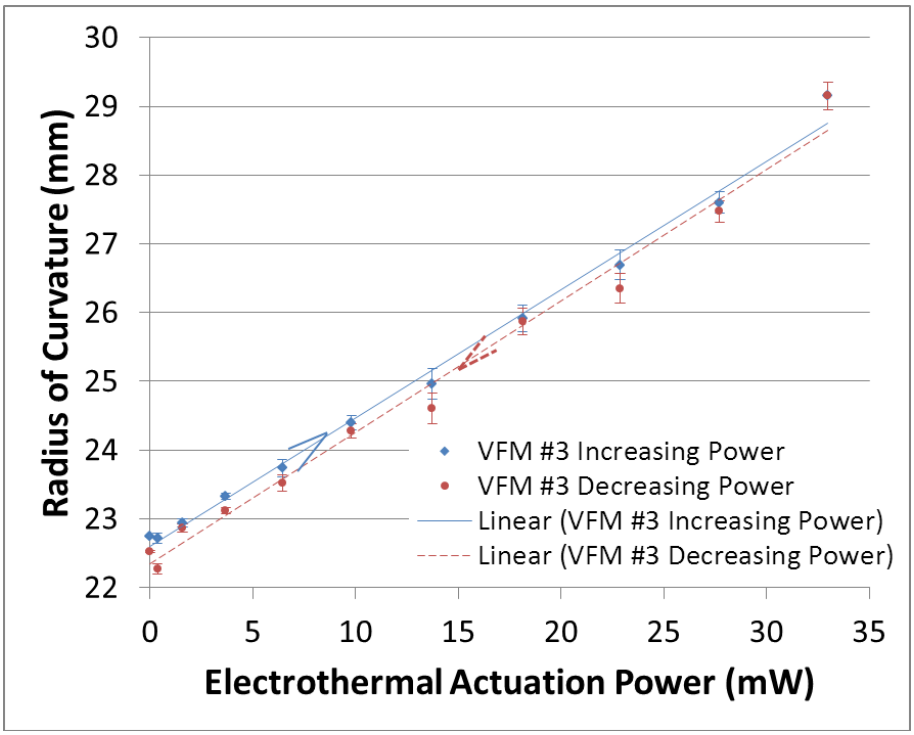

Figure 4.40: ROC variation of VFM sample #3 when the electrothermal actuation power increasing towards maximum values and then decreasing from maximum value to zero.

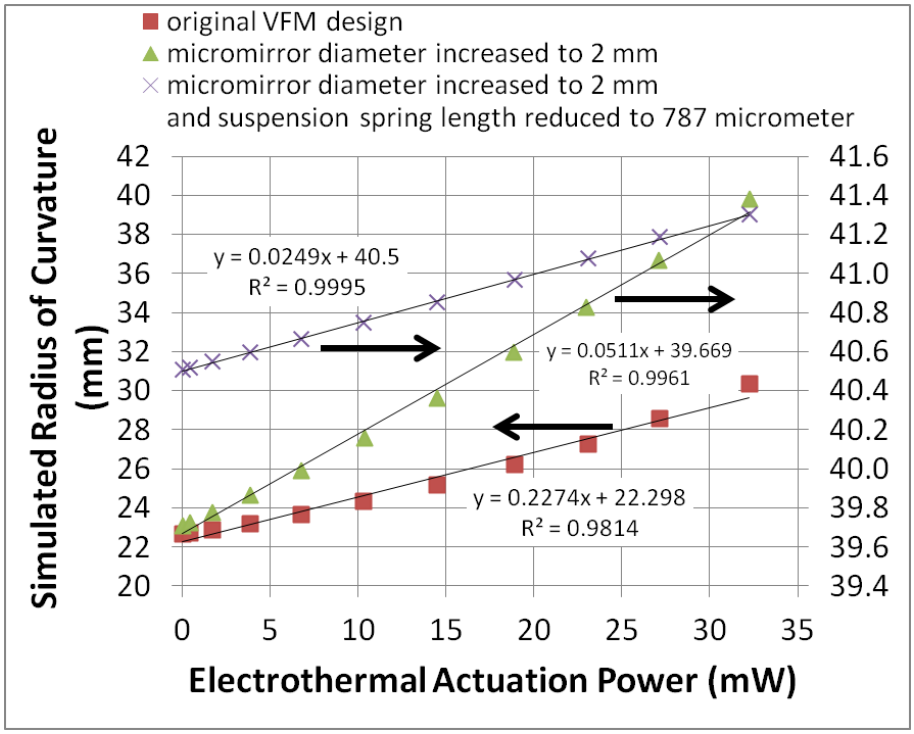

Figure 4.41: Estimated ROC variation of VFM model with micromirror diameter scaled from 1.2 mm to 2 mm.

References

[1] M. Lin, H.-T. Hsieh, W.-Y. Hsu, Y.-C. Cheng, C.-H. Wu, and G.-D. J. Su, "Auto-focus imaging systems with mems deformable mirrors," in *Proc. SPIE 7428, Current Developments in Lens Design and Optical Engineering X*, pp. 74280Q–9, Aug. 2009.

[2] W. Liu and J. J. Talghader, "Current-controlled curvature of coated micromirrors," *Optics Letters*, vol. 28, pp. 932–934, Jun. 2003.

[3] A. A. Alzaydi, J. T. Yeow, and S. L. Lee, "Hydraulic controlled polyester-based micro adaptive mirror with adjustable focal length," *Mechatronics*, vol. 18, no. 2, pp. 61 – 70, 2008.

[4] R. Hokari and K. Hane, "A varifocal micromirror with pure parabolic surface using bending moment drive," in *2008 IEEE/LEOS Internationall Conference on Optical MEMs and Nanophotonics*, pp. 92–93, 2008.

[5] R. Hokari and K. Hane, "A varifocal convex micromirror driven by a bending moment," *IEEE Journal of Selected Topics in Quantum Electronics*, vol. 15, pp. 1310 –1316, Sep.-Oct. 2009.

[6] T. Sasaki and K. Hane, "Initial deflection of silicon-on-insulator thin membrane micro-mirror and fabrication of varifocal mirror," *Sensors and Actuators A: Physical*, vol. 172, no. 2, pp. 516 – 522, 2011.

[7] T. Sasaki and K. Hane, "Varifocal micromirror integrated with comb-drive scanner on silicon-on-insulator wafer," *Journal of Microelectromechanical Systems*, vol. 21, pp. 971 –980, Aug. 2012.

[8] H.-T. Hsieh, H.-C. Wei, M.-H. Lin, W.-Y. Hsu, Y.-C. Cheng, and G.-D. J. Su, "Thin autofocus camera module by a large-stroke micromachined deformable mirror," *Optics Express*, vol. 18, pp. 11097–11104, May 2010.

[9] VEECO, "Wyko NT1100 Optical Profiling System." http://www.veeco.com/.

[10] M. Servin and M. Kujawinska, *Handbook of Optical Engineering*. 207 Madison Avenue, New York, NY 10016: Marcel Dekker Inc., 2001.

[11] L. Thibos, R. A. Applegate, J. T. Schwiegerling, and R. Webb, "Standards for reporting the optical aberrations of eyes," in *Vision Science and its Applications*, p. SuC1, Optical Society of America, 2000.

[12] J. M. H. R. W. Gray, "A MATLAB function to work with Zernike polynomials over circular and non-circular pupils." `http://www.mathworks.com/matlabcentral/fileexchange/33330-zernikecalc`, Oct. 18 2011.

[13] THORLABS, "Optical wavefront sensor (Shack-Hartmann sensors) WFS series operation manual," 2011.

[14] M. Born and E. Wolf, *Principles of Optics*. Cambridge, UK: Cambridge Univeristy Press, 7th ed., 1999.

[15] J. Schwiegerling, "Scaling Zernike expansion coefficients to different pupil sizes," *J. Opt. Soc. Am. A*, vol. 19, pp. 1937–1945, Oct. 2002.

[16] L. Lundström and P. Unsbo, "Transformation of zernike coefficients: scaled, translated, and rotated wavefronts with circular and elliptical pupils," *Journal of the Optical Society America A*, vol. 24, pp. 569–577, Mar 2007.

[17] J. W. J. Raymond A. Serway, *Physics for Scientists and Engineers with Modern Physics*, vol. 2nd. Cengage Learning, 7nd ed., 2007.

[18] S. Ray, *Applied Photographic Optics: Lenses and Optical Systems for Photography, Film, Video, Electronic and Digital Imaging*. Englewood Cliffs: Oxford: Focal Press, 3rd ed ed., 2002.

Chapter 5

2D MEMS Scanner With Hybrid Actuation – Case Study

5.1 Overview

The MEMS two dimensional (2D) scanning mirror is an important component for imaging applications. Many have been developed for digital imaging and biomedical imaging systems, such as the in-vivo imaging, optical coherence tomography (OCT), confocal endoscopic probe. Most of the reported 2D scanning micromirrors for imaging applications use the same type of actuation mechanisms for both scanning directions, either electrostatic [1], electrothermal [2] or electromagnetic [3] actuators. Taking electrostatic and electrothermal actuation schemes for examples, both types of actuators are relatively easy to be fabricated using multi-users MEMS fabrication processes. Electrostatic comb-drives are commonly used in microscanner designs to excite rotational motion at structural resonant frequency. In order to obtain a sufficient scan angle, one common method is to increase the maximum capacitance variation range of the comb-drives, it can be achieved by either increasing the number of electrode pairs for each scanning axis or increase the overlapping area between the electrodes [4, 5]. In order to make electrostatic MEMS scanner to scan in two

orthogonal directions, either two independent pairs of comb-drives are connected to rotate the micromirror in two orthogonal directions [4], or one pair of comb-drives is actuated with superimposed resonant frequencies to scan a Lissajous pattern [6]. The dynamic actuation using electrostatic comb-drives could have nonlinearity response and even instability resulting in pull-in failure mode, which is the short circuit of comb-drives. Therefore, the synchronization between control and measurement signals are relative complicated [7]. Besides, the driving voltage required is usually ranging from at least several tens of up to hundreds of volts. However, the power consumption is low and mainly from the current generated from the charging and discharging electrons. To the contrary, operation of electrothermal actuated 2D microscanners requires low voltage levels, typically less than 20 V. The electrothermal actuation utilises Joule heating to convert electrical power to thermal expansion force up to micro-Newton range [8, 9, 10]. However, due to the principle of Joule heating, it consumes high power ranging from several tens of to hundreds of milliwatts. Electrothermal actuators also generate large amount of heat within the actuator; some structure design could have the maximum temperature up to around hundreds of degree Celsius. In addition, the response speed of electrothermal actuators is limited by thermal response time ($\sim$ 50 - 60 ms). Therefore, unlike electrostatic comb-drives, the electrothermal actuators are usually operated by DC or low frequency electrical signal. Moreover, the displacement magnitudes of electrothermal actuators are usually linear to their actuation voltages. The controlling and synchronising of electrothermally-actuated microscanner are relatively less complicated than the electrostatic actuated microscanner.

In this chapter, the case study of a hybrid-actuated 2D microscanner sample which is first designed by G. Brown [11] as a concept trial is presented. First of all, the structure and the actuation principles of electrothermal actuator and electrostatic comb-drives applied for the microscanner are introduced in Section 5.2. Then in Section 5.3, the layout, the structure and fabrication processes of this microscanner are introduced. Section 5.4 presents the performance quantification in terms of the maximum scan angles by each type of actuator individually. Section 5.5 demonstrates the raster

scan patterns produced by the microscanner when both types of actuators are driven at the same time. Section 5.6 illustrates the simulated motions of the microscanner using FEM software, CoventorWare. By comparing the simulated motions with the measurements, the sources of limitation is visualised and analysed. In Section 5.7, the performance limitations of this hybrid scanner are summarised.

5.2 Actuation Principles

This section introduces the structural design and the actuation principles of electrothermal actuator and electrostatic comb-drives which is used for hybrid-actuated microscanners.

5.2.1 Electrothermal actuator

The layout design of electrothermal actuator used for hybrid-actuated 2D microscanner is inherited from the design introduced in [12]. As shown in Figure 5.1, the shape of electrothermal actuator is designed to be fabricated within the SOI layer (red). It consists three 1800-μm-long and 50-μm-wide cantilevers equally spaced by 150 μm. The three cantilevers are anchored at the same side to the substrate, the free ends of which are joined by a 450-μm-long and 60-μm-wide joint beam. At each anchor, a gold coated (orange) square electrical pad fixed to the substrate is connected to cantilever for electrical pathway. Under the silicon electrothermal actuator structure, there is a trench hole throughout the thickness of the substrate (gray).

To demonstrate the actuation of SOIMUMPs fabricated electrothermal actuator, the FEM model was built in CoventorWare and the static electro-thermo-mechanical behaviour was simulated. The silicon material properties of the SOI layer are summarised in Table 2.3 in page 29. In the FEM model of the electrothermal actuator, the three cantilevers are set to be fixed at surfaces connected to the electrical pads. The temperature of those three fixed ends is assumed to be 20^{o}C. As already described in

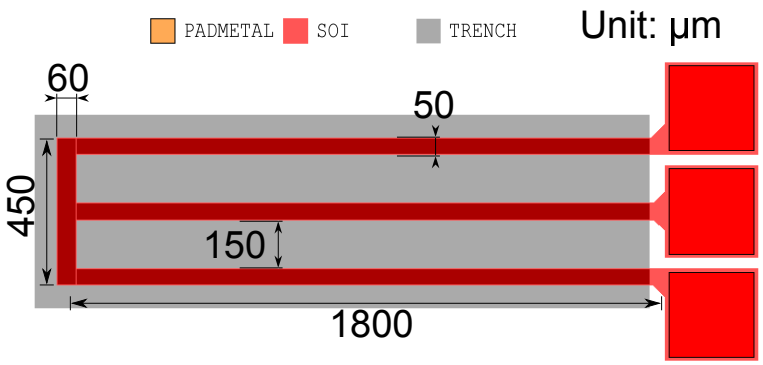

Figure 5.1: The 2D layout design of the electrothermal actuator used in the hybrid actuated 2D microscanner.

[12], the electrothermal actuator provides vertical displacement at the free end when a current is flowing through the outer and the joint beam. Therefore, an 8 V voltage potential was defined across the surfaces of fixed ends of two outer beams. The rest of the silicon surfaces on the electrothermal actuator model are defined as the convection and radiation surfaces with convection coefficient to be around 25 $Wm^{-2}K$ and emissivity to be 0.6. The ambient temperature for these heat convective and radiative surfaces is assumed to be 20°C.

Figure 5.2 displays the estimated temperature distribution and the mechanical deformation of electrothermal actuator at 0 V and 8 V. In the mechanical displacement results at 0 V in Figure 5.2a, the electrothermal actuator has an initial vertical displacement of around 24.6 μm at the tip of free end due to stress gradient as mentioned earlier. In the temperature profiles of electrothermal actuator in Figure 5.2b and Figure 5.2d, when 8 V voltage level is applied to the ends of two outer cantilevers with 12 mA resulting current, the average temperature of two outer cantilevers is simulated to be around 526 °C, and the average temperature of the inner cantilever is simulated to be around 278 °C. Due to the higher average temperature, the outer cantilevers expand more than the inner one along the length dimension and initial angle. The less expanded inner cantilever constrains the expansion of two outer cantilevers through the joint beam. Under the stress introduced by thermal expansion, the two constrained outer cantilevers buckle at around middle section while the inner cantilever stretched. Therefore, the expansion difference between the outer and inner

cantilevers results in the buckling of the outer two cantilevers and out-of-plane rotation of the inner cantilever about the fixed end. The maximum vertical tip displacement of electrothermal actuator at 8 V was estimated to be around 98.5 μm as demonstrated in Figure 5.2c.

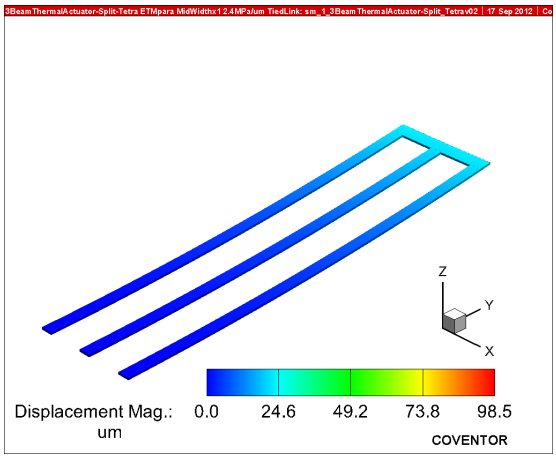

(a) Displacement at 0 V

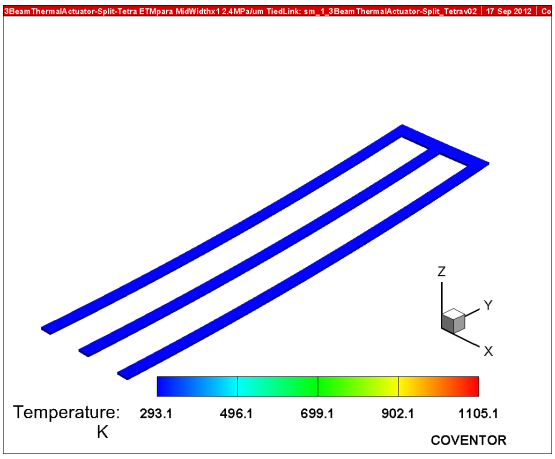

(b) Temperature profile at 0 V

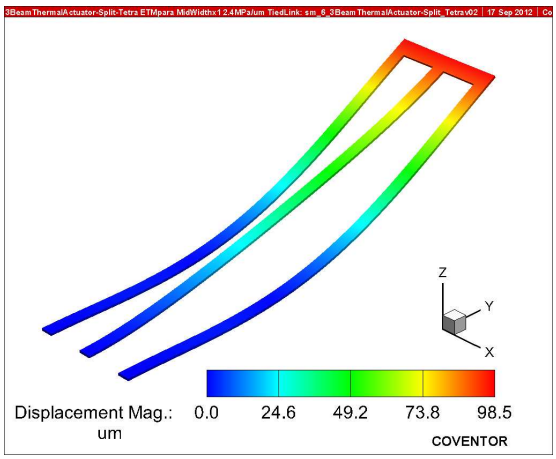

(c) Displacement at 8 V

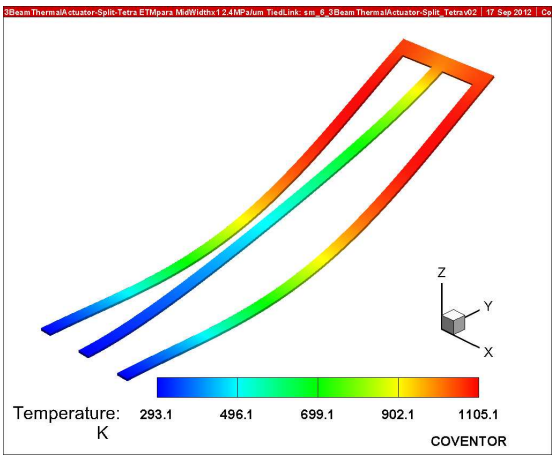

(d) Temperature profile at 8 V

Figure 5.2: The demonstration of static actuation of the electrothermal actuator simulated using FEM software, CoventorWare (displacement of the electrothermal actuator is exaggerated by x5 times.)

5.2.2 Electrostatic comb-drives

The electrostatic actuators used in hybrid-actuated micromirror consist of two pairs of comb-drives. Each pair of electrostatic comb-drives consists of a group of fixed-finger structures interdigitated with the other group of movable fingers which is identical to

the fixed fingers as shown in Figure 5.3. Either fixed or movable group has finger structures equally spaced by 22 μm and fixed to an object on the same side like a comb. The gap between the sides of fixed and movable fingers is 6 μm. The distance from finger tips and joint ends is 8 μm. The two groups of movable fingers of each pair of comb-drives are symmetrically fixed to a 30 μm wide and 532 μm long torsion bar. The fixed fingers of comb-drives are anchor to the substrate through an extension sheet. This extension sheet is a 290-μm-by-309-μm square sheet engraved with three rectangular openings and coated with tensile stressed BlanketMetal and PadMetal gold layers (blue and orange colours in Figure 5.4) in the SOIMUMPs. The purpose of coating the extra layers of tensile stressed BlanketMetal and PadMetal gold layers is to increase the out-of-plane vertical deflection of the fixed fingers and form an initial angle between two electrodes. This comb-drives with initial rotation angle, namely the angular vertical comb-drives (AVC), has been theorically and experimentally reported to be able to produce higher maximum scan angle than staggered vertical comb-drives [13, 14].

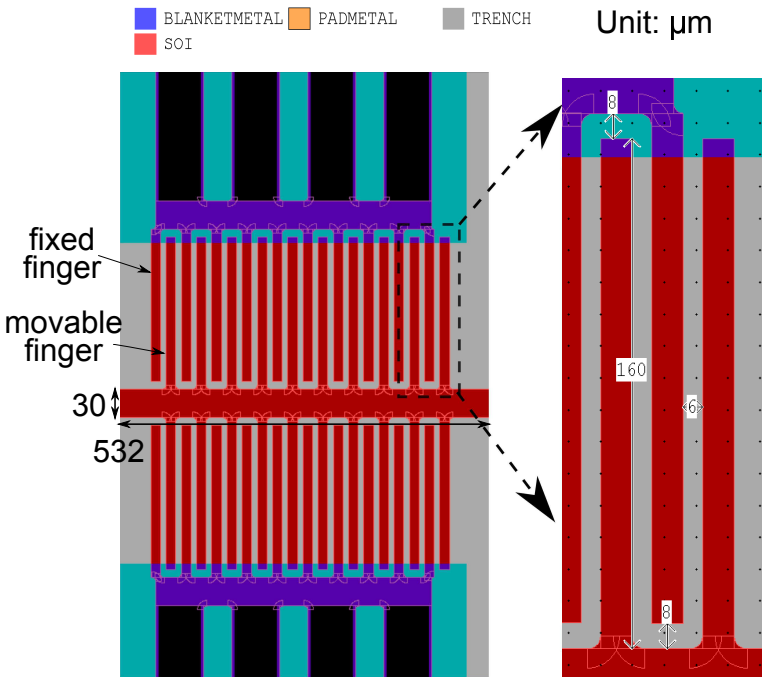

Figure 5.3: The 2D layout view of finger-structures of electrostatic comb-drives of microscanner design in L-Edit.

During actuation, one pair of comb-drives is actuated with a periodic voltage signal to excite the resonant mode where the micromirror is rotating about the torsion bar

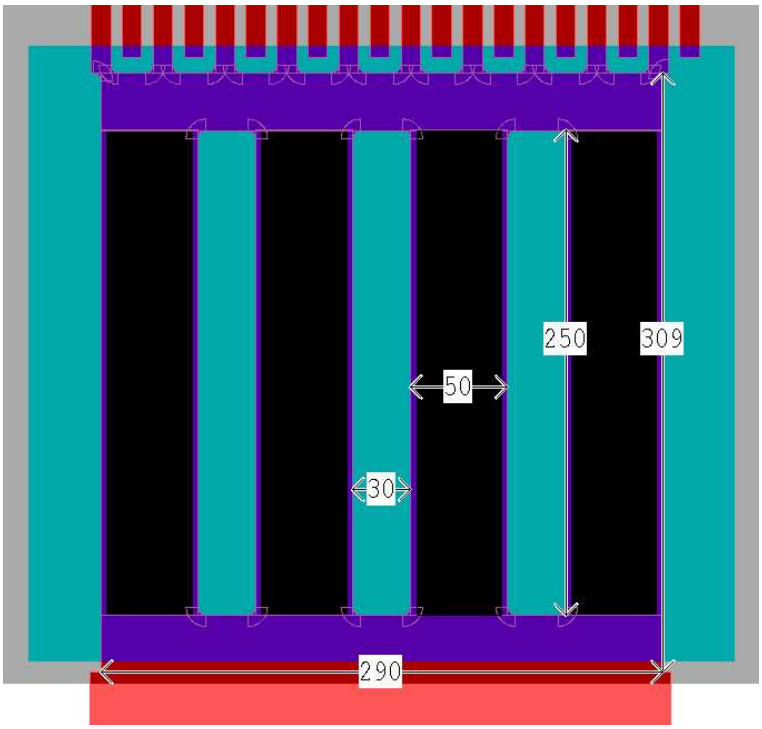

Figure 5.4: The 2D layout view of extension sheet of electrostatic comb-drives of microscanner design in L-Edit.

of electrostatic comb-drives. The detailed characterisation and mode analysis of this resonant mode will be described in the following characterisation and simulation sections.

This section first introduces the arrangement of hybrid-actuated microscanner. Then, the characterisation results of microscanner scan angles in two directions are described. The two dimensional scanning pattern of microscanner is demonstrated by reflecting a laser beam onto a screen. Finally, the modal analysis and the electrothermal actuation are simulated using CoventorWare.

5.3 Structure And Fabrication

In order to test the feasibility of scanning one micromirror in two directions using two different types of actuation mechanisms respectively; the electrostatic comb-drives from [15] and the electrothermal actuator from [12] are arranged around a circular

micromirror as demonstrated in the SEM image in Figure 5.5.

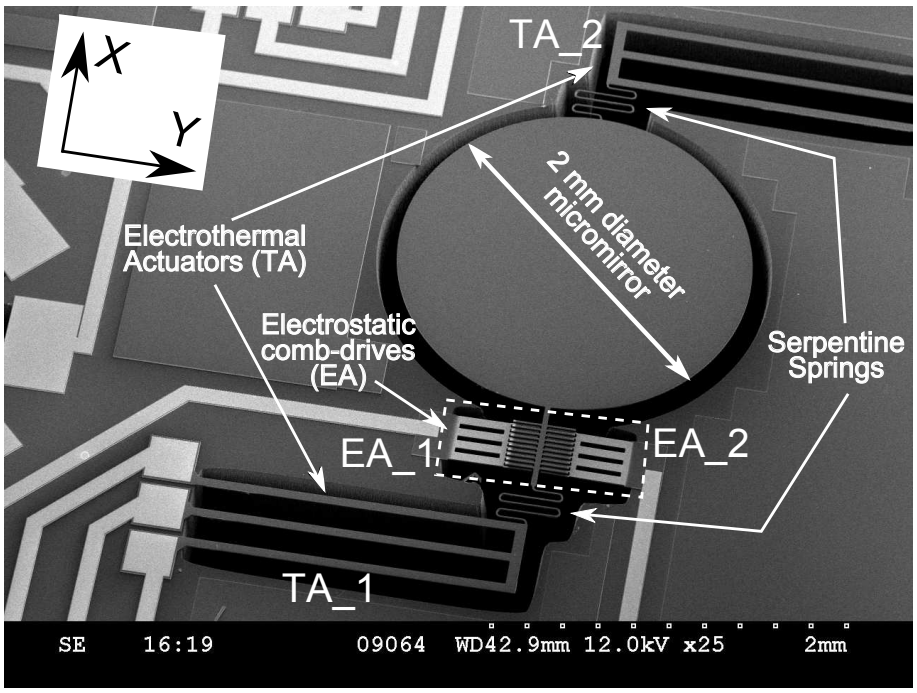

Figure 5.5: The SEM image of the hybrid actuated scanning micromirror [11].

This hybrid-actuated 2D microscanner consists of a circular micromirror, two pairs of electrostatic comb-drives and two electrothermal actuators. The circular micromirror is 2 mm in diameter. The electrostatic comb-drives are connected to the micromirror through a 530-μm-long and 30-μm-wide torsion bar. The two electrothermal actuators are aligned perpendicular to the torsion bar. One of the electrothermal actuators is connected to the edge of the micromirror through a serpentine spring and the other one is connected to the torsion bar also through a serpentine spring.

The micromirror, the electrostatic comb-drives and the electrothermal actuators are all patterned from a single layer of 10 μm thick SOI using SOIMUMPs. The detailed description of fabrication processes are introduced in Section 2.5.1. Due to the 2.4 MPa/μm stress gradient of SOI layer, the cantilever-like structure fabricated within which curves out-of-plane and the micromirror surface has a concave curvature. Therefore, after releasing from the substrate, the structure of the microscanner curves out-of-plane as presented in the 3D view of measured using the white light interferometer in Figure 5.6. The cantilever-like electrothermal actuators curve out of the plane at the free end even there is constraint from the connecting micromirror. The

single layer silicon micromirror have a concave surface radius of curvature of 0.1 m. Notice that the micromirror is not parallel to substrate due to the non-symmetric layout design and silicon structural deformation after fabrication.

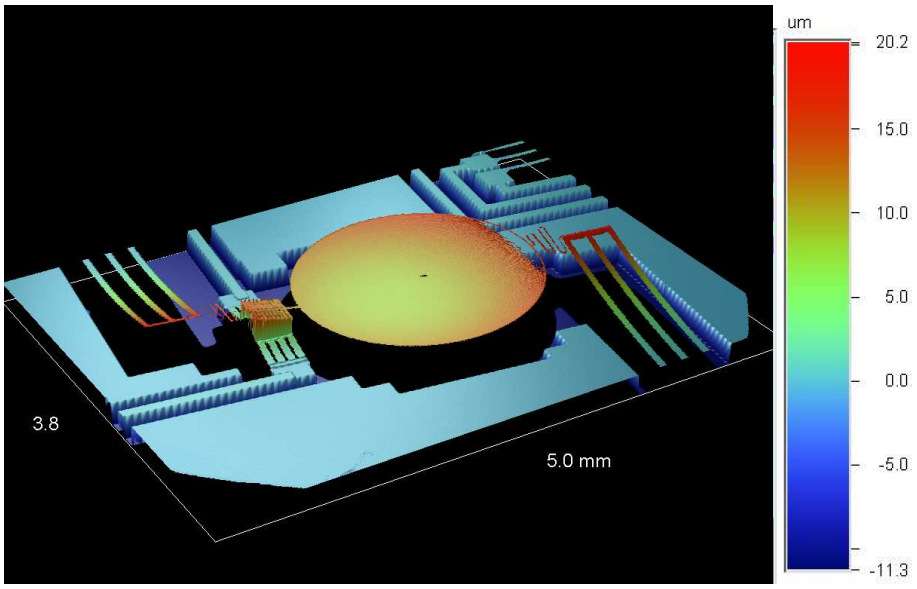

Figure 5.6: The 3D view of the hybrid actuated scanning micromirror measured by the white light interferometer.

To achieve the dual-axis scanning pattern, one electrothermal actuator is driven by stair-case voltage signal to tilt the micromirror out-of-plane from the connected edge. Meanwhile, within each step of staircase signal for the electrothermal actuator, one pair of electrostatic comb-drives is driven by AC voltage signal to rotate the micromirror about torsion bar at resonant frequency. The detailed mechanical scanning performance will be presented in the following section.

5.4 Characterisation

The 2D microscanner is characterised first by measuring the maximum optical scan angle in one direction driven by one of the electrothermal actuators and then in the other direction driven by one pair of the electrostatic comb-drives. The experimental setup of measuring optical scan angles of the microscanner is illustrated in Figure 5.7. The main source of measurement error when using this experimental

setup was the $< \pm 0.5$ mm reading estimation for the laser spot position on the grid screen. Afterwards measuring the optical angles, the 2D raster scan pattern is then produced using the same measurement setup by synchronising the driving signals for electrothermal actuator and electrostatic comb-drives.

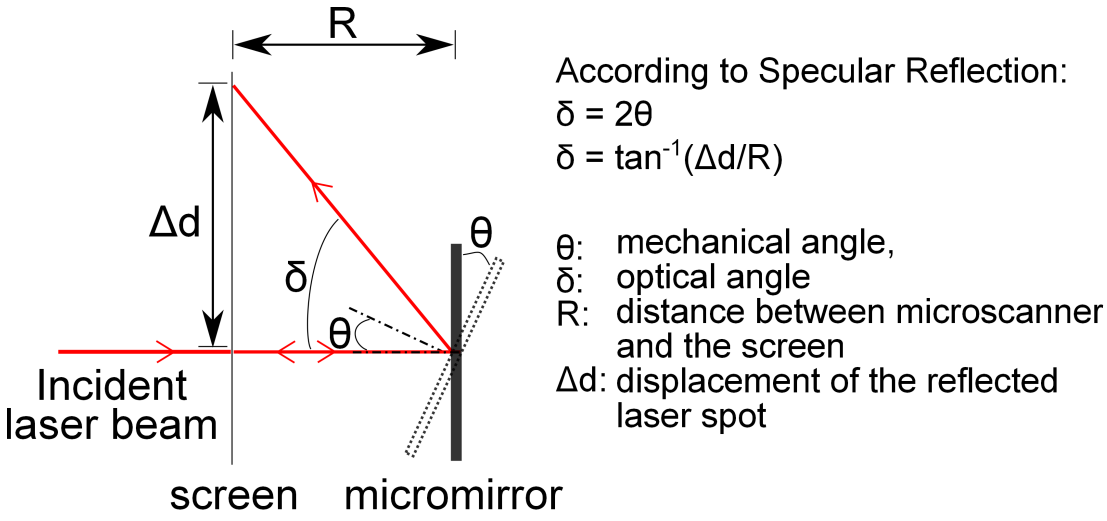

Figure 5.7: The illustration of measuring the optical tilt/scan angle of the microscanner by using the reflected laser spot.

First the optical angle of microscanner is characterised by measuring the laser spot displacement when applying one electrothermal actuator with DC voltage levels up to 15 V. Since the electrothermal actuator provides a static tilting of the microscanner when driving by DC voltage level, the optical angle by the electrothermal actuator is described as optical tilt angle.

Figure 5.8 displays measurements of the optical tilt angles of microscanner by each electrothermal actuator. The diagram shows that optical tilt angles do not response till the driving voltage reaches to 5 V (47 mW). And the optical tilt angles are linear to electrothermal actuation power from 47 mW to 270 mW. The maximum optical scan angles by each electrothermal actuator are -4.5^o and 4.7^o respectively. And the reflected laser spot scan in the direction by $\pm 33^o$ off the vertical direction of the grid screen when electrothermal actuators are aligned with horizontal direction. Table C.9 summarises the measurements of optical tilt angles by each electrothermal actuator. The analysis of tilt orientation of microscanner by the electrothermal actuator is described later in the simulation section.

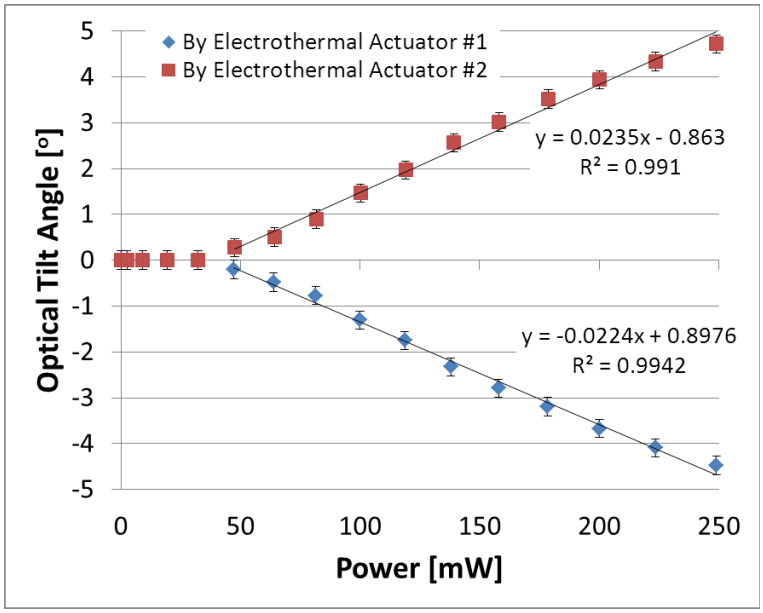

(a)

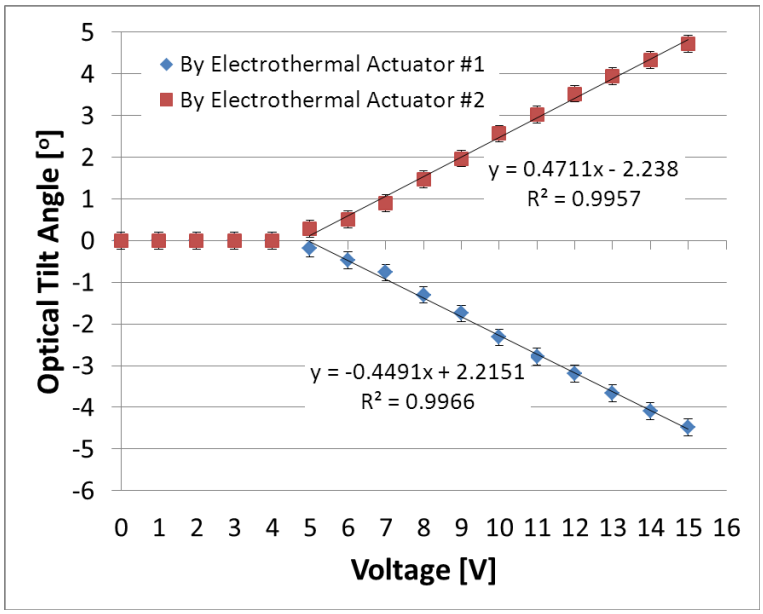

(b)

Figure 5.8: The measured static optical tilt angles of microscanner by each electrothermal actuator.

Besides of optical tilt angle, the surface profiles of hybrid-actuated microscanner were measured using white light interferometer when each of the electrothermal actuator is actuated at 7 V. Figure 5.9a has demonstrated the micromirror tilt position when the electrothermal actuator #1 was driven at 7 V, and the Figure 5.9b has demonstrated the orientation of micromirror tilting when electrothermal actuator #2 was driven at 7 V.

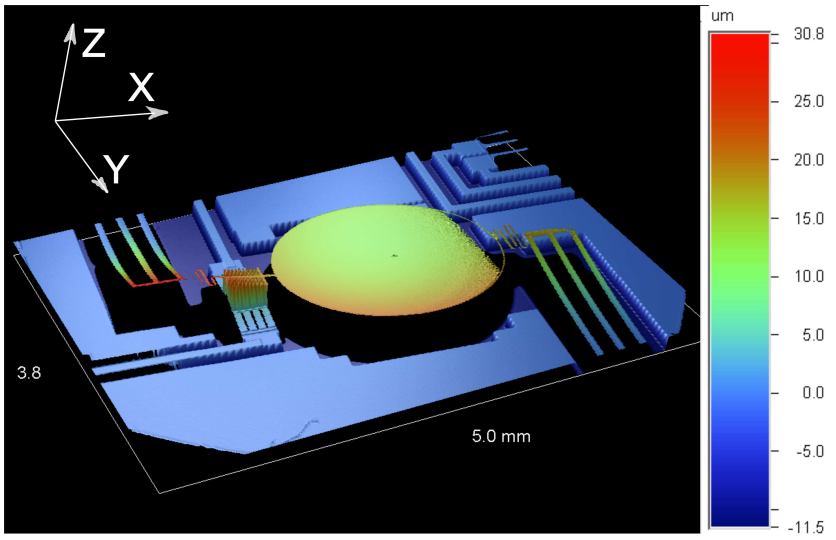

(a) Electrothermal actuator #1 (TA 1) is actuated at 7V

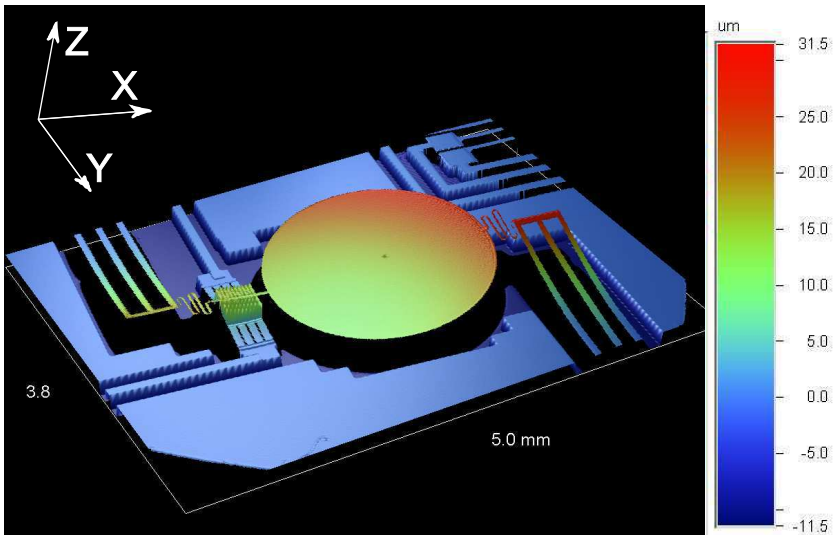

(b) Electrothermal actuator #2 (TA 2) is actuated at 7V

Figure 5.9: The measured surface profiles of hybrid actuated microscanner when each of electrothermal actuators was actuated at 7 V.

Then, the optical angle of microscanner by driving one pair of electrostatic comb-drives at resonant frequencies of around 380 Hz is characterised by measuring the laser spot scan length on grid screen using the same experimental setup. As illustrated in Figure 5.10 when actuating through electrostatic comb pair # 1, the fixed combs are connected to the positive potential (red colour) of the signal generator output while the movable combs and the connected structure are connected to the negative potential (blue colour). There is a protective serial resistance (Rs=10 kΩ) connected in case of pull-in of the comb-drives, which is the short circuit of capacitor between two

electrodes caused by the attractive force.

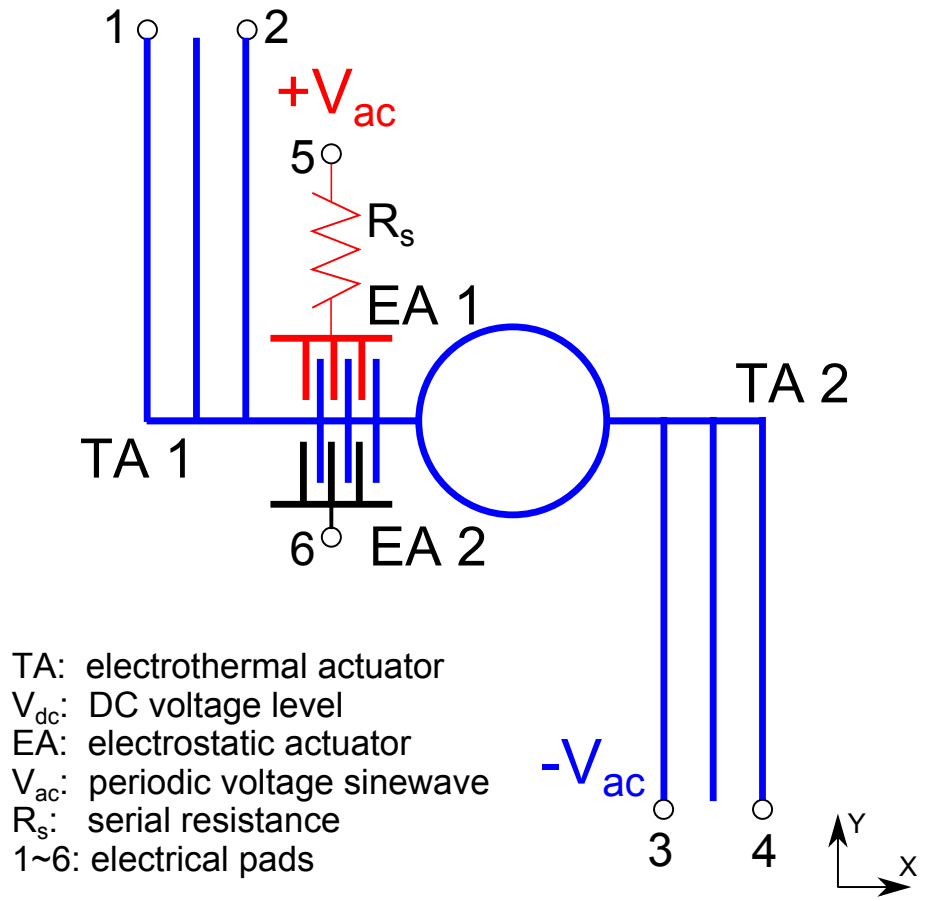

Figure 5.10: The illustration of electrical connection of electrostatic comb-drives of the microscanner to rotate micromirror at structure resonant.

Since the laser spot on measuring screen reflected by resonantly rotating microscanner appears to be a line, the measured optical angle by driving electrostatic comb-drives is noted as the optical scan angle. During the characterisation, an offset sinewave were used to drive one pair of electrostatic comb-drives. Figure 5.11 demonstrates the maximum optical scan angle of microscanner as a function the peak voltage of the offset sinewave at resonate frequency. As it can be seen, the optical scan angles of microscanner are linear with increasing peak voltage level. These measurements are also summarised in Table C.10.

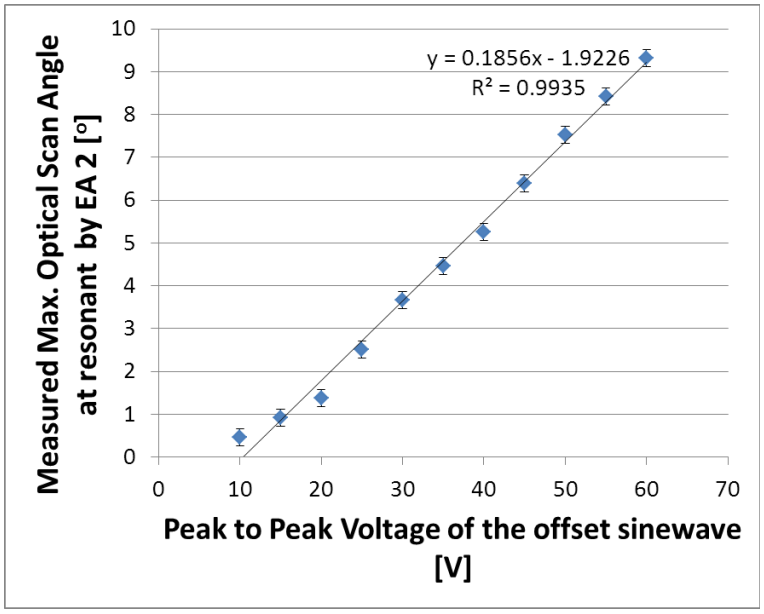

Figure 5.11: The dynamic optical scan angle of the microscanner by one pair of electrostatic comb-drives, EA2.

5.5 Scanning Pattern

To obtain a 2D scan pattern, the electrostatic comb-drives are driven at or close to resonant to provide fast line scan in one direction, and the electrothermal actuator is actuated by staircase voltage signal to translate the resonant scanning lines in, ideally, the orthogonal direction. As shown in Figure 5.12, the four raster scan patterns were obtained by selectively actuating one of electrothermal actuators and one pairs of electrostatic comb-drives in synchronisation when the screen is placed at a distance of 98 mm to microscanner. The actuation signal for the electrothermal actuator was a four-step staircase voltage signal increasing from 5 V, 8 V, 11 V to 15 V with duration of each step of 0.2 s; during each voltage step for electrothermal actuator, one pair of electrostatic comb-drives was actuated by a 380 Hz offset sinewave with 60 V peak voltage.

In Figure 5.12, the length of each scanning line indicates the dynamic optical scanning angles of microscanner when electrostatic comb-drives are driven at frequency of 380 Hz. From the photographs of the 2D scanning patterns, the length of scanning lines is not consistent. In Figure 5.12a, Figure 5.12b and Figure 5.12c, the lengths

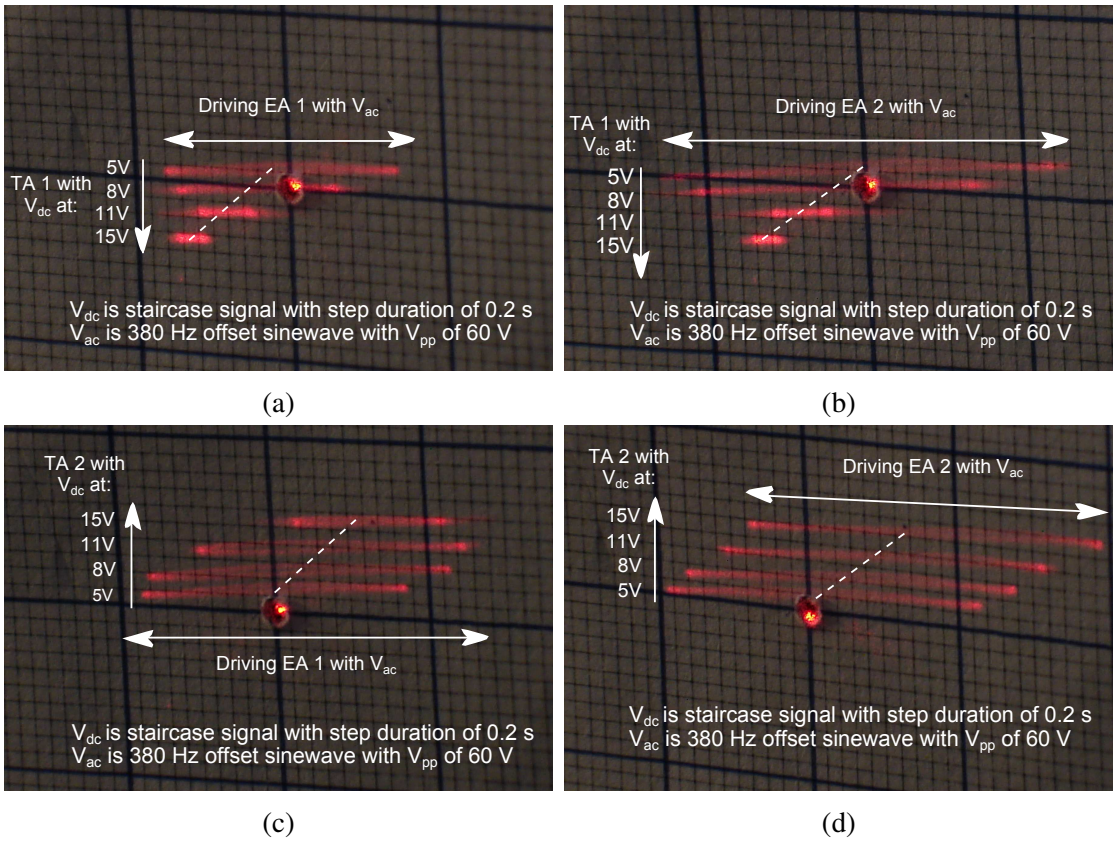

Figure 5.12: The 2D scanning pattern produced by the hybrid actuated microscanner.

of the scanning lines when electrothermal actuator is driven at 5 V is longer than the one when electrothermal actuator was driven at 15 V; while the length of scanning lines in Figure 5.12d are almost the same. This is because of the in-line connection between the actuators and micromirror, the relative position between the movable and the fixed combs are changed while driving either electrothermal actuator. Also, the magnitude of dynamic actuation of the comb-drives are determined by relative vertical offset etc. [14]. Therefore, the maximum resonant scanning angle is changed by vertical displacement driven by electrothermal actuator. Besides, the alignment between the demonstrated four scanning lines obtained by any actuation combination is interfered with by actuations of the electrothermal actuators. By connecting the middle point of each scanning line of each scanning pattern, it indicates that dynamic rotation centres of the micromirror are modified by the actuation of the electrothermal actuator. This demonstrations show that the tilting axis of microscanner by the electrothermal actuator is not orthogonal to its rotating axis driven by the electrostatic actuator and

the raster scan pattern produced by the microscanner is not in rectangular shape. The analysis of the sources of the non-rectangular 2D scan pattern is described in the following simulation section.

5.6 FEM Simulation

From the characterisation results, the two scanning directions of hybrid-actuated microscanner are not orthogonal to each other. Furthermore, the produced raster scanning pattern is not rectangular. To visually understand and verify the motion of microscanner during characterisation, the modal analysis and the static mechanical deformations of microscanner due to intrinsic stress and electrothermal actuation are simulated using FEM software, CoventorWare.

5.6.1 Modal analysis

First, the natural frequency and the corresponding mode shape when the micromirror is rotating about the torsion bar are simulated. Figure 5.13a displays the simulated rotational mode shape of microscanner at natural frequency of 395 Hz, and the colour coded surface demonstrates micromirror rotating about the torsion bar in X-axis. However, by reducing the scale of displacement, a thinner rotational axis of the micromirror is displayed in Figure 5.13b, which is around 2.3^{o} the X-axis or off to the torsion bar.

5.6.2 Mechanical analysis

From the surface profile of microscanner in Figure 5.6, the microscanner at rest deforms due to the intrinsic stress gradient. In the FEM model, the characterised stress gradient of 2.4 MPa/μm (Section 2.5.2.1) is applied within the SOI layer of microscanner model. The surfaces at anchors of all the electrothermal actuators and

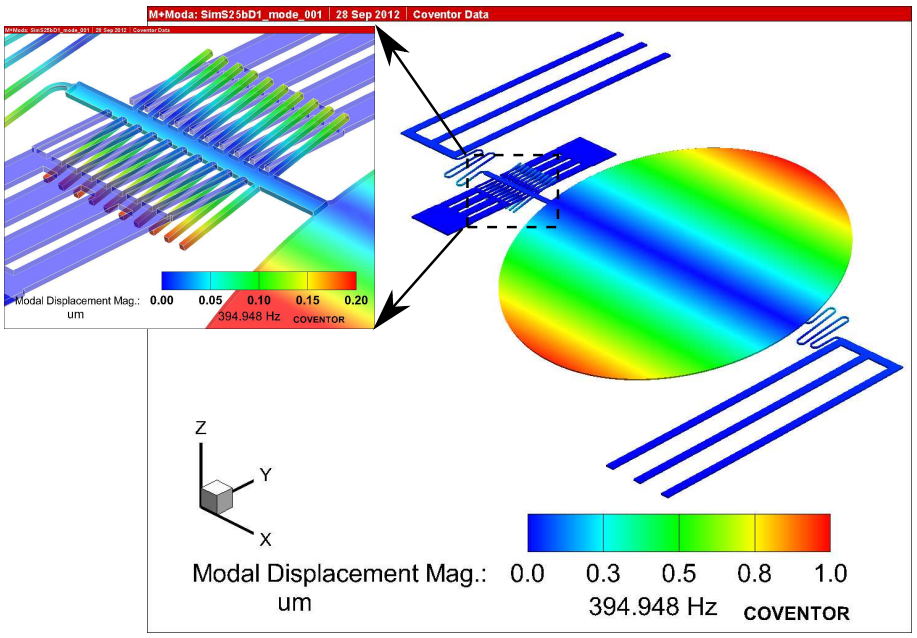

(a) Overview

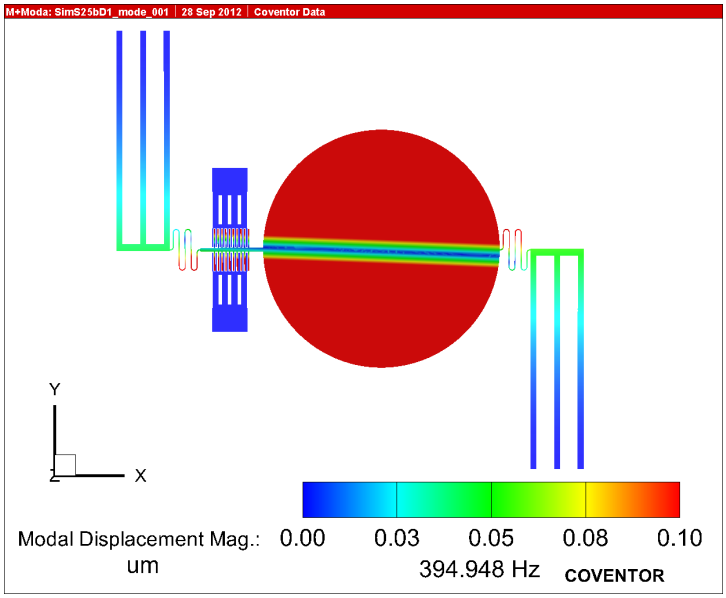

(b) Highlight the rotational axis of the micromirror

Figure 5.13: The resonant rotating mode of microscanner at natural frequency of 395 Hz simulated by FEM software, CoventorWare (with displacement exaggerated by x250 times).

on the bottom of fixed combs are assumed to be fixed. By performing the mechanical analysis of such model, the estimated deformation at 0 V is obtained and displayed in Figure 5.14. In Figure 5.14a, the micromirror at rest is not flat to the X-Y plane despite of the fact that both electrothermal actuators have the same vertical displacement of 20.4 μm at the free ends. In the inset of Figure 5.14a, the close view of electrostatic

comb-drives shows that the movable fingers are higher than the fixed fingers.

In Figure 5.14b, a rescale is only applied onto the micromirror. By locating the two points of the maximum (A) and the minimum (B) displacements on the micromirror rim, the initial mechanical angle of micromirror of around 0.2° can be calculated using the triangle equation. However, the result shows that the micromirror is not tilted about Y-axis. By connecting the two points with the same vertical displacement magnitude of around 16 μm along the micromirror rim, the tilting axis of the micromirror can be displayed as the dashed line in the illustration. The tilting axis of micromirror while not driven is 21° off to the Y-axis.

5.6.3 Electro-thermo-mechanical analysis

The static deformation of microscanner by actuating one electrothermal actuator is simulated by applying the electrothermal actuator with a DC potential of 7 V across the two fixed ends of outer cantilevers. The fixed surfaces of microscanner model are also assumed to be 20°C for the heat conduction to the substrate. The rest of the surfaces are defined with convective coefficient of 25 $Wm^{-2}K$ and surface emissivity of 0.6 [16].

Figure 5.15 displays the simulated mechanical deformation of microscanner when electrothermal actuators #1 or #2 is applied with 7 V respectively. First, the maximum vertical magnitude of microscanner by driving electrothermal actuator #1 or #2 are 86 μm or 88 μm respectively which only differs by 2 μm. The resulting mechanical angles by driving different electrothermal actuators differ by the maximum of 0.5° at a voltage of 7 V. By connecting the two points of the same vertical level on the rim of micromirror, the tilting axes of micromirror when driving by each electrothermal actuator are the same and are around 27.2° off to the X-axis.

Recall the rotational axis of micromirror during modal analysis in Figure 5.13b. Assume that the rotating axis of micromirror by comb-drives is approximately about X-axis which has an angle of 27.2° to the tilt axis driven by electrothermal actuator.

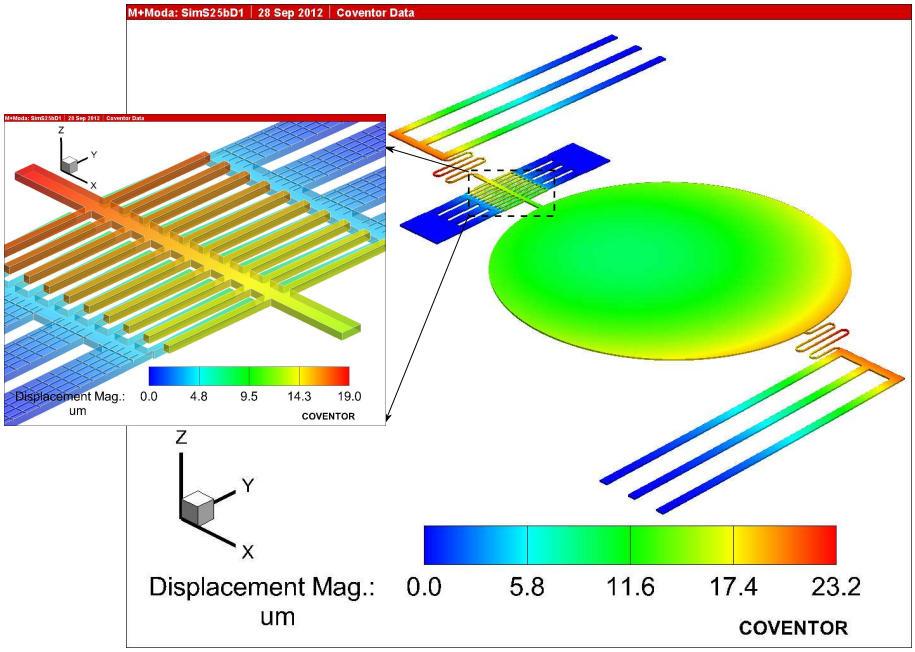

(a) Overview

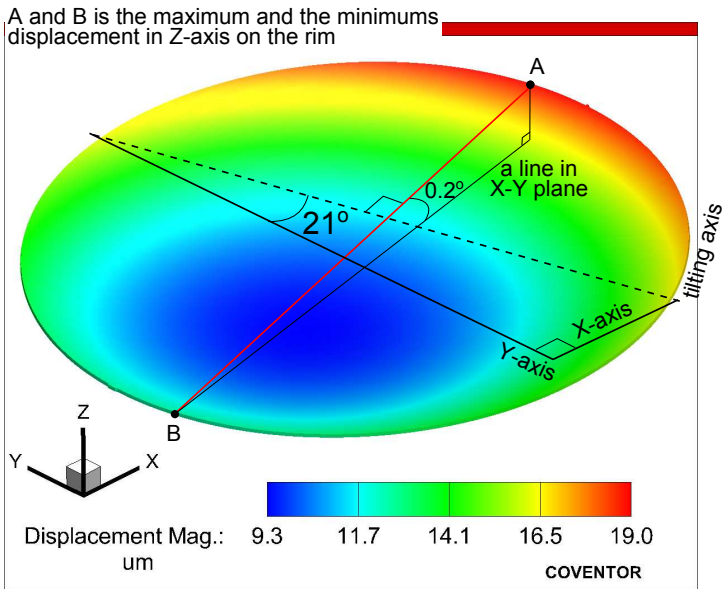

(b) Close view of displacement of the micromirror

Figure 5.14: FEM simulation of mechanical deformation of hybrid-actuated microscanner due to the internal stress gradient within the SOI layer.

Therefore, the reason for non-orthogonal scanning directions of this hybrid actuated microscanner design is because of the arrangement of two electrothermal actuators around the micromirror.

By comparing the colour coded displacement of movable combs in the insets of Figure 5.15a and Figure 5.15b, actuating the electrothermal actuator #1 results in

movable combs directly lifted at the connected end, while the vertical displacement by actuating the electrothermal actuator #2 is less. In both cases, the displacements of movable combs on two sides of the torsion bar are not identical. The unequal vertical displacement of the movable combs result in the non-equal overlapping area between two comb-drives during electrothermal actuation. This is the reason for the inconsistent maximum scan angles during 2D scanning pattern shown in Figure 5.12 when the actuation of the electrostatic comb-drives is coupled with the actuation of the electrothermal actuator.

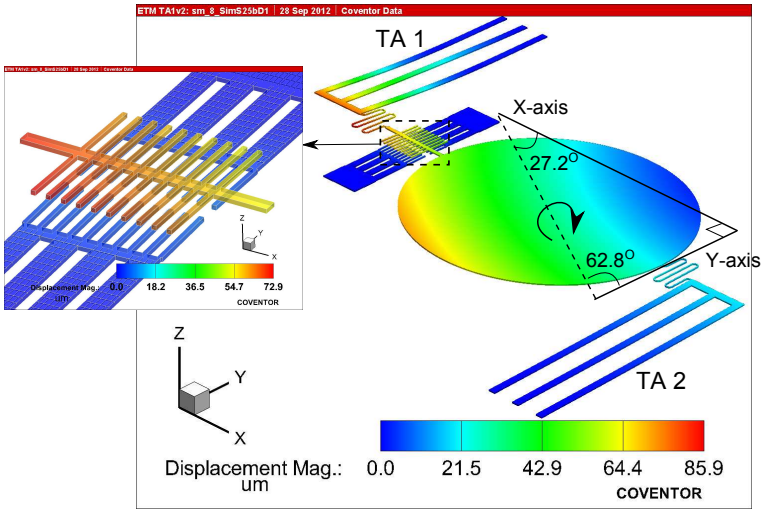

(a) Displacement when TA 1 is actuated at 7 V

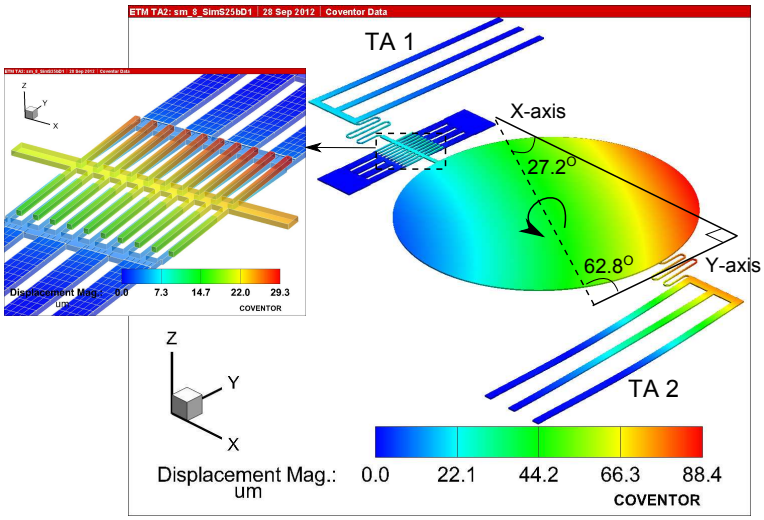

(b) Displacement when TA 2 is actuated at 7 V

Figure 5.15: The static tilt of the microscanner when applying either TA 1 (a) or TA 2 (b) with 7 V in the FEM software, CoventorWare (the displacement is exaggerated by x1 times).

5.7 Summary

This case study demonstrates the realisation of scanning a micromirror in one direction by electrothermal actuator and in the other direction by electrostatic comb-drives. Through experimental characterisation, two problems limiting the performance of microscanner are identified. First of all, the optical scan angles driven by electrostatic comb-drives can be varied by the actuation level of either of the two electrothermal actuators. Secondly, rotational axis of this dynamic scanning provided by electrostatic comb-drives is not only varied by the actuation level of electrothermal actuators, but also is non-orthogonal to the tilt axis provided by the electrothermal actuator. The resulting raster scan pattern presented is not rectangular due to the non-orthogonal scanning directions.

From measuring the surface deformation and simulating the mechanical behaviour of microscanner, it can be seen that the vertical and lateral positions of the movable combs are constantly changed by driving of electrothermal actuator. It can also be found that the variation of the tilting axis and non-orthogonal motion axis are determined by the arrangement of the electrothermal actuators. Since the electrostatic comb-drives, the electrothermal actuators and the micromirror are connected in line though a torsion bar and serpentine springs, the dynamic rotation provided by the electrostatic comb-drives is unavoidably affected by the movement changes driven by the electrothermal actuator. Besides, while one electrothermal actuator is driven for 2D scanning pattern, the other electrothermal actuator stays idle. In summary, to obtain two orthogonal scanning directions, the arrangement of electrothermal actuators around the micromirror is required to be modified.

References

[1] H. Schenk, P. Durr, D. Kunze, H. Lakner, and H. Kuck, “A resonantly excited 2D-micro-scanning-mirror with large deflection,” *Sensors and Actuators A: Physical*, vol. 89, pp. 104–111, MAR 20 2001.

[2] A. Jain, A. Kopa, Y. Pan, G. Fedder, and H. Xie, "A two-axis electrothermal micromirror for endoscopic optical coherence tomography," *IEEE Journal of Selected Topics in Quantum Electronics*, vol. 10, pp. 636 – 642, May-Jun. 2004.

[3] A. D. Yalcinkaya, H. Urey, D. Brown, T. Montague, and R. Sprague, "Two-axis electromagnetic microscanner for high resolution displays," *Journal of Microelectromechanical Systems*, vol. 15, pp. 786–794, Aug. 2006.

[4] W. Piyawattanametha, P. Patterson, D. Hah, H. Toshiyoshi, and M. Wu, "Surface- and bulk- micromachined two-dimensional scanner driven by angular vertical comb actuators," *Journal of Microelectromechanical Systems*, vol. 14, pp. 1329 – 1338, Dec. 2005.

[5] J. Kim, D. Christensen, and L. Lin, "Monolithic 2-D scanning mirror using self-aligned angular vertical comb drives," *Photonics Technology Letters, IEEE*, vol. 17, pp. 2307 – 2309, Nov. 2005.

[6] M. Scholles, A. Bruer, K. Frommhagen, C. Gerwig, H. Lakner, H. Schenk, and M. Schwarzenberg, "Ultracompact laser projection systems based on two-dimensional resonant microscanning mirrors," *Journal of Micro/Nanolithography, MEMS, and MOEMS*, vol. 7, no. 2, pp. 021001–021001–11, 2008.

[7] A. Tortschanoff, A. Frank, M. Lenzhofer, M. Wildenhain, T. Sandner, and A. Kenda, "Closed-loop synchronization scheme of resonant MOEMS-mirrors with two axes," in *Smart Sensors, Actuators, and MEMS V* (Schmid, U and SanchezRojas, JL and LeesterSchaedel, M, ed.), vol. 8066 of *Proceedings of SPIE*, 2011.

[8] J. Wei, T. C. Duc, G. K. Lau, and P. M. Sarro, "Novel electrothermal bimorph actuator for large out-of-plane displacement and force," in *MEMS 2008: 21ST IEEE INTERNATIONAL CONFERENCE ON MICRO ELECTRO MECHANICAL SYSTEMS, TECHNICAL DIGEST*, PROCEEDINGS: IEEE MICRO ELECTRO MECHANICAL SYSTEMS, pp. 46–49, 2008.

[9] J. Maloney, D. Schreiber, and D. DeVoe, "Large-force electrothermal linear micromotors," *Journal of Micromechanics and Microengineering*, vol. 14, pp. 226–234, Feb. 2004.

[10] L. Que, J. Park, and Y. Gianchandani, "Bent-beam electrothermal actuators - part I: Single beam and cascaded devices," *Journal of Microelectromechanical Systems*, vol. 10, pp. 247–254, Jun. 2001.

[11] G. Brown, L. Li, R. Bauer, J. Liu, and D. Uttamchandani, "A two-axis hybrid MEMS scanner incorporating electrothermal and electrostatic actuators," in *Optical MEMS and Nanophotonics (OPT MEMS), 2010 International Conference on*, pp. 115 –116, Aug. 2010.

[12] L. Li and D. Uttamchandani, "Dynamic response modelling and characterization of a vertical electrothermal actuator," *Journal of Micromechanics and Microengineering*, vol. 19, no. 7, p. 075014, 2009.

[13] P. Patterson, D. Hah, H. Nguyen, H. Toshiyoshi, R.-M. Chao, and M. Wu, "A scanning micromirror with angular comb drive actuation," in *Micro Electro Mechanical Systems, 2002. The Fifteenth IEEE International Conference on*, pp. 544 –547, 2002.

[14] D. Hah, P. Patterson, H. Nguyen, H. Toshiyoshi, and M. Wu, "Theory and experiments of angular vertical comb-drive actuators for scanning micromirrors," *IEEE Journal of Selected Topics in Quantum Electronics*, vol. 10, pp. 505 – 513, May-Jun. 2004.

[15] R. Bauer, G. Brown, and D. Uttamchandani, "Comparison of the curvature homogeneity and dynamic behaviour of framed and frameless electrostatic X/Y scanning micromirrors," *Micro Nano Letters, IET*, vol. 6, pp. 425 –428, june 2011.

[16] P. J. Timans, "Emissivity of silicon at elevated temperatures," *Journal of Applied Physics*, vol. 74, pp. 6353 –6364, Nov. 1993.

Chapter 6

2D MEMS Scanner With Hybrid Actuation – Design Optimisation

6.1 Overview

Using the SOIMUMPs, the electrothermally [1] and the electrostatically [2, 3] actuated 2D microscanners have been successfully fabricated in the 10-μm-thick SOI (Silicon-on-Insulator) wafers. Generally, electrostatic comb-drives actuated microscanners require high actuation voltage level ($>$ 100 V) but low power consumption when scanning at resonant frequencies of kilohertz range. The 2D electrothermal microscanner requires 5 - 15 V DC voltage range for each scanning axes and consumes a total of $\sim$ 500 mW when the micromirror is tilted at the maximum angles in both directions; and it has a low frame rate limited by the response time of $\sim$50-60 milliseconds when the microscanner is switched from one position to the next [4]. Generally the advantages and the disadvantages between electrostatic and electrothermal actuation schemes are opposite to each other, notice which, A. Alwan and N. Aluru introduced a novel idea of combining the two actuation mechanisms into one actuator [5] for communication RF switches. The same idea can be implemented to the 2D scanning micromirrors, such as applying electrostatic and electrothermal

actuators to scan one micromirror in two directions [6, 7].

For example, in the previously reported research work about a single pixel imaging system [1], it requires a micromirror scanning the focal plane of a targeted object over a single photon detector in a raster scan pattern, so that the photon detector can measure the light density of the image pixel by pixel. Such optical imaging method can reduce system the cost, especially for infrared and terahertz imaging applications, by replacing the 2D array photodetectors with only a single photodetector. An electrothermally-actuated 2D scanning micromirror of 2 mm diameter is implemented in this single pixel imaging system. Due to the slow response time of the electrothermal actuators, the scan speed for reconstructing a 128 x 128 pixels image requires around 2 minutes. If the actuation scheme for one scanning axis of 2D microscanner is replaced by electrostatic comb-drives with the other axis still utilising electrothermal actuator, the 2D scan pattern of resulting scanner can produce fast line-scanning at no less than hundreds of hertz in one direction and stepping the position of this line-scanning in an orthogonal direction within several milliseconds time. Such 2D scanning micromirror combining two different actuation schemes is described as hybrid actuated 2D scanning micromirror, or hybrid 2D microscanner for short, in this thesis.

Learned from the microscanner design introduced in Chapter 5, the design optimisation, the simulation and characterisation of a MEMS hybrid 2D scanner combining electrostatic comb-drives and electrothermal actuators are presented in this chapter. The purpose of designing this hybrid-actuated 2D microscanner is to improve the frame refreshing speed of raster scanning pattern and the scan angles than the microscanner reported in [1]. First, in Section 6.2, the optimisation of geometric design and the functionality of each part are described. Next, in Section 6.3 the modal analysis and the simulation of static tilt angles using FEM (Finite Element Method) software CoventorWare are presented. In Section 6.4, the experimental characterisation of resonant frequencies and optical angles in two orthogonal axes are described and compared with the simulation results. Moreover, a 2D raster scan pattern of this microscanner obtained by synchronising the driving signals of two types

of actuators is also demonstrated in this section. Finally, advantages, limitations and possible improvements of this MEMS hybrid 2D scanner design will be discussed and summarised in Section 6.5.

6.2 Structure Design and Fabrication

The 2D hybrid microscanner (Figure 6.1) consists of a framed circular micromirror, two electrothermal actuators and two pairs of electrostatic comb-drives. The micromirror of 1200 μm diameter is gold coated to increase reflectivity and is framed by a ring-shape. The micromirror is fixed to the ring frame through two inner torsion bars located symmetrically at two opposing sides of the micromirror along the Y-axis (Figure 6.1b). The two electrothermal actuators, parallel to the Y-axis, are symmetrically arranged at each side of micromirror. Each electrothermal actuator is connected to the micromirror frame through classic serpentine springs (Figure 6.1c). The free ends of both electrothermal actuators are connected to the micromirror frame edge at points in line with the micromirror centroid in the X-axis. Every electrothermal actuator is fixed to the substrate and connected to a square pad which is gold coated to provide the electrical pathway. The electrostatic comb-drives (Figure 6.1d) consist of two identical groups which are symmetrically arranged on each side of the torsion bar. Each group of electrostatic comb-drives is made up of 20 fixed fingers anchored to the substrate interdigitated with 21 movable fingers anchored to the torsion bar. Every finger of comb-drives are identically designed and equally spaced. Each group of the electrostatic comb-drives can generate a torque about the torsion bar when actuated by an AC electrical signal at structural resonant frequency. This torsion bar of electrostatic comb-drives is aligned to the Y-axis and is parallel to the two electrothermal actuators, one end of which is connected to the micromirror frame edge and the other end of which is anchored to the substrate and connected to an electrical pad.

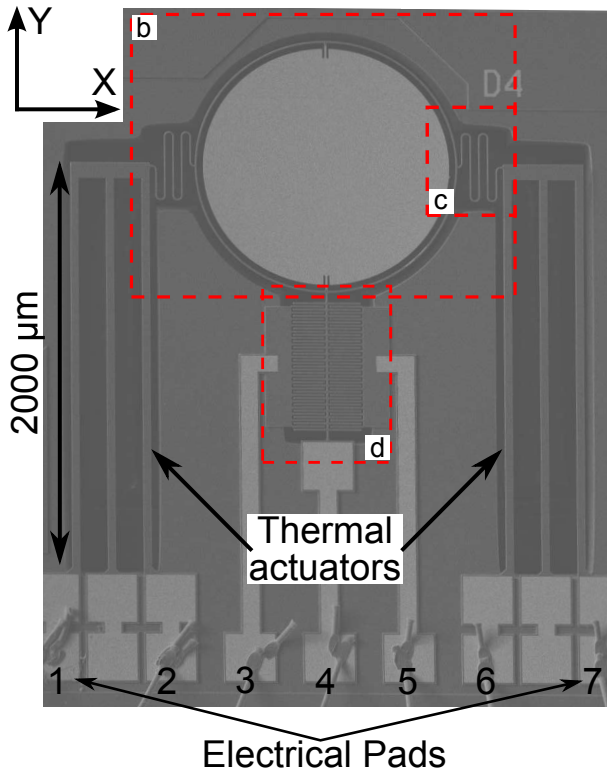

(a) Overview

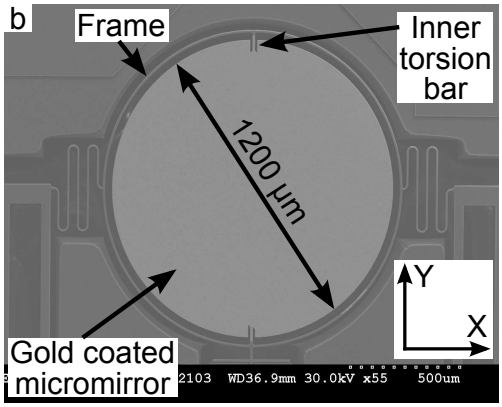

(b) Framed micromirror with gold coated on the top

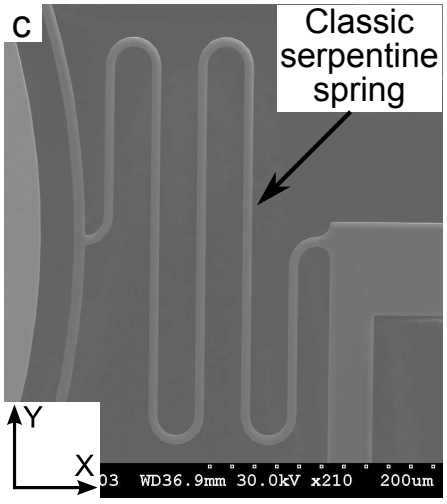

(c) One of serpentine springs

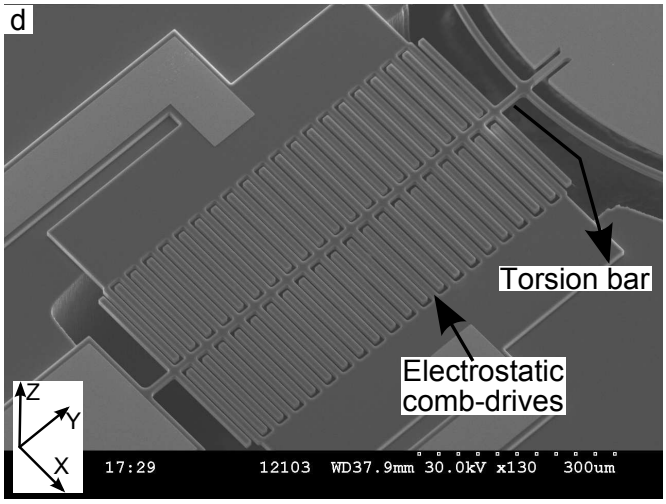

(d) Combs

Figure 6.1: The SEM images of the hybrid-actuated microscanner.

6.2.1 Fabrication

This 2D microscanner was fabricated using commercial SOIMUMPs using the 10-μm-thick Silicon-On-Insulator (SOI) wafer. All the parts, the silicon layer of micromirror, the frame, the serpentine springs, the electrothermal actuators and the electrostatic comb-drives, are patterned in the same silicon or SOI layer; then BlanketMetal gold was evaporated on the top of the silicon micromirror. The single layer structure and the mechanical properties of single-crystal-silicon material guarantee the throughput of fabrication process and the device lifetime. Due to the phosphorous doping process [8], the 10 μm thick SOI layer has an intrinsic stress gradient measured to be around 2.4 MPa/μm [1].

The structure dimension and function of each part of the microscanner are described separately in each of the following subsections.

6.2.2 Electrothermal actuators — geometric optimisation

In order to fabricate the hybrid actuated scanner using SOIMUMPs, the successful electrothermal actuator design of [4] which using the same fabrication processes is inherited. This section studies the impact of geometric variation on the performance of this electrothermal actuator using FEM software, CoventorWare.

As already introduced in section 5.2.1, this type of SOIMUMPs fabricated electrothermal actuated has been simulated. Since the electrothermal actuator converts the electrical signal to Joule heating and then to mechanical displacement during electrothermal actuation, the Joule heating determined by the path resistance which is further determined by the geometry of the electrothermal actuator, such as widths and lengths of the outer cantilevers and the joint beam. As shown in Figure 6.2, during electro-thermo-mechanical analysis of the actuator, the width of two outer cantilevers, the width of inner cantilever are scaled by factors ranging from 0.6 to 1.6 with increment of 0.2; the length of cantilevers are scaled by factors ranging from 0.8

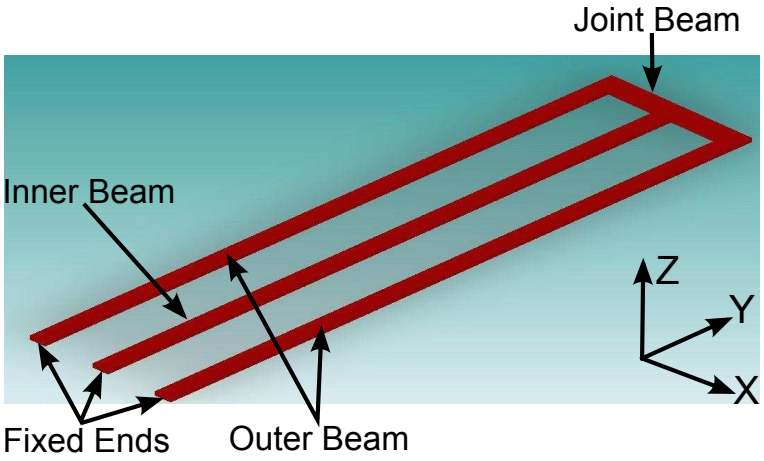

(a) Name of surfaces and parts

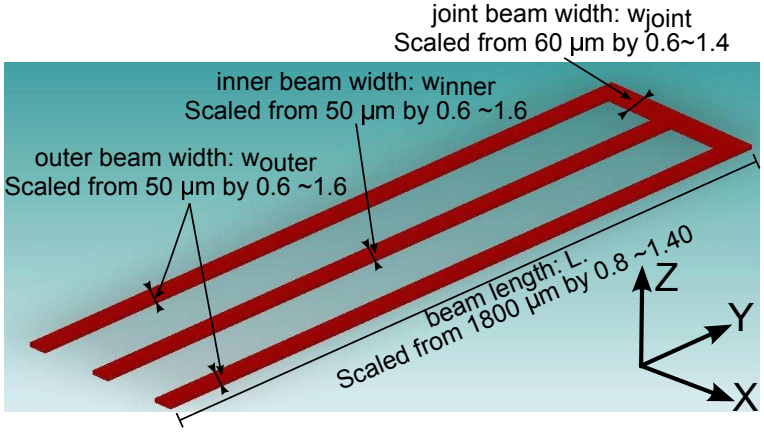

(b) Parametric dimension

Figure 6.2: FEM model of the three-parallel-beam electrothermal actuator design.

to 1.4 with increment of 0.1; the width of joint beam is scaled by factors ranging from 0.6 to 1.4 with increment of 0.2 with its length fixed. In each simulation, DC voltage levels of 0, 2, 4, 6, 7 and 8 V are applied to the fixed ends of two outer cantilevers, and the static vertical displacement, the consumed power and the maximum temperature of the electrothermal actuator model are calculated at each voltage level. The material properties of the SOI layer are summarised in Table 2.3. The temperature of the fixed ends and the ambient temperature are assumed to be fixed at 20°C. The rest of the silicon surfaces are maintained to have convective coefficient of 25 $Wm^{-2}K$ and emissivity of 0.6.

First, the electro-thermo-mechanical behaviour was simulated with variable width of the two outer cantilevers (W_{outer}). W_{outer} is scaled from 50 μm by factors ranging

from 0.4 to 1.6 with an increment of 0.2. In Figure 6.3a, the tip vertical positions of actuators with different outer cantilevers widths are plotted against the actuation power. The initial tip positions of electrothermal actuators with various W_{outer} remain at 23.2 μm. As the width of outer cantilevers increases from 20 μm to 80 μm, the actuation power consumption increases from 33 mW to 107 mW at 8 V. In Figure 6.3b, the tip displacement, calculated by subtracting the initial vertical tip position from the one at the maximum simulated voltage of 8 V, is plotted against the scale factor of W_{outer}. The maximum vertical tip displacement occurs when the width of the outer cantilevers W_{outer} is scaled by $\times 1$ (50 μm) with other parameters remaining the same as the original design. By increasing W_{outer} from 20 μm to 50 μm, the vertical tip displacement at 8 V increases by 12% but increasing W_{outer} from 50 μm to 80 μm, the tip displacement reduces from the maximum value despite the increasing actuation power. In the same figure, it can be seen that both the maximum temperature and the actuation power at 8 V increase as W_{outer} increases. This is because the overall resistance reduces as the width of the heated outer cantilevers is increasing [1]. The vertical displacement of the electrothermal actuator is estimated to be increased by increasing W_{outer} or the width ratio between outer and inner cantilevers, however, the actuating power consumed and the maximum temperature generated are also increased. Therefore, it is not efficient to improve the performance of the electrothermal actuator by increasing the width of the outer cantilevers.

As already described, the inner cantilever of the electrothermal actuator functions as the constraint for the expanding outer cantilevers and results in the vertical tip displacement motion during actuation. To estimate the impact of inner cantilever width (W_{inner}) on the performance of electrothermal actuator, W_{inner} was scaled from 50 μm by factors ranging from 0.4 to 1.6 while the other parameters are fixed during the simulation. In Figure 6.4a, the vertical tip positions of the actuators and are seen to differ by 2% at most, are plotted as a function of actuation power. In Figure 6.4b, the vertical tip displacement, the power consumption and the maximum temperature at 8 V are plotted against the scaled factors of W_{inner}. The maximum tip

[1] R= ρ_0 L/A, where R is the resistance of the structure, ρ_0 is the resistivity of the material, L is the length and A is area of the cross section.

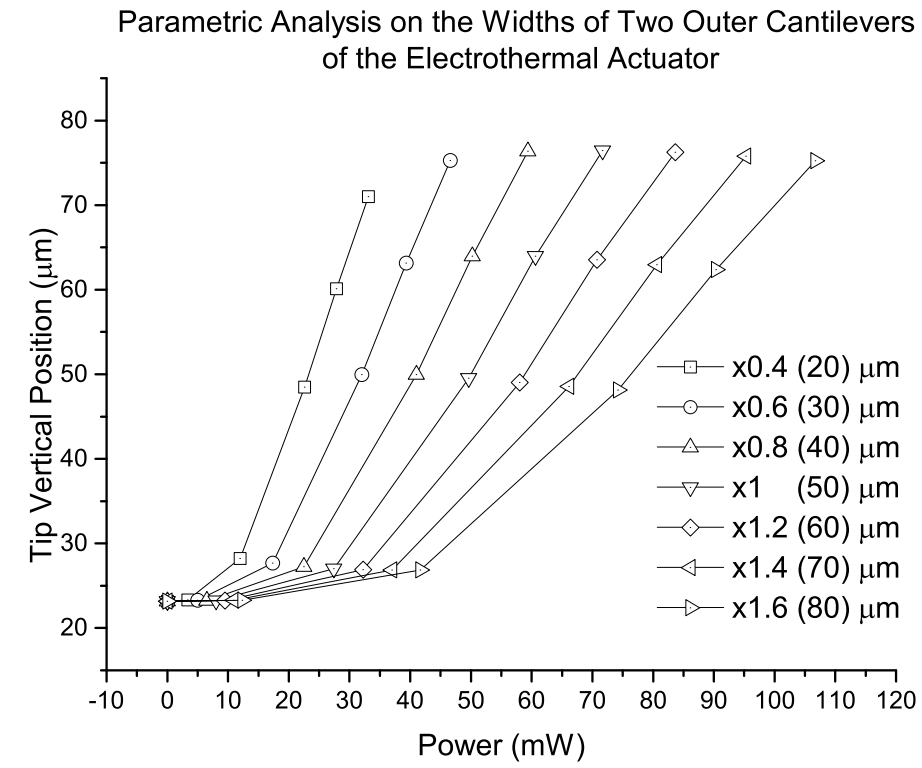

(a)

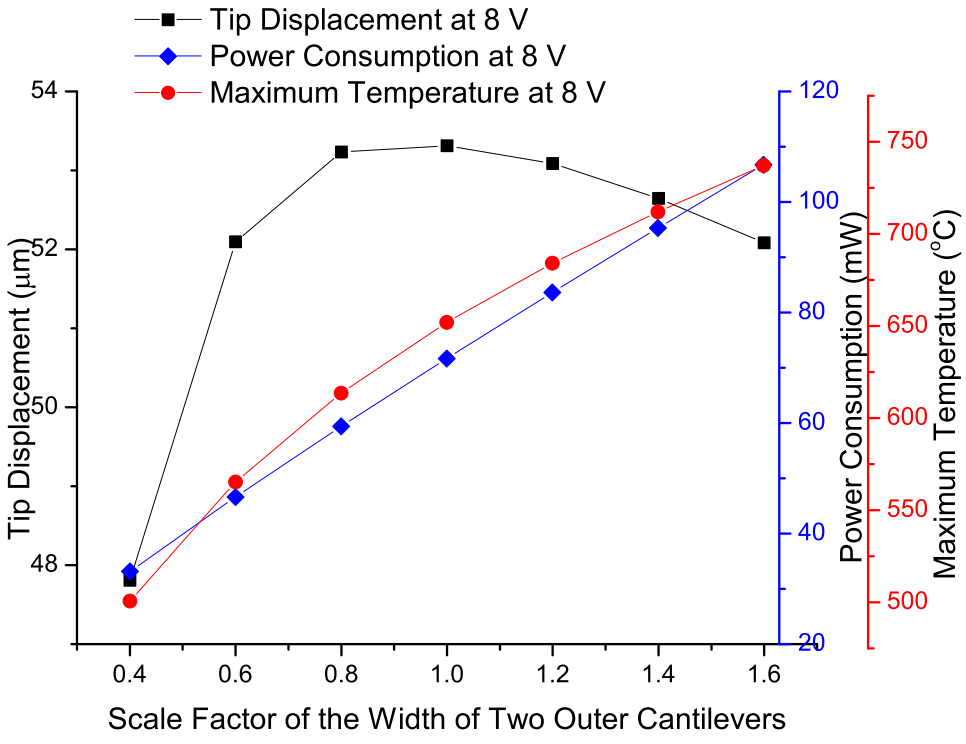

(b)

Figure 6.3: FEM simulation results of the electrothermal actuator with variable width of the two outer cantilevers.

displacement is 54.5 μm for the electrothermal actuator with an inner cantilever width scaled by 0.6 (30 μm). As the inner cantilever becomes wider, the tip displacement starts to reduce slowly by a rate of $\sim$-0.1 μm per micrometer increment of W_{inner}. With a wider inner cantilever, the thermal resistance between the outer cantilevers and the substrate is reduced; or in other words, the heat generated by Joule heating within the outer cantilevers is easier to be conducted to the substrate. Also due to this increasing heat conduction, the maximum temperature at 8 V reduces by 3^{o}C per micrometer increment of W_{inner}. Since, the resistivity of single-crystal-silicon decreases with decreasing temperature [9], the power consumption at 8 V increases by 0.01 mW per micrometer increment of W_{inner}. As can be seen, reducing the width of inner cantilever does not significantly improve the performance of the electrothermal actuator.

After simulating the effect of variable width of outer cantilevers and inner cantilever on the performance of electrothermal actuator individually, the width of all the three parallel cantilevers is scaled from 50 μm at the same time in the FEM model by factors from 0.6 to 1.6. In Figure 6.5a, the vertical tip positions of electrothermal actuator were plotted as a function of actuating power for varying cantilever widths. As the width of three cantilevers is increased, the vertical heights of actuators tips are around 78$\pm$2.8 μm when driven at 8 V. Similar to the results in Figure 6.3, the actuation power at each voltage is increasing. In Figure 6.5b, the maximum tip displacement of electrothermal actuator at 8 V, when the width of the three cantilevers is equal to 20 μm, are around 6 μm higher than the estimated tip displacement of the original design. As the width of cantilevers increases, the maximum temperature of the actuator and the power consumption during actuation at 8 V are both increasing monotonically from 611 ^{o}C to 664 ^{o}C and from 31 mW to 111 mW respectively. It can be deduced from the plot that reducing the width of the three cantilevers can effectively increase the mechanical performance as well as reduce the power consumption and the heat dissipation.

During actuation, the current passes through the outer cantilevers as well as the joint beam. However, the design of joint beam has to maintain its structural stiffness as a

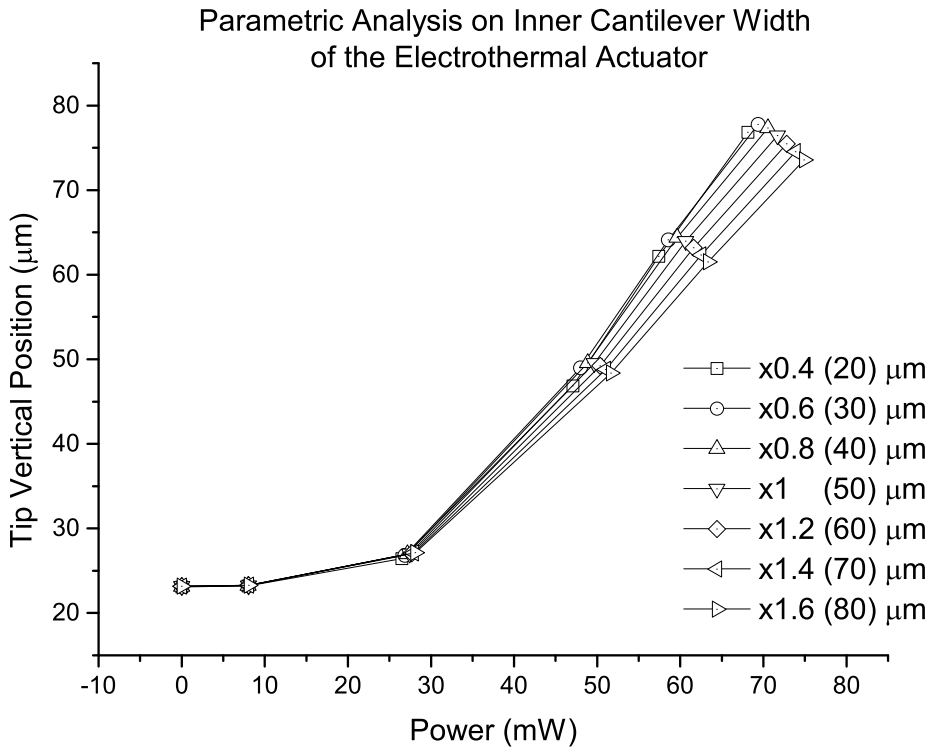

(a)

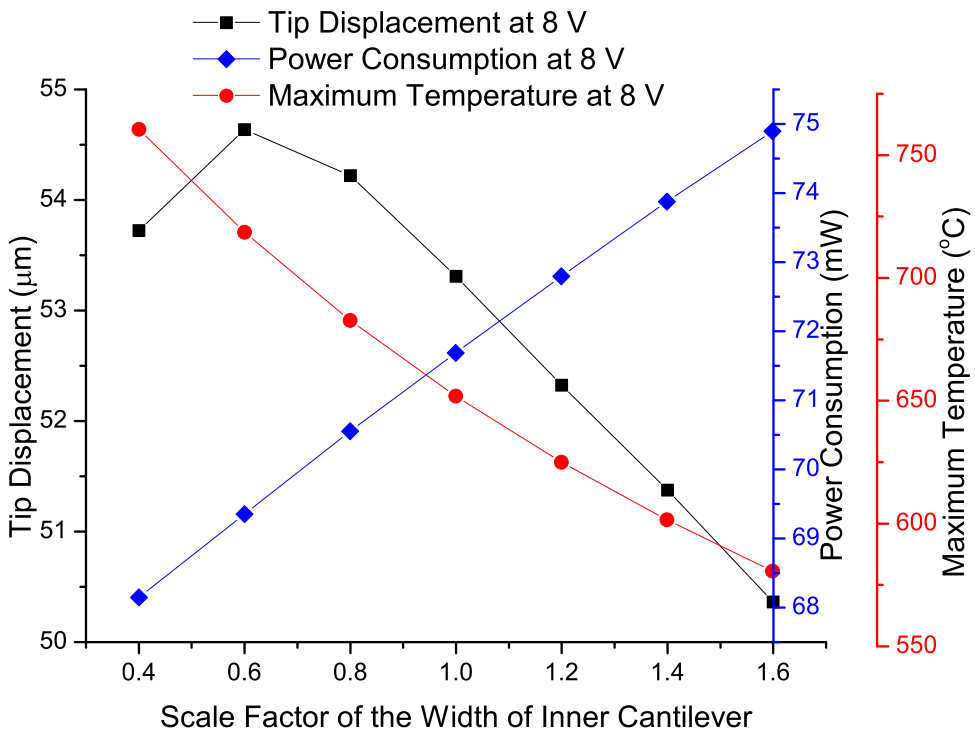

(b)

Figure 6.4: FEM simulation results of the electrothermal actuator with variable width of the inner cantilever.

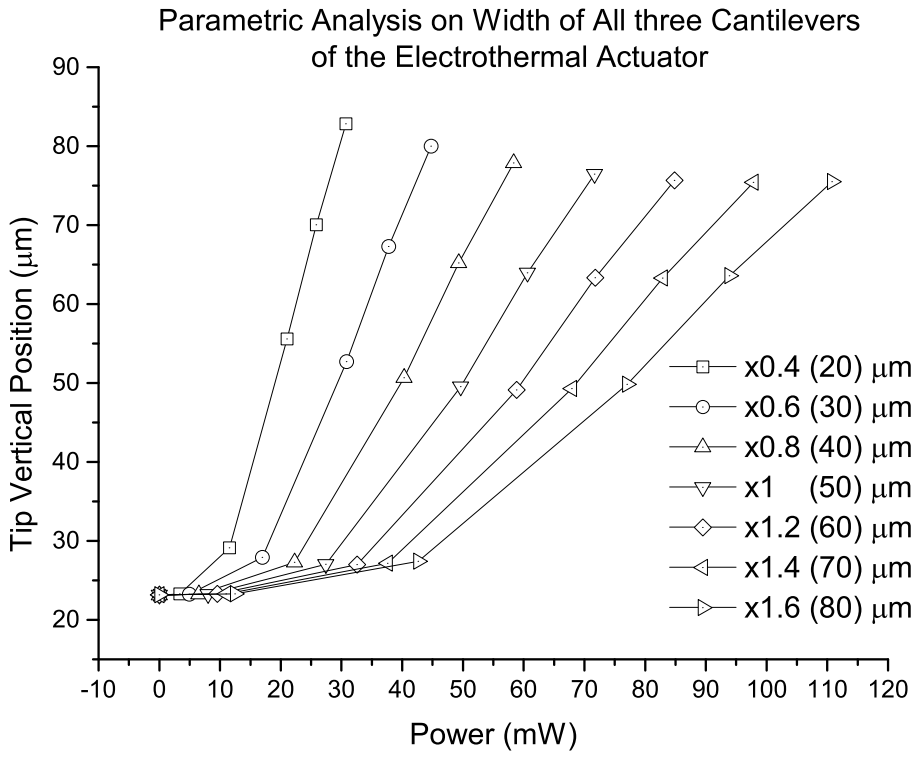

(a)

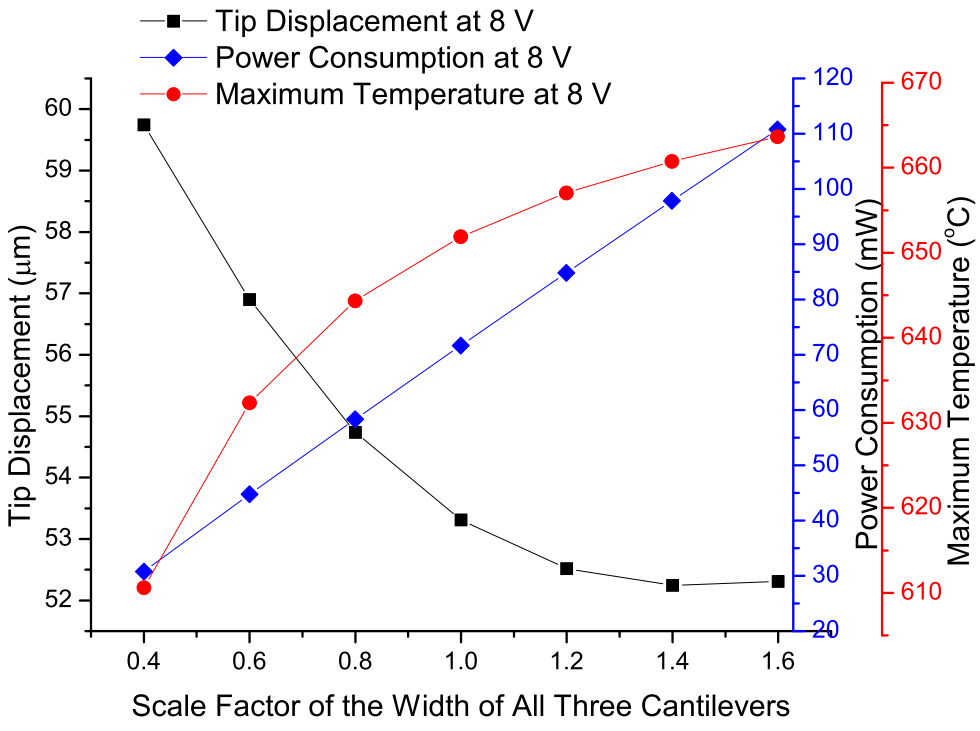

(b)

Figure 6.5: FEM simulation results of the electrothermal actuator with variable width of all the three paralleled cantilevers.

connecting beam rather than acts as a heat source, nor a part to provide the out-of-plane bending moment. Besides, the tip of the electrothermal actuator, where the joint beam is located, usually connects to the rest parts of the device, for example, to the micromirror. As such, the joint beam width (W_{joint}) is scaled from 60 μm by factors from 0.6 to 1.4 in the simulation while its length is fixed to be 450 μm. In Figure 6.6a, the simulated initial deflections of actuators with different width of the joint beam remain at the same value of around 23.2 μm, with a standard deviation of 0.5 μm. However, the tip vertical position of the actuator increases by 20% when 8 V is applied. The resulting actuation power at each simulated voltage level increases by only 7% as W_{joint} is increased from 36 μm to 84 μm.

In Figure 6.6b, the vertical tip displacement at 8 V increases monotonically with the increasing joint beam width. As W_{joint} increases, the resistance, the resulting Joule heating and the average temperature of the joint beam are reduced during actuation. Therefore, the heat conduction from the joint beam to the inner cantilever is subsequently reduced. As plotted in the inset of Figure 6.6b, the difference average temperature between the outer and inner cantilever is increasing as the increasing W_{joint}. This indicates the increased buckling effect of the electrothermal actuator caused by the combination of thermal stressed outer cantilever and constrained inner cantilever. This is similar to the principle of designing a bimorph electrothermal actuator, the mechanical performance of which is enhanced by utilising two layers of materials with largely different thermal expansion coefficients. Since the inner and the outer cantilevers of electrothermal actuator studied here are of the same material, the mechanical performance can be improved by enlarging the temperature difference between the inner and the outer cantilevers during actuation. The temperature difference enhancement of the two cantilevers by increasing the joint beam width follows such guideline. As also shown in Figure 6.6b, the electrothermal actuator with a wider joint beam consumes more actuating power due to the increasing current for the reduced resistance of the joint beam.

The length of all three parallel cantilevers (L) is scaled from 1800 μm by factors between 0.8 and 1.4 in the simulation. In Figure 6.7a, the initial vertical deflection

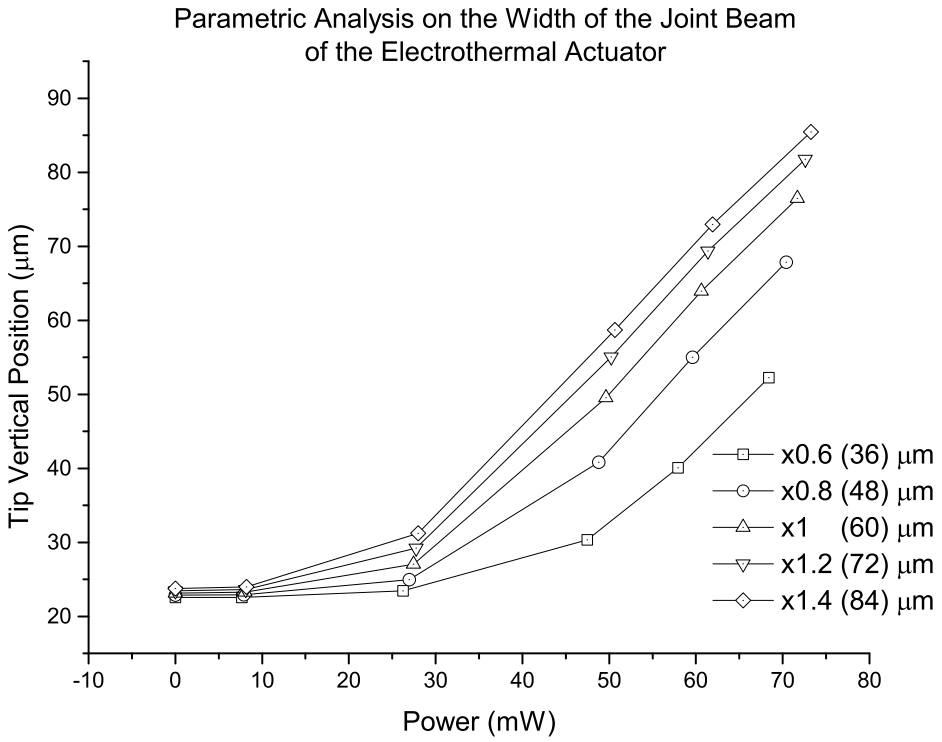

(a)

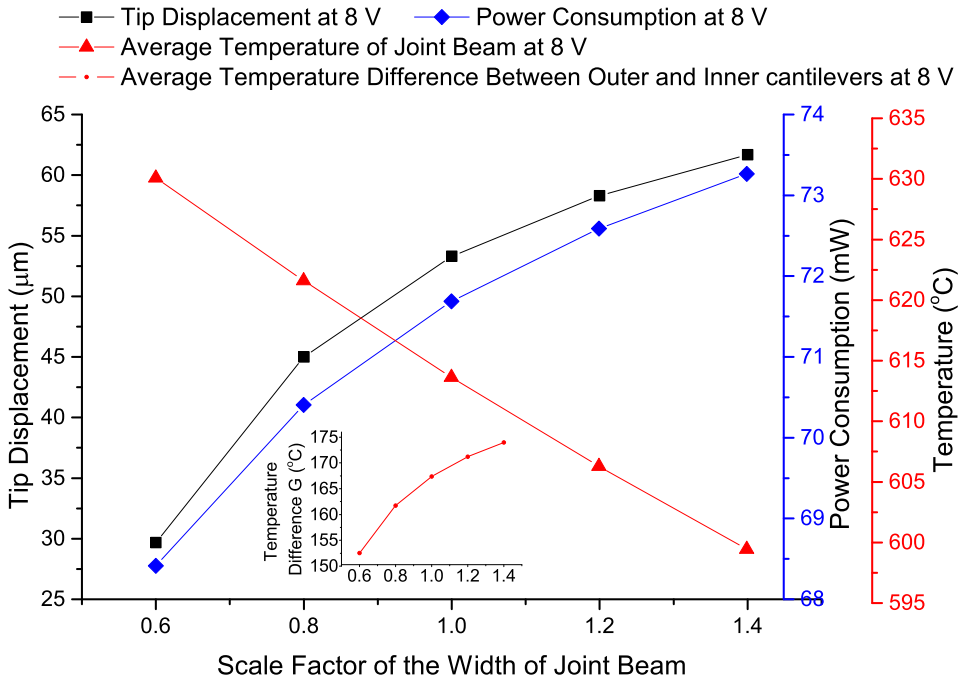

(b)

Figure 6.6: FEM simulation results of the electrothermal actuator with variable width of the joint beam.

of electrothermal actuator, represented by tip position at 0 V, increases from 15.1 μm to 44.4 μm when the length of three cantilevers increases from 1440 μm to 2520 μm. From the plot, the tip height of the 1440 μm long actuator does not respond or start to increase until the applied actuation power is increased to 37.7 mW at a voltage of 4 V. When the actuator length increases to 2520 μm, the tip height of actuator already starts to increase by 14 μm at a power of 20.3 mW corresponding to a voltage of 4 V. In Figure 6.7b, the tip displacement of at 8 V increases monotonically from 34 μm to 78 μm with increasing lengths of three cantilevers. In addition, the power consumption of electrothermal actuator at 8 V reduces from 86 mW to 55 mW and the simulated maximum temperature at 8 V reduces from 694 ^{o}C to 575 ^{o}C. When increasing the length of three cantilevers, not only do both the maximum temperature and the consumption power reduce, but also the threshold actuation power decreases. Therefore, increasing the length of three cantilevers is the most efficient geometric parameter to improve the performance of the electrothermal actuator design.

Based on the parametric study results of variable structural geometries of electrothermal actuator, increasing the length and reducing the width of three cantilevers, can not only improve the vertical tip displacement, reduce the actuation power and the maximum temperature during actuation, but also reduce the threshold actuating power. Moreover, increasing the joint beam width can also increase the vertical tip displacement of electrothermal actuator; however, the power consumption will increase. Therefore, the improved design of electrothermal actuator used for the hybrid actuated microscanner consists of three cantilevers of the same length of 2000 μm and the same width of 40 μm which are equally spaced by 145 μm. All cantilevers are anchored to the substrate at the same end and joined by an 80 μm wide joint beam at the free ends on the opposite side. The geometric summary is also listed in Table 6.1.

After determining the structure geometry of electrothermal actuator, identical electrothermal actuators are placed on each side of the micromirror along the Y-axis and are mirror symmetric to each other as shown in Figure 6.1. These two electrothermal actuators are actuated at the same time by the same voltage signal to tilt

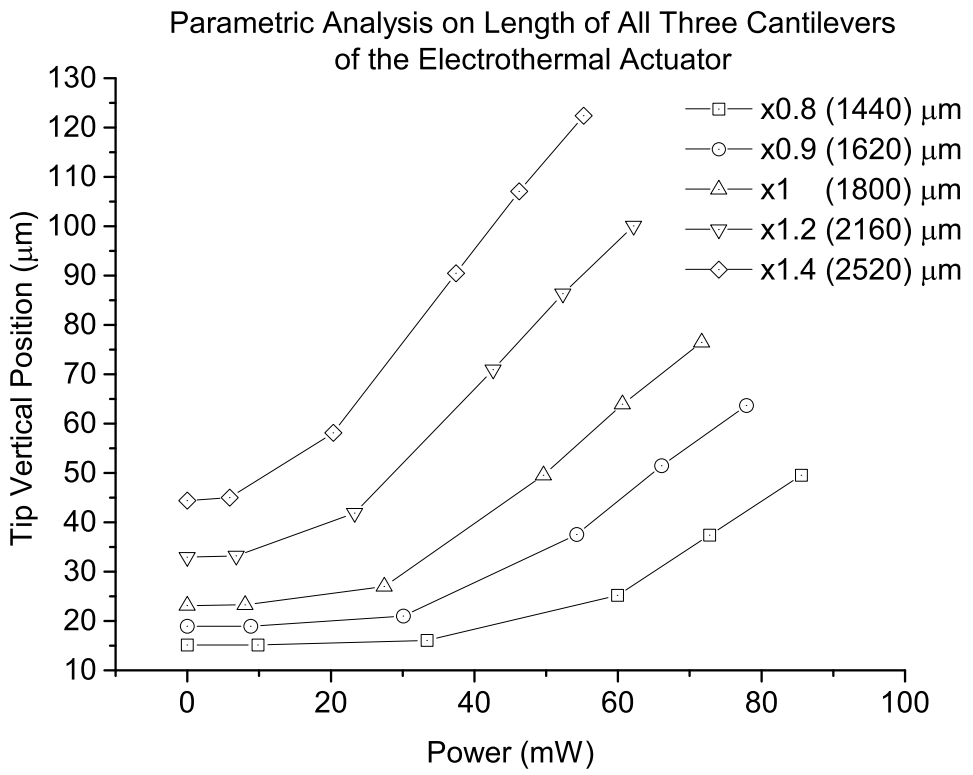

(a)

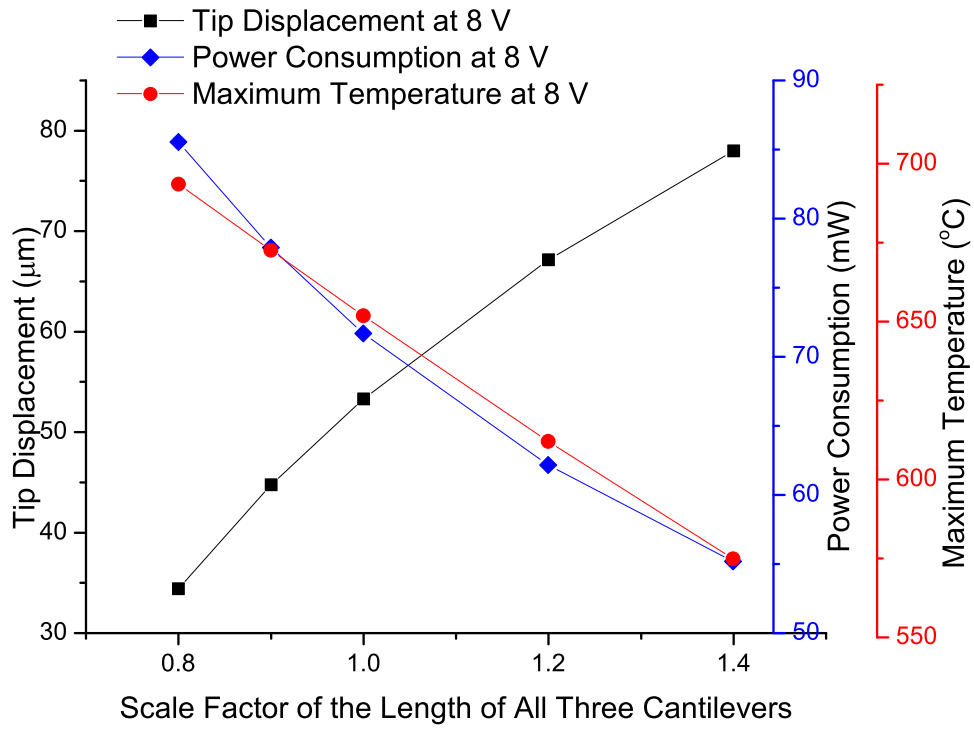

(b)

Figure 6.7: FEM simulation results of the electrothermal actuator with variable length of the three paralleled cantilevers.

the micromirror about the X-axis. When actuating, the two electrothermal actuators generate two equal upwards lifting displacements at two opposite connection points on the micromirror frame. Since the micromirror is fixed at the bottom to substrate through the torsion bar of electrostatic comb-drives, when the electrothermal actuators lift the micromirror at two connection points, the micromirror will lift out of the plane and tilt about the fixed point at the substrate. In the meanwhile the torsion bar of the electrostatic comb-drive is also lifted up and curved along with the micromirror motion. The functions of serpentine spring connected between micromirror and electrothermal actuators will be described in detail in the later sub-section 6.2.5.

6.2.3 Electrostatic comb-drives

Comb-drives, such as those shown in Figure 6.1d, can generate a torque about their torsion bar when driven at resonant frequency . This torque causes rotation of the connecting micromirror. This section describes the geometric design of electrostatic comb-drives to obtain adequate rotation scan angles.

The principle of dynamic rotation of an electrostatic comb-drive actuated microscanner can be mathematically described using the dynamic motion equation for a torsion oscillator [10]:

$$\frac{d^2\theta}{dt^2} + 2\zeta\omega_r\frac{d\theta}{dt} + \omega_r^2\theta = \frac{T(\theta)}{I} \tag{6.2.1}$$

where,

θ is the mechanical rotational angle of microscanner,

ζ is the damping ratio, and $\zeta = \frac{c}{2\sqrt{Ik}}$ (c is the viscous damping coefficient),

ω_r is the mechanical resonant frequency of microscanner, and $\omega_r = \sqrt{\frac{k}{I}}$,

$T(\theta)$ is the torque about the rotational axis,

I is the moment of inertia of microscanner.

The value of the damping ratio ζ can be obtained from experimental measurements

[11, chapter 2/3] using the equation below:

$$\zeta = \frac{\omega_2 - \omega_1}{2\omega_r} \tag{6.2.2}$$

where ω_1 and ω_2 are the angular frequencies at which the rotational angle of the microscanner falls to $1/\sqrt{2}$ of the resonance peak value.

The moment of inertia of a rotating microscanner (I) about Y-axis can be calculated using CoventorWare.

The torque ($T(\theta)$) generated by the angular vertical comb-drives during dynamic rotation of the microscanner, can be described as:

$$T(\theta) = N\frac{1}{2}\frac{\partial C}{\partial \theta}V^2 \tag{6.2.3}$$

where,

N is the number of electrodes or finger pairs of the comb-drives,

C is the capacitance between a pair of fingers,

V is the periodic driving signal.

It is assumed that the damping ratio ζ is constant during dynamic actuation for microscanner. In order to obtain large rotational angles, it is straight forward to increase the generated torque, $T(\theta)$, by increasing the pairs of fingers of comb-drives along the length of torsion bar.

There are two pairs of electrostatic comb-drives in the 2D microscanner design. The two pairs of comb-drives are symmetrically arranged on each side of the torsion bar as shown in Figure 6.1d. Each electrostatic comb-drive pair consists of 20 fixed comb fingers which are interdigitated with 21 movable comb fingers. The 20 fixed comb fingers are equally spaced by 22 μm and are fixed to the substrate at one end. The 21 movable comb fingers are also equally spaced by 22 μm and are connected to one side of a 10-μm-wide, 748-μm-long torsion bar. The other group of the 21 movable

fingers are symmetrically connected to the other side of the torsion bar. Every finger of the movable and fixed comb-drives has the length of 160 μm and the width of 10 μm. The gap between the fixed and the movable fingers is 6 μm, and the gap between the finger tip and the edge of the fixed end is 8 μm in the designed layout. The overlapping length is 152 μm. Due to the stress gradient present in the silicon, the fingers of the fixed and movable comb-drive curve slightly out-of-plane with an average tip displacement of $\sim$0.3 μm. This slight curvature of the fingers forms an AVC (angular vertical comb-drives) structure. However, after the structure is released from the substrate during fabrication, the overall vertical level of movable combs is higher than that of fixed combs which is characteristic of a SVC. Both initial angle of AVC and initial vertical offset of SVC are reported to enhance the dynamic rotation angle of electrostatic comb-drive actuated micromirror [12, 13], but the non-uniform overlapping between finger pairs introduces analysis complexity. This is beyond the scope of the thesis.

The torsion bar of electrostatic comb-drives is aligned to Y-axis of microscanner. One end of the torsion bar is connected to micromirror's frame edge and the other end is fixed to substrate. When supplying one pair of comb-drives with a sinusoidal signal of rotational resonant frequency, the resulting torque excites the microscanner rotating about torsion bar in the Y-axis. The rotational axis of this microscanner is orthogonal to the tilting axis generated by electrothermal actuators. This resonant rotation mode (no less than a few hundreds of Hertz) is faster than response time of the electrothermal actuators (typically several tens of milliseconds).

6.2.4 Framed micromirror

The micromirror is designed to be patterned in the 10 μm thick SOI layer with a circular shape of 1.2 mm diameters. The micromirror is suspended from a 10-μm-wide ring-shape frame through two 80-μm-long and 10-μm-wide inner torsion bars which is aligned to the micromirror rotational axis (Y-axis in Figure 6.1). The gap between the frame and the micromirror edge is 30 μm wide, and the edges of micromirror

where it is connected to the inner torsion bars are engraved to extend the length of each inner torsion bar to 80 μm. The framed micromirror actuated electrostatically has been experimentally characterised and shown to enhance the scanning linearity and reduce resonant hysteresis of dynamic rotation [2]; the frame also functions as a heat resistance between the electrothermal actuator and the micromirror. Each of these functions will be described in more detail with FEM simulation and experimental characterisation results in the later sections. Then, an extra layer of 0.65 μm thick BlanketMetal gold is chosen to be evaporated on the top of the silicon micromirror to increase its reflectivity.

6.2.5 Serpentine springs

The serpentine springs are commonly used as flexure connections in MEMS device designs. J. Singh et al demonstrated a two-dimensional electrothermal microscanner utilising the serpentine spring as the connection between electrothermal actuator and mirror [14]. S. H. Tsang et al presented an actuator which requires a pair of serpentine springs to allow a 90^{o} out-of-plane rotation as well as provide connections to the substrate [15]. G. Barillaro et al. [16] analysed and compared in detail the performance of two serpentine springs with different structure arrangement, namely the classic and rotational serpentine springs.

In the hybrid actuated microscanner design, the serpentine springs are the flexure connections between electrothermal actuators and micromirror. When the micromirror is rotating about the torsion bar in Y-axis, the frame is also rotating about the Y-axis along with the micromirror. There are two points on the rim of frame, the furthest away from the rotational centre, which have the largest rotational amplitude. However, these two points are also constrained and connected to the electrothermal actuators. Therefore, serpentine springs are chosen as the elastic connections between the vibrating framed micromirror and the relatively static vertical displacement at the tips of electrothermal actuators.

When the hybrid microscanner is rotating about the torsion bar, connections between the edge of frame micromirror and the electrothermal actuators need to be flexible enough to maintain deflection magnitude and have small stress no greater than the material fracture limit (which is around 2.27 GPa for 10-μm-thick SOI layer [17]). In this subsection, the mechanical performance of the serpentine spring design used for microscanner is simulated using FEM software, CoventorWare, and is compared with a SOI torsion bar of equivalent length. As shown in Figure 6.8, the FEM model of a serpentine spring and an equivalent torsion bar are equally meshed by $4\times4\times2$ μm^3 parabolic hexahedron element. To compare the mechanical performances of two structures, sequences of vertical displacements along the Z-axis (D_z) and rotation angles about the X-axis (R_x) are applied to 'End 2' of both models with 'End 1' fixed, and then the stiffness or the spring constant of two structures are calculated.

Figure 6.9a plots the FEM estimated spring constants (K_{Dz}) along the Z-axis when the spring and the equivalent torsion bar is fixed at one end while the other end deflects by D_z along the Z-axis. The spring constant of the serpentine spring along the Z-axis remains a constant value of 4.2 μN/μm. In contrast, spring constant of the torsion bar along the Z-axis increases almost linearly when bending magnitude is increased. This implies that the bending deformation of a torsion bar can stiffen the structure.

Figure 6.9b plots the FEM estimated spring constants (K_{Rx}) about the X-axis of the serpentine spring and the equivalent torsion bar which are both rotating at angles of R_x about the X-axis and are fixed at one end. From the results, the spring constants about the X-axis (K_{Rx}) of both the serpentine spring and the torsion bar remain approximately constants of around 1191 ± 0.4 μNμm/degree and around 4543 ± 5 μNμm/degree respectively during the rotation. However, the serpentine spring is almost 4 times more flexible than its equivalent torsion bar when one end is rotating.

From mechanical analysis of the serpentine spring and the torsion bar, it can be seen that serpentine spring is not only more flexible than the torsion bar in both bending and rotating deformation, but also maintains constant bending and rotating stiffness during deformation. Apart from the mechanical performance, the thin and long serpentine

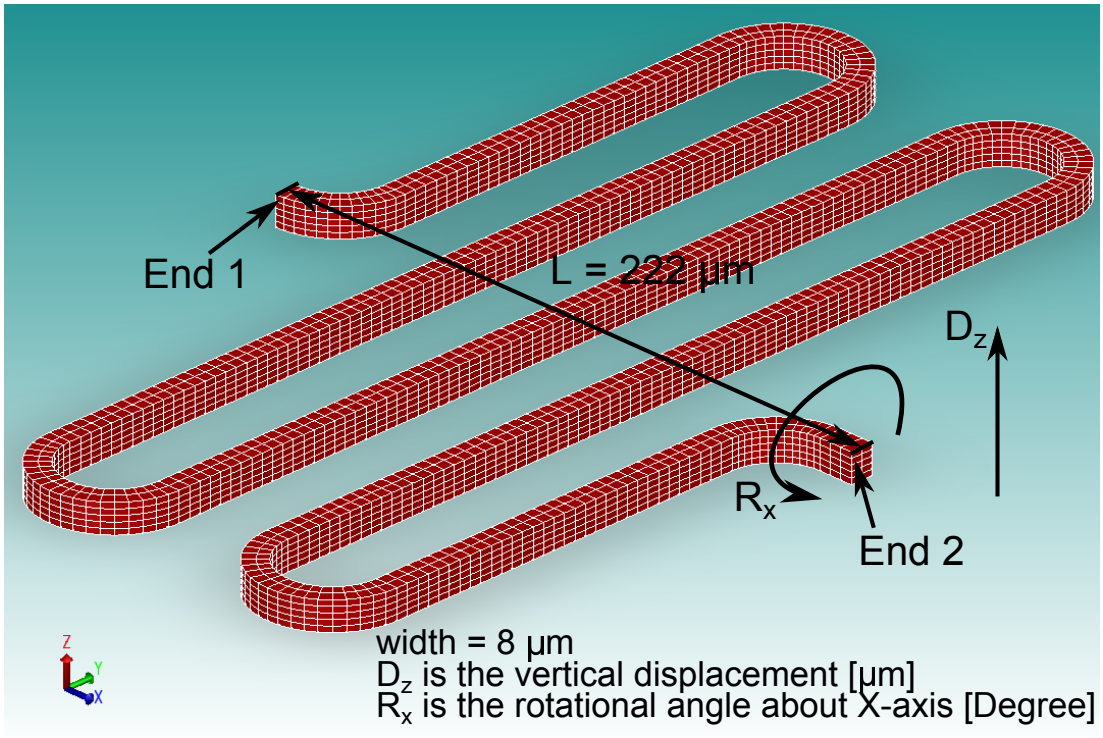

(a)

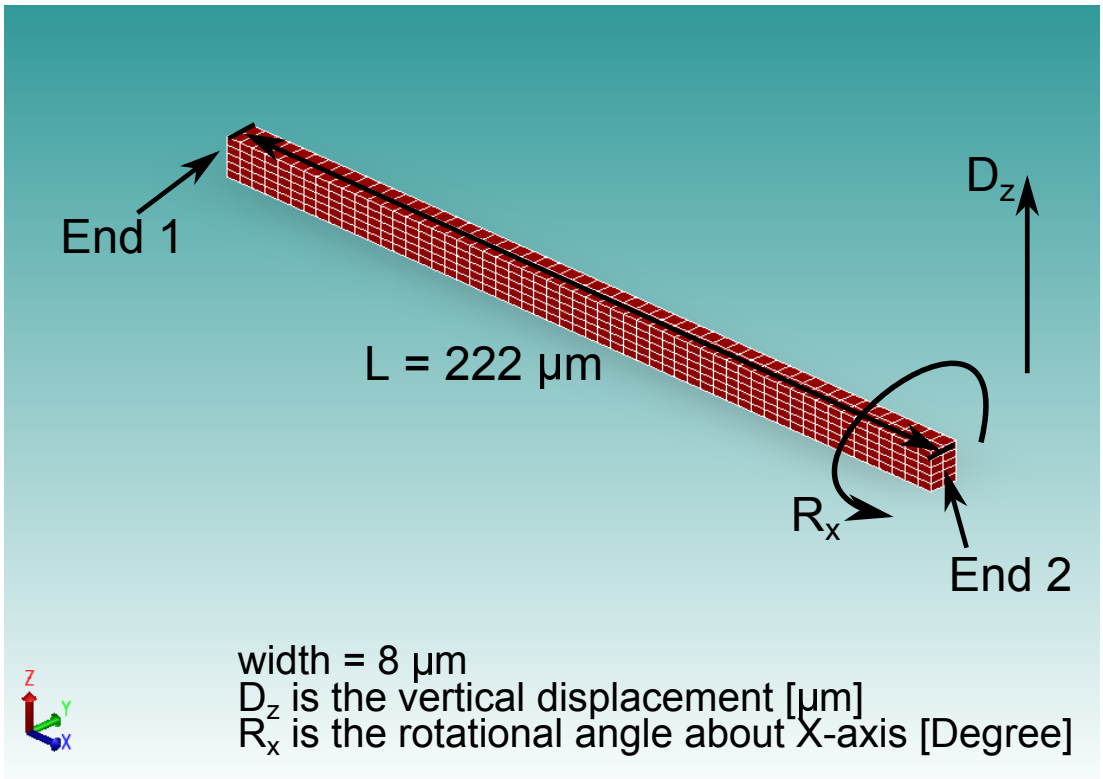

(b)

Figure 6.8: FEM model of the serpentine spring of microscanner (a) and the equivalent torsion bar (b).

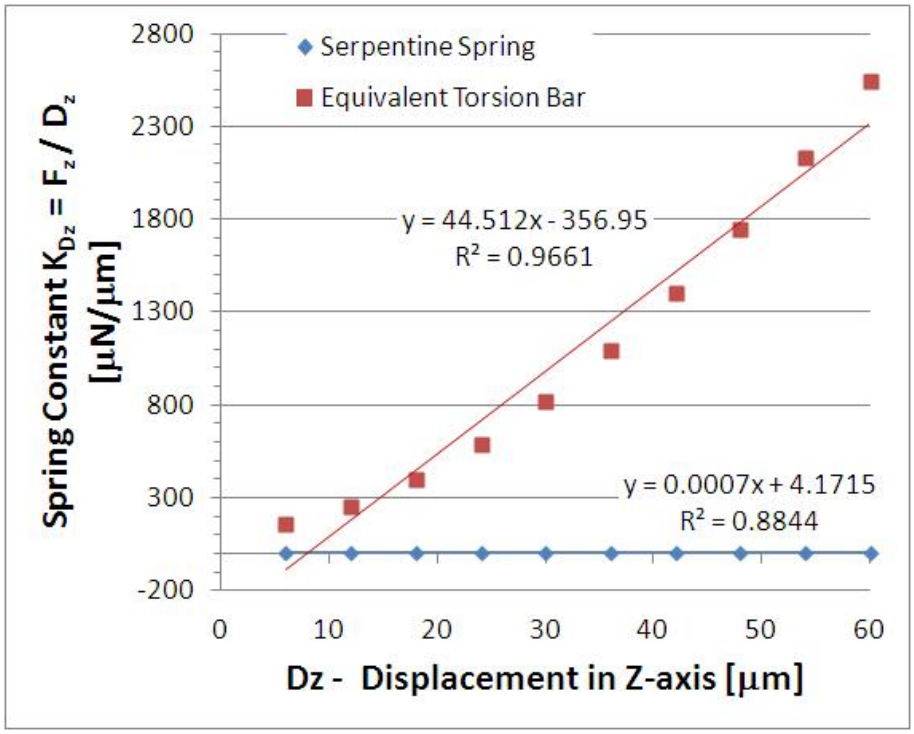

(a)

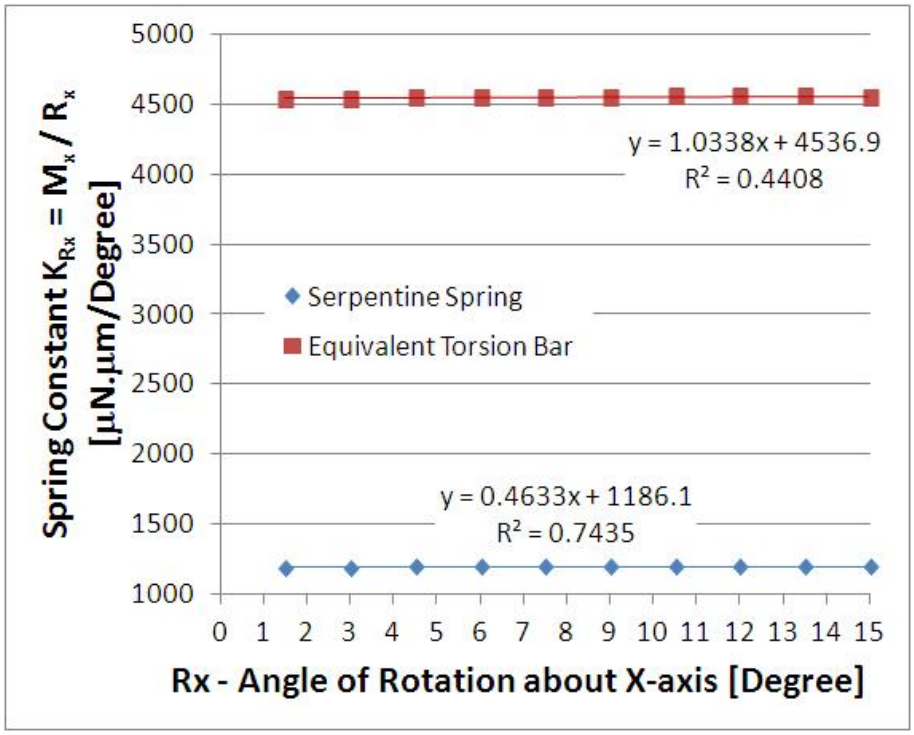

(b)

Figure 6.9: The calculated spring constants of the serpentine spring of microscanner and an equivalent torsion bar.

springs also function as electrical and thermal resistance between the electrothermal actuator and the micromirror in a similar manner to the ring-shape frame.

6.2.6 Geometric summary

The hybrid actuated 2D microscanner is made up of a framed circular micromirror, two electrothermal actuators, two pairs of electrostatic comb-drives and two serpentine springs as connections. The micromirror is 10-μm-thick and 1.2-mm-diameter single crystal silicon plate coated with a layer of 0.65-μm-thick gold. The bimorph micromirror is suspended from the ring-shape frame through two 10-μm-wide torsion bars. There is a 30-μm-wide gap between the micromirror and the frame. The points on the edge of micromirror which are connected to the inner torsion bars are engraved with a 50 μm long trench so that each inner torsion bar is extended to 80 μm long. Each serpentine spring, connected between frame and electrothermal actuator, is 8 μm wide and occupies the 222-μm-long gap. Each electrothermal actuator has three 40-μm-wide and 2000-μm-long cantilevers which are fixed to the substrate. The free ends of three cantilevers are connected by a 390-μm-long and 80-μm-wide joint beam. Each pair of electrostatic comb-drives is made up of 21 movable fingers interdigitised with another 20 fixed fingers. Every finger is a 160-μm-long and 10-μm-wide cantilever. Each pair of fixed and movable fingers is designed to be separated by 6 μm wide along the Y-axis and overlap by 152 μm long in the X direction. The fixed fingers are all anchored to the substrate and the movable fingers are all anchored to both sides of a torsion bar. The torsion bar is aligned to the rotational axis of microscanner and is the connection between the framed micromirror and the substrate, and it is 748 μm long and 10 μm wide. The frame, the inner torsion bars, the electrothermal actuators and the electrostatic comb-drives are all patterned in the 10 μm thick single crystal silicon. The geometric detail of the microscanner is summarized in Table 6.1.

Table 6.1: Geometrical dimension of the hybrid actuated 2D microscanner.

Framed Micromirror	
Diameter of the micromirror	1200 μm
Width of the ring frame	10 μm
Width of the inner torsion bar connections	10 μm
Length of the inner torsion bar connections	80 μm
Electrothermal actuators	
Length of three cantilevers	2000 μm
Width of three cantilevers	40 μm
Spacing between cantilevers	145 μm
Width of the joint beam	80 μm
Length of the joint beam	390 μm
Electrostatic comb-drives	
Length of the movable and fixed fingers	160 μm
Width of the movable and fixed fingers	10 μm
Overlapping length between the movable and the fixed fingers	152 μm
Spacing between the movable and the fixed fingers	6 μm
Length of the torsion bar	748 μm
Width of the torsion bar	10 μm
Number of Fixed Fingers	40
Number of Movable Fingers	42
Serpentine springs	
Width of serpentine springs	8 μm
Spacing of serpentine springs	34 μm
Length of serpentine springs	1489.86 μm

6.3 Finite Element Simulation

The FEM model of microscanner is built from the layout design file using CoventorWare. The mechanical resonant frequencies, the corresponding mode shapes and the mechanical deformation of the microscanner are simulated.

6.3.1 Meshing quality

FEM simulation of SOIMUMPs fabricated devices could be computationally expensive (hours of computation time and requires more than gigabyte data storage space). This is due to large displacement and nonlinear analysis of the problem, such as nonlinear geometry, nonlinear force load and nonlinear material properties

(residual stress, stress gradient and temperature dependent material properties). In order to achieve an accurate FEM simulation, expensive computation iterations and convergence check steps are required. Because of these properties of the problem, parabolic hexahedron meshing elements with aspect ratio less than 15 are suggested by CoventorWare for resolving stress gradients in order to obtain an efficient mechanical solution [18].

Based on the author's experience, the meshing quality will not only have an impact on the accuracy of FEM simulation results, but also affect the convergence speed and its rate of success of obtaining converged results. Ideally, the meshing element and meshing algorithm should be chosen specifically for each part of microscanner due to geometrical differences [2]. This requires extra computation resource for storing the nodes on surfaces different connecting parts. However, due to the limitation of 5 GB computation storage (2 GB RAM, 3 GB disk swap space) and the computation time cost (at least 12 hours for an convergence check of the mechanical simulation when using parabolic hexahedrons), such standards are hard to achieve especially for thin layer gold coated microscanner with high aspect ratio. Therefore, considering the trade-offs between available computational resources, the cost and simulation accuracy, a single layer of parabolic elements generated using the same meshing algorithm are applied.

First, within the available computation resource, one layer of parabolic hexahedrons is used for meshing the microscanner model and are generated using a 'Hex-Dominant' algorithm provided by CoventorWare. Table C.11 summarises the meshing quality of each part of the microscanner model using parabolic hexahedrons. As listed in the table, the gold layer of the micromirror has the highest aspect ratio of all parts of microscanner. This indicates that high meshing density is required for the gold layer. After meshed with hexahedrons, all the parts except the gold layer have achieved a very small average aspect ratio of meshing elements; all the parts have achieved a small element edge length with the largest value of 17 μm. In terms of element corner angle, generally, all the parts have achieved an average corner angle of around

[2] as examples shown in Figure B.2, B.3, B.4 and B.5

90°. The micromirror frame contains features of curves with various radii; thus, the resulting minimum and maximum element corner angles are 1.3° and 176°; such small or large corner angle of meshing element, especially located at places of high stress, could produce excessive element distortion and fail the mechanical simulation. This is one drawback resulting from meshing with a unique element type and algorithm. Figures B.2, B.3, B.4 and B.5 demonstrate an example of meshing each part of microscanner individually using different mesh generating algorithms and the meshing quality of such example is summarised in Table C.13.

In order to compare the simulation results using a different meshing element, all the parts of microscanner model are meshed with parabolic tetrahedrons. Modal analysis, and mechanical deformation are carried out for the tetrahedron meshed microscanner model as well, the meshing quality of which is summarised in Table C.12. The hexahedron can result in better meshing quality when comparing the average corner angle of meshing elements, though tetrahedrons are claimed to be suitable for any geometry in theory [18]. However, with equivalent meshing density, the FEM simulation using parabolic hexahedrons could take 4 times longer to complete than the one using parabolic tetrahedrons.

During simulation, the silicon oxide layer is assumed to be mechanically fixed and thermally constant at 20°C; the electrical and thermal conductivities of which are 0 S/μm and 1.42 $Wm^{-2}K$ respectively. Other properties, such as the elastic modulus, thermal expansion coefficient and specific heat, are set as the default values provided by CoventorWare, are not quoted in this document since the material is mechanically fixed and static thermo-mechanical behaviour is simulated rather than transient behaviour. The material properties of the SOI and BlanketMetal gold layer are listed in Table 2.3

6.3.2 Initial tilt angle

Initially, the mechanical deformation of microscanner due to only the intrinsic stresses within the materials, without actuation, is simulated. The microscanner is fixed rigidly to the substrate on one side, and the opposite end of the device is free. As shown in Figure 6.10a, the microscanner curves out-of-plane at the free end due to the stress gradient in SOI layer. By extracting the vertical displacements of four points on the micromirror edge, the initial tilt angles of microscanner are calculated to be 2.3^o about X-axis and 0^o about Y-axis. Figure 6.10b shows a closer view of the electrostatic comb-drives. Because of the deformation, the movable combs are also tilted upwards at the end connected to micromirror and are higher than the fixed combs. The maximum vertical offset between the movable and the fixed fingers of the combs is around 5 μm.

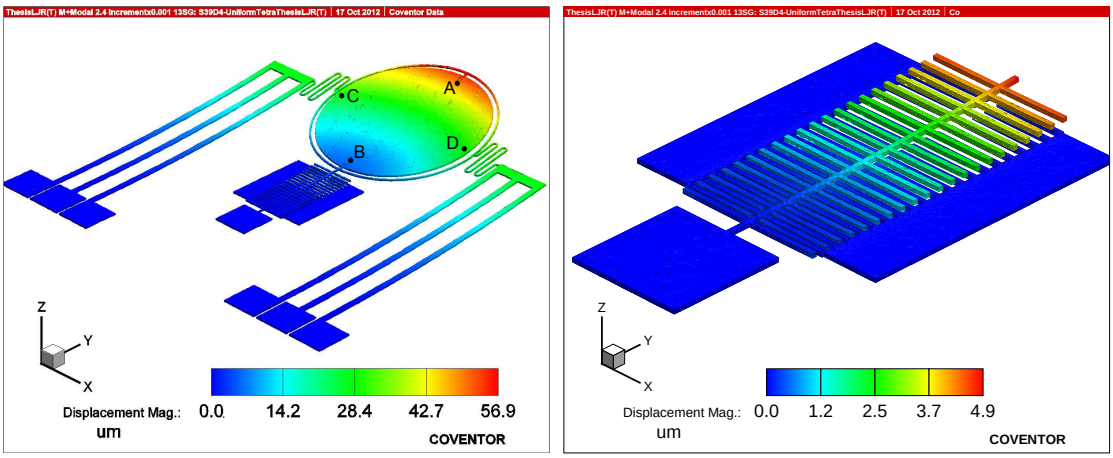

(a) (b)

Figure 6.10: FEM simulation of the initial mechanical deformation of microscanner after fabrication due to the stress gradient in the silicon layer (x5 displacement exaggeration).

6.3.3 Modal analysis

Table 6.2 summarises the first five natural frequencies of microscanner structure obtained by performing the modal analysis in CoventorWare. Figure 6.11a shows first mode shape of the structure at natural frequency 692 Hz, which is when the microscanner vibrates at the free end. Figure 6.11b shows mode shape of the rotational

mode at 1613 Hz when the microscanner is rotating about Y-axis. The colour-coded displacement indicates that the micromirror is rotating at a higher angle than the frame. Therefore, as described earlier in the last section, the frame designed can enhance the rotational angle of micromirror about the Y-axis. It can also be seen in Figure 6.11b, when resonant rotation mode is excited, the tips of two electrothermal actuators vibrate along with the rotating frame.

Table 6.2: Modal analysis results of microscanner showing the first five natural frequencies.

Order	Unit	1	2	3	4	5
Natural Frequency	Hz	692.2	1613.3	2470.5	4074.5	4135.4
Generalised Mass	—	1.86E-08	1.34E-08	4.04E-08	5.41E-09	5.05E-09

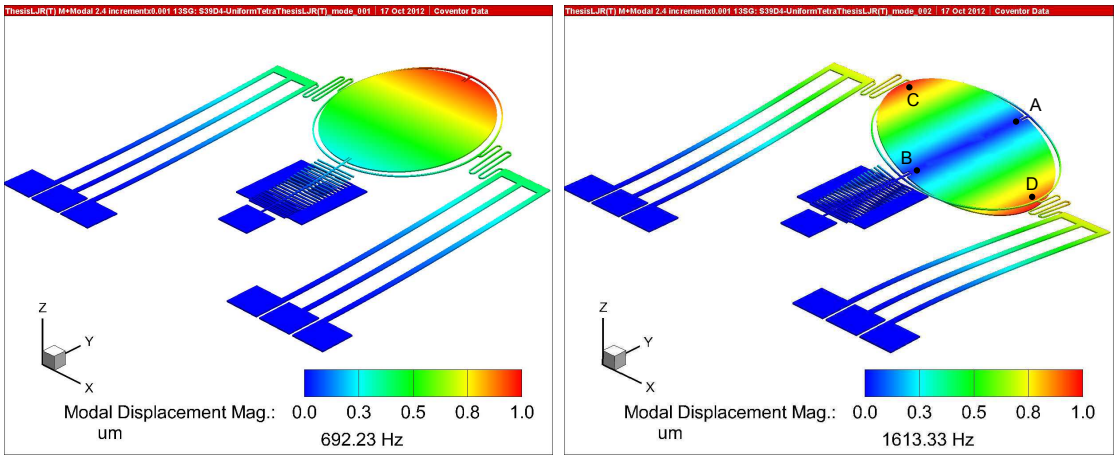

(a) (b)

Figure 6.11: The mode shapes of microscanner at the first (a) and the second (b) natural frequencies simulated using FEM software CoventorWare (with displacement exaggerated by x250 times).

6.3.4 Static electro-thermo-mechanical behaviour

The mechanical deformation of the microscanner due to actuation of the electrothermal actuators is simulated by performing electro-thermo-mechanical analysis on the device model using CoventorWare. In the simulation, a series of voltage levels is applied to the fixed ends of outer cantilevers of two electrothermal actuators. The electrothermal actuators and the electrostatic comb-drives are fixed to the substrate as indicated in the previous analysis. At the mechanically fixed surfaces, the temperature of which

is assumed to be fixed at 20 °C throughout the simulation. This value is also taken for the ambient temperature. Air convection coefficient is assumed to be 10 $Wm^{-2}K$. Emissivity of SOI and gold layers are assumed to be 0.6 and 0.02 respectively. The electric and mechanical material properties of silicon and gold are listed in Table 2.3 in Section 2.5.2 page 29.

With the electro-thermo-mechanical analysis, the temperature profile and the mechanical deformation of microscanner can be visually presented. The micromirror static tilt angles about the X- and Y-axes can be calculated from vertical displacements of the four points on micromirror edge.

6.3.4.1 Optical tilt angles

As already introduced, this layout of electrothermal actuator design provides vertical displacement at the free end. During electrothermal actuation of the hybrid actuated microscanner, the micromirror is lifted from the two points connecting to the electrothermal actuators. Since the micromirror is also fixed at the third point by electrostatic comb-drives, the electrothermal actuators rotate the micromirror about this fixed point when driven by voltage signals. In this part, this electrothermally actuated static rotation is of priority interest before actual fabrication of the design, followed by the description of other thermal related performances, such as temperature distribution and curvature of the bimorph micromirror.

Figure 6.12b illustrates simulated mechanical deformation of microscanner when both electrothermal actuators are excited at 8 V. The electrothermal actuators lift and tilt the micromirror about X-axis from its rest position. The serpentine springs between the electrothermal actuator tips and the framed micromirror sustain the displacements of electrothermal actuators and transfer these displacements to micromirror. The maximum vertical, or Z-axis, displacement of the micromirror is around 175 μm at the free end.

When only one electrothermal actuator is actuated at 8 V, as illustrated in Figure 6.12c,

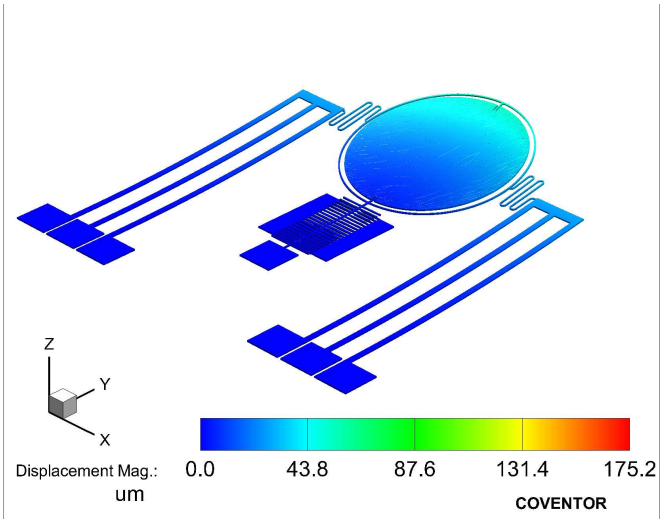

(a) no actuation

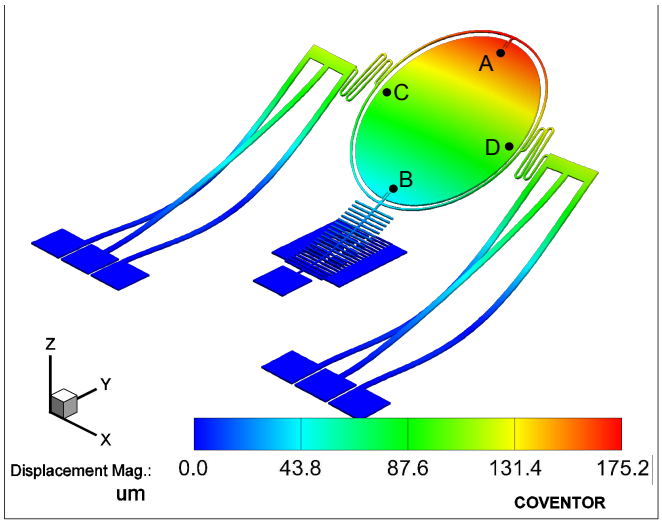

(b) actuation of two electrothermal actuators.

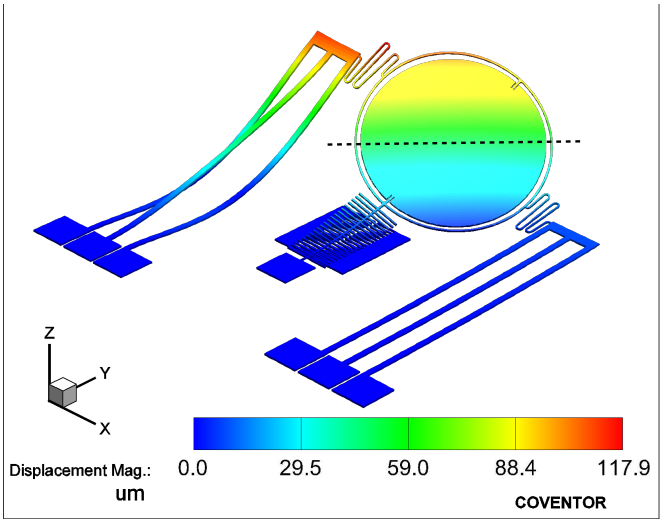

(c) actuation of one electrothermal actuator

Figure 6.12: FEM simulation of electro-thermo-mechanical behaviour of microscanner at 8 V per electrothermal actuator (with x5 displacement exaggeration).

the maximum vertical displacement is around 118 μm and is on the serpentine spring which is deformed. Besides, the mechanical deformation of the micromirror is not about the Y-axis but about an axis which is 56.4^{o} off the Y-axis. Therefore, the X-axis tilting of the micromirror by both electrothermal actuator is the motion will be used for the two orthogonal axis scans.

The optical tilt angle of the micromirror can be calculated from FEM simulation results by extracting the vertical dispalcements of the four points, A, B, C and D. Figure 6.13 plots the optical tilt angles against voltage per electrothermal actuator (Figure 6.13a) and total actuation power (Figure 6.13b) when microscanner is driven by both electrothermal actuators. The FEM model uses two different meshing elements, the parabolic tetrahedrons and the parabolic hexahedrons, are simulated, and the results are plotted in the diagrams to demonstrate consistency. The maximum optical tilt angle is estimated to be around 17.5^{o} at 18 V per electrothermal actuator or 672 mW in total. Also, the simulated results estimate a threshold of 4 V per electrothermal actuator, or 45 mW in total, for tilting angle about the X-axis.

6.3.4.2 Temperature distribution

Apart from the mechanical deformation, Figure 6.14a plots the temperature profile of the microscanner when the two electrothermal actuators are both actuated at 8 V. The maximum temperature is estimated to be around 776 ^{o}C and is located towards the free end of each outer cantilever of the electrothermal actuator. And the heat generated within the electrothermal actuators will be conducted to the micromirror through connecting springs and frame. Figure 6.14b displays temperature profile on the micromirror with a reduced scale. The maximum temperature on the micromirror is located at the edge which is connected to the top inner torsion bar, due to the heat conduction. The average temperature of micromirror is around 61 ^{o}C when both electrothermal actuators have the maximum temperature of 776 ^{o}C.

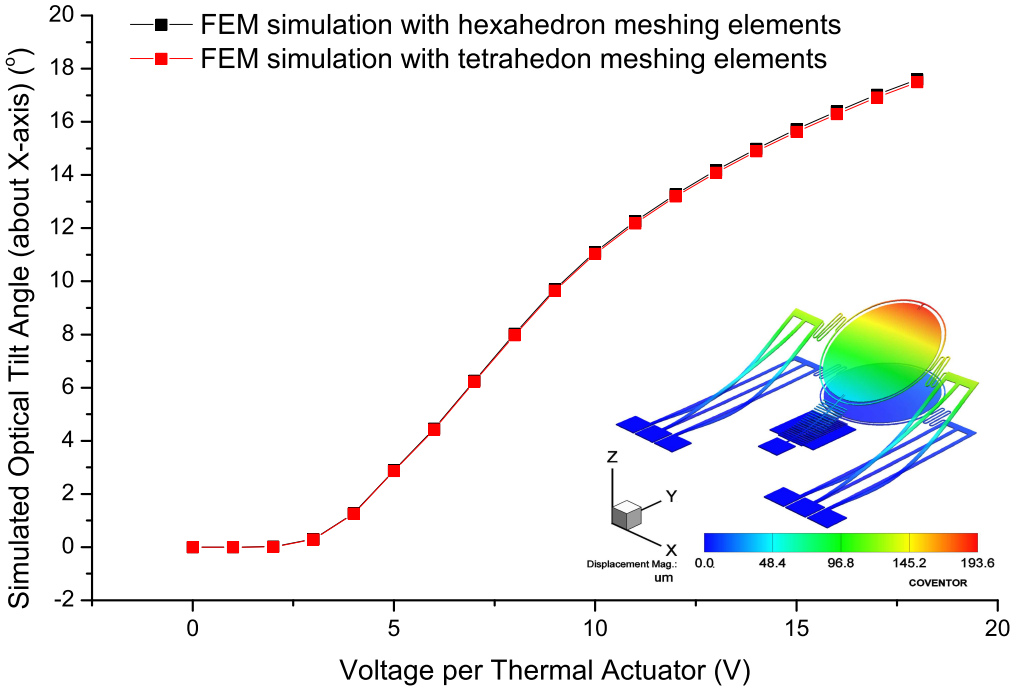

(a)

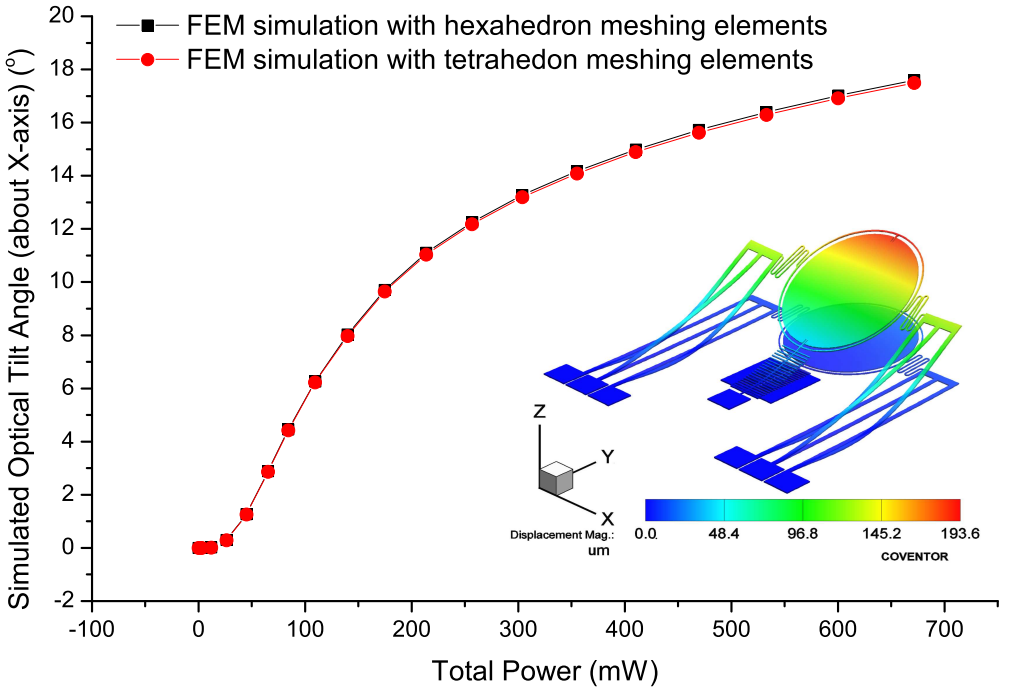

(b)

Figure 6.13: The optical tilt angle of microscanner by two electrothermal actuators simulated using FEM software, CoventorWare.

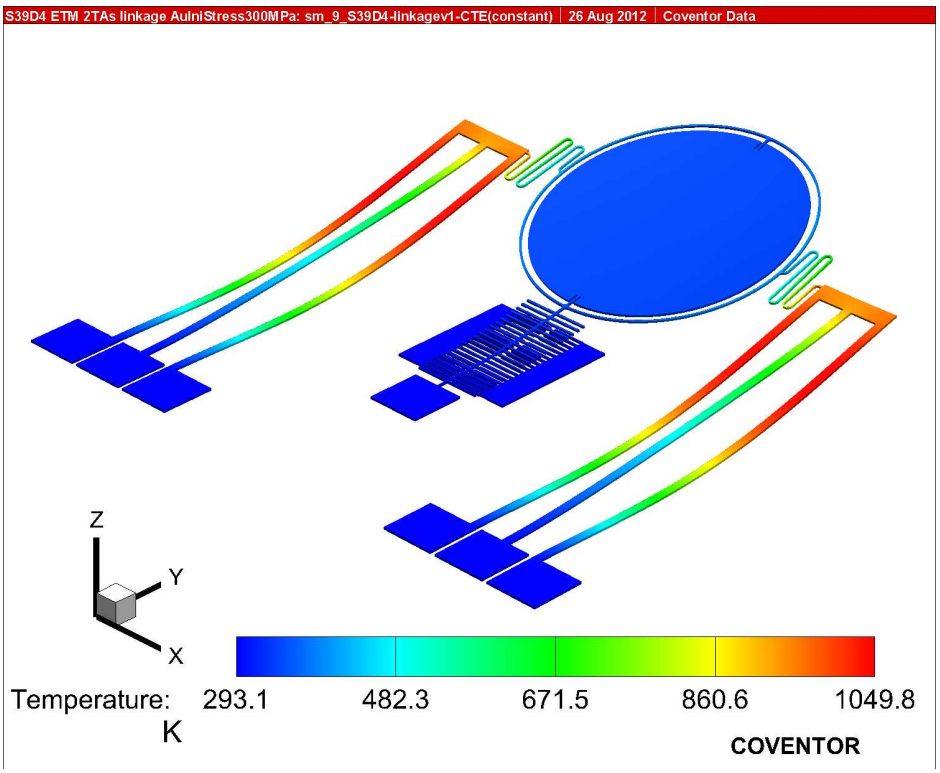

(a)

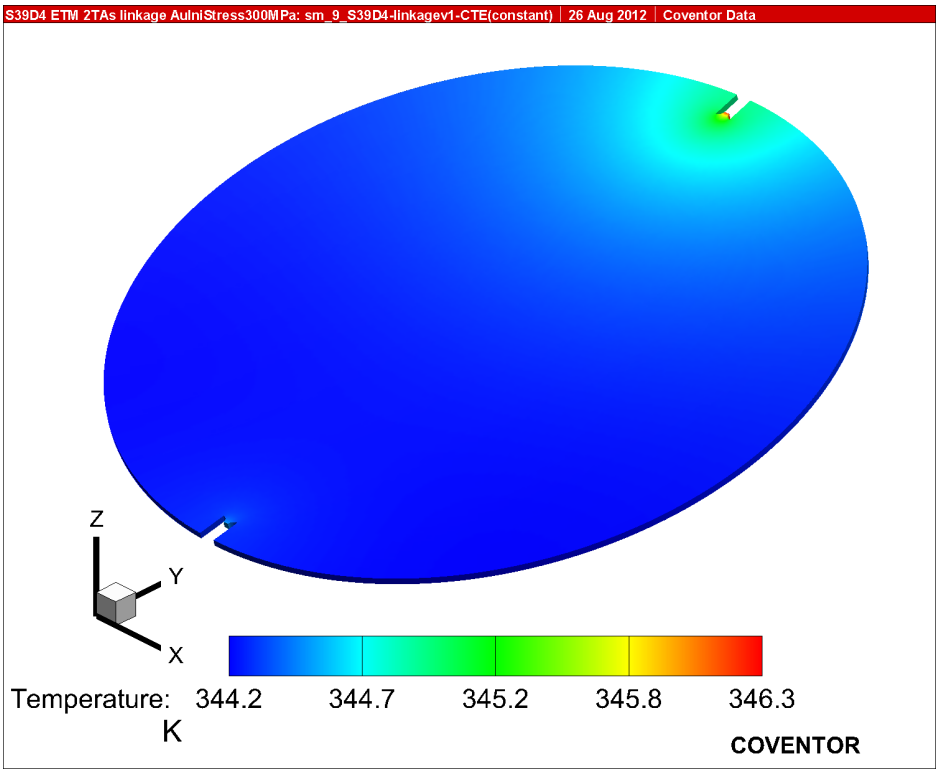

(b)

Figure 6.14: FEM simulated temperature distribution over the microscanner (a) and over the bimorph micromirror (b) at 8 V per electrothermal actuator (the displacement of the device is exaggerated by x5 times).

6.3.4.3 Micromirror curvature

Figure 6.15 plots both the maximum temperature on the electrothermal actuators and the average temperature of the micromirror as a function of total power during electrothermal actuation. As seen in the plot, the overall gradient of the maximum temperature on electrothermal actuators is much steeper than the averaged micromirror temperature gradient. Therefore, from these FEM simulation results, the serpentine springs and the frame can provide micromirror the thermal isolation from the heat source of electrothermal actuators during actuation. However, the temperature of the micromirror cannot be maintained to be a constant value. Moreover, it can be noticed that the estimated maximum temperature when both electrothermal actuators are driven at 18 V, or total power of 672 mW, is as high as 1857 ^{o}C which is far beyond the melting point of the silicon (1410 ^{o}C). This mismatch between the estimated temperature and the empirical temperature of SOI fabricated electrothermal actuator is believed to be caused by the difference between the actual material properties and the referenced ones, such as, the thermal conductivity of the highly doped silicon material; it also because of assumed air convective coefficient [19, 20]. Despite this discrepancy, the thermal resistance provided by the frame and serpentine springs is estimated to maintain the micromirror temperature at only 5% of the maximum temperature value when 18 V per electrothermal actuator is applied.

Next, the micromirror, made of stack of the tensile stressed gold layer and the compressive stressed silicon layer of bimorph micromirror, has an initial concave surface curvature. Due to the thermal expansion difference between the silicon and the gold materials (refer to CTE in Table 2.3), the mechanical deformation of this bimorph micromirror, or its surface curvature, is sensitive to temperature changes. As simulated above, the average temperature of bimorph micromirror is estimated to rise to 75 ^{o}C when both electrothermal actuators are driven at 18 V. The radius of curvature (ROC) of the micromirror is also obtained as the results of electro-thermo-mechanical analysis, and is estimated to be increased from 21 mm to 24 mm during electrothermal actuation. The estimated micromirror ROC variation is plotted together with measured

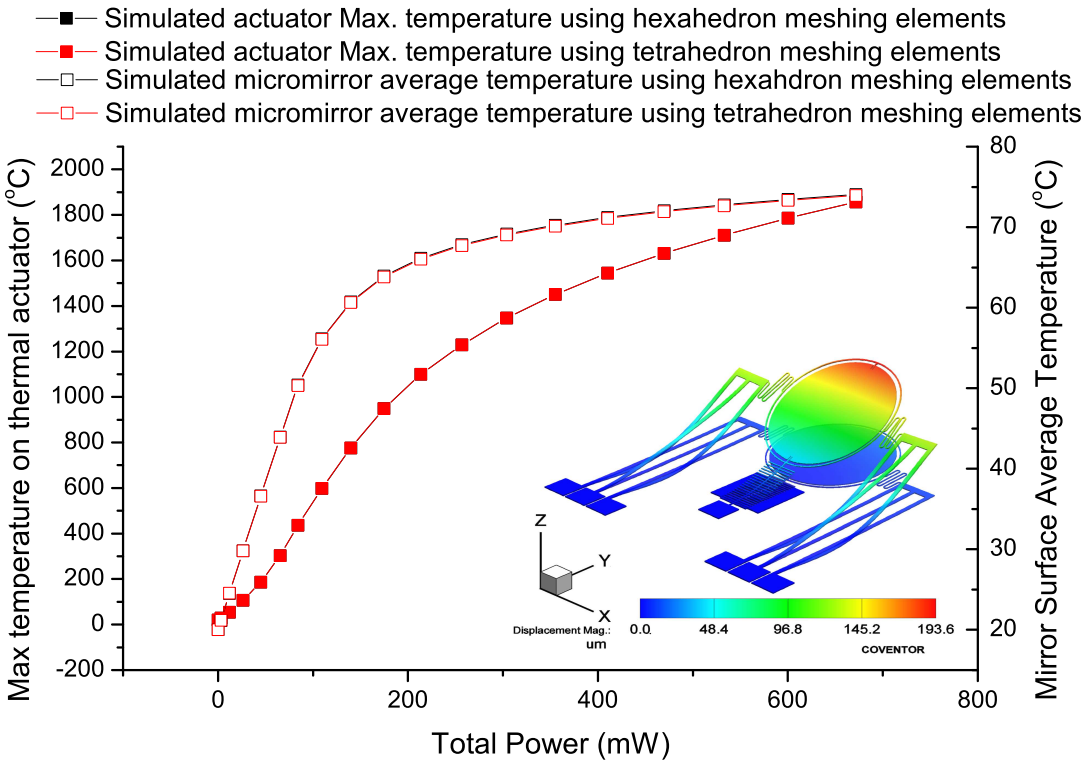

Figure 6.15: FEM simulated maximum temperature on the electrothermal actuators and averaged temperature on the micromirror.

results in the Section 6.4.1.2.

Table C.14 and Table C.15 summarise the simulated thermal and mechanical performance of microscanner FEM model using hexahedron and tetrahedron meshing elements during actuation of both electrothermal actuators.

6.4 Experimental Characterisation

The performance of the SOIMUMPs fabricated microscanner is characterised from the magnitude and the speed of optical scan angles in the two orthogonal axes driven by electrothermal and electrostatic actuators respectively. This section is divided into the electrothermal actuation, the electrostatic actuation and the 2D scanning of the microscanner. For electrothermal actuation, characterisation of optical angles about the X-axis driven by electrothermal actuators is described. The radius of curvature

(ROC) of the gold coated silicon micromirror at each electrothermal actuation power is measured using the white light interferometer. For the electrostatic actuation, measurements of scan angles driven by comb-drives are presented. During the measurement, dynamic response and resonant frequencies are characterised. Also, the characterisation results of dynamic rotation of micromirror about the Y-axis by the electrostatically-actuated while the micromirror is also tilted about the X-axis by electrothermal actuators are also described. Finally, programmed driven and images of 2D scanning pattern are presented.

Optical angles about the X-axis of microscanner caused by electrothermal actuators are described as the ”optical tilt angles”; optical angles about the Y-axis driven by the electrostatic comb-drives are described as the ”optical scan angles” since it is excited at resonance.

6.4.1 Electrothermal actuation

6.4.1.1 Static optical tilt angle

To measure the optical tilt angles of when the microscanner, DC voltage levels (V_{dc}) from 0 V to 18 V are applied to each electrothermal actuator as presented in Figure 6.16. The X-axis optical tilt angle can be calculated using the right-angle triangle formula from the displacement of the laser spot and the distance between screen and microscanner, as demonstrated in Figure 5.7.

From the results summarised in Table C.16 and the plot in Figure 6.17, the optical tilt angle of the microscanner increases linearly as the actuation voltage increasing from 4 V to 17.5 V, or as the actuation powers increasing from 54 mW to 532 mW, and the maximum value is 6.9^{o}. In these diagrams, the FEM simulated optical scan angles are also plotted. The simulated maximum optical tilt angle are around 160% higher than the experimental results. Also, the simulated results are not linear to either the voltage or the power of the electrothermal actuators. This is mainly because of

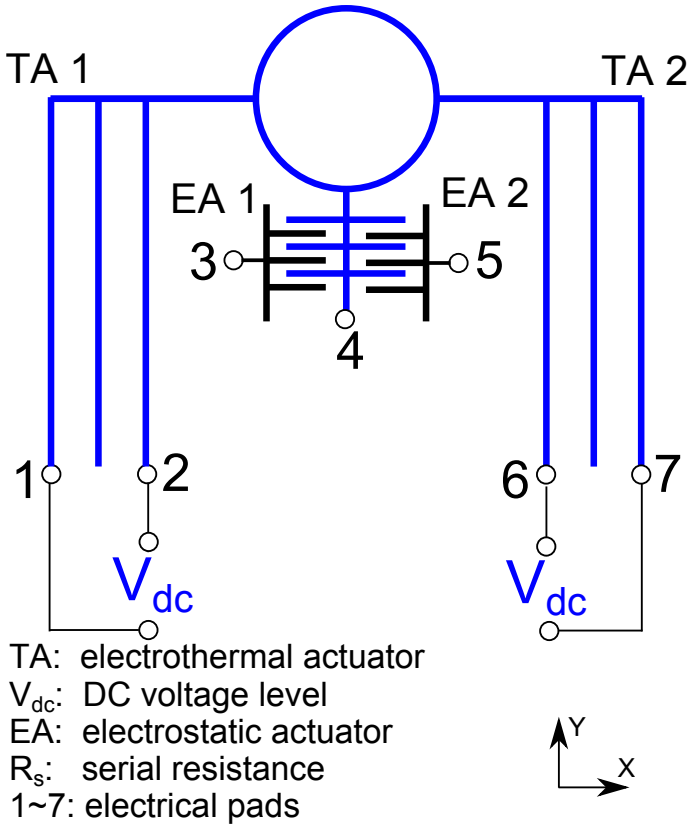

Figure 6.16: The scheme diagram of actuating the two electrothermal actuators of the microscanner.

the uncharacterised temperature depended thermal and electrical conductivities of the doped single-crystal-silicon material used during the simulation as suggested in the last section.

Both the measured and and simulated optical tilt angles of the microscanner, in Figure 6.17, have a threshold at 4 V per electrothermal actuator. In other words, both cases have shown that the micromirror does not tilt until the electrothermal actuator driven voltage of 4 V. At low actuating voltages ($V_{dc} < 4$ V), the combination of the expansion and the constraint forces does not generate buckling deformation of outer cantilevers of electrothermal actuator. Until the applied voltage per electrothermal actuator V_{dc} is greater than 4 V, the thermal expansion force of the outer cantilevers exceed the constraint force of electrothermal actuator, thereafter the buckling of outer cantilevers results in the vertical displacement of the electrothermal actuator.

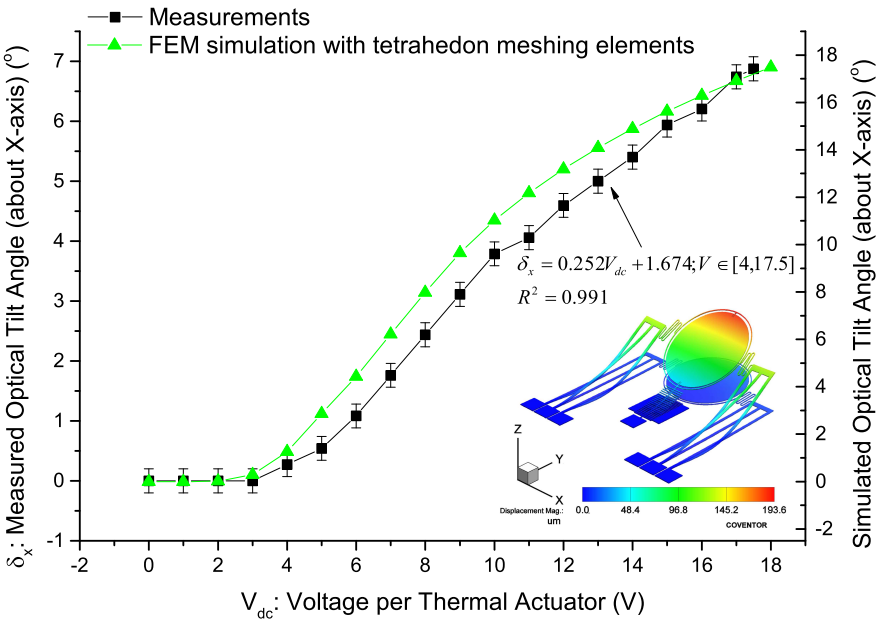

(a)

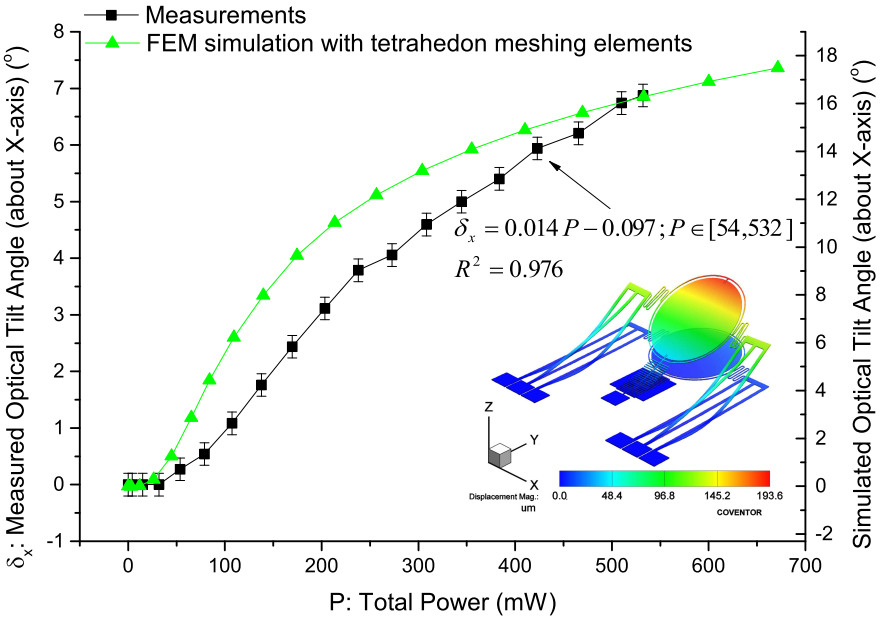

(b)

Figure 6.17: The experimental and simulation results of static optical tilt angles of the microscanner as a function of total driving voltage (a) and as a function of the electrothermal power of two electrothermal actuators (b).

6.4.1.2 Radius of Curvature

As analysed in the last section, the ROC of micromirror is sensitive to temperature variation. Since the micromirror is connected to the electrothermal actuator, the heat generated during electrothermal actuation is conducted to micromirror through the connecting springs and frame. To characterise this effect of electrothermal actuation, the micromirror surface profile of microscanner has been measured at each electrothermal actuation level using the white light interferometer.

The measured micromirror ROC at each power level of two electrothermal actuators is listed in Table C.16. Under the laboratory temperature of 20 ^{o}C, ROC has increased by 11.3 mm or by 64.6% when each electrothermal actuators is actuated at 18 V (or a total power of 628 mW). Figure 6.18 plots the measured ROC as a function of total electrothermal actuation power. The diagram shows that ROC increases almost linearly with the increasing total actuation power.

Ideally, the micromirror ROC should be constant throughout the static or dynamic scanning motion. Therefore, for a constant micromirror ROC during the actuation, only a singular layer of silicon should be chosen for the microscanner with the trade-off for a reduced reflectivity. The diagram of Figure 6.18 also includes the FEM simulated micromirror ROC. By comparison, the estimation only shows increment of 3 mm which is much less than the measured value. Since the deformation magnitude of a bimorph structure is dependent on the average temperature. This indicates that the average temperature of the micromirror is higher than the simulated value to result in such a mechanical discrepancy. One possible reason is that the thermal conductivity of the highly doped silicon material of the connecting spring and frame is higher than the reported value cited from literature.

6.4.1.3 Vertical offset between movable and fixed combs

During the actuation of both electrothermal actuators, the movable combs of electrostatic comb-drives are lifted up at the end connected to micromirror.

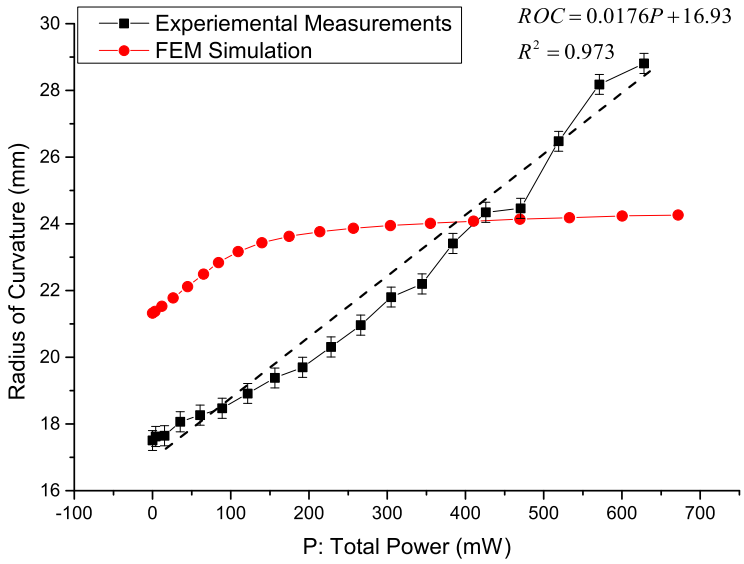

Figure 6.18: The measured and simulated radius of curvature of micromirror of the hybrid actuated microscanner as a function of the total actuation power of both electrothermal actuators (ambient laboratory temperature is 20 ^{o}C).

Figure 6.19a and Figure 6.19b display surface profiles of the electrostatic comb-drives when two electrothermal actuators are driven at a total voltage of 0 V and 36 V (628 mW) respectively. When there is no electrothermal actuation, the torsion bar of the movable combs deflects by around 5 μm (which is the same as the simulation in Figure 6.10b). The vertical level of movable combs increases with the increasing actuation of electrothermal actuators. At 36 V total actuation voltage, the vertical deflection of the torsion bar increases to around 32 μm. Besides, noted in Figure 6.19a, ROC of the torsion bar measured using white light interferometer is around 76.5 mm when there is no actuation, and it is reducing to around 10 mm when electrothermal actuators at driven at 36 V (Figure 6.19b). This measurement indicates that the $748 \times 10 \times 10$ μm^3 (length$\times$width$\times$thickness) torsion bar experiences bending deformation by a tip deflection of 27 μm during electrothermal actuation. As analysed in Section 6.2.5, the spring constant or the stiffness of a bending torsion bar increases almost linearly with the vertical deflection. Since the micromirror also rotates about this torsion bar during electrostatic actuation, this stiffness changes will affect the resonant rotation of the microscanner. The effect of this bending torsion bar, caused by electrothermal actuation, to the dynamic rotation will be characterised in the following subsection.

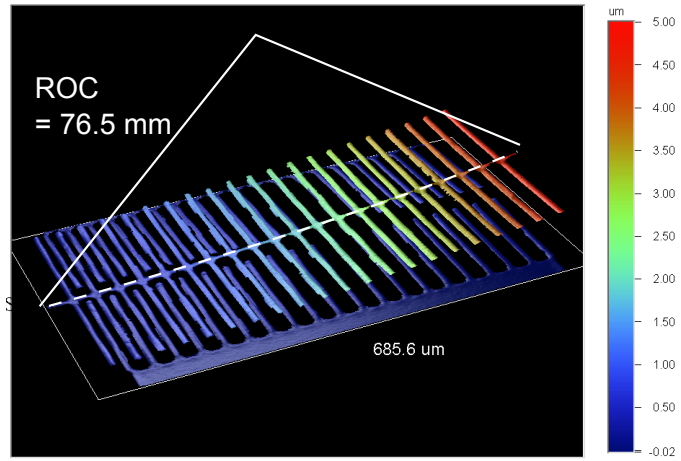

(a)

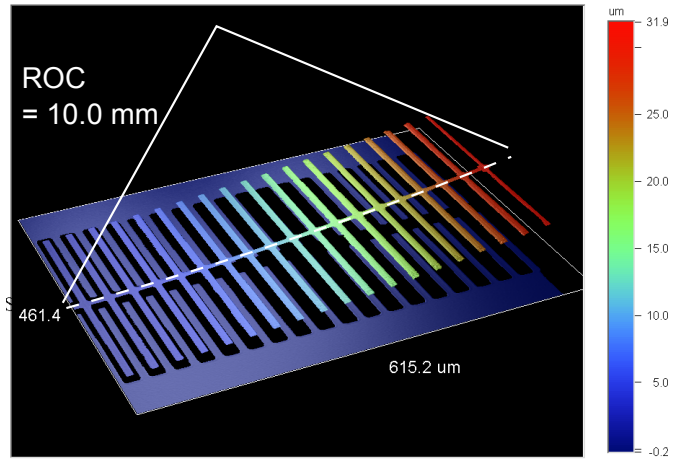

(b)

Figure 6.19: Surface profile measurement of the electrostatic comb-drives of microscanner when electrothermal actuators are applied with 0 V (a) and 36 V (b) in total.

6.4.2 Electrostatic actuation

Electrostatic actuation is performed by supplying an AC voltage signal to any pair of comb-drives, for example, through electrical pads 3-4, 4-5, or 3-5; in Figure 6.20, electrostatic actuation through electrical pads 3-4 is illustrated. During the actuation, a protective resistor of 10 kΩ is connected in series with electrostatic comb-drives in case of failure of pull-in between movable and fixed combs; a non-offset sinusoidal voltage signal was used to excite the Y-axis rotation of the microscanner. The resonant rotating mode of microscanner can be excited when the applied AC voltage signal (V_{ac}) carries its mechanical resonant frequency.

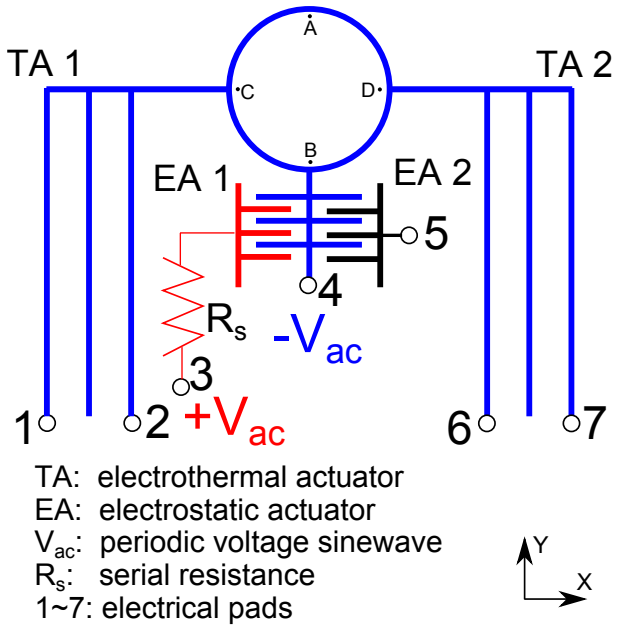

Figure 6.20: The scheme diagram of actuation through the electrostatic comb-drives of microscanner.

6.4.2.1 Resonant frequencies

In order to monitor the magnitude of dynamic rotation of microscanner with the increasing or decreasing frequency of the input signal V_{ac} for electrostatic comb-drives, the velocities of three locations have been measured using a Doppler laser vibrometer. As indicated in Figure 6.11b, point A is located on the free end of micromirror, and points C and D locate on the micromirror rim next to the springs. The frequency of a non-offset sinusoidal voltage signal with 120 V (peak-to-peak) is increased (or upsweeping frequencies) from 300 Hz to 900 Hz with each frequency maintained for 1 second.

The dynamic response has been characterised by measuring the peak velocity of points A, B and C in the vertical (Z-axis) direction of vibration. Since, it is the torque excites the rotation of the comb-drives, as described in Equation (6.2.3), the generated torque of the comb-drives is independent from the polarity of input signal V. Therefore, the response vibrating frequency of microscanner is 2 times the input frequency of the non-offset actuating sinewave. Also, only the peak velocity and response frequency of rotating frequency are characterised; the phase difference between the actuating

sinewave and the measured velocity signal are not discussed here. In Figure 6.21, at 686 Hz mechanical response frequency, all measured points on micromirror rim (A, C and D) have local peak values at its driving frequency. The peak velocity of point A at 686 Hz is 38.7 mm/s, whereas, the ones of points C and D are 28.1 mm/s (or -27.4% less) and 22.6 mm/s (or -41.6% less), respectively. This indicates that, at 686 Hz, the microscanner is vibrating resonantly with the maximum vertical displacement at the free end. Compared to the FEM modal analysis results in Figure 6.11, the estimated resonant frequency for this mode shape is 692 Hz which is 6 Hz higher than measured resonant frequency. Similar responses of the three points happen frequency of 1376 Hz. At this frequency, point A has a peak response of 56.8 mm/s, whereas points C and D have peak magnitude of 32.5 mm/s (-42.3%) and 35.3 mm/s (-37.8% less) respectively. Besides, this resonant motion at 1376 Hz, which frequency is 2 times higher than the resonant vibration motion measured at 686 Hz, the superharmonic vibration mode [21].

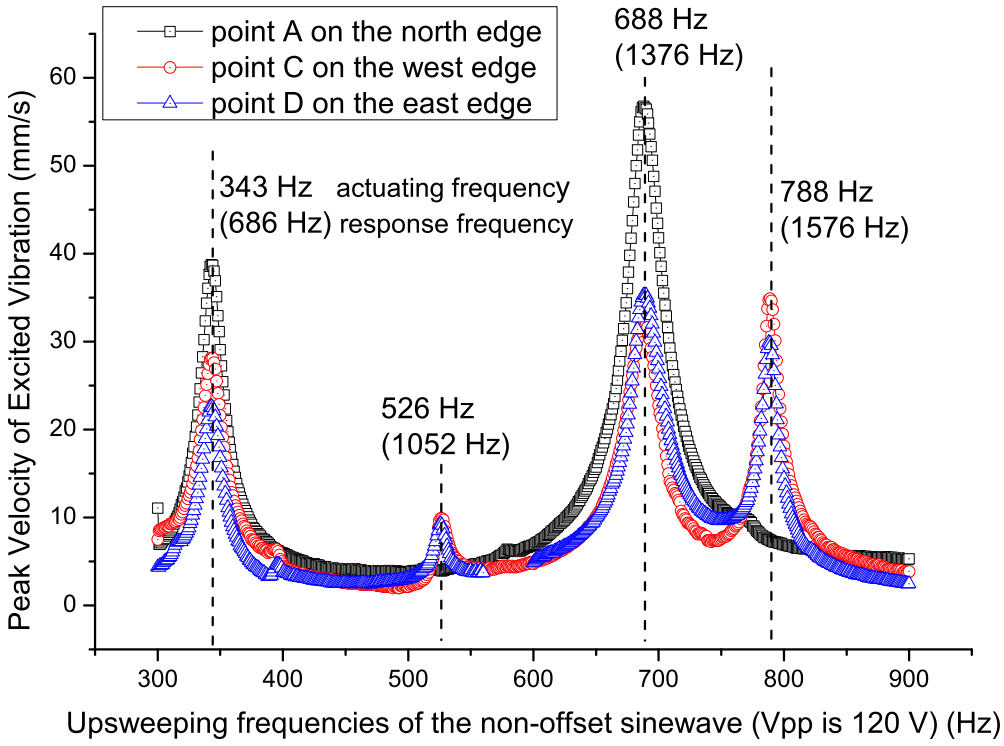

Figure 6.21: The velocity of the measured points on the edge of the micromirror responding to an upsweeping, non-offset sinewave with peak-to-peak value of 120 V.

There is no local peak value measured on point A from 500 Hz to 550 Hz as shown

in Figure 6.21. However, the local peak values at 526 Hz actuating frequency or at 1052 Hz of mechanical response frequency is 9.9 mm/s for point B and is 9.3 mm/s for point C, which is at least 59% smaller than other local peak values. Since the amplitude is small, and it is not expected in the FEM simulation either, this resonance is ignored during the characterisation and analysis.

At measured response frequency of 1576 Hz, there is no local peak response between 750 Hz and 850 Hz on the measuring point A; however, both points C and D have local peak responses of 35 mm/s and 30 mm/s at this frequency. Therefore, at this resonant mode, point A does not have vertical displacement measured, and point C and D have almost equal displacement. This indicates the resonant motion is the rotation of micromirror about its torsion bar. Compared to the FEM simulation, the estimated resonant frequency for the mode shape is 1613 Hz, which is 37 Hz higher than measured resonant frequency. Since the rotational mode is the resonant mode utilised for the fast line-scan of 2D scanning pattern of microscanner, the behaviour of this rotational mode will be mainly characterised in this section.

6.4.2.2 Dynamic response with no electrothermal actuation

When microscanner is resonantly rotating about Y-axis at 1576 Hz, the maximum displacement on micromirror edge is observed at two symmetric points: C and D. The dynamic angles of microscanner excited by tuning frequencies and amplitudes of the actuating signal were characterised by measuring the peak velocity of one of the two points. Then, the optical scan angles can be calculated from velocity measurements using the following equation:

$$\theta = 4arctan(\frac{\frac{V_{max}}{2\pi f}}{d}) \tag{6.4.1}$$

where,

θ is the optical scan angle of microscanner;

V_{max} is the peak velocity of the measured point while the microscanner is excited

at frequency f;

f is the response frequency of microscanner;

and d is the distance between the measured point and the rotational centre which is 0.6 mm for the microscanner.

Figure 6.22 shows Y-axis optical scan angles of microscanner when the driving signal frequency is sweeping between 760 Hz and 820 Hz. As shown in the diagram, the maximum optical scan angle increases from 1.3^{o} to 4.5^{o} when the peak-to-peak amplitude of driving signal is increased from 120 V to 320 V. Each trajectory at a certain sinusoidal voltage level shows linear dynamic response indicating a linear spring constant during the Y-axis rotation of microscanner [22]. However, the resonant frequency of the maximum optical scan angle shifts to a higher value when the actuating sinusoidal voltage is increasing. This frequency shifting phenomena due to the increasing driving voltage indicates that the torsional bar of the rotating microscanner has been stiffened [3]. Since the actuating sinewave is non-offset or non-biased, the spring constant of the rotating microscanner has not been stiffened by the biased voltage [23]. When driven at a higher sinusoidal peak-to-peak voltage, higher deflection will result in an change in the length of the torsion bar [23], which can results in spring stiffening [4]. Next paragraph will show the magnitude of the frequency shift. Beyond 320 V, the in-plane attracting force between the electrodes are significant to cause a non-stable rotation motion and then the 'pull-in' failure of electrostatic comb-drives (which is the contact between electrodes).

To compare the repeatability of resonant Y-axis rotation of the microscanner when the driving frequency is upsweeping (increasing) and downsweeping (decreasing), the maximum optical scan angles and the corresponding resonant frequencies are extracted from the measurements and are plotted against the peak-to-peak voltage amplitude of the driving signal in Figure 6.23. In the left diagram of Figure 6.23, optical scan angles are consistent between upsweeping and downsweeping actuating frequencies. The resonant optical scan angle increases linearly, by a rate of 0.02 ^{o}/V, when the

[3] the angular frequency ω_r is $\sqrt{k/I}$

[4] the effective torsion stiffness k_t is proportional to wt^3/l, where w, t and l are the width, thickness and the length of the torsion bar respectively [24, 25]

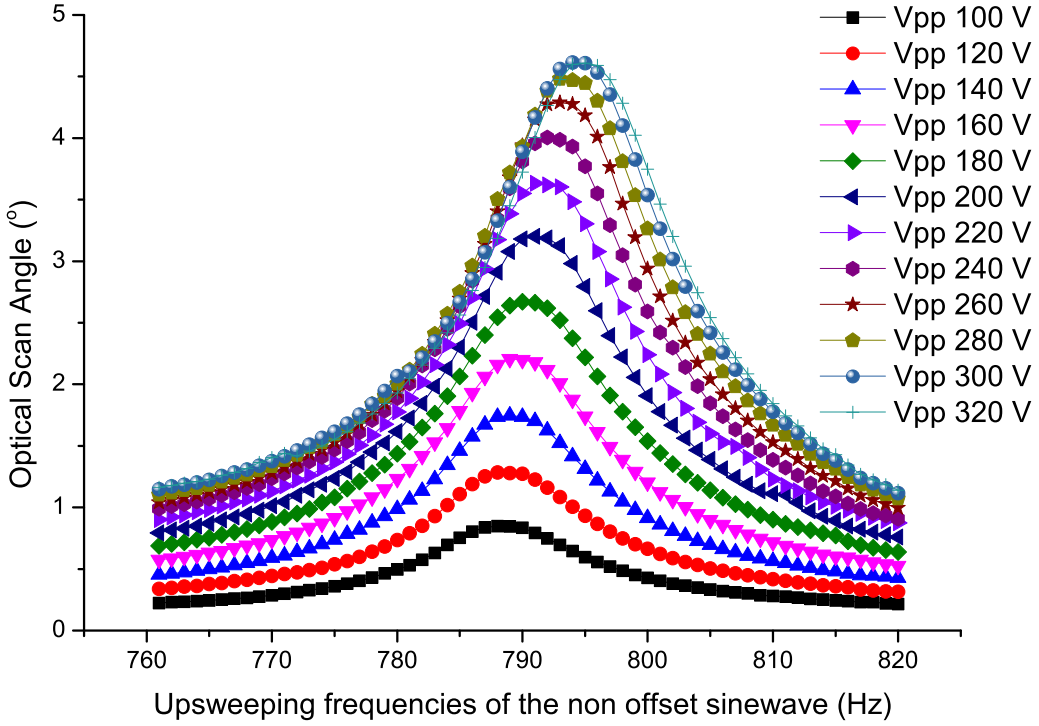

(a) Upsweeping frequencies.

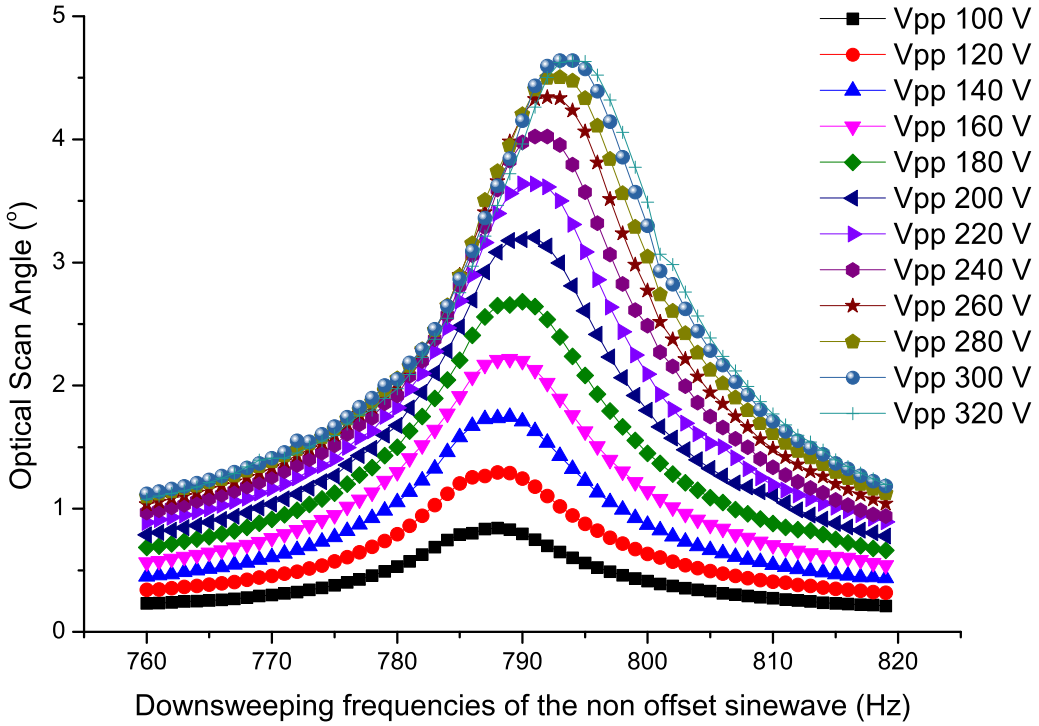

(b) Downsweeping frequencies.

Figure 6.22: Optical scan angle as a function of sweeping frequencies of non-offset sinewave at different peak-to-peak voltage value.

peak-to-peak voltage level has increased from 100 V to 260 V. This linear relationship begins to fail as the driving voltage amplitude is increased above 260 V. The right diagram in Figure 6.23 plots the response frequencies of the maximum optical scan angles as a function of increasing driving signal amplitude. It can be seen that the response resonant frequencies of microscanner are consistent for both the upsweeping and downsweeping actuating sinewaves. Besides, the resonant frequency shifts linearly from 1576 Hz to 1590 Hz at a rate of ∼0.03 Hz/V, as the peak-to-peak voltage level is increasing.

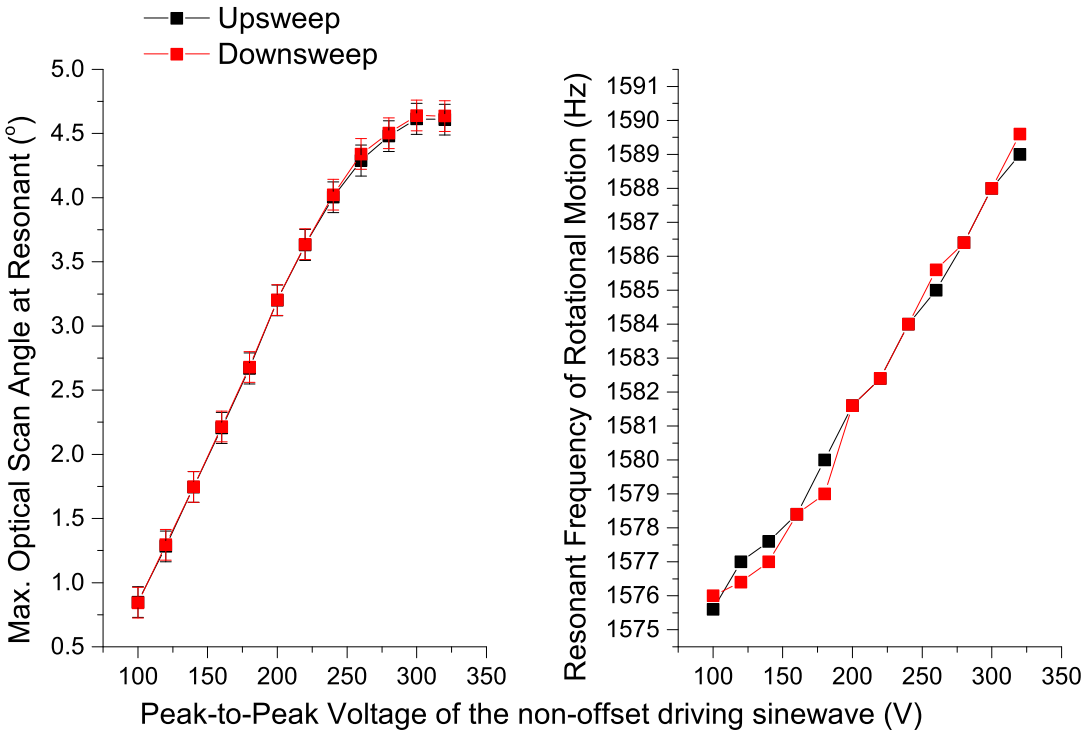

Figure 6.23: The maximum optical scan angles and corresponding resonant frequencies of microscanner driven by electrostatic actuation only.

6.4.2.3 Dynamic response with electrothermal actuation

As the study reported in [26], the motion amplitude of a comb-drive actuated microscanner at resonance is dependent on the vertical offset between the movable and the fixed combs. In subsection 6.4.1, the surface profile measurements have showed that the overall vertical offset between movable and fixed combs and the

curvature of connecting torsion bar increase with the increasing out-of-plane actuation of the electrothermal actuators. Therefore, the effect of electrothermal actuation to the amplitudes and the resonant frequencies of electrostatically-driven scan angles are characterised using a Doppler laser vibrometer.

During the measurements, both electrothermal actuators are driven by DC voltage level, V_{dc}, varying from 0 V to 16 V; at each electrothermal actuation level, the electrostatic comb-drives are driven by a non-offset sinewave (V_{ac}) with peak-to-peak voltage amplitude increases from 120 V to 320 V, through electrical pads 3-4, as displayed in Figure 6.24. At each electrothermal actuation level, the dynamic response of microscanner at resonance is obtained from the velocity of point C on the micromirror using Equation (6.4.1). Due to the limited microscope aperture size of Doppler laser vibrometer, the maximum measurable optical scan angle of microscanner is around 20°. Scan data beyond the vibrometer measurable limitation is calculated from the scan length of a reflected laser spot using setup in Figure 5.7.

Figure 6.25 demonstrates the maximum optical scan angles about the Y-axis and the corresponding resonant frequencies of microscanner when driven both electrothermal actuators. When both electrothermal actuators are driven at voltage level increasing from 2 V to 10 V, the vertical offset between electrodes increases. As shown in Figure 6.25a, the maximum optical scan angles increase with increasing vertical offset between combs. Beyond total power of 266 mW or 10 V per electrothermal actuator, the magnitude of resonant optical scan angles appear to be saturated and does not increase as the electrothermal actuation level increases.

In Figure 6.25b, the response resonant frequencies at each electrothermal actuation level are plotted against the electrostatic actuation amplitude. From the simulation described early in Section 6.2.5, the spring constant of a torsion bar remains a constant during rotation deformation. In corresponding with the simulated results, each line of the resonant frequencies of microscanner in Figure 6.25b has small changes (at most 5 Hz) at the same electrothermal actuation level. However, as the increasing electrothermal actuation, the resonant frequencies of microscanner increase

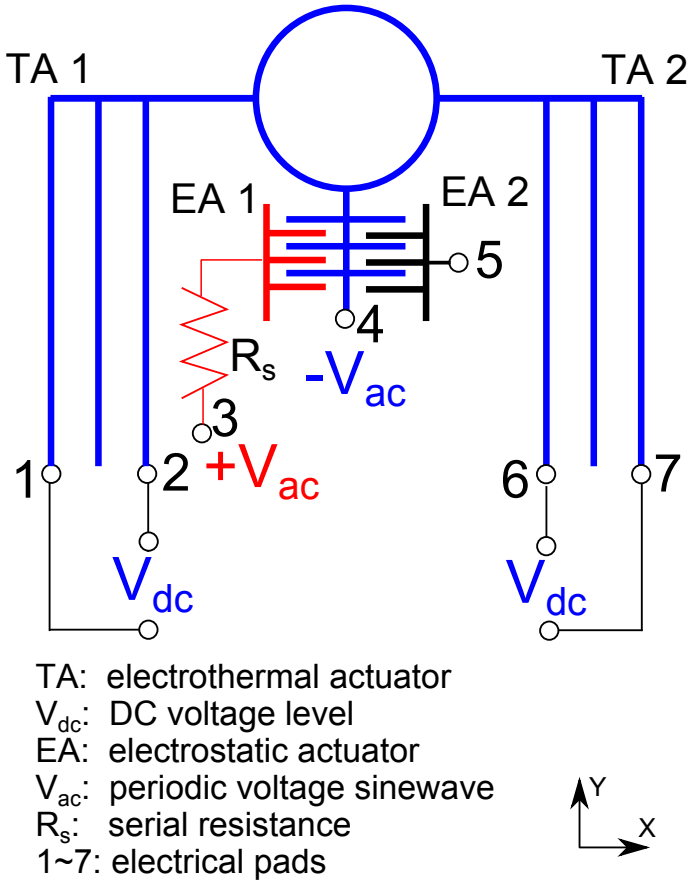

Figure 6.24: The scheme diagram of actuating both electrothermal and electrostatic actuators of the hybrid actuated microscanner.

nonlinearly. This resonant frequency of the rotating microscanner rotational mode is analysed by plotting resonant frequencies driven by 200 V peak-to-peak voltage non-offset sinewave as a function of electrothermal actuation level in Figure 6.26. In the diagram, the resonant frequency of the Y-axis rotating mode of microscanner increases nonlinearly from 1576 Hz to 1696 Hz when the electrothermal actuation power is increased from 0 mW to 520 mW. This is because of the structure stiffening during the electrothermal actuation; in particular the stiffness of torsion bar increases with the bending magnitude as simulated earlier in Section 6.2.5. In Figure 6.26, variations of the maximum optical scan angles and the corresponding resonant frequencies are plotted as a function of the electrothermal actuation power. The maximum optical scan angle first increases as electrothermal actuation power is increased from 0 mW to 266 mW; however, after 266 mW or 10 V per electrothermal actuator, the maximum optical scan angle starts to reduce by 10% with increasing

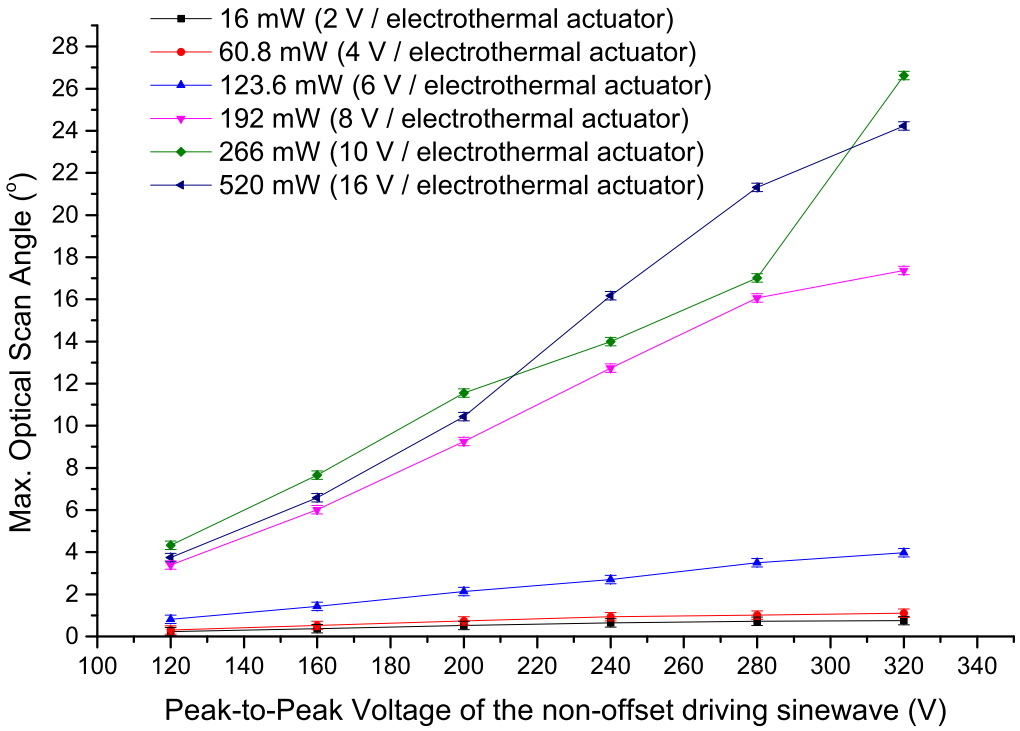

(a)

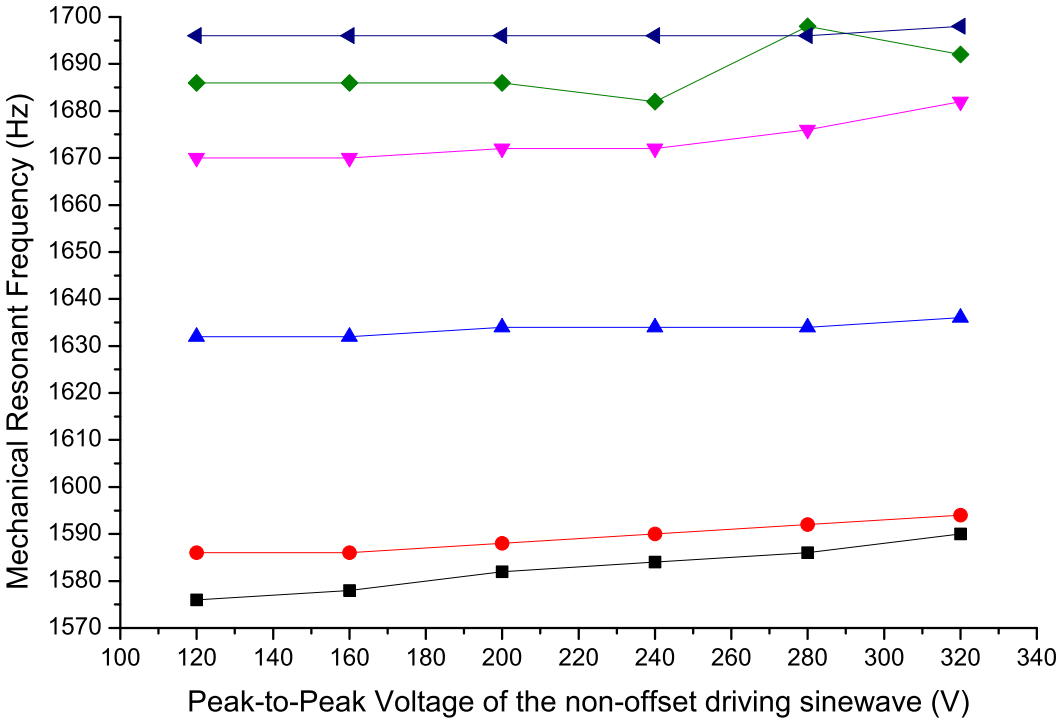

(b)

Figure 6.25: The maximum optical scan angles (a) and the corresponding resonant frequency (b) of microscanner as a function of driving signal for by electrostatic comb-drives while both electrothermal actuators are driven equally.

electrothermal actuation level.

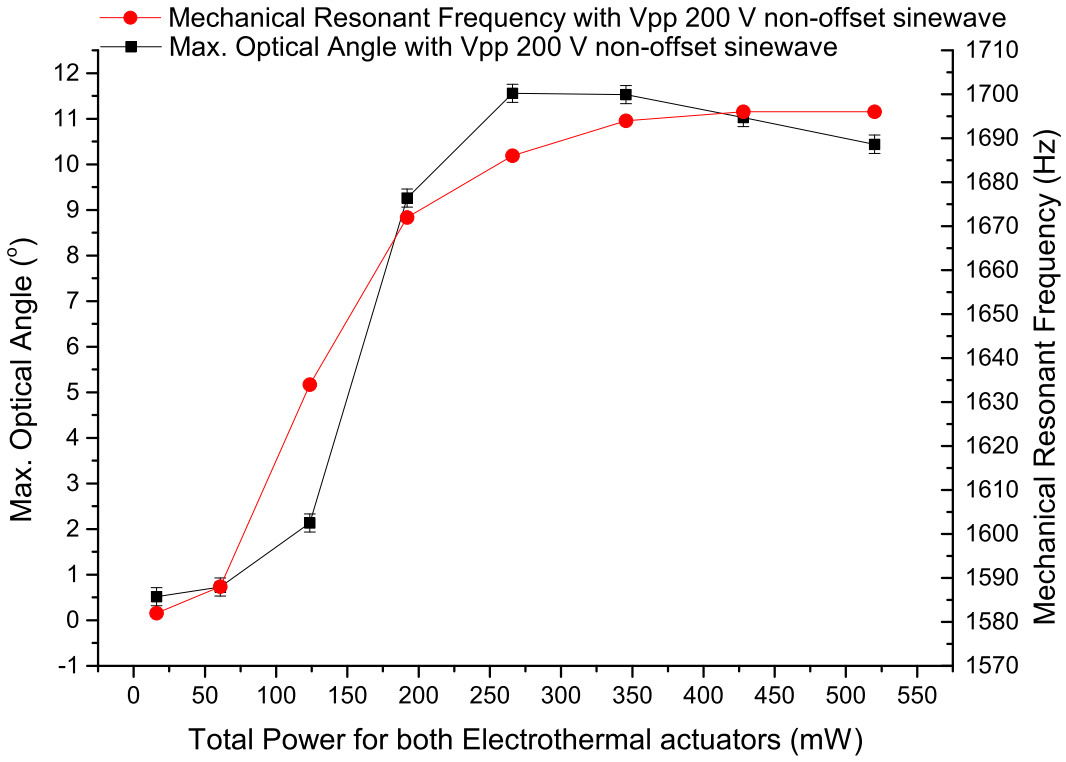

Figure 6.26: The maximum optical scan angle and the mechanical resonant frequencies of the microscanner as a function of the total actuation power of two electrothermal actuators when electrostatic comb-drives are driven by a 200 V peak-to-peak non-offset sinewave.

6.4.3 2D raster scan pattern

Having characterised optical tilt and scan angles of microscanner in two orthogonal scanning axes, a 2D raster scan pattern is demonstrated using a reflected laser spot as the experimental setup shown in Figure 5.7 of Section 5.4 on page 140.

As illustrated in Figure 6.27, two electrical voltage waveforms, the sinewave (V_{ac}) and the staircase (V_{dc}), are programmed using National Instruments LabView software and are generated using Data Acquisition (DAQ) devices. The staircase voltage signal is applied to both electrothermal actuators through electrical pads 1-2 and 6-7 with the maximum magnitude of 18 V; each step of the staircase signal has a duration time τ. The sinewave voltage signal is applied to electrostatic comb-drives through

electrical pads 3-4. The two waveforms are programmed to be in synchronisation such that, within the duration of each step of staircase signal, the sinewave V_{ac} with unique amplitude and frequency is generated.

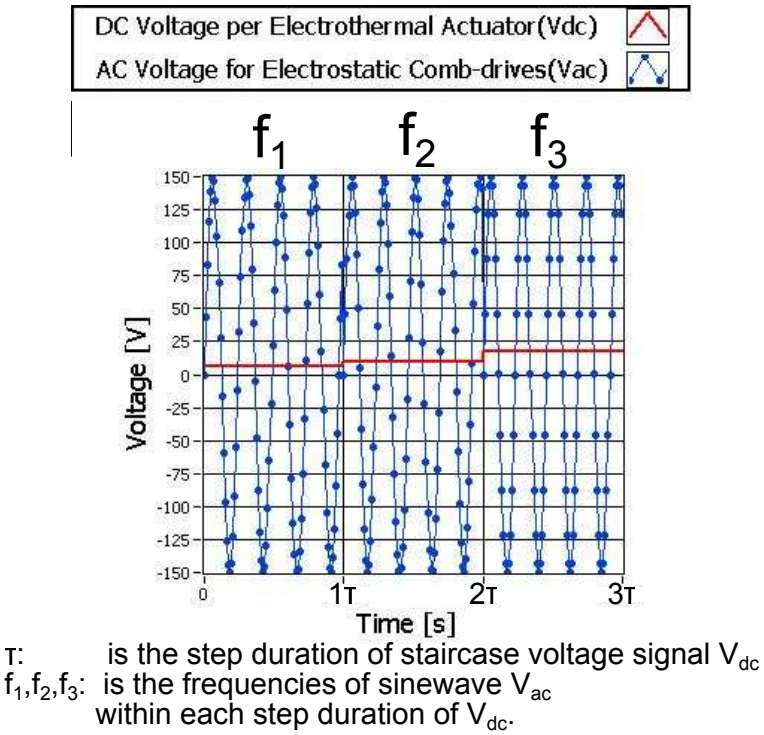

Figure 6.27: Illustration of the two synchronised actuation voltage signals, V_{ac} and V_{dc}, for electrostatic comb-drives and electrothermal actuators respectively.

As summarised in the last section, magnitudes of the maximum scan angles excited resonantly by electrostatic comb-drives increase with increasing vertical offset between movable and fixed combs, or with increasing the electrothermal actuation level. It can be expected that the scanning lines of a 2D scanning pattern have different lengths when micromirror is tilted by both electrothermal actuators.

First, the frequencies of sinewave signal V_{ac} within each step of staircase signal V_{dc} are tuned at resonance so that the maximum optical scan angles are obtained. In Figure 6.28, due to the curvature of micromirror, only three scanning lines are displayed. Three steps at 6 V, 10 V and 18 V have been chosen for the staircase signal V_{dc} with 0.2 s duration of each step to obtain three distinguishable scanning lines; the peak-to-peak voltage of V_{ac} held constant at 300 V and the frequencies are 1656 Hz, 1742 Hz and 1760 Hz for each step of V_{dc}. Another sample of microscanner (different

to the one used for characterisation) was used to demonstrate the 2D scanning pattern, therefore the resonant frequencies demonstrated were different. As the 2D scanning pattern demonstrated in Figure 6.28a, at 6 V per electrothermal actuator, the maximum optical scan angle of microscanner is 10°; at 18 V per electrothermal actuator, the maximum optical scan angle is around 26°. The translation of scanning lines in the orthogonal direction on the screen indicates the microscanner tilts by around 7° when both electrothermal actuators are driven from 6 V to 18 V.

Moreover, optical scan angles caused by electrostatic comb-drives are also dependent on voltage amplitude and frequency of the driving signal. The resonant frequency of microscanner is shifted by 120 Hz when electrothermal actuators are driven to the maximum; and the resonant response bandwidth at each electrothermal actuation level microscanner is much smaller than 120 Hz. Therefore, tuning the voltage of electrostatic comb-drive actuating signal cannot be achieved for the microscanner design.

In order to obtain a rectangular shape 2D raster scan pattern, the frequency of electrostatic comb-drives' actuating sinewave V_{ac} is tuned accordingly for each electrothermal actuation level so that each fast scanning line has the same length on the measuring screen. As demonstrated in Figure 6.28b, the frequencies of V_{ac} are changed to 1656 Hz, 1718 Hz and 1732 Hz for each step of V_{dc}. In this way, a 7° × 10° rectangular shape 2D raster scan pattern has been obtained by tuning the frequency of comb-drive actuating signal.

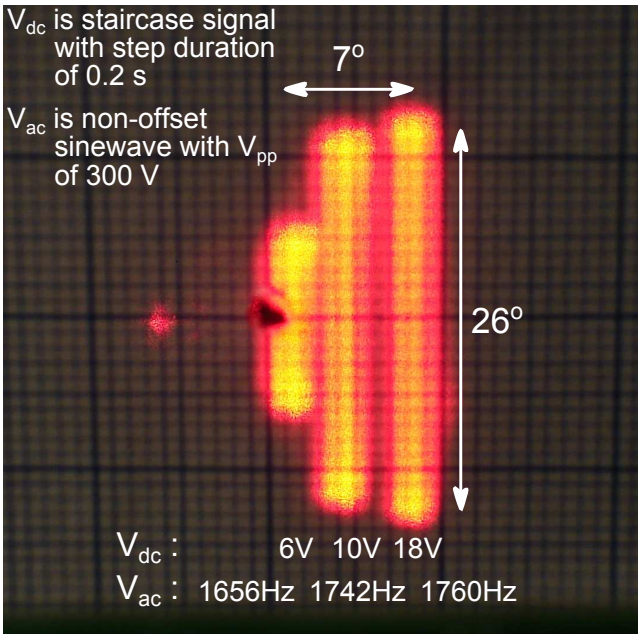

(a)

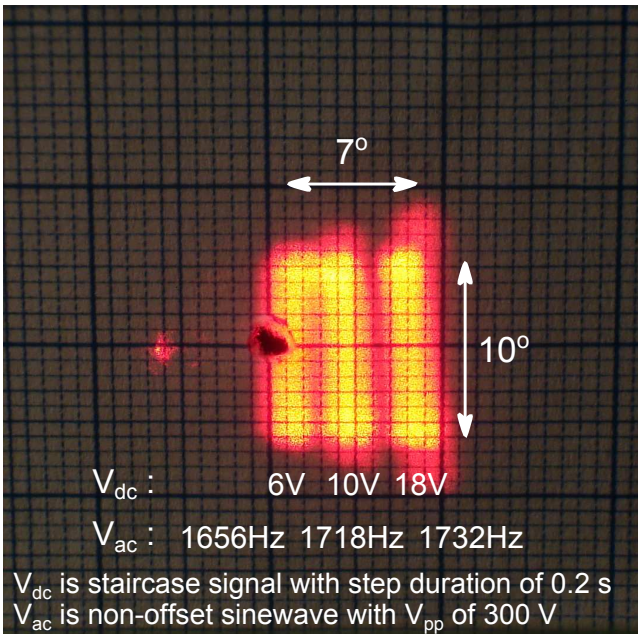

(b)

Figure 6.28: The 2D scanning pattern of microscanner when screen is 60 mm away from microscanner (the reflected laser spot is around 2 mm in diameter).

6.5 Discussion

By analysing and optimising from the case study of a previously microscanner, the characterised results of an optimised hybrid-actuated 2D scanning micromirror show that the maximum optical tilt angle by electrothermal actuators is around 47%

higher than the case study result; and the maximum achievable optical scan angle by electrostatic actuators (including the ones coupled actuated with electrothermal actuation) is around 190% higher. This is not only because that the micromirror diameter of optimised microscanner design is reduced by -41% than the one shown in the case study, but also because that connection between electrostatic comb-drives and micromirror allows the vertical offset of electrodes of comb-drives increase with increasing electrothermal actuation. By increasing the offset between the movable and the fixed combs, its capacitance tunable range has also increased when the movable combs are rotating about the torsion bar. Then, a stable rectangular shape raster scan pattern is produced by driving the electrothermal and electrostatic actuators using two synchronised signals.

Despite the improved microscanner design, there are four limitations about this structure. Firstly, the tilting motion of this microscanner, caused by the electrothermal actuators, does not tilt about an axis passing through the centroid of micromirror; or in the other words, the micromirror is lifted up by electrothermal actuation with centroid of which is constantly displacing during the tilting motion. In order to have a micromirror rotating with a fixed centroid, the actuator arrangement should be symmetric. Secondly, the magnitude of electrostatic driving optical scan angle and its resonant frequency are dependent on the electrothermal actuation or, more precisely, on the relative vertical offset between the two electrodes and torsion bar stiffness changed by electrothermal actuation. These resonant frequencies of the microscanners rotational motion shift with the electrothermal actuation level due to the torsion bar stiffening as bending. The rotating frequency shifting during electrothermal actuation is over 100 Hz which limits the voltage tuning of the fast line-scan in 2D scanning patterns. Thirdly, the ROC of micromirror surface is about 17 mm at room temperature of 20^{o}C after coating a 0.65 μm thick gold layer on top of silicon layer. The curvature of bimorph micromirror is sensitive to temperature and is changed by 65% during electrothermal actuation. Therefore, although the optical reflectivity can be improved by the gold coating, the mechanical performance of resulting bimorph structure is prone to change because of the temperature change by heat conduction from the

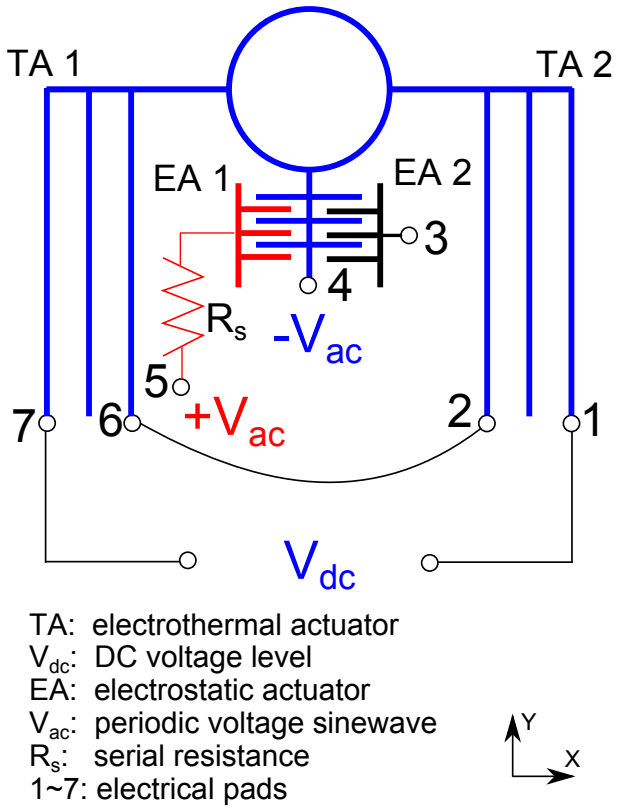

Figure 6.29: The scheme diagram of actuating both electrothermal and electrostatic actuators of the hybrid actuated microscanner with two electrothermal actuators electrically connected in series.

electrothermal actuators. Fourthly, the gold coated silicon micromirror has a reduced electrical resistance when compared to a single layer silicon micromirror of the same dimensions. During synchronised actuation of electrostatic and electrothermal actuators, two electrothermal actuators cannot be electrically connected in series. If two electrothermal actuators of this hybrid microscanner are electrical connected in series as shown in Figure 6.29, during electrostatic actuation through pads 3-4, current passes through the bimorph micromirror as well as through the spring and section of frame. The spring and part of the frame between electrical pads 3-4 can be burnt due to this operation, causing irreversible damage and changing the resonant frequency of microscanner permanently. Besides, micromirror temperature rises due to the heat conducted from spring and frame results in the surface flattening.

Apart from these performance limitations, the simulated mechanical and thermal performances are about 160% higher than the characterised mechanical and empirical

thermal data. This large difference is believed to be caused by the applied material property of thermal conductivity and the applied convective coefficient. First, the thermal conductivity of single-crystal-silicon is doping level dependent [27, 28]. Because of the lack of thermal conductivity characterisation facility, the thermal conductivity of non-doped, pure single-crystal-silicon reported in the literature are applied in the device FEM model. Second, the air convective coefficient could account for 75% of total heat dissipation [19]. In the presented electro-thermo-mechanical analysis, the free air convective coefficient of 10 $Wm^{-2}K$ was applied. However, M. Guvench and J. Crosby [29] have reported air convective coefficients of 170 $Wm^{-2}K$ for the top surfaces and 85 $Wm^{-2}K$ for the bottom and side surfaces of an silicon in-plane electrothermal actuator during their electro-thermo-mechanical analysis. Since there is a trench under the hybrid-actuated microscanner, the assumptions of convective coefficients of the surfaces of our microscanner model of doped silicon were modified to be 250 $Wm^{-2}K$. After reran the FEM simulation of the microscanner, the maximum temperature, when two electrothermal actuators were both actuated at 18 V, was as high as 1012 ^{o}C. With further modified the assumption of thermal conductivity to increase by around 3.2 times, the electro-thermo-mechanical analysis of electrothermally-actuated microscanner model was rerun. The estimated optical tilt angles, as plotted in Figure 6.30, has increased linearly with the actuation level of two electrothermal actuator but still had difference to the measured results by 20% when actuated at the maximum voltage. The maximum temperature of electrothermal actuators of the microscanner model was estimated to be 730 ^{o}C as displayed in Figure 6.31 from the modified analysis.

The dynamic actuation of this microscanner around its resonant frequency can be excited through one pair of electrostatic comb-drives. The other pair of electrothermal comb-drives has the option of being used as a capacitance sensor to feedback the dynamic rotation amplitude of microscanner and even as a phase shift sensor [30, 31, 32, 33].

Since this hybrid-actuated 2D microscanner is designed to be fabricated using commercial multi-users MEMS processes (SOIMUMPs provided by MEMSCAP

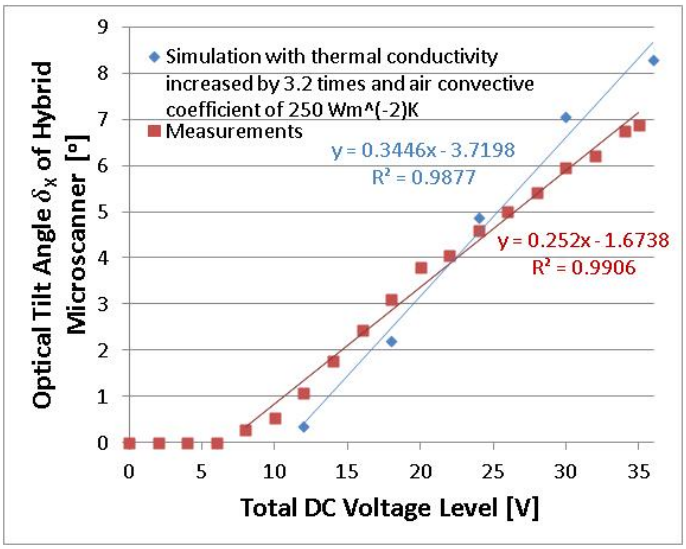

(a)

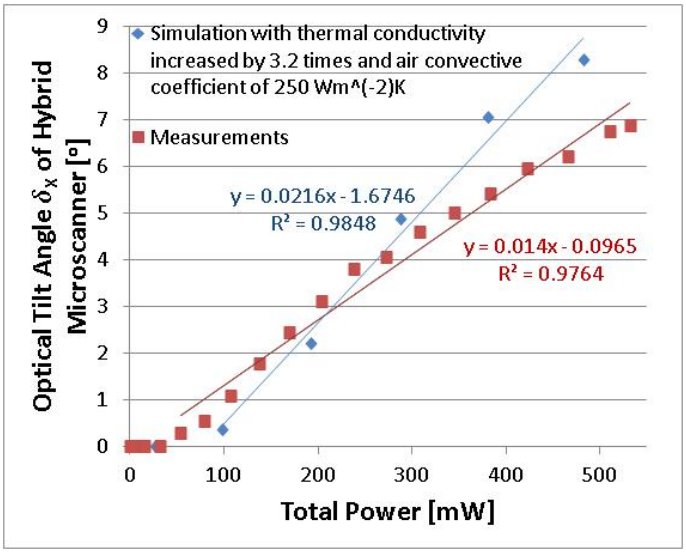

(b)

Figure 6.30: FEM simulation of optical scan angles of hybrid-actuated 2D microscanner with silicon surface convective coefficient of 250 $Wm^{-2}K$ and increased thermal conductivity.

Inc.), several limitation and trade-offs need to be considered. First, because the actuators, connections and micromirror are patterned within a phosphorous doped single-crystal-silicon layer, the thickness is the same for all parts of microscanner. Usually, the electrostatic comb-drives and the micromirror are fabricated in thicker silicon, i.e. 60 μm [34], or maintain substrate attached to back of the micromirror [35], in order to generate large torque and surface flatness respectively. The geometric design of flexure connection and electrothermal actuators are preferable for a thinner

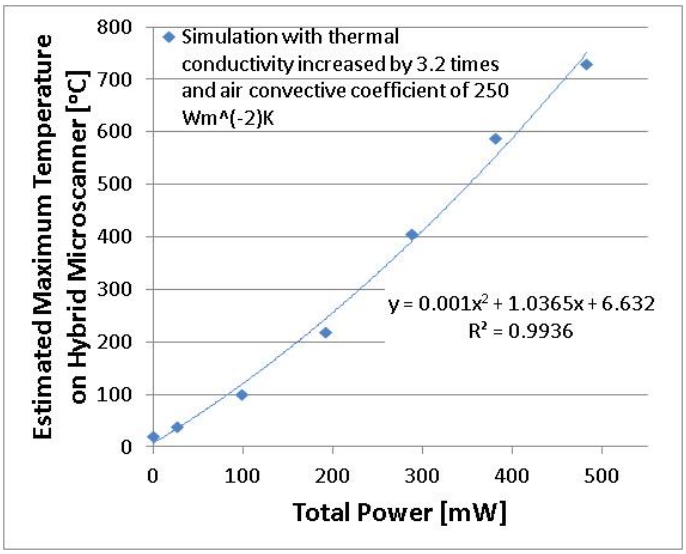

Figure 6.31: The FEM simulation of maximum temperature of microscanner with silicon surface convective coefficient of 250 $Wm^{-2}K$ and increased thermal conductivity.

structure for a higher displacement and bending. Besides, due to the same material for all parts of microscanner, the electrical and thermal isolations between the actuators and the micromirror are not ideal. There is limited thermal isolation between electrothermal actuators and micromirror which is presented as the ROC variation of the micromirror during the electrothermal actuation.

References

[1] L. Li, V. Stankovic, L. Stankovic, L. Li, S. Cheng, and D. Uttamchandani, "Single pixel optical imaging using a scanning MEMS mirror," *Journal of Micromechanics and Microengineering*, vol. 21, no. 2, p. 025022, 2011.

[2] R. Bauer, G. Brown, and D. Uttamchandani, "Comparison of the curvature homogeneity and dynamic behaviour of framed and frameless electrostatic X/Y scanning micromirrors," *Micro Nano Letters, IET*, vol. 6, pp. 425 –428, june 2011.

[3] R. Bauer, W. Lubeigt, and D. Uttamchandani, "Dual Q-switched laser outputs

from a single lasing medium using an intracavity MEMS micromirror array," *Opt. Lett.*, vol. 37, pp. 3567–3569, Sep. 2012.

[4] L. Li and D. Uttamchandani, "Dynamic response modelling and characterization of a vertical electrothermal actuator," *Journal of Micromechanics and Microengineering*, vol. 19, no. 7, p. 075014, 2009.

[5] A. Alwan and N. Aluru, "Analysis of hybrid electrothermomechanical microactuators with integrated electrothermal and electrostatic actuation," *Journal of Microelectromechanical Systems*, vol. 18, pp. 1126 –1136, Oct. 2009.

[6] G. Brown, L. Li, R. Bauer, J. Liu, and D. Uttamchandani, "A two-axis hybrid MEMS scanner incorporating electrothermal and electrostatic actuators," in *Optical MEMS and Nanophotonics (OPT MEMS), 2010 International Conference on*, pp. 115 –116, Aug. 2010.

[7] K. Koh and C. Lee, "A two-dimensional MEMS scanning mirror using hybrid actuation mechanisms with low operation voltage," *Journal of Microelectromechanical Systems*, vol. 21, no. 5, pp. 1124–1135, 2012.

[8] A. Cowen, G. Hames, D. Monk, S. Wilcenski, and B. Hardy, *SOIMUMPs Design Handbook*. MEMSCAP Inc., Revison 8.0 ed. http://www.memscap.com/products/mumps/soimumps/reference-material.

[9] P. W. Chapman, O. N. Tufte, J. D. Zook, and D. Long, "Electrical properties of heavily doped silicon," *Journal of Applied Physics*, vol. 34, pp. 3291 –3295, Nov. 1963.

[10] Y. K. Hong and R. Syms, "Dynamic response modeling of MEMS micromirror corner cube reflectors with angular vertical combdrives," *Journal of Lightwave Technology*, vol. 25, pp. 472 –480, Feb. 2007.

[11] W. T. Thomson and M. D. Dahleh, *Theory of Vibration With Applications*. MEMS REFERENCE SHELF, Englewood Cliffs: NJ: Prentice-Hall, 5th ed ed., 1998.

[12] J. Yao, "RF MEMS from a device perspective," *Journal of Micromechanics and Microengineering*, vol. 10, pp. R9–R38, Dec. 2000.

[13] D. Hah, P. Patterson, H. Nguyen, H. Toshiyoshi, and M. Wu, "Theory and experiments of angular vertical comb-drive actuators for scanning micromirrors," *IEEE Journal of Selected Topics in Quantum Electronics*, vol. 10, pp. 505 – 513, May-Jun. 2004.

[14] J. Singh, J. H. S. Teo, Y. Xu, C. S. Premachandran, N. Chen, R. Kotlanka, M. Olivo, and C. J. R. Sheppard, "A two axes scanning SOI mems micromirror for endoscopic bioimaging," *Journal of Micromechanics and Microengineering*, vol. 18, no. 2, p. 025001, 2008.

[15] S.-H. Tsang, D. Sameoto, and M. Parameswaran, "Out-of-plane electrothermal actuators in silicon-on-insulator technology," *Electrical and Computer Engineering, Canadian Journal of*, vol. 31, no. 2, pp. 97 –103, 2006.

[16] G. Barillaro, A. Molfese, A. Nannini, and F. Pieri, "Analysis, simulation and relative performances of two kinds of serpentine springs," *Journal of Micromechanics and Microengineering*, vol. 15, no. 4, p. 736, 2005.

[17] D. C. Miller, B. L. Boyce, M. T. Dugger, T. E. Buchheit, and K. Gall, "Characteristics of a commercially available silicon-on-insulator MEMS material," *Sensors and Actuators A: Physical*, vol. 138, no. 1, pp. 130 – 144, 2007.

[18] CoventorWare, *ANALYZER Reference: Standard Capabilities*. CoventorWare Inc., version 2012 ed., 2012.

[19] E. S. J. G. S. Astie, A.M. Gue, "Design of a low power SnO2 gas sensor integrated on silicon oxynitride membrane," *Sensors and Actuators B: Chemical*, vol. 67, no. 1-2, pp. 84 – 88, 2000.

[20] S. Astie, A. Gue, E. Scheid, L. Lescouzeres, and A. Cassagnes, "Optimization of

an integrated SnO2 gas sensor using a FEM simulator," *Sensors and Actuators A: Physical*, vol. 69, no. 3, pp. 205 – 211, 1998.

[21] A. H. Nayfeh and M. I. Younis, "Dynamics of MEMS resonators under superharmonic and subharmonic excitations," *Journal of Micromechanics and Microengineering*, vol. 15, no. 10, p. 1840, 2005.

[22] E. M. L. L. D. Landau, *Mechanics*. Oxford, U.K.: Butterworth-Heinemann, 3rd Ed. ed., 1999.

[23] V. Kaajakari, T. Mattila, A. Oja, and H. Seppa, "Nonlinear limits for single-crystal silicon microresonators," *Journal of Microelectromechanical Systems*, vol. 13, pp. 715 – 724, Oct. 2004.

[24] S. Timoshenko and J. Goodier, *Theory of elasticity*. McGraw-Hill classic textbook reissue series, McGraw-Hill, 3rd Ed. ed., 1969.

[25] F. Khatami and G. Rezazadeh, "Dynamic response of a torsional micromirror to electrostatic force and mechanical shock," *Microsystem Technologies*, vol. 15, pp. 535–545, 2009.

[26] U. Krishnamoorthy, D. Lee, and O. Solgaard, "Self-aligned vertical electrostatic combdrives for micromirror actuation," *Journal of Microelectromechanical Systems*, vol. 12, pp. 458 – 464, Aug. 2003.

[27] M. Asheghi, K. Kurabayashi, R. Kasnavi, and K. E. Goodson, "Thermal conduction in doped single-crystal silicon films," *Journal of Applied Physics*, vol. 91, no. 8, pp. 5079–5088, 2002.

[28] "Thermal conductivity of doped, porous and isotopically pure silicon," *Electronics Cooling*, vol. 12, no. 2, pp. 8 – 9, 2006.

[29] M. Guvench and J. Crosby, "Experimentally matched finite element modeling of thermally actuated SOI MEMS micro-grippers using COMSOL multiphysics," in

Proceedings of the COMSOL Conference 2009, pp. 1–9, COMSOL Multiphysics, 2009.

[30] A. Lee, C. McConaghy, G. Sommargren, P. Krulevitch, and E. Campbell, "Vertical-actuated electrostatic comb drive with in situ capacitive position correction for application in phase shifting diffraction interferometry," *Journal of Microelectromechanical Systems*, vol. 12, pp. 960 – 971, Dec. 2003.

[31] J. Wang, Z. Yang, and G. Yan, "Silicon-on-insulator out-of-plane electrostatic actuator with in situ capacitive position sensing," *Journal of micro-nanolithography MEMS and MOEMS*, vol. 11, Jul.-Sep. 2012.

[32] K. Oda, H. Takao, K. Terao, T. Suzuki, F. Shimokawa, I. Ishimaru, and F. Oohira, "Vertical comb-drive MEMS mirror with sensing function for phase-shift device," *Sensors and Actuators A: Physical*, vol. 181, no. 0, pp. 61 – 69, 2012.

[33] B. Borovic, A. Q. Liu, D. Popa, H. Cai, and F. L. Lewis, "Open-loop versus closed-loop control of MEMS devices: choices and issues," *Journal of Micromechanics and Microengineering*, vol. 15, no. 10, p. 1917, 2005.

[34] K. Isamoto, K. Totsuka, T. Suzuki, T. Sakai, A. Morosawa, C. Chong, H. Fujita, and H. Toshiyoshi, "A high speed MEMS scanner for 140-kHz SS-OCT," in *Optical MEMS and Nanophotonics (OMN), 2011 International Conference on*, pp. 73 –74, Aug. 2011.

[35] K. H. Koh, T. Kobayashi, and C. Lee, "A 2-D raster scanning mirror driven by piezoelectric cantilever actuator array in combinational mode: Bending and torsional," in *Optical MEMS and Nanophotonics (OMN), 2011 International Conference on*, pp. 41 –42, Aug. 2011.

Chapter 7

Conclusion and Future Work

7.1 Conclusion

The thesis has presented the research work on design, characterisation and simulation of two optical MEMS devices: a varifocal micromirror and a 2D hybrid-actuated scanning micromirror, focused on imaging and projection applications.

First, Chapter 2 introduced the general design flow for MEMS devices. The design flow of a MEMS device includes its 2D layout design, structure fabrication, performance characterisation and behaviour simulation. Through this design flow, the structure and functionality of MEMS device can be determined upon results matching between characterisation and simulation as well as application requirements. For the two optical MEMS micromirrors introduced in this thesis, both of them have been fabricated using SOIMUMPs in the 10-μm-thick SOI wafer and simulated with FEM model using CoventorWare. Particularly, the stress gradient of SOI layer has been characterised to be 2.4$\pm$0.12 MPa/μm; and the residual stress of gold layer in SOIMUMPs used for increasing optical reflectivity has been measured to be 247.7$\pm$11 MPa and is tensile stressed. These mechanical properties of silicon and gold are summarised together with other properties in a table and are used for performing FEM simulation. The main state-of-the-art of related topics of this thesis, such as

the geometric design of electrothermal and electrostatic actuator, MEMS optics with tunable focal length and scanning micromirrors, are reviewed.

Chapter 3 and 4 introduced the structure, simulation and characterisation of a gold-silicon varifocal micromirror (VFM). This VFM has 1-mm-diameter aperture and is fabricated using SOIMUMPs. It consists of eight serpentine suspensions and gold coated silicon micromirror. The suspensions and the 1.2-mm-diameter micromirror were fabricated in the 10-μm-thick SOI layer. And then a 1-mm-diameter and 0.65-μm-thick gold was concentrically coated on the silicon micromirror. This bimorph VFM changes its surface radius-of-curvature (ROC) at a temperature change due to thermal expansion difference of silicon and gold materials. First, the maximum electrothermal actuation of 10 V and 3.3 mA has been determined through the voltage-current experiment. The ROC tuning range characterisation demonstrated that, by applying the electrothermal power of 33 mW and optothermal actuation power 26 mW using 488 nm wavelength lasers, the maximum radius-of-curvature (ROC) variation range has achieved for of 6 mm and 11 mm respectively. Within the electrothermal actuation limitation, ROC tuning level and range are repeatable for the same device over four months and when the actuation power was delivered through different combination of suspensions. Moreover, the mechanical rise and fall times of VFM respond to voltage pulse have been measured to be 130 ms and 120 ms respectively. Apart from the electrothermal actuation, the optothermal actuation using normally incident laser beam at 488 nm, 514 nm and 532 nm wavelengths has also been performed. The average ROC variation sensitivity of VFM to the absorbed optothermal power have been measured to be 0.47 mm/mW, 0.31 mm/mW and 0.52 mm/mW when using laser source at 488 nm, 514 nm and 532 nm wavelengths respectively; yet it is only 0.16 mm/mW for the electrothermally actuated VFM. The FEM simulated temperature distribution of VFM model has explained that the micromirror average temperature actuated by optothermal power increases at a rate of 7.2 ^{o}C/mW whereas the one generated by electrothermal actuation power increases at a rate of 3.2 ^{o}C/mW. FEM simulations of ROC variation of a VFM model actuated using electrothermal and optothermal power have shown to be at least 93% agreement with

the measurements. Optical aberrations have be quantified by calculating the Zernike coefficients produced by VFM reflective surface and also by measuring the wavefront of a <1 mW He-Ne laser beam reflected by VFM. Both methods have obtained only several micrometers defocus aberration and nanometres higher order aberrations such as astigmatism, coma, trefoil and spherical. Both characterisation and simulation have demonstrated and proved that ROC variation range of VFM design is depended on not only the thermal actuation schemes but also its initial ROC which is fundamentally resulted from the material properties. Based on simulation results for the 10-μm-thick 1.2-mm-diameter SOI VFM coated with gold, it suggests that the VFM with higher initial ROC could result in higher ROC tunable range, and coating thick gold could results in higher ROC tunable range as well under conditions of remain the same initial ROC. A VFM based imaging system has been assembled and has achieved tracking objects along its optical axis. The tracking range is tested for various sensor distances for both thermal actuation schemes together with sharp image results, i.e. 134 mm tracking range with electrothermally actuated VFM when sensor distance is 15 mm. Table 7.1 summarises the performance of the VFM introduced in this thesis and its comparison to other varifocal micromirrors reported in the literature.

Table 7.1: Summary of thermally actuated varifocal micromirror and its comparison with some reported VFM in the literature.

VFM	Thick-ness [μm]	Aperture Diameter [mm]	Rest ROC [mm]	Actuated ROC [mm]	Focal Length Tuning Range [mm]	Optical Power Tuning Range [m^{-1}]	Actuation Method	Max. Voltage [V]	Max. Current [mA]	Response Time [ms]	Optical Aberration
1997 [1]	0.5 – 1	10	∞	500	∞ – 250	4	ES	200	–	10	ASG
2001 [2]	1	1	720	72	324	50	ES	100	–		
2003 [3]	1.5	0.1	2.5	8.2	3	556	ET		11	2	
2005 [4]	-	20	2000	200	900	9	EM	12	110		
2006 [5]	5.02	>5	∞	200	∞–100	10	ES	150	–		none*
2008 [6]	0.5	0.95	200	5	97	323	HP	(22.5 kPa)		33	
2009 [7]	10	0.5	∞	48	∞ – 24	42	ES	215	–		none*
2011 [8]	1	0.4	-56	42	49	167	ES	22			
2012 [9, 10]	~4	4.5	∞	100	∞ – 50	20	ES	~150		0.4	ASG&DIST
2012 [11]	1	0.3	-256	186	221	18.6	ES	50		~2.5	
2013 [12]$\star$	10.7	1	23	29	3	18	ET	10	3.3	~130	negligible
2013 [12]$\star$	10.7	1	23	34	6	28	Laser	(25.8 mW)			negligible

* = Quantified by fitting surface shape with parabolic curve shape.
$\star$ = Device presented in this thesis.
ES = Electrostatic ET = Electrothermal EM = Electromagnetic
HP = Hydraulic pressure ASG = Astigmatism DIST = Distorsion

Chapter 5 and 6 described the structure design, characterisation and simulation of a novel hybrid actuated 2D scanning micromirror using electrothermal actuators and

electrostatic comb-drives. This 2D microscanner is designed for imaging system with a single photodetector, where the image is required to scan over which in a pixel-by-pixel pattern in order to reconstruct the image of an object. A case study of previously SOIMUMPs fabricated hybrid-actuated 2D microscanner has shown an irregular scanning pattern. Characterisation and FEM simulation have identified that the two non-orthogonal rotation axes has been caused by the direct connection between electrothermal actuators and comb-drives through a torsion bar. After analysis this premier design, a modified structure design is suggested. The geometry and structure of actuators, flexure connections and gold coated micromirror of this modified microscanner have been optimised using FEM simulation software, CoventorWare. The modified microscanner consists of 1.2 mm diameter gold coated silicon micromirror, two electrothermal actuators and two pairs of electrostatic comb-drives. Using CoventorWare, deformation of this microscanner design only due to the intrinsic stresses within the materials has been simulated and shown an initial tilting angle by about 2.3°; also, the movable combs have been lifted vertically by 5 μm at the end connecting to micromirror. The electro-thermo-mechanical simulation displays that an 18° optical scan angle of micromirror about one off-centroid axis has been generated when a 18 V is assumed to be applied to each of the two electrothermal actuators; and ROC of micromirror has increased by 3 μm. Modal analysis of this 2D microscanner has estimated a resonant rotational mode at 1613 Hz about an orthogonal axis. A prototype of this modified design has been fabricated using SOIMUMPs in the 10-μm-thick SOI wafer. When driving both electrothermal actuators equally at DC 17.5 V, the maximum optical tilt angle has been measured at around 7°, which is around 60% smaller than the estimated value. The bimorph micromirror ROC has increased by 11.3 mm which is 8 mm higher than the simulated value at this driving voltage. The main reason for such discrepancy between the measurement and simulation has been suggested to be the application of thermal conductivity of the non-doped single-crystal-silicon in FEM model rather than the one for doped silicon material. Resonant excitation of rotating microscanner has been measured to be at 1576 Hz which has an agreement of over 97% with the simulated value. Synchronised actuation of electrothermal actuators and electrostatic comb-drives displays a cross-talk between

motions in the two orthogonal axes. The magnitude of resonant rotation angles driven by comb-drives have increased by the increasing actuation level of electrothermal actuators, which is fundamentally resulting from the increased capacitance variation range when the maximum vertical offset between the movable and the fixed combs has increased by 27 μm. Also, their torsion bar ROC has reduced from 76.5 mm to 10 mm which resulting in the structure stiffening when driving both electrothermal actuators at 18 V. By programming comb-drives actuation voltage signal and synchronising it with electrothermal actuators driving voltage signal, a rectangular 2D raster scan pattern has been demonstrated and has a $7^o \times 10^o$ angular field-of-view with line-scan rate of no less than 1656 Hz. Table 7.2 summarises the results of this hybrid actuated 2D scanning micromirror and its comparison to other 2D scanning micromirrors reported in the literature.

Table 7.2: Summary of hybrid-actuated 2D scanning micromirror and its comparison to the ones in the literature.

2D scanning micromirror	micromirror size		Actuation Method	Max. Voltage	Max. Current	Max. Optical Scan Angles	Resonant Frequency	Scan Patten
	Thickness	Area						
	[μm]	[mm]		[V]	[mA]	[^{o}]	[Hz]	
2004 [13]	$\sim$45	1^2	ET	15, 17 V_{dc}	6.3, 8	$40^o \times 25^o$	445, 259	–
2005 [14]	50	0.65^2	ES	$20V_{dc}$+$15V_{pp}$, $30V_{dc}$+$25V_{pp}$	–	$27^o \times 20^o$	10.65, 1540	Lissajous
2005 [15]	35	$1^2\pi$	ES	55, 50 V_{dc}	–	$12^o \times 8^o$	315, 144	–
2006 [16]	30	0.75^2	ES	45,58 V_{pp}	–	16^o, 6^o	1760, 1020	–
2008 [17]	230	5^2	EM	–	250(dc)	10^o, 140^o	647, 414	Lissajous
2012 [18]	$\sim$450	1.5×1	ET&EM	$10V_{dc}$, $1V_{ac}$	12,1.26	$\pm 1.5^o$,$\pm 10^o$	74,202	Lissajous
2012 [19]$\star$	10.65	$1.2^2\pi$	ES&ET	$160V_{pp}$, $18V_{dc}$	–,30	4.5^o, 6.9^o	1590, –	Raster

$\star$ = Device presented in this thesis.
ES = Electrostatic ET = Electrothermal EM = Electromagnetic

7.2 Future Work

Current design of hybrid actuated scanning micromirror has two orthogonal scanning axes, however, the axis of the tilt motion driven by electrothermal actuators are off the centroid of the micromirror, which results in the relative position of the micromirror centroid changing during such tilt movement. Therefore, the layout design of this microscanner, or the arrangement of actuators around micromirror,

should be symmetric about two orthogonal scanning axes, such as the example illustrated in Figure 7.1a. However, this design is limited within the materials and number of layers available during SOIMUMPs. Such constraints limit the 3D structure design of microscanner as well as the functions of flexure connections. For example, one of the structure design which cannot be achieved using SOIMUMPs is that electrostatic comb-drives are patterned between the micromirror and the frame edges (Figure 7.1b). Moreover, since the structure are pattern in the same layer in SOIMUMPs, there is no electrical isolation between the two electrodes. Next, the material of flexure connections between electrothermal actuators and micromirror should be using a different material as used for the electrothermal actuator so that the thermal conductivity of connections could be lower than the silicon material to achieve better thermal isolation. Finally, magnitude of 2D scanning pattern is limited by the maximum tilting angle driven by electrothermal actuators. This is because that the anchored torsion bar of current design limits the maximum displacement during electrothermal actuations. Besides, this electrothermal actuator design functions based on the buckling of constrained outer beam structures under stresses introduced by thermal expansion. In this case, the higher the magnitude of buckling, the larger the vertical displacement that could be produced by electrothermal actuators. However, the buckling of the beam structures will not happen until the constrained structures are stressed, which is when the thermal expansion exceed its elastic deformation. Therefore, by externally introducing constraints at only the free end of electrothermal actuator, the beam structure is strictly constrained as a clamped bridge. In this way, as soon as the structure are heated and the thermal expansion will result in vertical displacement. These suggestions can be achieved in the future research with consideration of an alternative or modified fabrication processes using selected materials.

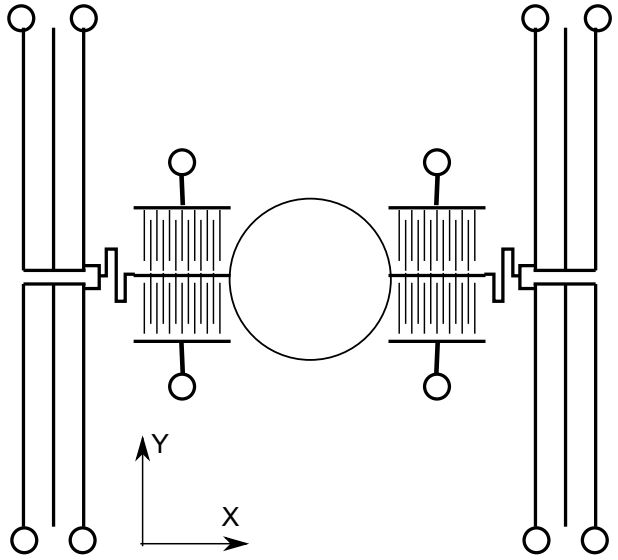

(a)

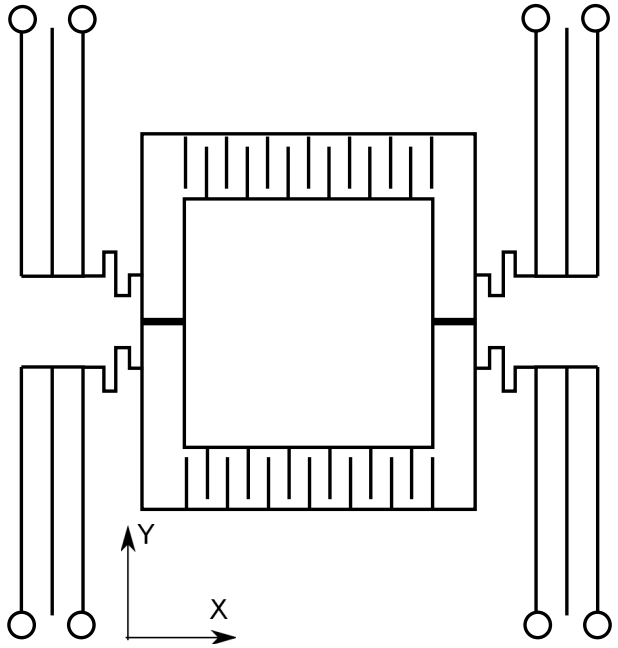

(b)

Figure 7.1: The scheme of hybrid actuated microscanner with actuators symmetric layout about two orthogonal scanning axes.

References

[1] G. Vdovin, "Quick focusing of imaging optics using micromachined adaptive mirrors," *Optics Communications*, vol. 140, no. 46, pp. 187 – 190, 1997.

[2] P. A. Himmer, D. L. Dickensheets, and R. A. Friholm, "Micromachined silicon nitride deformable mirrors for focus control," *Optics Letters*, vol. 26, pp. 1280–1282, Aug. 2001.

[3] W. Liu and J. J. Talghader, "Current-controlled curvature of coated micromirrors," *Optics Letters*, vol. 28, pp. 932–934, Jun. 2003.

[4] W. Greger, D. Arnold, R. Jurischka, A. Schoth, C. Muller, J. Wilde, and H. Reinecke, "A new approach for focusing deformable mirrors fabricated in polymer technology," in *Optical MEMS and Their Applications Conference, 2005. IEEE/LEOS International Conference on*, pp. 45 –46, Aug. 2005.

[5] U. M. Mescheder, C. Esta, G. Somogyi, and M. Freudenreich, "Distortion optimized focusing mirror device with large aperture," *Sensors and Actuators A: Physical*, vol. 130131, no. 0, pp. 20 – 27, 2006.

[6] A. A. Alzaydi, J. T. Yeow, and S. L. Lee, "Hydraulic controlled polyester-based micro adaptive mirror with adjustable focal length," *Mechatronics*, vol. 18, no. 2, pp. 61 – 70, 2008.

[7] R. Hokari and K. Hane, "A varifocal convex micromirror driven by a bending moment," *IEEE Journal of Selected Topics in Quantum Electronics*, vol. 15, pp. 1310 –1316, Sep.-Oct. 2009.

[8] T. Sasaki and K. Hane, "Initial deflection of silicon-on-insulator thin membrane micro-mirror and fabrication of varifocal mirror," *Sensors and Actuators A: Physical*, vol. 172, no. 2, pp. 516 – 522, 2011.

[9] H.-C. Wei, Y.-H. Chien, W.-Y. Hsu, Y.-C. Cheng, and G.-D. J. Su, "Controlling

a MEMS deformable mirror in a miniature auto focusing imaging system," *IEEE Transactions on Control Systems Technology*, vol. 20, pp. 1592–1596, Nov. 2012.

[10] J.-L. Wang, T.-Y. Chen, Y.-H. Chien, and G.-D. J. Su, "Miniature optical autofocus camera by micromachined fluoropolymer deformable mirror," *Optics Express*, vol. 17, pp. 6268–6274, Apr. 2009.

[11] T. Sasaki and K. Hane, "Varifocal micromirror integrated with comb-drive scanner on silicon-on-insulator wafer," *Journal of Microelectromechanical Systems*, vol. 21, pp. 971 –980, Aug. 2012.

[12] L. Li, R. Li, W. Lubeigt, and D. Uttamchandani, "Design, simulation, and characterization of a bimorph varifocal micromirror and its application in an optical imaging system," *Journal of Microelectromechanical Systems*, vol. 22, no. 2, pp. 285–294, 2013.

[13] A. Jain, A. Kopa, Y. Pan, G. Fedder, and H. Xie, "A two-axis electrothermal micromirror for endoscopic optical coherence tomography," *IEEE Journal of Selected Topics in Quantum Electronics*, vol. 10, pp. 636 – 642, May-Jun. 2004.

[14] J. Kim, D. Christensen, and L. Lin, "Monolithic 2-D scanning mirror using self-aligned angular vertical comb drives," *Photonics Technology Letters, IEEE*, vol. 17, pp. 2307 – 2309, Nov. 2005.

[15] W. Piyawattanametha, P. Patterson, D. Hah, H. Toshiyoshi, and M. Wu, "Surface- and bulk- micromachined two-dimensional scanner driven by angular vertical comb actuators," *Journal of Microelectromechanical Systems*, vol. 14, pp. 1329 – 1338, Dec. 2005.

[16] W. Piyawattanametha, R. P. J. Barretto, T. H. Ko, B. A. Flusberg, E. D. Cocker, H. Ra, D. Lee, O. Solgaard, and M. J. Schnitzer, "Fast-scanning two-photon fluorescence imaging based on a microelectromechanical systems two- dimensional scanning mirror," *Optics Letters*, vol. 31, pp. 2018–2020, Jul. 2006.

[17] H. Urey, S. Holmstrom, and A. Yalcinkaya, "Electromagnetically actuated FR4 scanners," *Photonics Technology Letters, IEEE*, vol. 20, pp. 30 –32, Jan.1, 2008.

[18] K. Koh and C. Lee, "A two-dimensional MEMS scanning mirror using hybrid actuation mechanisms with low operation voltage," *Journal of Microelectromechanical Systems*, vol. 21, no. 5, pp. 1124–1135, 2012.

[19] L. Li, R. Bauer, G. Brown, and D. Uttamchandani, "A 2D MEMS scanning micromirror with electrothermal and electrostatic actuators," in *Optical MEMS and Nanophotonics (OMN), 2012 International Conference on*, pp. 73–74, 2012.

Appendix A

Publications

Journal Publications

Euan J. Boyd, Li Li, Robert Blue, Deepak Uttamchandani, *"Measurement of the temperature coefficient of Young's modulus of single crystal silicon and 3C silicon carbide below 273 K using micro-cantilevers"*, Sensors and Actuators A: Physical, Volume 198, August 2013, Pages 75-80, DOI: 10.1016/j.sna.2013.04.032.

Li Li, Ran Li, Walter Lubeigt, Deepak Uttamchandani, *"Design, simulation and characterisation of a bimorph varifocal micromirror and its application in an optical imaging system"*, Journal of Microelectromechanical Systems, vol.22, no.2, pp.285,294, April 2013, DOI: 10.1109/JMEMS.2012.2220337.

Robert Blue, Li Li, Gordon M H Flockhart and Deepak Uttamchandani, *"MEMS-actuated wavelength drop filter based on microsphere whispering gallery modes"*, J. Micromech. Microeng., vol. 21, pp. 115020, October 2011, DOI: 10.1088/0960-1317/21/11/115020

Li Li, Vladimir Stankovic, Lina Stankovic, Lijie Li, Samuel Cheng and Deepak Uttamchandani1, *"Single pixel optical imaging using a scanning MEMS mirror"*, J. Micromech. Microeng, Vol. 21, 025022, January 2011. DOI: 10.1088/0960-1317/21/2/025022

Conference Publications

Li Li, G. Bauer, G. Brown, D. Uttamchandani, *"A 2D MEMS scanning micromirror with electrothermal and electrostatic actuators,"*, Optical MEMS and Nanophotonics (OMN), 2012 International Conference on , vol., no., pp.73-74, 6-9 Aug. 2012. doi: 10.1109/OMEMS.2012.6318808

L. Li, R. Bauer, G. Brown, D. Uttamchandani, *"A symmetric hybrid MEMS scanner with electrothermal and electrostatic actuators"*, OMN, Istanbul, Turkey, August 2011. DOI: 10.1109/OMEMS.2011.6031038

R. Blue, L. Li, G. M. H. Flockhart, D. Uttamchandani, *"Wavelength filtering using MEMS actuated coupling from optical fibres to spherical resonators"*, OMN, Istanbul, Turkey, August 2011. DOI: 10.1109/OMEMS.2011.6031024

G. Brown, L. Li, R.Bauer, J. Liu and D. Uttamchandani, *"A two-axis hybrid MEMS scanner incorporating electrothermal and electrostatic actuators"*, OPT MEMS, Sapporo, Japan, 9-12 August 2010. DOI: 10.1109/OMEMS.2010.5672156

L. Li, LJ. Li, V. Stankovic, L. Stankovic and D. Uttamchandani, *Single pixel camera using MEMS scanners*, 35th Annual Conference of IEEE Industrial Electronics Society (IECON 2009), Porto, Portugal, November 2009.

L. Li, M. Mirza, V. Stankovic, LJ. Li, L Stankovic, D. Uttamchandani, S. Cheng, *Optical imaging with scanning MEMS micromirror a single photodetector approach*, IEEE International Conference on Imaging Processing, Cairo, Egypt, November 7-11 2009.

Appendix B

Additional Figures

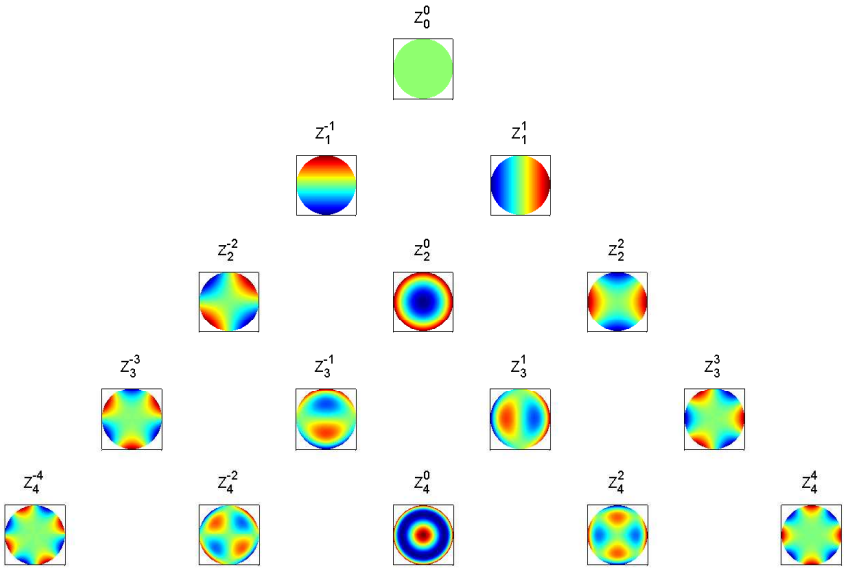

Figure B.1: The first 15 Zernike functions plotted by programing Equation (4.2.4) using MATLAB.

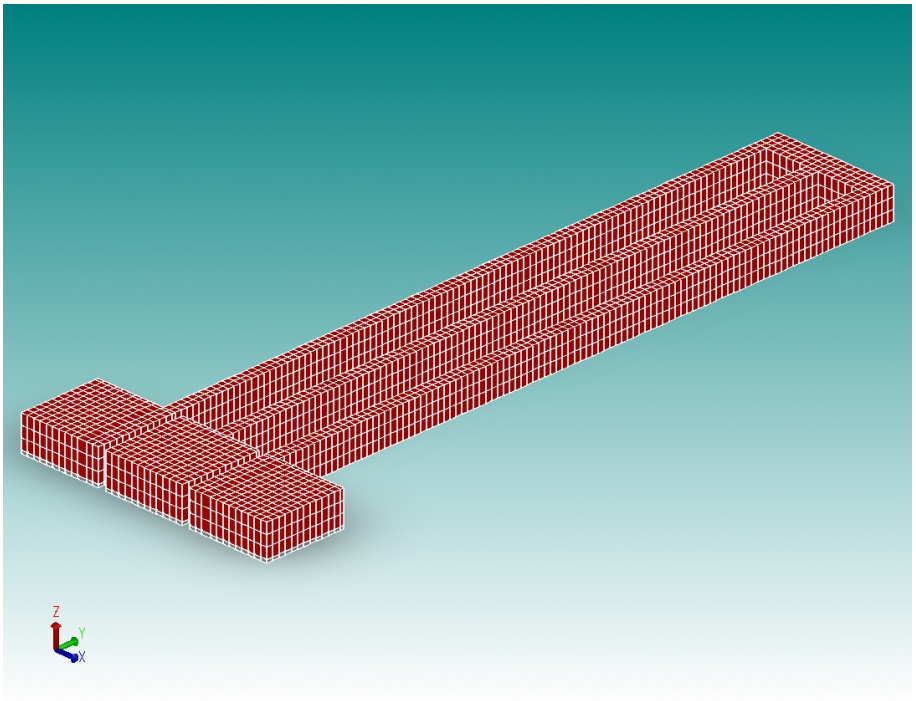

Figure B.2: Meshing of electrothermal actuator of microscanner #S39D4 model (x10 magnification in Z-axis direction).

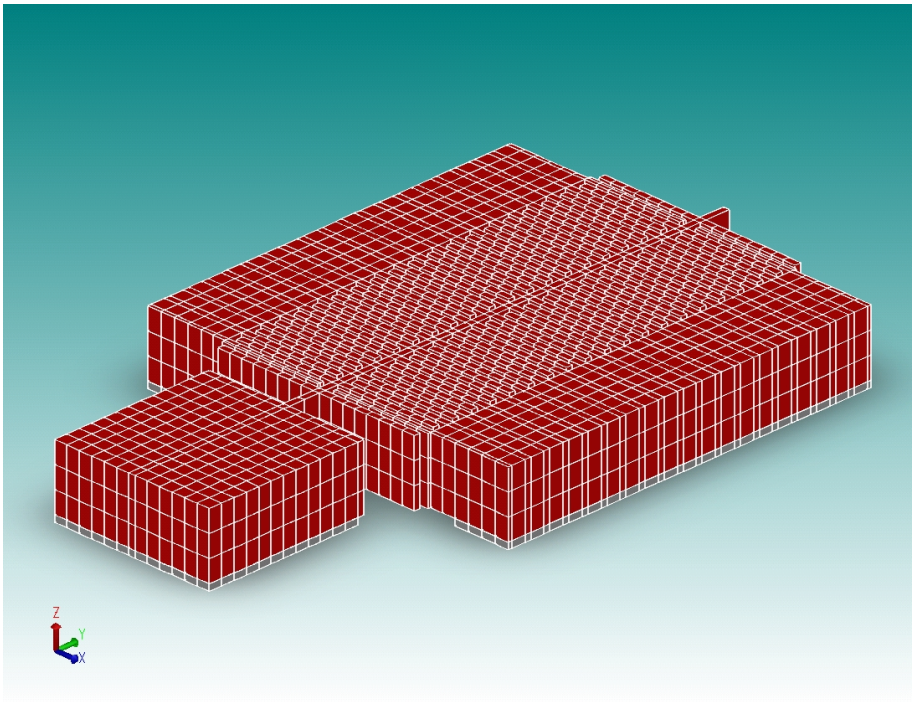

Figure B.3: Meshing of electrostatic comb-drives of microscanner #S39D4 model (x10 magnification in Z-axis direction).

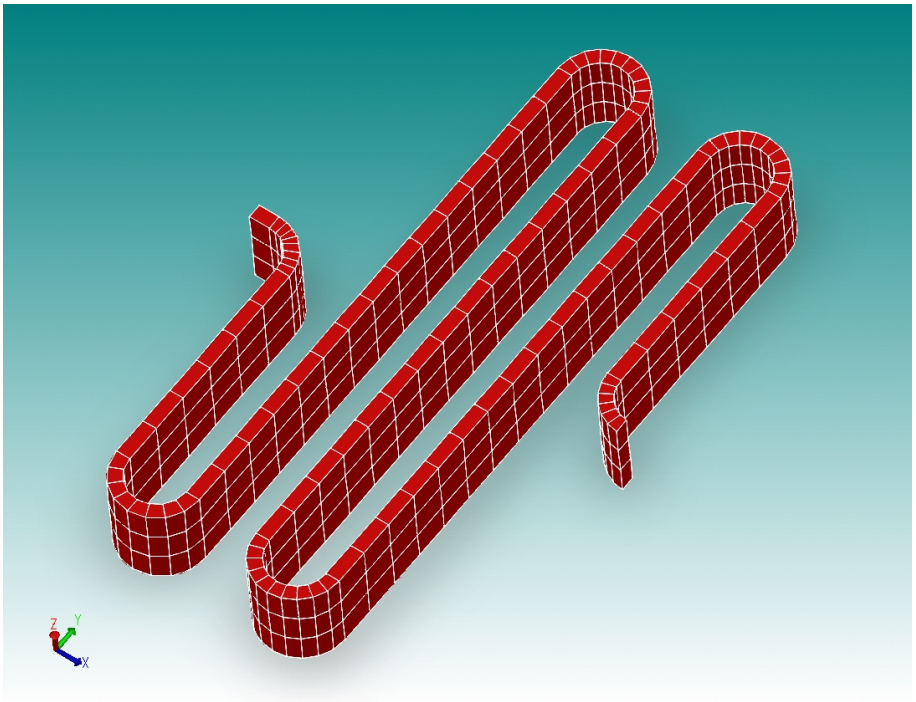

Figure B.4: Meshing of classical serpentine spring of microscanner #S39D4 model (x5 magnification in Z-axis direction).

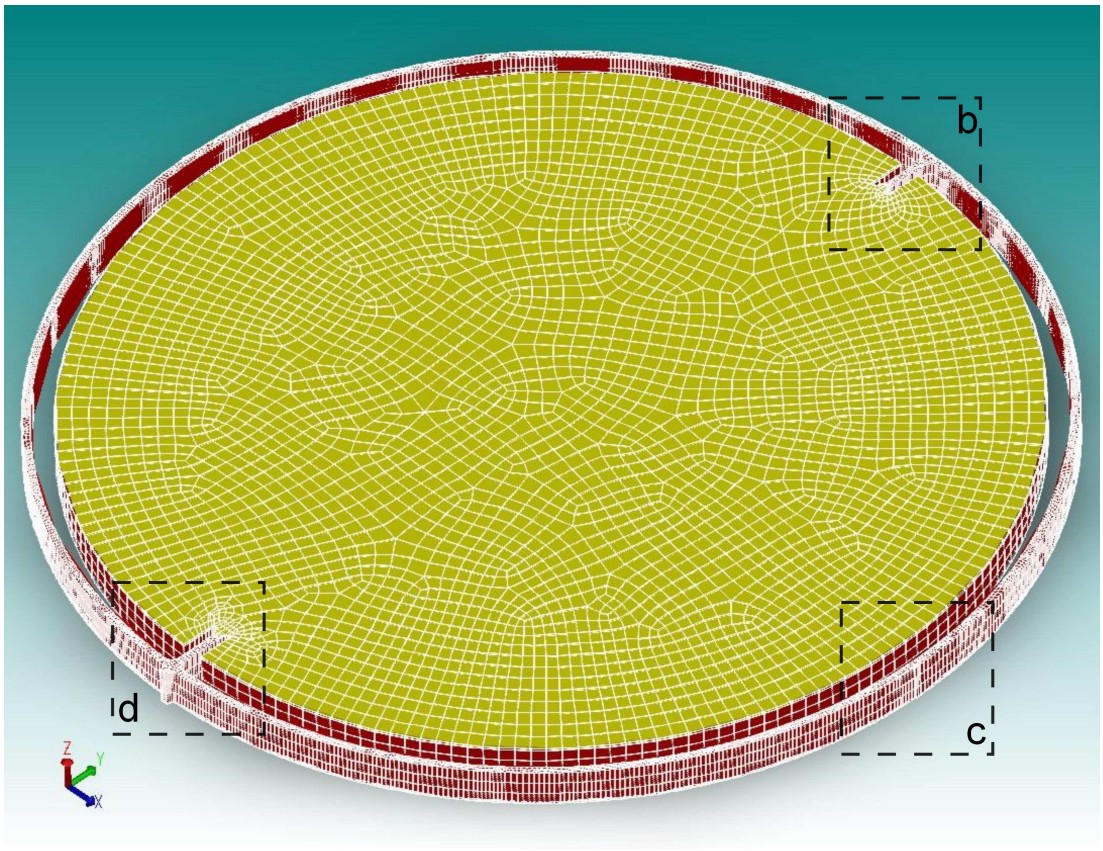

(a)

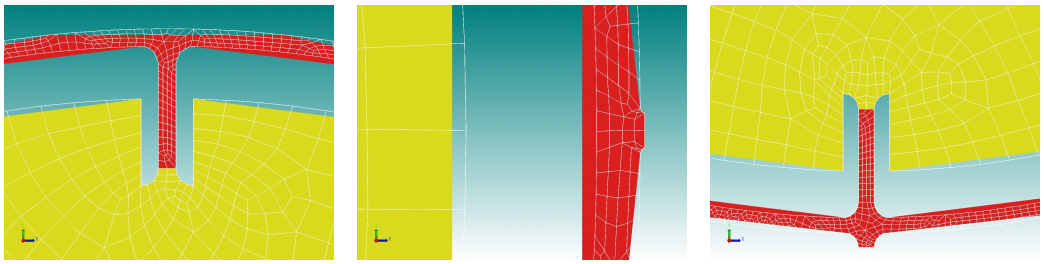

(b) (c) (d)

Figure B.5: Meshing of framed micromirror of microscanner #S39D4 model (x5 magnification in Z-axis direction).

Appendix C

Additional Tables

Table C.1: The FEM simulation of the electrothermally actuated VFM using tetrahedron meshing elements.

DC Voltage [V]	Current [mA]	Power [mW]	Radius of Curvature [mm]	Average Mirror Surface Temperature [^{O}C]	Maximum Temperature on VFM device [^{O}C]	Sensitivity [mm/mW]
1	0.4	0.4	22.5	22	24	0.12
2	0.9	1.7	22.6	26	37	0.12
3	1.3	3.8	22.7	32	59	0.13
4	1.7	6.7	23.0	41	95	0.14
5	2.0	10.2	23.4	53	144	0.16
6	2.4	14.3	24.0	66	210	0.18
7	2.6	18.5	25.5	80	297	0.20
8	2.8	22.3	26.4	93	398	0.23
9	2.9	26.5	27.5	106	514	0.25
10	3.2	31.7	28.8	121	662	0.27

Table C.2: The FEM simulation of the electrothermally actuated VFM using hexahedron meshing elements.

DC Voltage [V]	Current [mA]	Power [mW]	Radius of Curvature [mm]	Average Mirror Surface Temperature [^{O}C]	Maximum Temperature on VFM device [^{O}C]	Sensitivity [mm/mW]
0	0.0	0.0	22.6	20.0	20	
1	0.4	0.4	22.7	21.4	24	0.12
2	0.9	1.7	22.8	25.4	37	0.12
3	1.3	3.8	23.1	32.1	59	0.13
4	1.7	6.7	23.5	41.2	95	0.14
5	2.0	10.2	24.0	52.6	144	0.15
6	2.4	14.3	24.7	65.9	210	0.17
7	2.6	18.4	25.5	79.8	297	0.19
8	2.8	22.3	26.3	92.5	398	0.21
9	2.9	26.5	27.2	105.8	514	0.22
10	3.2	31.6	28.4	121.0	662	0.23

Table C.3: The FEM simulation results of the VFM by optothermal actuation power

	Total Power [mW]	Absorbed Power [mW]	Radius of Curvature [mm]	Mirror Surface Average Temperature [°C]	Sensitivity [mm/mW]
488 nm			21.0	20.0	
	6	3.6	21.8	44.5	0.2
	12	7.2	22.8	70.2	0.3
	22	13.2	25.1	114.1	0.4
	30	18	27.7	148.8	0.6
	43	25.8	35.3	204.6	1.0
514 nm	0	0	21.0	20.0	
	3	2	21.5	35.5	0.2
	6.2	4.1	22.1	52.5	0.3
	10	6.5	22.9	72.7	0.3
	15	9.8	24.3	101.3	0.4
	23	15	27.5	146.3	0.6
532 nm	0	0	20.0	20.0	
	7.7	4.8	21.0	51.8	0.2
	15	9.9	22.4	87.4	0.3
	28	18.6	26.3	148.0	0.4
	35.5	23.6	30.0	182.3	0.7

Table C.4: The Zernike coefficients calculated from the surface profile measurements of the electrothermally actuated VFM.

V [V]				0	1	2	3	4	5	6	7	8	9	10
I [mA]				0	0.37	0.79	1.2	1.58	1.94	2.29	2.59	2.86	3.08	3.3
Electrothermal Actuation Power [mW]				0	0.37	1.58	3.6	6.32	9.7	13.74	18.13	22.88	27.72	33
Z_j **[mm]**	**Name**	**n**	**m**	**Zernike coefficient [μm]**										
Z_1	Piston	0	0	4.89	-2.00	-1.95	-1.89	-1.76	-1.69	-1.41	-1.29	-1.09	-0.93	6.57
Z_2	Tip y	1	-1	-0.13	-0.24	-0.34	-0.28	-0.38	-0.26	0.20	-0.33	-0.28	-0.29	-0.12
Z_3	Tilt x	1	1	0.07	0.30	0.05	0.25	0.16	0.16	-0.32	0.08	0.21	0.24	0.13
Z_4	Astigmatism $\pm 45^o$	2	-2	-9.6E-03	-1.3E-02	-9.4E-03	-8.5E-03	-7.0E-03	-6.5E-03	-7.0E-03	-8.0E-03	-6.7E-03	-5.3E-03	-1.2E-02
Z_5	Defocus	2	0	3.25	3.19	3.16	3.09	3.04	2.89	2.90	2.75	2.67	2.57	2.48
Z_6	Astigmatism 0/90Deg	2	2	-3.6E-03	-1.6E-02	-1.4E-02	-1.4E-02	-3.8E-03	-6.0E-03	-7.8E-03	4.4E-03	1.4E-02	1.6E-02	1.9E-02
Z_7	Astigmatism trefoil (30)	3	-3	-1.0E-02	-1.1E-02	-1.1E-02	-1.1E-02	-1.0E-02	-6.9E-03	-1.8E-03	-8.8E-03	-8.5E-03	-9.4E-03	-8.8E-03
Z_8	Coma Y	3	-1	-5.1E-02	-3.7E-02	-1.7E-02	-2.8E-02	-8.7E-03	-2.3E-02	-1.8E-02	-1.0E-02	-2.2E-02	-1.7E-02	-4.1E-02
Z_9	Coma X	3	1	-1.1E-02	-3.3E-02	-1.1E-02	-2.6E-02	-1.8E-02	-1.4E-02	-1.2E-02	-5.3E-04	-1.4E-02	-2.1E-02	-4.7E-02
Z_{10}	Astigmatism trefoil (0)	3	3	-3.4E-03	2.2E-03	-9.0E-03	-2.0E-04	-2.7E-03	-3.3E-03	1.1E-02	-4.3E-03	4.5E-03	5.9E-03	6.2E-03
Z_{11}		4	-4	2.3E-03	4.4E-03	4.4E-03	3.8E-03	1.7E-03	2.7E-03	-1.4E-03	-3.5E-04	2.9E-04	-5.5E-04	-6.1E-04
Z_{12}		4	-2	-9.6E-03	-1.3E-02	-1.2E-02	-7.4E-03	-6.3E-03	-5.1E-03	-4.7E-03	-7.8E-03	-3.4E-03	-1.2E-03	-9.8E-03
Z_{13}	Sphere aberration	4	0	-2.1E-02	3.0E-02	2.4E-02	2.9E-02	1.7E-02	3.7E-02	-9.7E-03	6.7E-04	-1.6E-02	-1.8E-02	-5.9E-02
Z_{14}		4	2	2.0E-02	4.4E-04	1.0E-03	-7.6E-04	1.0E-02	-7.2E-04	-1.6E-02	3.8E-03	1.3E-02	1.0E-02	9.8E-03
Z_{15}		4	4	3.5E-02	3.3E-02	3.0E-02	3.0E-02	2.8E-02	2.8E-02	3.0E-02	2.8E-02	3.0E-02	2.8E-02	2.7E-02
	ROC [mm]			-22.63	-23.10	-23.27	-23.81	-24.19	-25.47	-25.42	-26.73	-27.60	-28.63	-29.73

Table C.5: Table of Zernike coefficients of the electrothermal actuated VFM measured using wavefront sensor.

V [V]				0	1	2	3	4	5	6	7	8	9	10
I [mA]				0	0.42	0.84	1.24	1.65	2	2.33	2.63	2.89	3.13	3.34
P [mW]				0	0.42	1.68	3.72	6.6	10	13.98	18.41	23.12	28.17	33.4
Pupil Diameter [mm]				0.37	0.372	0.372	0.376	0.378	0.381	0.384	0.391	0.396	0.4	0.405
Z_j **[mm]**	**Name**	**n**	**m**	**Zernike coefficient [μm]**										
Z_1	Piston	0	0	-1.47±0.09	-1.26±0.06	-1.28±0.03	-1.27±0.02	-1.26±0.12	-1.65±0.01	-1.51±0.03	-1.46±0.05	-1.35±0.01	-1.33±0.06	-1.43±0.04
Z_2	Tip y	1	-1	-0.00±0.04	-0.11±0.04	-0.10±0.02	-0.12±0.02	-0.11±0.05	0.43±0.01	0.23±0.04	0.29±0.04	0.19±0.01	0.18±0.04	0.30±0.03
Z_3	Tilt x	1	1	1.05±0.01	0.94±0.01	0.96±0.02	0.96±0.02	0.94±0.02	0.79±0.02	0.86±0.01	0.74±0.02	0.74±0.01	0.73±0.02	0.72±0.01
4_Z	Astigmatism ±45°	2	-2	(1.0±0.2)E-02	(1.1±0.5)E-02	(1.0±0.2)E-02	(9.0±0.1)E-03	(8.0±0.6)E-03	(8.0±1.5)E-03	(8.0±6.5)E-03	(6.0±2.9)E-03	(7.0±6.4)E-03	(7.0±3.8)E-03	(6.0±5.0)E-03
Z_5	Defocus	2	0	0.408±0.054	0.41±0.018	0.407±0.012	0.408±0.020	0.408±0.072	0.407±0.013	0.404±0.020	0.4060.039	0.403±0.004	0.398±0.023	0.3950.017
Z_6	Astigmatism 0/90Deg	2	2	(9.0±1.7)E-03	(8.0±2.7)E-03	(9.0±2.1)E-03	(9.0±0.6)E-03	(9.0±2.3)E-03	(1.0±0.1)E-02	(9.0±6.4)E-03	(9.0±2.9)E-03	(8.0±2.1)E-03	(9.0±5.3)E-03	(9.0±6.8)E-03
	ROC [mm]			24.11	24.19	24.41	24.72	25.11	25.61	26.22	26.94	27.77	28.67	29.61

Table C.6: The Zernike coefficient calculated from the surface profile measurements of the optothermally actuated VFM.

				488nm					514					532		
Total Laser Actuation Power [mW]				0	6	12.3	30	43	3	6	10	15	23	0	16	35.5
Z [mm]	**Name**	**n**	**m**	**Zernike coefficient [μm]**												
Z_1	Piston	0	0	-1.13	-1.11	-1.07	-0.80	-0.79	-1.15	-1.17	-1.12	-1.05	-0.88	-1.17	-1.05	-0.74
Z_2	Tip y	1	-1	5.5E-02	-2.7E-02	-9.6E-02	-2.6E-01	-5.1E-02	-1.6E-02	-1.4E-01	-1.2E-01	-9.6E-02	-3.1E-01	-4.9E-03	2.8E-03	4.0E-03
Z_3	Tilt x	1	1	-3.9E-03	4.2E-02	7.6E-02	7.9E-02	8.4E-02	4.6E-02	7.8E-02	9.1E-02	9.0E-02	9.7E-02	-1.0E-01	-7.9E-02	-6.9E-02
Z_4	Astigmatism +45/-45Deg	2	-2	9.6E-04	8.8E-04	1.8E-03	2.2E-03	2.0E-03	1.1E-03	1.5E-03	1.8E-03	2.3E-03	2.9E-03	-3.5E-04	-3.5E-04	-2.7E-04
Z_5	Defocus	2	0	2.33	2.22	2.09	1.75	1.53	2.29	2.22	2.16	2.07	1.95	2.31	2.00	1.56
Z_6	Astigmatism 0/90Deg	2	2	4.8E-03	4.7E-03	5.0E-03	5.6E-03	5.9E-03	4.3E-03	4.5E-03	4.7E-03	5.0E-03	5.5E-03	5.0E-03	5.5E-03	6.1E-03
Z_7	Astigmatism trefoil (30)	3	-3	4.7E-03	4.4E-03	3.8E-03	2.7E-03	2.0E-03	4.6E-03	4.3E-03	4.1E-03	3.9E-03	3.4E-03	5.0E-03	4.0E-03	2.7E-03
Z_8	Coma Y	3	-1	4.3E-03	4.5E-03	2.4E-03	6.9E-04	-5.4E-04	4.1E-03	3.6E-03	3.1E-03	2.4E-03	1.4E-03	4.0E-03	2.4E-03	2.0E-04
Z_9	Coma X	3	1	2.9E-02	2.5E-02	2.0E-02	1.1E-02	5.5E-03	2.7E-02	2.5E-02	2.2E-02	1.9E-02	1.5E-02	3.0E-02	2.2E-02	1.1E-02
Z_{10}	Astigmatism trefoil (0)	3	3	-8.9E-03	-8.1E-03	-7.0E-03	-4.7E-03	-3.6E-03	-8.9E-03	-8.3E-03	-7.8E-03	-7.0E-03	-6.0E-03	-9.0E-03	-7.4E-03	-5.2E-03
Z_{11}		4	-4	-5.2E-04	-5.3E-04	-5.2E-04	-4.2E-04	-4.3E-04	-5.4E-04	-5.6E-04	-5.1E-04	-4.9E-04	-4.9E-04	-4.0E-04	-4.1E-04	-4.0E-04
Z_{12}		4	-2	-1.9E-04	-1.8E-04	-4.6E-04	-6.4E-04	-7.5E-04	-2.7E-04	-3.7E-04	-4.4E-04	-5.8E-04	-7.4E-04	-4.8E-04	-5.1E-04	-5.1E-04
Z_{13}	Sphere aberration	4	0	4.6E-02	4.0E-02	3.4E-02	2.1E-02	1.5E-02	4.3E-02	4.0E-02	3.7E-02	3.3E-02	2.8E-02	4.0E-02	2.9E-02	1.3E-02
Z_{14}		4	2	5.2E-05	9.6E-05	-1.3E-05	-1.3E-04	-1.5E-04	1.9E-04	1.4E-04	9.5E-05	3.8E-05	-5.8E-05	1.5E-04	1.4E-04	1.5E-04
Z_{15}		4	4	4.6E-03	5.0E-03	5.4E-03	5.3E-03	4.7E-03	4.8E-03	5.0E-03	5.2E-03	5.3E-03	5.4E-03	4.9E-03	5.0E-03	5.1E-03
	ROC			22.36	23.52	24.98	29.77	34.08	22.77	23.47	24.12	25.16	26.80	21.50	24.91	31.82

Table C.7: The Zernike coefficient of the optothermally actuated VFM measured in the optical setup using Shack-Hartmann Wavefront Sensor.

Laser Source				488 nm					514 nm						532 nm				
Output Power [mW]				6	12	22	30	38	0	3	6	10	15	19	0	13	24	29	50
Absorbed Power [mW]				3.6	7.2	13.2	18	22.8	0	2	4	6.5	9.8	12.4	0	8.6	16.3	19.3	33.2
Pupil Diameter X [mm]				0.742	0.74	0.747	0.756	0.762	0.745	0.749	0.745	0.74	0.742	0.749	0.738	0.741	0.751	0.766	0.759
Pupil Diameter Y [mm]				0.723	0.729	0.744	0.755	0.758	0.714	0.72	0.719	0.725	0.731	0.738	0.714	0.727	0.71	0.717	0.72
Z [mm]	**Name**	**n**	**m**	**Zernike coefficient [μm]**															
Z_1	Piston	0	0	-0.707	-0.67	-0.59	-0.549	-0.531	-0.696	-0.688	-0.672	-0.664	-0.63	-0.588	-0.762	-0.625	-0.679	-0.659	-0.61
Z_2	Tip y	1	-1	-0.033	-0.03	-0.038	-0.031	-0.026	-0.068	-0.064	-0.055	-0.051	-0.05	-0.047	-0.227	-0.081	-0.194	-0.212	-0.183
Z_3	Tilt x	1	1	0.202	0.192	0.166	0.154	0.152	0.206	0.205	0.196	0.201	0.184	0.166	0.413	0.164	0.344	0.349	0.301
Z_4	Astigmatism +45/-45Deg	0.007	0.003	-0.001	-0.004	-0.003	0.006	0.005	0.007	0.003	0.007	0.003	0.016	0.006	0.015	0.017	0.016		
Z_5	Defocus	2	0	0.54	0.512	0.473	0.439	0.416	0.565	0.553	0.537	0.52	0.498	0.477	0.56	0.54	0.513	0.503	0.475
Z_6	Astigmatism 0/90Deg	2	2	-0.008	-0.006	-0.01	-0.008	-0.009	-0.013	-0.01	-0.012	-0.01	-0.009	-0.01	0	-0.004	0.001	0.002	0.001

Table C.8: List of the sensor distance (D_s) and object distances (L_{omax}, L_{omin}), object tracking range (ΔL) of the varifocal optical imaging system.

Actuation Methods		**Actuation Power**	D_s	**ROC**	**Calculated** L	**Measured** L'	**Difference** $\frac{\lvert L_0 - L'_0 \rvert}{L_0}$	**Object Tracking Range: ΔL**	D_n	D_f	**DOF**
		[mW]	[mm]	[mm]	[mm]	[mm]	[%]	[mm]	[mm]	[mm]	[mm]
ETM	Figure 4.35	0	15	22	41.25	41.5±1.5	0.60%	134	38.4	44.7	6.2
		31		27.6	175.7	175.5±1.5	0.10%		125.4	29.32	167.8
ETM	Figure 4.36	0	16.5	22	33	32.5±1	1.50%	52	31.1	35.1	4.0
		31		27.6	85	85±1	0%		71.2	105.4	34.2
ETM	Figure 4.37	0	17.5	22	29.6	30.5±2	3%	36	28.1	31.3	3.2
		31		27.6	65.7	66.5±1.5	1.20%		57.1	77.3	20.1
OT	Figure 4.38	0	15	22.5	45	44±1	2.2%	165*	41.7	48.9	7.2
		22.8		27.5	165	209	27%		133.1	217.1	84.0

ETM and OT are short for electrothermal and optothermal actuation methods respectively. The value of optothermal actuation power listed is the incident laser power with the absorption of 60%. (* this value has an error due to depth of field as described in the text.)

Table C.9: The experimental measurements of static tilt angles of microscanner, in Section 5.4, when driving each of the electrothermal actuator.

Electrothermal actuator #1									Electrothermal actuator #2						
Voltage	Current [mA]	Power [mW]	R [mm]	Horizontal [mm]	Vertical [mm]		Δd [mm]	θ [°]	Current [mA]	Power [mW]	Horizontal [mm]	Vertical [mm]		Δd [mm]	θ [°]
0	0.3	0.0		0	0		0	0.0	0.4	0.0	0	0		0	0.0
1	2.5	2.5		0	0		0	0.0	2.5	2.5	0	0		0	0.0
2	4.6	9.1		0	0		0	0.0	4.6	9.2	0	0		0	0.0
3	6.4	19.3		0	0		0	0.0	6.5	19.4	0	0		0	0.0
4	8.1	32.2		0	0		0	0.0	8.1	32.4	0	0		0	0.0
5	9.5	47.3		-0.5	-0.5	45	0.7	-0.2	9.5	47.5	0.7	0.7	45	1.0	0.3
6	10.6	63.8		-1.2	-1.2	45	1.7	-0.5	10.7	64.1	1.5	1.0	34	1.8	0.5
7	11.7	81.6	205	-2.3	-1.5	33	2.7	-0.8	11.7	81.7	2.5	2.0	39	3.2	0.9
8	12.5	99.9		-3.8	-2.7	35	4.7	-1.3	12.5	100.2	4.3	3.0	35	5.2	1.5
9	13.2	118.7		-5.2	-3.5	34	6.3	-1.8	13.2	119.1	5.8	4.0	35	7.0	2.0
10	13.8	138.0		-7.0	-4.5	33	8.3	-2.3	13.9	139.3	7.7	5.0	33	9.2	2.6
11	14.4	157.9		-8.4	-5.4	33	10.0	-2.8	14.4	158.2	9.0	6.0	34	10.8	3.0
12	14.9	178.4		-9.6	-6.2	33	11.4	-3.2	14.9	178.7	10.5	7.0	34	12.6	3.5
13	15.4	200.1		-11.0	-7.2	33	13.1	-3.7	15.4	200.2	11.7	7.9	34	14.1	3.9
14	16.0	223.4		-12.3	-8.0	33	14.7	-4.1	16.0	223.4	13.0	8.5	33	15.5	4.3
15	16.6	249.0		-13.3	-9.0	34	16.1	-4.5	16.6	249.0	14.2	9.2	33	16.9	4.7

Table C.10: The results of optical scan angles when driven electrostatic comb-drives of the microscanner in Section 5.4.

Signal type		Offset Sinusoidal Voltage Signal			
V_{P-P} [V]	R [mm]	Resonant Frequency [Hz]	Scan Direction	Δd [mm]	δ [°]
10		383.4		2	0.5
15				4	0.9
20		381.4		6	1.4
25				11	2.5
30		381.6		16	3.7
35	250		almost vertical	19.5	4.5
40		382.4		23	5.3
45				28	6.4
50		382.7		33	7.5
55				37	8.4
60		383.5		41	9.3

V_{P-P} is the peak to peak voltage level of the AC voltage signal,
R is the distance between the screen and the microscanner,
Δd is the scan length of the reflected laser spot,
δ is the characterised optical scan angle of the microscanner.

Table C.11: Summary of the geometry and the meshing quality of each part in microscanner FEM model meshed using hexahedrons and generated by the same algorithm.

Parts		Unit	Two Electrothermal actuators	Electrostatic comb-drives	Two Serpentine Springs	Ring Shape Frame	Gold Coated Micromirror	
							Silicon Layer	Gold Layer
Volume		μm^3	5.4E+06	3.0E+06	2.40E+05	4.15E+05	1.13E+07	7.33E+05
Maximum Model Sufrace Area		μm^2	271200	111300 , 75182.7	11987.8	41517.7	1.13E6	1.13E6
Parts Aspect Ratio			52	27.5	11	20	106	1634
Meshing Element Shape			Parabolic Hexaderons					
Meshing Algorithm			Hex-Dominant					
Number of volume meshing elements			2706	2233	348	556	3246	3246
Number of volume meshing nodes			37413	35433	5724	8934	39561	39561
Element Aspect Ratio	Min		1	1	1	1	1.1	14.3
	Max		3.5	8.5	15.1	39.8	4.3	65.9
	Average		2.1	1.5	1.8	1.8	2.5	38.9
Element Corner Angle	Min		21.5	14	12.6	1.3	35.2	35.2
	Max	^{o}	156.1	165.5	161.9	176	137.7	137.7
	Average		89.9	89.8	89.4	89.4	90.0	90.0
Edge Length	Min		2.6	1.4	0.03	0.02	6.7	0.65
	Max	μm	28.8	31.1	19.2	17.4	31.7	31.7
	Average		16.8	11.5	9.5	9.6	17	15.1

Table C.12: Summary of the geometry and the meshing quality of each part of microscanner FEM model meshed using tetrahedrons.

Parts		Unit	Two Electrothermal actuators	Electrostatic comb-drives	Two Serpentine Springs	Ring Shape Frame	Gold Coated Micromirror (*)	
							Silicon Layer	Gold Layer
Volume		μm^3	5.4E+06	3.0E+06	2.40E+05	4.15E+05	1.13E+07	7.33E+05
Maximum Model Sufrace Area		μm^2	271200	111300 , 75182.7	11987.8	41517.7	1.13E6	1.13E6
Parts Aspect Ratio			52	27.5	11	20	106	1634
Meshing Element Shape			Parabolic Tetrahedrons					
Meshing Algorithm			-	-	-	-	-	
Number of volume meshing elements			7060	8753	2605	2761	6290	5792
Number of volume meshing nodes			16985	22430	6503	6684	13142	12224
Element Aspect Ratio	Min		1	1	2.1	1	1	3.4
	Max		15.7	23.6	1.0	249.9	18.8	290
	Average		3.6	2.3	10.2	3.1	3.5	51.3
Element Corner Angle	Min		4.4	3	0.2	0.23	2.7	0.2
	Max	^{o}	160	160	144.8	157.4	165	178
	Average		70	70	69.7	70	70.1	69.9
Edge Length	Min		2.4	1.9	0.02	0.02	1.6	0.3
	Max	μm	118.0	96	45	47.7	188.5	188.5
	Average		28.5	17	10.4	11.9	26.8	27

(*): Due to convergence difficulty, the effective stress gradient of the 13 MPa/μm is applied to the SOI layer of the micromirror, in stead of applying the residual stresses of gold and SOI layer and stress gradient of 2.4 MPa/μm.

Table C.13: Summary of the geometry and the meshing quality of parts in microscanner FEM model meshed using hexahedrons with different meshing algorithm.

Parts		Unit	Two Electrothermal actuators	Electrostatic comb-drives	Two Serpentine Springs	Ring Shape Frame	Gold Coated Micromirror	
							Silicon Layer	Gold Layer
Volume		μm^3	5.4E+06	3.0E+06	2.40E+05	4.15E+05	1.13E+07	7.33E+05
Maximum Model Sufrace Area		μm^2	271200	111300 , 75182.7	11987.8	41517.7	1.13E6	1.13E6
Parts Aspect Ratio			52	27.5	11	20	106	1634
Meshing Element Shape			Manhattan Bricks		Extruded Bricks		Extruded Bricks(*)	
Meshing Algorithm			-	-	Partition	Split and Merge	Pave, Qmorph	
Number of volume meshing elements			6840	4107	660	1563	10332	25553
Number of volume meshing nodes			12256	8768	1776	3112	14260	51736
Element Aspect Ratio	Min		6	3	2.4	1.2	1.7	5.5
	Max		9	11.85	6.5	9.4	12.7	23.7
	Average		6.3	6.2	4.5	5.2	7.2	13.7
Element Corner Angle	Min		90	90	70	7.3	35.3	46.6
	Max	o	90	90	112.5	170.6	138.2	134.9
	Average		90	90	90	90	90	90
Edge Length	Min		15.2	3.3	1.8	0.01	2.7	0.65
	Max	μm	3.3	39.5	21.5	19.5	35.8	5.4
	Average		30	12.9	8.9	9.2	13.9	13.8

Table C.14: The finite element simulation results of the electro-thermo-mechanical behaviour of the hexahedrons meshed microscanner model when driving both two electrothermal actuators equally.

Thermal Actuators				Vertical Displacement				Mechanical Tilt Angle		Optical Tilt Angle			
Voltage per Thermal Actuator [V]	Current per Thermal Actuator [mA]	Total Power [mW]	Max Temperature on thermal actuator [°C]	Point A [μm]	Point B [μm]	Point C [μm]	Point D [μm]	about X-axis [°]	about Y-axis [°]	about X-axis [°]	about Y-axis [°]	Mirror Surface Average Temperature [°C]	Mirror Surface Curvature [mm]
0	0.0	0.0	20.0	53.0	5.7	29.7	29.5	2.3	0.0	0.0	0.0	20.0	21.7
1	1.5	3.0	28.3	53.0	5.7	29.7	29.5	2.3	0.0	0.0	0.0	21.2	21.8
2	3.0	12.0	54.8	53.4	5.9	30.0	29.8	2.3	0.0	0.0	0.0	24.5	21.9
3	4.4	26.3	106.9	57.6	7.1	32.7	32.5	2.4	0.0	0.3	0.0	29.8	22.2
4	5.6	45.0	186.5	71.8	11.2	41.8	41.6	2.9	0.0	1.3	0.0	36.6	22.5
5	6.5	65.3	302.5	95.3	17.7	56.9	56.7	3.7	0.0	2.9	0.0	44.0	22.9
6	7.0	84.2	436.9	118.1	24.2	71.5	71.3	4.5	0.0	4.5	0.0	50.4	23.2
7	7.8	109.4	598.7	144.4	31.6	88.4	88.0	5.4	0.0	6.3	0.0	56.2	23.5
8	8.7	139.8	776.0	170.0	38.9	104.9	104.5	6.3	0.0	8.0	0.0	60.7	23.8
9	9.7	174.6	949.3	194.5	45.9	120.6	120.2	7.1	0.0	9.7	0.0	63.9	24.0
10	10.7	213.6	1099.6	214.7	51.7	133.7	133.2	7.8	0.0	11.1	0.0	66.1	24.1
11	11.7	256.7	1229.5	231.6	56.6	144.6	144.1	8.4	0.0	12.3	0.0	67.8	24.2
12	12.7	303.9	1346.5	246.4	60.9	154.2	153.6	8.9	0.0	13.3	0.0	69.2	24.3
13	13.7	355.1	1450.7	259.6	64.7	162.7	162.1	9.3	0.0	14.2	0.1	70.3	24.4
14	14.7	410.4	1544.5	271.5	68.2	170.4	169.8	9.8	0.0	15.0	0.1	71.2	24.5
15	15.7	469.7	1630.7	282.2	71.4	177.4	176.7	10.1	0.0	15.7	0.1	72.0	24.5
16	16.7	533.0	1710.8	292.1	74.3	183.8	183.1	10.5	0.0	16.4	0.1	72.8	24.6
17	17.7	600.3	1786.0	301.2	77.0	189.7	189.0	10.8	0.0	17.0	0.1	73.4	24.6
18	18.7	671.7	1857.2	309.7	79.6	195.2	194.5	11.1	0.0	17.6	0.1	74.1	24.6

Table C.15: The finite element simulation results of the electro-thermo-mechanical behaviour of the tetrahedrons meshed microscanner model when driving both two electrothermal actuators equally.

Thermal Actuators				Vertical Displacement				Mechanical Tilt Angle		Optical Tilt Angle			
Voltage per Thermal Actuator [V]	Current per Thermal Actuator [mA]	Total Power [mW]	Max Temperature on thermal actuator [^{o}C]	Point A [μm]	Point B [μm]	Point C [μm]	Point D [μm]	about X-axis [^{o}]	about Y-axis [^{o}]	about X-axis [^{o}]	about Y-axis [^{o}]	Mirror Surface Average Temperature [^{o}C]	Mirror Surface Curvature (*) [mm]
0	0.0	0.0	20.0	53.0	5.7	29.5	29.6	2.3	0.0	0.0	0.0	20.0	21.3
1	1.5	3.0	28.3	53.0	5.7	29.5	29.6	2.3	0.0	0.0	0.0	21.2	21.4
2	3.0	12.0	54.8	53.4	5.9	29.8	29.9	2.3	0.0	0.0	0.0	24.5	21.5
3	4.4	26.3	106.9	57.5	7.1	32.5	32.5	2.4	0.0	0.3	0.0	29.8	21.8
4	5.6	45.0	186.5	71.6	11.1	41.5	41.5	2.9	0.0	1.3	0.0	36.6	22.1
5	6.5	65.3	302.5	95.0	17.7	56.4	56.5	3.7	0.0	2.9	0.0	43.9	22.5
6	7.0	84.2	437.0	117.7	24.1	71.0	71.1	4.5	0.0	4.4	0.0	50.3	22.8
7	7.8	109.4	598.7	143.8	31.5	87.7	87.8	5.4	0.0	6.2	0.0	56.1	23.2
8	8.7	139.8	776.0	169.4	38.8	104.0	104.2	6.2	0.0	8.0	0.0	60.6	23.4
9	9.7	174.6	949.3	193.7	45.7	119.7	119.8	7.1	0.0	9.6	0.0	63.8	23.6
10	10.7	213.6	1099.6	213.9	51.5	132.6	132.8	7.8	0.0	11.0	0.0	66.0	23.8
11	11.7	256.7	1229.5	230.7	56.4	143.4	143.6	8.4	0.0	12.2	0.0	67.7	23.9
12	12.7	303.9	1346.5	245.4	60.7	152.9	153.1	8.9	0.0	13.2	0.0	69.0	24.0
13	13.7	355.1	1450.6	258.6	64.6	161.4	161.6	9.3	0.0	14.1	0.0	70.1	24.0
14	14.7	410.3	1544.5	270.4	68.0	169.0	169.2	9.7	0.0	14.9	0.0	71.1	24.1
15	15.7	469.6	1630.6	281.1	71.2	176.0	176.1	10.1	0.0	15.6	0.0	71.9	24.1
16	16.7	532.9	1710.7	290.9	74.1	182.3	182.5	10.4	0.0	16.3	0.0	72.7	24.2
17	17.7	600.2	1785.9	300.0	76.8	188.2	188.4	10.7	0.0	16.9	0.0	73.3	24.2
18	18.7	671.6	1857.1	308.4	79.4	193.7	193.9	11.0	0.0	17.5	0.0	73.9	24.3

(*): Due to convergency difficulty, the effective stress gradient of the 13 MPa/μm is applied to the SOI layer of the micromirror, in stead of applying the residual stresses of gold and SOI layer and stress gradient of 2.4 MPa/μm.

Table C.16: The measured optical tilt angles of the microscanner by actuating both electrothermal actuators equally (ambient laboratory temperature is 20 ^{o}C).

V_{dc} [V]	I_{dc} [mA]	Total Power [mW]	Δd [cm]	R [cm]	Static Optical Tilt Angle θ_X [^{o}]	micromirror ROC [mm]
0	0.345	0	0		0.0	17.5
1	2.1	4.2	0		0.0	17.6
2	3.75	15.0	0		0.0	17.6
3	5.3	31.8	0		0.0	18.1
4	6.7	53.6	0.1		0.3	18.3
5	7.9	79.0	0.2		0.5	18.5
6	8.95	107.4	0.4		1.1	18.9
7	9.85	137.9	0.7		1.8	19.4
8	10.6	169.6	0.9		2.4	19.7
9	11.3	203.4	1.2	21.15	3.1	20.3
10	11.9	238.0	1.4		3.8	21.0
11	12.4	272.8	1.5		4.1	21.8
12	12.85	308.4	1.7		4.6	22.2
13	13.25	344.5	1.9		5.0	23.4
14	13.7	383.6	2.0		5.4	24.3
15	14.1	423.0	2.2		5.9	24.5
16	14.55	465.6	2.3		6.2	26.5
17	15	510.0	2.5		6.7	28.2
17.5	15.2	532.0	2.6		6.9	28.8

V_{dc} is the voltage applied to each electrothermal actuator,
I_{dc} is the current through each electrothermal actuator,
Δd is the displacement length of reflected laser spot,
R is the distance from the microscanner to the microscanner.

Appendix D

MATLAB Codes

M-file code for calculate the Zernike coefficient from the surface profile

```
% This file is created by Li Li on 20th May 2012.
% The purpose of this file is to prepare the data of the
% curved fitted surface profile measurement for the
% 'ZernikeCalc'function to calculate and plot the Zernike
% coefficients of the varifocal micromirorr (S25bD2).

clear all; clc; close all;

%Import data
filenameraw = 'CLC70DegC-subfitscale.dat'; % all data in [mm]
data = importdata(filenameraw);

% Extra measurement data array, size from the imported data.
wykoraw = importdata(filenameraw,'\t',1);
wykoraw = wykoraw.data;
rowsize = data(1,1);
colsize = data(1,2);

% Create row and col index(position) array
row = zeros(rowsize,1);     % [mm]
```

```
col = wykoraw(1:colsize,2); % [mm]
datar = zeros(rowsize,colsize); %[mm]

% Reshape 1D data array into 2D data
for m = 1:rowsize
    row(m) = wykoraw((m-1)*colsize+1,1);
    for n = 1:colsize
          datar(m,:)=wykoraw((m-1)*colsize+1:m*colsize,3);%[mm]ETM
    end
end

% Plot the curve fitted surface profile data
figure(1)
imshow(datar,[min(min(datar)),max(max(datar))]);
title(filenameraw)

% plot zernike fit
zernikelist = [0 1 1 2 2 2 3 3 3 3 4 4 4 4 4;...
               0 -1 1 -2 0 2 -3 -1 1 3 -4 -2 0 2 4]
ZernikeCalc(zernikelist, datar, [], 'STANDARD')

% Calculate the zernike coefficients
z = ZernikeCalc(zernikelist, datar, [], 'STANDARD')
```

IOP PUBLISHING JOURNAL OF MICROMECHANICS AND MICROENGINEERING
J. Micromech. Microeng. **21** (2011) 025022 (9pp) doi:10.1088/0960-1317/21/2/025022

Single pixel optical imaging using a scanning MEMS mirror

Li Li[1], Vladimir Stankovic[1], Lina Stankovic[1], Lijie Li[2], Samuel Cheng[3] and Deepak Uttamchandani[1]

[1] Department Electronic and Electrical Engineering, University of Strathclyde, Glasgow, G1 1XW, UK
[2] School of Engineering, Swansea University, Swansea, SA2 8PP, UK
[3] School of Electrical and Computer Engineering, University of Oklahoma, Tulsa, OK 74135-2512, USA

E-mail: vladimir.stankovic@eee.strath.ac.uk

Received 9 November 2010, in final form 17 December 2010
Published 27 January 2011
Online at stacks.iop.org/JMM/21/025022

Abstract
The paper describes a low-complexity optical imaging system using demagnifying optics, a single scanning MEMS mirror and a single photodetector. Light at visible wavelengths from the object passes through a lens assembly and is incident on a scanning MEMS micromirror. After reflection from the micromirror, a complete image of the object is projected at the image plane of the optical system where a single-element photodetector with a pinhole at its entrance is located. By tilting the micromirror in the *x* and *y* directions, the projected image is translated across the image plane in the *x* and *y* directions. The photodetector sequentially detects the intensity of different areas of the projected optical image, thereby enabling a digital image to be generated pixel-by-pixel. However, due to the noisy raw image obtained experimentally, an image enhancement algorithm based on iterative-combined wavelet and curvelet denoising has been developed. Using blind image quality indices (BIQI) as an objective performance measure, it is shown that the proposed image enhancement method enhances the raw image by up to 40% and outperforms state-of-the-art denoising methods for up to 10 units of BIQI.

(Some figures in this article are in colour only in the electronic version)

1. Introduction

In the field of optical imaging the development of smaller, faster and cheaper image acquisition systems is a constant challenge. Image acquisition systems incorporating optical MEMS components have included *in-vivo* medical imaging [1, 2]; high resolution microscopic imaging [3]; adaptive imaging [4, 5] and low-cost variable focus imaging in consumer devices [6, 7].

In many safety and surveillance requirements, infrared image acquisition (or indeed imaging at other non-visible wavelengths) is required to detect concealed targets [8] or objects [9] and there is also a requirement for high-sensitivity imaging at visible wavelengths at very low ambient light levels [10]. Imaging arrays having non-visible wavelength response or very low light level response are costly to manufacture. For example, an infrared array would cost around 100 times more than a visible array of comparable resolution. An alternative approach to imaging arrays is to use a single photodetection element having the required wavelength sensitivity or light level sensitivity, and then generating images from the single detector by combination with suitable optics and electronics. Such an image acquisition system can be described as a 'single-pixel imager'. One embodiment of a single-pixel imager has incorporated a digital micromirror device (DMD) at its core, and applied the relatively new mathematical theory and algorithms of compressive sampling to produce images using just a single photodetection element [11]. Detailed description of 'compressive imaging' [11, 12], where the number of physical measurements is much smaller than the number of desired or reconstructed image pixels, is beyond the scope of this paper. However, the cost and size of the DMDs employed in single-pixel imagers using compressive imaging, together with problems of coherence and diffraction due to the small size of the individual elements of the DMD array, make this architecture still unacceptable for many imaging applications at non-visible wavelengths.

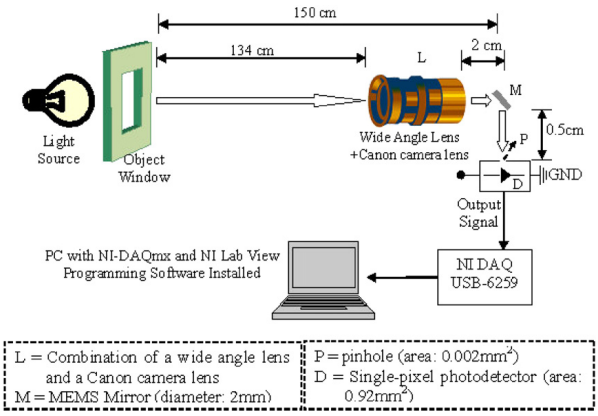

Figure 1. Schematic diagram of an optical setup.

In this paper, an alternative concept of a single-pixel imager using a single MEMS scanner and a single photodetection element is presented. The imaging system described here is fundamentally different from the compressive imager of [11, 12] because in the present system each measurement corresponds to one part of the object only (one pixel in the resulting raw image) and by tilting the micromirror in the horizontal and vertical directions the entire object is scanned; on the other hand, in compressive imaging a DMD is employed to provide successive measurements, where each measurement 'covers' the entire object but where mirrors in the DMD are randomly activated. Both approaches then use computational techniques to obtain more pixel values than the actual number of measurements conducted. The key features of our proposed method are low cost and small size of the imager due to a single detector and a single scanning mirror being employed. Moreover, the MEMS scanning mirror used is far easier to fabricate and operate compared to the DMD used in compressive imagers.

The remainder of this paper is organized as follows: section 2 describes our experimental single-pixel imaging system; section 3 presents the design, fabrication and characterization of the MEMS scanner used; in section 4, we discuss experimental results; section 5 describes the image enhancement algorithms for improving the raw experimental images and results, and the final section summarizes the main achievements of this work.

2. System setup

This section gives a description of the optical setup of our single-pixel imager. For demonstration purposes, the experimental architecture was built for visible wavelengths, but the concept can easily be translated to the infrared or other wavelengths.

The experimental setup is shown in figure 1. Light originating from the object passes through a lens system which demagnifies the object so that the light can be intercepted by the MEMS mirror surface (2 mm in diameter). To achieve this, the combination of a Canon EFS 18–55 mm lens and a wide lens (fish-eye lens) L is used to direct the optical path towards the MEMS scanner. After reflecting from the surface of the MEMS scanning micromirror M, light from the object forms an image at the image plane of the optical system. Located at this image plane is a pinhole of diameter 50 μm. Immediately behind the pinhole is the single photodetector. The image formed by the optics can be laterally shifted in the x–y directions in the image plane under the control of the MEMS scanner so that the optical intensity of a small part of the image (a part whose area equals that of the pinhole) is converted into a voltage signal by the photodetector.

The use of a MEMS scanner to move an image in steps of a few microns has been previously encountered in the context of generating super-resolved digital images [3] in microscopy. In the work of [3], a MEMS scanner is used to shift an image produced from an optical microscope system across the face of a photodetector array. The image is only shifted by fractions of a pixel size, corresponding to displacements of less than 10 μm across the entire imaging array. Several low-resolution shifted images are captured by the imaging array and entered into a super-resolution algorithm to produce a final image with an increased effective pixel number and a better modulation depth (pixel luminance). The above application of image scanning by a MEMS device to improve image quality differs from the image scanning work presented here, which concentrates on using a single photodetector for generating a digital image.

The electrothermal MEMS micromirror employed in our imager deflects the optical image in the x–y plane and experimental results show it can be typically tilted by 1.3 degrees when a maximum dc voltage of 14 V is applied to the long actuator (1800 μm) of the micromirror and by 0.68 degrees when the same voltage level is applied to the short actuator (1600 μm). In the application described in this paper, the scanner is operated with dc voltages applied

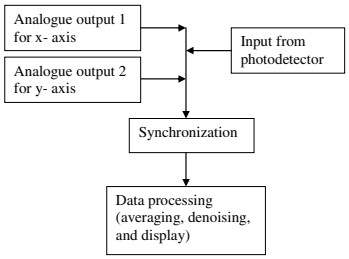

Figure 2. Schematic diagram of LabVIEW control blocks.

in step increments. With the present optical setup, the above maximum tilting angles correspond to a rectangular scan field of roughly 6 cm × 3.2 cm when the scene is 134 cm away from the optical system. More details of the MEMS scanner are in section 3.

The photodetector is an L/V (light to voltage) sensor with integrated transimpedance amplifier. The area of the detector is 0.92 mm^2, and it has a peak sensitivity at a wavelength of 635 nm. A National Instruments Digital Acquisition (NI DAQ) module, which contains a microcontroller programmable by a PC, is used to adjust the mirror orientation in programmable steps. The same PC is also used to collect readings from the photodetector output which is also connected to the NI DAQ module. The scanning rate of the MEMS scanner varies from 50 steps per second to 500 steps per second. We have used in our experiments 100 steps per second which was found to be the rate that offered the best trade-off between acquisition time and image quality. At each step, 100 voltage samples are read from the photodetector output and averaged to generate a pixel value. A control program was developed in LabVIEW in order to drive the scanner as well as to acquire data from the photodetector through the NI DAQ box. The schematic diagram of the LabVIEW function blocks is shown in figure 2. It is seen that the program performs four basic functions: generating signals for the x-axis and the y-axis of the scanner; acquiring measurements from the photodetector; synchronizing the output signals with the input signals; and processing the measurements and displaying images. First, we fixed the control voltage on one actuator (which controls vertical shift) and increased the voltage on the other actuator (which controls horizontal shift) by a fixed voltage step ΔV. For each voltage level, the photodetector measures one part of the projected image. The reading that corresponds to the accumulated brightness of this area is recorded by the PC. By changing the actuator voltage by increments of ΔV, the area seen by the detector shifts from left to right (figure 3(a)). After the entire row is scanned, the voltage on the horizontal actuator is reset and the voltage on the vertical actuator increased in steps (figure 3(b)). This corresponds to conventional scanning with a negative scanning raster. The photograph of the optical setup in our laboratory is shown in figure 4. The dashed arrow shows the path of the light from the object to the photodetector.

3. MEMS scanner: design and characterization

MEMS scanners have been in existence for a long time, and many types of silicon-based scanners have been developed using various driving mechanisms including electrostatic [13, 14], electromagnetic [15, 16], and electrothermal [17, 18]. An electrothermal scanner has been used in this work.

The commercial fabrication process, SOIMUMPs [19], has been used to fabricate the MEMS scanner used in the work, and the fabricated device is shown in figure 5. The fabrication process uses only one structural layer of SOI of a nominal thickness 10 μm in which every part of the scanner is fabricated, namely the micromirror, actuators, micro-suspensions and all electric current carrying tracks and bonding pads. The vertically (i.e. out-of-plane) moving thermal actuators are a single-layer three-beam structure. The three longitudinal beams have an equal width of 50 μm and are equally spaced by 150 μm, and they are all interconnected at the same ends through a 60 μm wide and 450 μm long

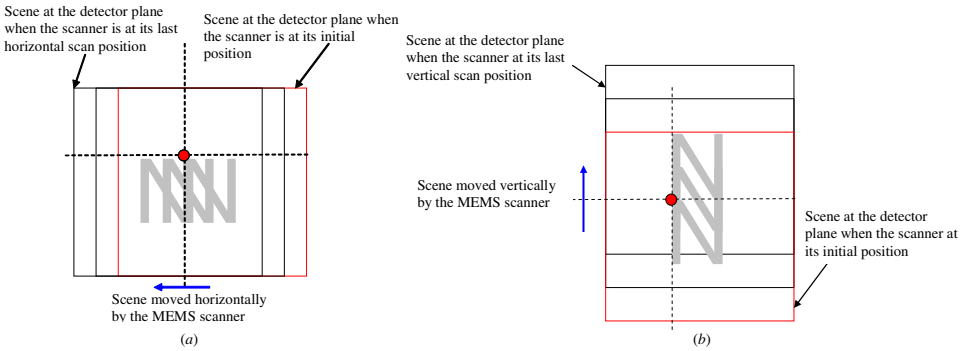

Figure 3. Schematic of stepped scanning of an image using the single MEMS scanner.

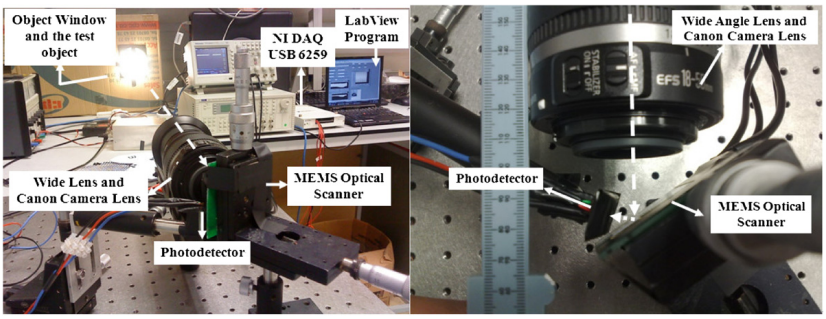

(*a*) (*b*)

Figure 4. (*a*) Photograph of the optical setup (left). (*b*) Top view photograph of an optical setup (right).

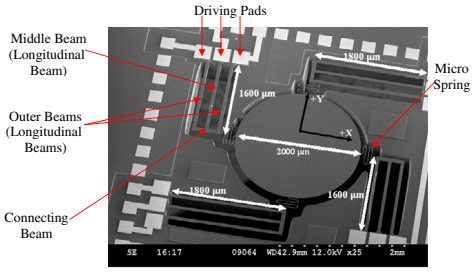

Figure 5. SEM image of the electrothermal MEMS scanner.

connecting beam. Due to the stress gradient through the thickness of the SOI layer, the thermal actuator has an initial out-of-plane displacement when no voltage is applied. When a dc voltage level is applied to the two outer beams of the thermal actuator, the Joule heating causes the outer beams to expand along their longitudinal direction. The combined forces of the thermal expansion of the outer beams and the constraint of the middle beam result in the out-of-plane movement of the thermal actuators and the micromirror [20]. Compared with other types of thermal microactuators, our single-layer unimorph design is effective since the alternative bimorph designs have the potential of delamination between the layers [17]. Other single-layer thermal actuators either deliver in-plane movement [21] or are fabricated with a step structure to differentiate the vertical directions of the expansion force and constraint force to realize the out-of-plane movement [22, 23].

The MEMS scanner used in this work is different from our previous design of [20] in two important ways. Firstly, it has a 12 times increase in the mirror area (from 0.25 mm^2 in [20] to 3.14 mm^2 in this paper) in order to achieve better light collection, and secondly it has the thermal actuators orthogonally connected to the micromirror in order to achieve two-dimensional scanning, compared to one-dimensional scanning of our previous device [20]. For the MEMS scanner used in this paper, experimental scan angles measurements are obtained by measuring the displacement produced on a screen of a laser spot reflected from the micromirror, then converting these into angles by using the screen-to-micromirror distance. The two curves of the scan angle against the dc voltage level for the two orthogonal axes are plotted in figure 6 when driving each of the thermal actuators separately.

The experimental measurements of the micromirror scan angles are plotted together with the Coventorware simulation results of the same device in figure 6. The Coventorware electro-thermal-mechanical displacement simulation of the vertically actuated MEMS scanner takes conduction and convection as the heat loss mechanism. For each simulation result, the displacements at four symmetrical points near the connecting springs on the micromirror were recorded. The micromirror is assumed to be rigid and flat and the tilt angles can be calculated from the displacements and the diameter of the micromirror. The simulations show that below the 5V threshold, this electrothermal scanner produces no significant angular deflection. This feature of the scanner is also observed in the experimental measurements of the device. Typical temperature-dependent properties such as electrical conductivity, thermal conductivity and thermal expansion coefficients are assumed to remain constant during the simulation. This is considered to be the main reason for the increasing difference between the simulated and the measured results at higher voltages. Also, due to the increasing difference between the simulation and experimental results, the simulations go up to 9 V for the 1800 μm thermal actuator and 10 V for the 1600 μm one. The simulation results above the mentioned voltages give non-realistic temperature (about 2000 K) and are not included in the diagram. However, there is good agreement at lower voltages where both simulation and experiments show a threshold voltage of around 5 V and a nonlinear displacement versus voltage behaviour.

4. Experiments

The objects used are the black letters '*R*', '*G*', and '*B*' laser printed on a white sheet of paper as shown in figure 7 (left

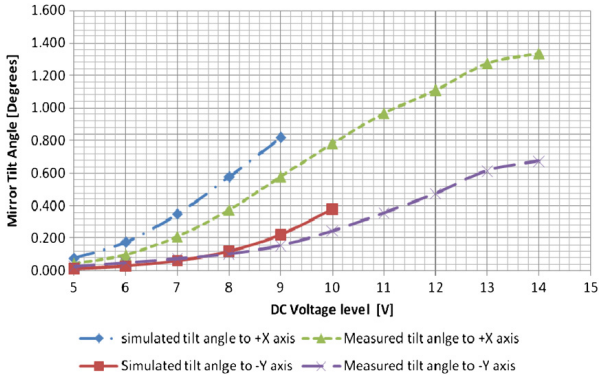

Figure 6. Mirror scan angle of the MEMS scanner shown in figure 5.

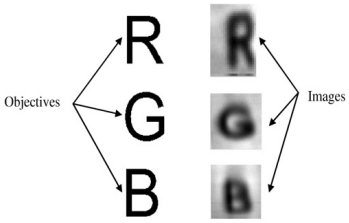

Figure 7. Experimental results of the imaging system; left column: objects; right column: images from the imaging setup.

column). The 32 × 32 pixel images are generated from 1024 measurements obtained by driving each of the two orthogonal thermal actuators with 32 steps of 0.28 volts/step to perform a raster scan of 32 rows and 32 points per row. These voltage steps correspond to an average of 0.021 deg/step in the x direction and an average of 0.043 deg/step in the y direction. The measured data is then arranged as a 32 × 32 pixel image shown in figure 7 (right column). As expected, by directly mapping the measurements into the image matrix, a noisy and blurred image is obtained. At low resolution, images with roughly 20 pixels per inch (ppi) are obtained from raw 32 × 32 pixel images. As shown in figures 9(*a*), 10(*a*) and 11(*a*), the 32 × 32 pixel images have a blocking effect due to large tilt step size. A similar image acquisition procedure was followed to obtain increased resolutions of 40 ppi and 80 ppi, obtained from raw images of 64 × 64 and 128 × 128 pixels, respectively. This was achieved by reducing the voltage steps of both thermal actuators to 64 steps of 0.14 volts/step and 128 steps of 0.07 volts/step, respectively. For the 64 × 64 pixel images, the mirror tilting step is reduced down to an average of 0.011 deg/step in the x direction and an average of 0.022 deg/step in the y direction. For the 128 × 128 pixel images, the mirror tilting steps is an average of 0.005 deg/step in the x direction and an average of 0.011 deg/step in the y direction. In this way, the physical overlapping regions between adjacent reading points are increased and result in much smoother images as shown in figures 9(*b*), 10(*b*) and 11(*b*). However, the increased resolution (decreased step size) also enlarges the information overlapping space between adjacent pixels. This results in a blurring effect at the edges of the black patterns and white background. The raw imaging acquisition time is largely dependent on the image size and the scanning rate of the MEMS scanner.

Image resolution, i.e. the number of pixels per inch, also depends on the ratio of the image size at pinhole plane to the pinhole size; the higher this ratio is, the higher the resolution. Thus, there are two practical approaches that can increase the raw image resolution: (1) reduce size of the pinhole and (2) increase size of the image at pinhole plane. For the first approach, a much smaller pinhole will yield a reduced signal-to-noise ratio. Indeed, an attempt to use a pinhole of 25 μm in diameter was not successful. For the second approach, increasing image size at the image plane involves generating a wider scan angle from the MEMS scanner to capture the complete image.

5. Image enhancement

As seen above, due to the very low complexity of the optical system, the resulting images are blurred and noisy. Thus, image enhancement is an essential next step in the overall operation of the single-pixel imager. In this section, we propose a method that iteratively combines wavelet and curvelet transforms to enhance the image quality, and assess the effect of the enhancement algorithm on the experimentally acquired images both visually and objectively using the blind image quality indices (BIQI) [24].

The acquired images suffer from severe random noise, low resolution, and blurring. Due to the specific nature of the images and significant distortion of the resulting raw images, there does not exist a single transform that can lead to a satisfactory enhanced result. For example, the discrete wavelet transform (DWT) is good for representing edges

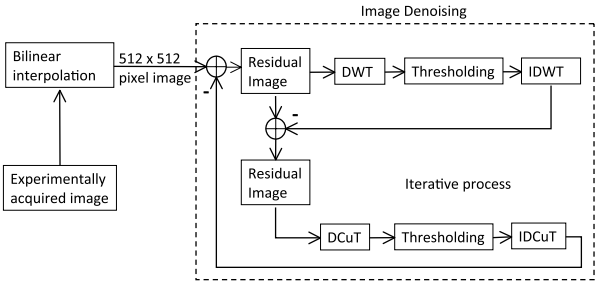

Figure 8. Iterative wavelet-curvelet denoising algorithm.

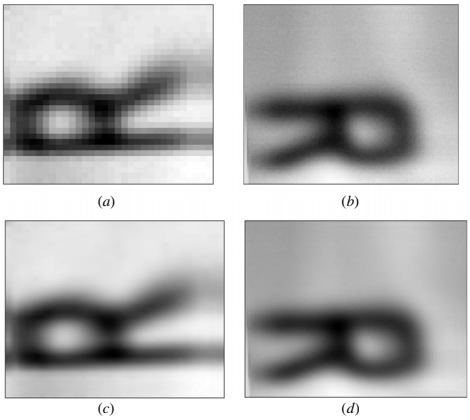

Figure 9. (*a*) and (*b*) Raw image R at 32 × 32 and 128 × 128 pixels, respectively. (*c*) and (*d*) Image R, post image processing, recovered from (*a*) and (*b*), respectively.

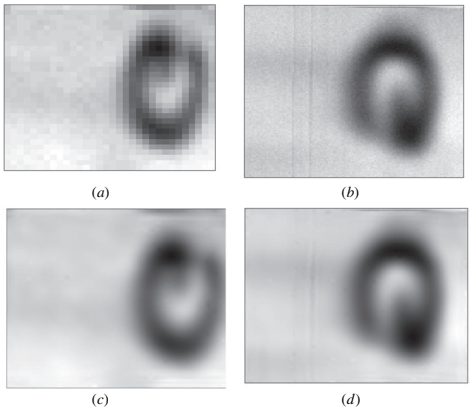

Figure 10. (*a*) and (*b*) Raw image G at 32 × 32 and 128 × 128 pixels, respectively. (*c*) and (*d*) Image G, post image processing, recovered from (*a*) and (*b*), respectively.

and singularities, Fourier transform for some textures, and curvelets for ridges and curvilinear features. One way of taking advantage of different transforms is to iteratively combine them. This leads to the combined transform method, proposed in [25]. In general, any set of transforms can be combined. In this paper, we propose to iteratively combine DWT and the digital curvelet transform in order to exploit the fundamental complementarities of wavelets and curvelets. Curvelets work well for long curves but poorly for sharp edges, and wavelets handle sharp edges very well but they are not successful with anisotropic objects. Thus, the combination of DWT and curvelet transform should capture well both sharp edges and curve portions in the experimental raw images.

5.1. Background on wavelet and curvelet denoising

Wavelet denoising by soft thresholding [26, 27] is a proven technique for reducing the level of noise in measured data. Its goal is to minimize the mean square error (MSE) of the reconstructed function compared to the original function under the constraint that with high probability the reconstruction is at least as smooth as the original. This constraint is imposed to remove undesirable noise ripples or oscillations, which a straightforward MSE minimization would not be capable of removing. The idea of wavelet denoising by soft thresholding is to first decompose the noisy signal into N levels using a pyramidal wavelet filter, and then apply thresholding on the wavelet coefficients coordinate-wise with a specially selected threshold. Finally, the inverse transform is applied to recover the original data. The DWT provides a multi-resolution representation of a signal by compacting its energy and spreading the energy of the noise, and is often used for image compression. That is, the energy of the signal is concentrated in only a few DWT coefficients having high magnitudes, and the energy of the noise is spread across a large number of DWT coefficients that have low magnitudes. This way a sparse representation of image singularities (corners in an image) is obtained. The DWT of a signal is calculated by passing it through a series of filters. The signal is first passed simultaneously through a low-pass filter and a high-pass filter. To avoid over-completeness of the transform coefficients, the filter outputs are down-sampled.

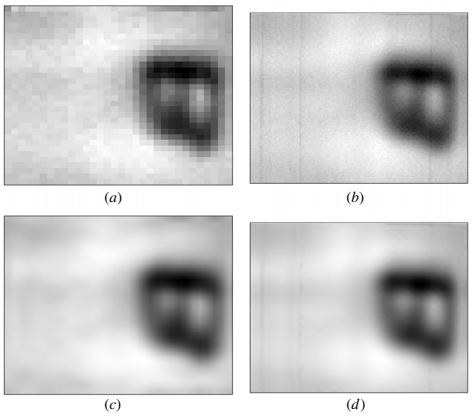

Figure 11. (*a*) and (*b*) Raw image B at 32 × 32 and 128 × 128 pixels, respectively. (*c*) and (*d*) Image B, post image processing, recovered from (*a*) and (*b*), respectively.

This procedure is repeated on the low-pass coefficients to further increase frequency resolution. Unfortunately, DWT does not capture well anisotropic objects, i.e. objects that exhibit properties with different values when measured in different directions.

Curvelets, designed to improve wavelet decomposition for curvy objects, are based on decomposing the image into sub-bands of several different types of transforms: ridgelets [28], multiscale ridgelets, and band-pass filtering. As shown recently in [29], the 'à trous' subband filtering algorithm is especially well suited to the needs of the digital curvelet transform. The algorithm decomposes the full image as a superposition comprising a coarse or a smooth version of the original image together with a representation of the details of the image at a very small scale. The digital curvelet transform [30] comprises four stages: (i) sub-band decomposition, (ii) smooth partitioning, (iii) renormalization, and (iv) ridgelet analysis. Sub-band decomposition decomposes the image into different layers, each carrying details of different frequencies. Smooth partitioning is applied to generate a smooth dissection of the function into 'squares' forming a grid of dyadic squares where the energy of each pixel is divided between all the windows of the grid. Renormalization centres each dyadic square to the unit square. Finally, the ridgelet transform is performed. Based on the sparsity of data in the transform domain, curvelets have been successfully used for enhancing and denoising different types of anisotropic images, including images obtained from astronomy and biomedical applications [25].

5.2. The proposed algorithm

Two techniques are employed on our experimental raw images: (1) interpolation, to improve perceptual quality and (2) denoising, to remove 'measurement noise'. First, we apply bilinear interpolation [31] which interpolates two-dimensional functions, by performing first linear interpolation in one direction and then in the other. This way, the raw image can achieve the desired resolution. Then, the following denoising algorithm is applied on the resulting image.

Wavelet denoising is carried out based on wavelet transformation followed by soft thresholding as explained in the previous section. All DWT coefficients whose absolute value is less than a predefined threshold are set to zeros, whereas the remaining coefficients will have the magnitudes reduced by the threshold. This way, small DWT coefficients which represent noise and the curved portions are removed. The image after the inverse DWT is subtracted from the original interpolated image yielding the residual image. Next, the digital curvelet transform (DCuT) is applied to the residual image. Thresholding is applied on the curvelet coefficients to eliminate small coefficients, that is all DCuT coefficients whose absolute value is smaller than a threshold are set to zero, whereas the magnitudes of the remaining ones are reduced by the threshold. Then, the new residual is obtained by subtracting the inverse curvelet transform result from the previous residual. The above procedure is repeated until a pre-set maximum number of iterations is reached. The appropriate thresholds are found heuristically. The algorithm is represented schematically in figure 8.

At each iteration, the algorithm only computes the wavelet and curvelet transforms of an image. Thus, it is of low complexity and has fast execution time. The algorithm can run in near real time when implemented on hardware or on a PC fitted with graphics processing unit (GPU), as was shown for the wavelet transform in [32]. The only constraint is the image size since the algorithm requires the entire image to be scanned first before processing.

5.3. Visual results

In this subsection we present results of the proposed algorithm applied on the raw image data obtained using the proposed system. Raw images of sizes 32 × 32 pixels and 128 × 128 pixels were used. In all our simulations we used 20 iterations and a three-level biorthogonal (bior5.5) wavelet function in our algorithm to achieve a tradeoff between complexity and performance.

Figures 9–11 show the difference pre- and post-image processing for images R, G and B, respectively, for both image resolutions. Figures 9(*a*) and (*b*) show raw images obtained using the proposed system at 32 × 32 and 128×128 pixel resolution, respectively. Blocking effects present due to a large pixel size are obvious in figure 9(*a*). On the other hand, the 128 × 128 pixel image in figure 9(*b*) suffers from high measurement noise and it is still blurred. Figures 9(*c*) and (*d*) are obtained using the algorithm proposed in section 5.2 with raw images of figures 9(*a*) and (*b*), respectively. The raw images are always interpolated first to 512 × 512 pixel size before denoising. It can be seen that the blocking effects are removed by bilinear interpolation. The effect of noise in image (b) is reduced and the image is sharper. An interesting observation is that the qualities of images (c) and (d) are very similar.

Table 1. Comparison between five different image enhancement algorithms in terms of BIQI for three different images. Original image refers to the image obtained with the experimental setup of section 2 prior to image processing.

	Letter *G*		Letter *B*		Letter *R*	
Resolution	32 × 32	128 × 128	32 × 32	128 × 128	32 × 32	128 × 128
Original image (no denoising)	64.05	88.95	62.13	95.69	69.99	100
FD	57.79	68.71	61.9	61.9	73.29	62.12
DT-DWT	50.54	60.57	61.41	61.41	86.45	60.99
DD-DT-DWT	61.92	87.61	93.83	93.83	73.66	99.38
ST	51.24	78.44	87.75	87.75	78.07	77.98
Proposed	52.53	55.48	58.87	69.89	64.02	58.55

Similar results are obtained for images of G and B as shown in figures 10 and 11. The 32 × 32 raw images again suffer from blocking effects, whereas 'salt and pepper noise' dominates in the 128 × 128 pixel images. The recovered images shown in figures 10(*c*) and (*d*), from figures 10(*a*) and (*b*), respectively, improve overall visual experience.

In summary, it can be seen that the image processing algorithm has improved overall visual quality of the raw images produced from a very simple image acquisition system. An even more interesting observation is that there is a barely noticeable quality difference between the recovered images from the original 32 × 32 pixels and 128 × 128 pixels. This leads to the significant implication that a low-resolution image can be captured by an imaging system having low acquisition complexity and still be recovered with quality almost equivalent to the case if a higher resolution image was captured.

5.4. Objective measures

In this subsection we present results of the proposed algorithm applied on the raw image data obtained using the proposed system and four other recent denoising algorithms for comparison using an objective measure.

Four advanced image denoising techniques were used to enhance the experimental acquired image: (i) framelet denoising (FD) [33], (ii) complex 2D dual-tree DWT (DT-DWT) [34], (iii) complex 2D double-density dual-tree DWT (DD-DT-DWT) [35], and (iv) wavelet denoising with soft thresholding (ST) [26, 27]. Since we do not have a reference image, we have to resort to non-referenced (or blind) quality measures. As an objective blind quality measure we used blind image quality indices (BIQI) [24], which provide a quality index between 0 and 100 (0 being the best quality and 100 the worst). It takes into account artefacts due to white Gaussian noise, blurring, fast fading and jpeg and jpeg2000 compression relying on visual experience. The results for the letters *G* and *R* with two different resolutions of the original image (32 × 32 and 128× 128) are given in table 1.

It can be seen from table 1 that the proposed iterative wavelet-curvelet algorithm outperforms the other methods in all cases except 32 × 32 Letter *G* and 128 × 128 Letter *B*, when DT-DWT is the best. Note that the image processing algorithms perform in general better for 128 × 128 resolution images leading to a larger improvement compared to the original image. However, the final results are not necessarily better with 128 × 128 images compared to 32 × 32 images.

6. Conclusion and future work

The paper presents a proof-of-concept image acquisition system based on a single MEMS micromirror and a single photodetector with a pinhole at its entrance. The research undertaken lays the foundation for developing imaging sensors at wavelengths where detector arrays are unavailable, costly or have poor performance, and so single detectors have to be used. The problem of very low resolution has been discussed and several approaches to improve the image quality are presented. An image-enhancement algorithm based on wavelet and curvelet denoising was proposed to improve the quality of the raw images acquired experimentally. The proposed algorithm was compared with other advanced image enhancement algorithms, using the objective BIQI measure, and found to generate the best results in most cases.

Various techniques that can be used for improving the image resolution have been outlined including using a smaller pinhole, employing wider angle scanners, and using some advanced image processing techniques to eliminate uncertainties from the overlapped readings. The application of the above hardware and algorithms to the non-visible wavelengths is part of our future work.

Acknowledgments

The authors wish to acknowledge support from the University of Strathclyde 2008 Annual Research Prize Award and support from the Glasgow Research Partnership in Engineering (GRPE). The work reported in this paper is also partly supported by the Electro-Magnetic Remote Sensing (EMRS) Defence Technology Centre established by the UK Ministry of Defence and run by a consortium of SELEX Galileo, Thales UK, Roke Manor Research and Filtronics.

References

[1] Dickensheets D L and Kino G S 1998 Silicon-micromachined scanning confocal microscope *J. Microelectromech. Syst.* **7** 38–47

[2] Miyajima H, Asaoka N, Isokawa T, Ogata M, Aoki Y, Imai M, Fujimori O, Katashiro M and Matsumoto K 2003 A MEMS electromagnetic optical scanner for a commercial confocal laser scanning microscope *J. Microelectromech. Syst.* **12** 243–51

[3] Yu K, Park N, Lee D and Solgaard O 2007 Superresolution digital image enhancement by subpixel image translation with a scanning micromirror *IEEE J. Sel. Top. Quantum Electron.* **13** 304–11

[4] Perreault J A, Bifano T G, Levine M B and Horenstein M N 2002 Adaptive optics correction using microelectromechanical deformable mirror *Opt. Eng.* **41** 561–6

[5] Dagel D J, Cowan W D, Spahn B, Grossetete G D, Grine A J, Shaw M J, Resnick P J and Jokie B Jr 2006 Large-stroke MEMS deformable mirrors for adaptive optics *J. Microelectromech. Syst.* **15** 571–83

[6] Wang W S, Fang J and Warahramyan K 2005 Compact variable-focusing microlens with integrated thermal actuator and sensor *IEEE Photonics Technol. Lett.* **17** 2643–5

[7] Cheng C C and Yeh J A 2007 Dielectrically actuated liquid lens *Opt. Express* **15** 7140–5

[8] Tsao S *et al* 2004 InGaAs/InGaP Quantum dots and nanopillar structures for infrared focal plane array applications *Proc. SPIE* **5563** 74–87

[9] Federici J F, Gary D, Schulkin B, Huang F, Altan H, Barat R and Zimdars D 2003 Terahertz imaging using an interferometric array *Appl. Phys. Lett.* **83** 2477–9

[10] Marino R M and Davis W R Jr 2005 Jigsaw: a foliage-penetrating 3D imaging laser radar system *Linc. Lab. J.* **15** 23–36 www.ll.mit.edu/publications/journal/pdf/vol15_no1/15_1jigsaw.pdf

[11] Durate M, Davenport M A, Takhar D, Laska J N, Sun T, Kelly K F and Baraniuk R G 2008 Single-pixel imaging via compressive sampling *IEEE Signal Process. Magn.* **25** (2) 83–91

[12] Takhar D, Laska J N, Wakin M B, Duarte M E, Baron D, Sarvotham S, Kelly K E and Baraniuk R G 2006 A new compressive imaging camera architecture using optical-domain compression *Proc. SPIE* **6065** 6509–9

[13] Lee D and Solgaard O 2008 Pull-in analysis of torsional scanners actuated by electrostatic vertical combdrive *J. Microelectromech. Syst.* **17** 1228–38

[14] Noge H, Hagihara Y, Kawano K and Ueda H 2008 Electrostatically actuated two-dimensional optical scanner having a high resonant frequency ratio of fast/slow axes *IEICE Trans. Electron.* **E91C** 1611–5

[15] Urey H, Holmstrom S and Yalcinkaya A D 2008 Electromagnetically actuated FR4 scanners *IEEE Photonics Technol. Lett.* **20** 30–2

[16] Mitsui T, Takahashi Y and Watanabe Y 2006 A 2-axis optical scanner driven nonresonantly by electromagnetic force for OCT imaging *J. Micromech. Microeng.* **16** 1482–2487

[17] Jain A and Xie H K 2006 A single-crystal silicon micromirror for large bi-directional 2D scanning applications *Sensors Actuators* A **130** 454–60

[18] Singh J, Gan T, Agarwal A, Mohanraj S and Liw S 2005 3D free space thermally actuated micromirror device *Sensors Actuators* A **123–124** 468–75

[19] SOIMUMPs Multi-User Process, MEMSCAP Inc. http://www.memscap.com/en_mumps.html

[20] Li L, Begbie M, Brown J G and Uttamchandani D G 2007 Design, simulation and characterization of a MEMS optical scanner *J. Micromech. Microeng.* **17** 1781–7

[21] Huang Q A and Lee K S Neville 1999 Analysis and design of polysilicon thermal flexure actuator *J. Micromech. Microeng.* **9** 64–70

[22] Atre A 2006 Analysis of out-of-plane thermal microactuators *J. Micromech. Microeng.* **16** 205–13

[23] Elbuken C, Topaloglu N, Nieva P M, Yavuz M and Huissoon J P 2009 Modeling and analysis of a 2-DOF bidirectional electro-thermal microactuator *Microsyst. Technol.* **15** 713–22

[24] Moorthy A K and Bovik A C 2010 A two-step framework for constructing blind image quality indices *IEEE Signal Process. Lett.* **17** 513–6

[25] Starck J L, Donoho D L and Candes E J 2001 Very high quality image restoration by combining wavelets and curvelets *Proc. SPIE* **4478** 9–19

[26] Donoho D L 1995 Denoising by soft-thresholding *IEEE Trans. Inform. Theory* **41** 613–27

[27] Gunawan D 1999 Denoising images using wavelet transform *Proc. IEEE Pacific Rim Conf. Commun., Computers and Signal Proc. (22–24 August 1999, Victoria, BC, Canada)* pp C-41 doi:10.1109/PACRIM.1999.799483

[28] Do M and Vetterli M N 2003 The finite ridgelet transform for image representation *IEEE Trans. Image Process.* **12** 16–28

[29] Starck J L, Donoho D L and Candes E J 2003 Astronomical image representation by the curvelet transform *Astron. Astrophys.* **398** 785–800

[30] Candes E J and Donoho D L 2000 Curvelets: a surprisingly effective nonadaptive representation of objects with edges *Technical Report*, Statistics, Stanford University

[31] Gonzalez R C and Woods R E 2008 *Digital Image Processing* (Englewood Cliffs, NJ: Prentice Hall) 3rd ed.

[32] Wang J, Wong T T, Heng P A and Leung C S 2004 The discrete wavelet transform on a GPU *Proc. ACM Workshop General Purpose Computing Graphics Proc.* http://gpgpu.org/2004/03/23/the-discrete-wavelet-transform-on-a-gpu

[33] Daubechies I, Han B, Ron A and Shen Z 2003 Framelets: MRA-based constructions of wavelet frames *Appl. Comput. Harmon. Anal.* **14** 1–46

[34] Kingsbury N G 2001 Complex wavelets for shift invariant analysis and filtering of signals *Appl. Comput. Harmon. Anal.* **10** 234–53

[35] Selesnick I W and Abdelnour A Farras 2004 Symmetric wavelet tight frames with two generators *Appl. Comput. Harmon. Anal.* **17** 211–25

Design, Simulation, and Characterization of a Bimorph Varifocal Micromirror and Its Application in an Optical Imaging System

Li Li, Ran Li, Walter Lubeigt, and Deepak Uttamchandani, *Senior Member, IEEE*

***Abstract*—A 1.2-mm-diameter gold–silicon bimorph varifocal micromirror (VFM) has been designed and investigated for imaging applications. Several prototypes have been fabricated in a 10-μm-thick single-crystal silicon-on-insulator material. Controlled variation of the radius of curvature using electrothermal and optothermal actuation has been demonstrated. A finite-element-based simulation of the device behavior has been undertaken. Experimental characterization has shown that the device focusing power varied from an initial 87 dioptre to 69 dioptre by applying dc electrical power of 33 mW and produced a focusing power value of 59 dioptre when optothermally actuated with a normally incident laser beam of 488-nm wavelength and 43 mW. When electrothermally driven, the mechanical rise and fall times of the device were measured as 130 and 120 ms, respectively. Experimental and theoretical analyses using Zernike coefficients show that, throughout the actuation range, the aberration of the VFM is mainly a small defocus term, with negligible higher order aberrations. A compact active imaging system incorporating the VFM has been also demonstrated. This system was capable of focusing several objects located along the optical axis with a maximum tracking range of 134 mm. [2012-0175]**

***Index Terms*—Imaging, Silicon-on-Insulator Multi-User-MEMS Processes (SOIMUMPs), thermal actuation, varifocal micromirror (VFM).**

I. Introduction

VARIFOCAL micromirrors (VFMs) enable the miniaturization of adaptive imaging and laser focusing systems. This has significant potential for biomedical imaging applications [1] where a single system can image several planes. Such systems are based on a miniature focal-length-variable component such as a varifocal microlens [2], [3] or a VFM or membrane, which can be driven either electrothermally [4], electrostatically [5], [6], piezoelectrically [7], [8], or pneumatically [9].

Liu and Talghader [10] have incorporated an electrothermal VFM into a tunable optical cavity for sensing applications. Their 1.5-μm-thick and 100-μm-diameter polysilicon VFM was gold coated to achieve a radius of curvature (ROC) variation from 2.5 to 8.2 mm. However, the small size of their VFM aperture required the use of tightly focused optical beams. Sasaki and Hane [11] have fabricated a 400-μm-diameter electrostatic VFM from a 1-μm-thick silicon-on-insulator (SOI) wafer, which is capable of varying its focus from -28 to 21 mm with an applied dc voltage of 22 V. Hsieh *et al.* [12] have demonstrated an autofocus system using a 3-mm-diameter electrostatically actuated varifocal membrane. Their Z-shaped optical imaging system was capable of focusing objects at distances of 160 and 78 mm by changing the focusing power from 0 to 20 dioptre following the application of a 150-V dc actuation voltage.

In this paper, the design, simulation, and characterization of a 1.2-mm-diameter thermally actuated gold/single-crystal silicon bimorph VFM are described. The micromirror used in this paper is more than one order of magnitude larger in diameter and around six times thicker than the device of Liu and Talghader in [10]. It is also fabricated in single-crystal silicon in contrast to the device of Liu and Talghader that is fabricated in polysilicon. As opposed to the multiple-electrostatic-actuator-driven deformable mirror used in [11] and [12], our device is a thermally actuated VFM providing a uniformly expanding mirror surface that exhibits negligible higher order aberrations. Furthermore, its implementation into an active optical imaging system is described, and the imaging results are presented.

The micromirror geometric design, fabrication, and the actuation principle are described in the next section. In Section III, the characterization of the curvature variation, including the measurement of the optical aberrations from the VFM, is presented. Temperature distribution in the device and the simulated ROC variation calculated by finite-element-method (FEM)-based software are also presented in this section. In Section IV, an active optical imaging system featuring the VFM is described and the imaging results are presented. Finally, the design, performance, and the potential improvements of the VFM are discussed in Section V.

II. Device Design and Fabrication

The VFM design consists of a gold/silicon bimorph micromirror of 1.2-mm diameter. The 10-μm-thick single-crystal silicon circular plate is concentrically coated with a 0.65-μm-thick and 1-mm-diameter gold layer. The bimorph micromirror is suspended by eight serpentine springs (see Fig. 1), which are 10-μm thick and 8-μm wide and arranged around the

Manuscript received June 25, 2012; revised September 6, 2012; accepted September 10, 2012. Date of publication October 9, 2012; date of current version March 29, 2013. Subject Editor O. Solgaard.

The authors are with the Centre for Microsystems and Photonics, Department of Electronic and Electrical Engineering, University of Strathclyde, Glasgow, G1 1XW, U.K. (e-mail: ntb09220@eee.strath.ac.uk).

Color versions of one or more of the figures in this paper are available online at http://ieeexplore.ieee.org.

Digital Object Identifier 10.1109/JMEMS.2012.2220337

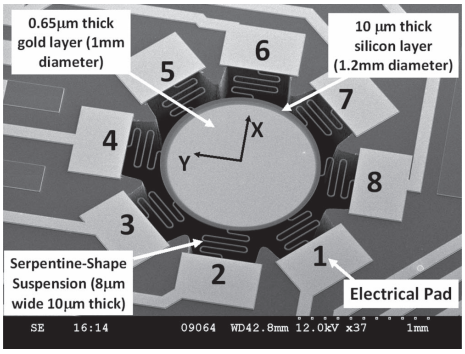

Fig. 1. SEM image of the bimorph VFM fabricated using SOIMUMPs.

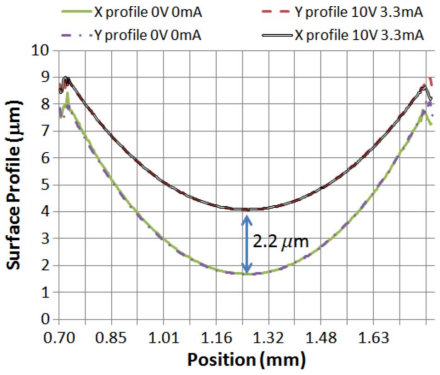

Fig. 2. Surface profile along the X- and Y-axes when actuated at 0 and 10 V at 3.3 mA.

micromirror in an equally spaced radial pattern. The outer ends of the suspension springs are anchored to the substrate. At each serpentine suspension anchor, a $590\ \mu$m $\times$ $390\ \mu$m gold pad is connected to provide an electrical connection. Therefore, the springs provide the functions of the suspensions and electrical current pathways to the micromirror.

The VFMs were fabricated using the SOI Multi-User-MEMS Processes (SOIMUMPs) from MEMSCAP Inc., which allows the realization of fully released single-crystal silicon MEMS structures. Full fabrication steps are detailed in [13]. The structural silicon layer of the SOI wafers used in the SOIMUMPs experiences a through-thickness stress gradient due to polishing and doping processes. This stress gradient, in addition to the compressive residual stress of the SOI layer together with the tensile residual stress of the gold layer [14], results in an initial concave curvature of the mirror surface, described here as the initial ROC of the mirror. The ROC can be altered by producing a temperature change of the mirror. A temperature rise can be obtained by using Joule heating where a dc current flows from one or more of the electrical pads and the corresponding serpentine spring(s) through the mirror cross section before exiting via another electrical pad(s), thereby completing the electrical circuit. Alternatively, the temperature of the VFM can be also increased by the absorption of optical radiation in the silicon layer when a laser beam is focused onto the rear surface of the micromirror. Due to the mismatched coefficients of thermal expansion (CTEs) between the gold and silicon layers, the gold layer with a higher CTE (1.41×10^{-5} K^{-1} [15]) expands more than the silicon layer (2.5×10^{-6} K^{-1} [16]) when heated. Through this differential expansion, the bimorph micromirror has a "flatter" surface, i.e., a higher ROC, as the temperature increases. The next section quantifies the ROC variation as a function of the actuating power.

III. Device Simulation and Characterization

A. Static Response

The "static" performance of the VFMs was characterized using two different measurement techniques. First, the surface shape and ROC variations were directly measured using a white-light interferometer (VEECO NT1100). Then, optical properties such as defocus and astigmatism were measured by a Shack–Hartmann wavefront sensor (Thorlabs and MLA 150-5C) using a low-power ($\sim$1 mW) probe He–Ne laser. During both characterization experiments, dc voltage levels were applied to one or more pairs of electrical pads for the electrothermal actuation. In a subsequent experiment, the output beam of two laser systems was focused onto the rear surface of the VFM. Two wavelengths were used (i.e., 488 and 532 nm) to generate optothermal actuation. These experiments will be described in detail in the following sections.

1) Characterization Using the White-Light Interferometer: During electrothermal actuation, the VFMs were driven at 11 electrical voltage levels from 0 to 10 V and the corresponding electrical power values are used to represent the actuation levels. At each electrical power value, the average ROC was calculated from

$$\text{ROC} = \frac{\text{ROC}_x + \text{ROC}_y}{2} \tag{1}$$

where ROC_x and ROC_y are the ROC values of the mirror surface measured along the X- and Y-axes, respectively (see Fig. 1) using the white-light interferometer. At electrical power values greater than 50 mW, thermal damage was observed, preventing the VFMs from returning to their original curvature after the driving power was switched off. To avoid such overheating and to maintain repeatable ROC variations during actuation, the electrothermal dc driving voltage was therefore limited to 10 V ($\sim 32 \pm 1$ mW). In Fig. 2, the lower traces correspond to 0 mW applied to the VFM, representing the initial profile of the VFM at laboratory temperature ($20\ ^\circ$C). The upper traces correspond to the application of 33 mW (10 V, 3.3 mA) to the VFM.

The curve profiles along the X- and Y-axes obtained at 0 and 33 mW were fitted to the conic section equation described in (2), and the fitted curves are shown in Fig. 3

$$z = \frac{cr^2}{1 + \sqrt{1 - (1+k)c^2r^2}}. \tag{2}$$

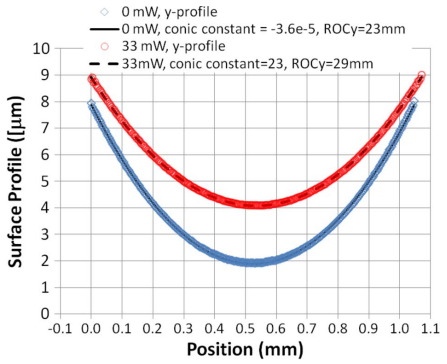

Fig. 3. Surface profile along the Y-axis at 0 and 33 mW, including a conic curve fit.

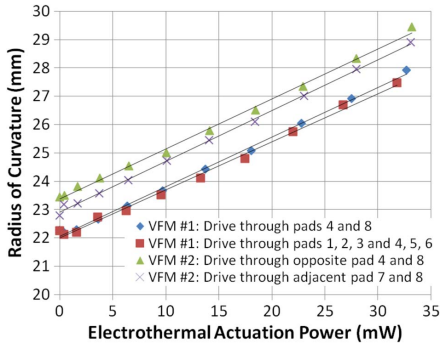

Fig. 4. ROC variation of VFM by driving through different combinations of electrical pads.

In (2), z is the sag of the surface, c is curvature, r is the radial coordinate in the VFM, and k is the conic constant [17]. The resulting conic constants were found to be 0 and 23 for 0 and 33 mW of electrical power, respectively. The average ROC is 23 mm (87 dioptre) at 0 mW and 29 mm (69 dioptre) at 33 mW, corresponding to a total focusing power variation of 18 dioptre, i.e., a 21% decrease in the initial value.

To investigate the effects of the electrothermal actuation through different combinations of the eight suspensions, the ROC variations by driving through two opposite electrical pads (pad numbers 4 and 8; see Fig. 1) and through two adjacent pads (pad numbers 7 and 8; see Fig. 1) were measured. The results are presented in Fig. 4 and show only 2% difference in the VFM ROC variations. Furthermore, three pairs of electrical pads were also connected in parallel to actuate one VFM. In Fig. 4, the ROC variation by actuation through three pairs of electrical pads is 99% equal to the measurement obtained through actuation with only one pair of electrical pads at the same driving power.

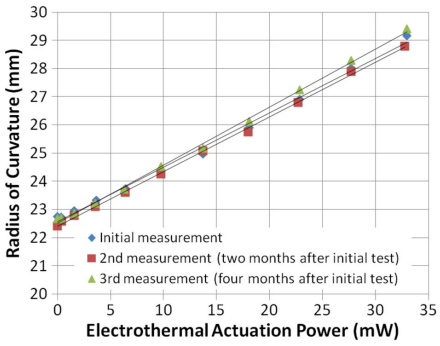

Fig. 5. ROC measurements of the same VFM as a function of driving power repeated at two-month intervals.

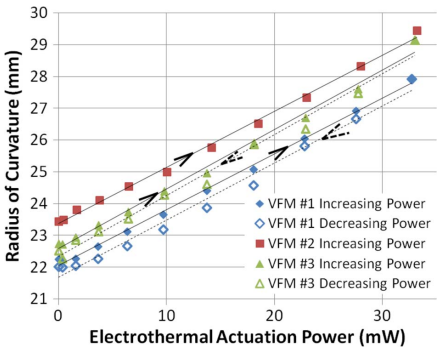

Fig. 6. ROC variation of three VFM devices as a function of electrothermal actuation power.

The repeatability of the VFM response was also investigated. Three ROC measurements of the same VFM were repeated at a two-month interval and are displayed in Fig. 5. The measurements differ by less than 1%. Therefore, the VFM demonstrated good repeatability over the four-month period during which the device had been in regular use for characterization. Fig. 6 shows the results obtained by testing three different VFM devices fabricated in the same process run. The response slope, i.e., ROC per actuation power, within experimental error, is similar for all three devices. Slight initial ROC differences are observed, most probably due to material and process variations such as the thickness of the gold layer deposited on each device during fabrication. Additionally, the hysteresis behavior of the VFM was measured for two different VFM devices, and results are also shown in Fig. 6. During the experiment, the steady-state ROC of each VFM was measured using the white-light interferometer when a dc voltage level was applied to two diametrically opposite pads. Voltage was increased from 0 to 10 V (33 mW) in 1-V steps, and ROC measurements were taken at each step after allowing approximately 30-s settling time. The voltage was then decreased from 10 to 0 V again in 1-V

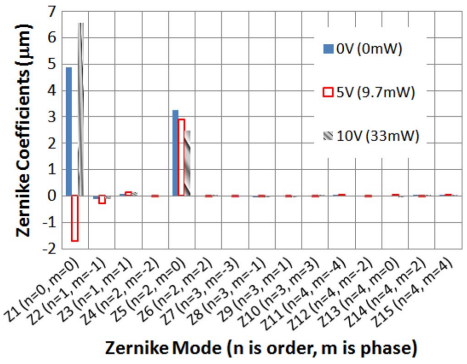

Fig. 7. Zernike coefficients calculated using surface profile measurements of the electrothermally actuated VFM.

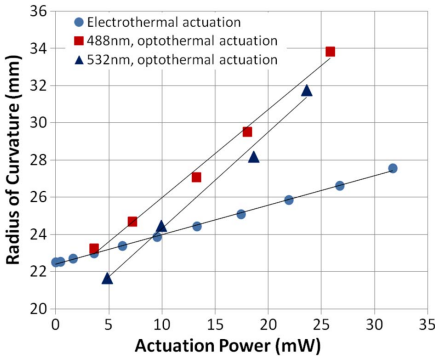

Fig. 8. ROC of VFM by electrothermal and optothermal actuation methods.

steps, and ROC measurements were repeated. It can be seen that, for both devices, the ROC variation during decreasing actuation power (down cycle) has a constant difference of around -0.3 mm from the ROC variation plot for increasing actuation power (up cycle). This offset represents a 1.4% difference in ROC between "up" and "down" actuation.

The optical aberration of the VFMs has been characterized on the basis of Zernike polynomials [18]. To achieve this, a MATLAB-based program was used to analyze the VFM surface profiles measured by the white-light interferometer and to calculate the resulting Zernike coefficients [19]. This was repeated for different actuation power levels. Fig. 7 illustrates the calculated Zernike coefficients at 0, 5, and 10 V. The first three Zernike coefficients, i.e., Z_1, Z_2, and Z_3, are the measurements of the alignment between the VFM and the optical experimental setup. The values of the three indicate the location of the focused image referring to the optical axis. Therefore, in the experimental setup, Z_1, Z_2, and Z_3 are not measurements of the optical imaging performance of the VFMs nor have the effect of qualifying the sharpness of the imaging results. Apart from the piston term (Z_1) and tilt term (Z_2, Z_3) resulting from alignment of the measuring system, the defocus (Z_5) is the main aberration, whereas other aberrations such as astigmatism (Z_4 and Z_6), coma (Z_8 and Z_9), trefoil (Z_7 and Z_{10}), and spherical aberration (Z_{13}) are negligible. The low values of the coefficients shown in Fig. 7 indicate that these electrothermally actuated VFMs should produce minimally distorted images in a practical system.

For optothermal actuation, a laser beam was normally incident onto the rear surface of the VFM. Two laser wavelengths, i.e., 488 and 532 nm, were used during characterization experiments. The 488-nm wavelength was generated from an argon ion laser, whereas the 532-nm light was generated from a frequency-doubled Nd:YAG laser. The ROC variation of the VFM, as a function of the measured absorbed laser optical actuation power, was measured for both cases using a white-light interferometer, and it is displayed in Fig. 8. The ROC variation sensitivities to the absorbed optothermal actuation power are 0.47 and 0.52 mm/mW for 488- and 532-nm wavelengths,

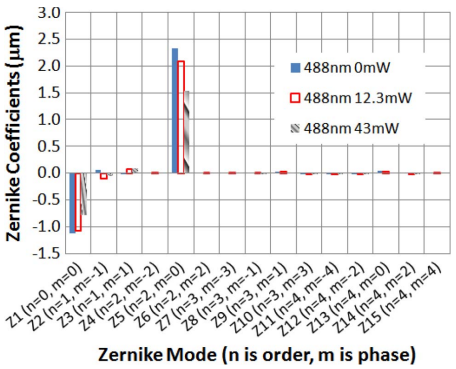

Fig. 9. Zernike coefficients calculated using surface profile measurements of the optothermally actuated VFM (actuation by a 488-nm laser).

respectively, which, within experimental uncertainty of the exact value of absorbed laser power in the VFM, are reasonably consistent. These sensitivities are higher than that of an electrothermally actuated VFM (0.16 mm/mW). This is due to the fact that optothermal actuation delivers the power directly to the micromirror while electrothermal actuation heats up not only the micromirror but also the suspensions. This leads to a higher average temperature increment for the same applied power. This is analyzed later in this paper. The calculated Zernike coefficients corresponding to the optothermally actuated VFM have identical pattern for the two wavelengths through the actuation range. Fig. 9 displays the wavefront results obtained using the 488-nm laser radiation. Again, excluding the piston term that is related to alignment, the defocus coefficient (Z_5), although small in value, is the main source of aberration.

2) Characterization Using the Wavefront Sensor: In order to further characterize the VFM, a wavefront sensor-based system was set up to measure the optical aberrations of the VFM by reflecting a monochromatic plane wavefront from the VFM surface. As shown in Fig. 10, a collimated low-power ($<$ 1 mW) He–Ne laser beam was normally incident on the

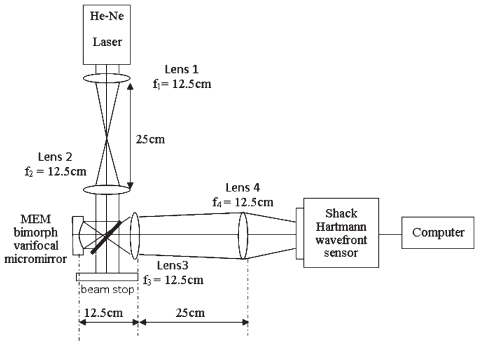

Fig. 10. Optical measurement setup with the Shack–Hartmann wavefront sensor.

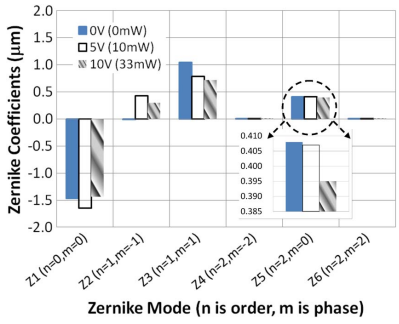

Fig. 11. Zernike coefficients of the electrothermally actuated VFM measured by the Shack–Hartmann wavefront sensor.

VFM surface. The reflected beam was then directed toward the Shack–Hartmann wavefront sensor. The VFM surface plane was imaged onto the lenslet plane using a pair of identical lenses (lens 3 and lens 4). This way, the properties of the optical wavefront directly formed by the curved VFM surface could be measured by the Shack–Hartmann sensor. Due to the small VFM aperture size (1-mm diameter), only Zernike terms of the defocus (Z_5) and astigmatism (Z_4 and Z_6) could be stably measured in our experiment. The defocus (Z_5) and astigmatism (Z_6) were measured at 11 electrothermal power levels ranging from 0 mW (0 V) to 33 mW (10 V). With the pupil diameter at the wavefront sensor plane being around 0.4 mm, the measured first six Zernike coefficients are plotted in Fig. 11 for three actuation levels. Z_1, Z_2, and Z_3 originate from slight optical misalignments in the measurement setup. The astigmatism values (Z_4 and Z_6) were in the nanometer range, which were negligible compared with the defocus term, and did not significantly vary during the experiment. The inset in Fig. 11 shows that the small defocus, i.e., Z_5, decreased during the electrothermal actuation, which is also observed in the results calculated from the surface profile measurement shown in Fig. 7. The resulting Zernike coefficients slightly

TABLE I
MATERIAL PROPERTIES OF THE VFM USED IN THE FEM SIMULATION MODEL

	Unit	Silicon	Gold
Density	kg/m^3	2331 [24]	19300 [24]
Elastic Modulus	GPa	$E_{X[100]}=E_{y[010]}=E_{z[001]}=130$ $G_{yz}=G_{zx}=G_{xy}=0.796$ [26]	57 [25]
Poisson		$\nu_{yz}=\nu_{zy}=\nu_{xy}=0.28$ [26]	0.42 [25]
TCE	1/K	$2.5\text{x}10^{-6}$ [16]	$1.4\text{x}10^{-5}$ [15]
Thermal Conductivity	W/mK	150 at 300K 111 at 345K [27] 100 at 400K	317 [24]
Specific Heat	J/kgK	5 at 300K 755 at 345K [27] 789 at 400K	129 [24]
Electric Conductivity	Ω*μm	56.2 at 200K 60.6 at 300K [28] 64.9 at 400K	0.023 at 300K [24] 0.031 at 400K
Surface Emissivity		0.6 [29]	0.02 [30]

differ from the values calculated using the VFM surface profile measurements where the pupil diameter was the diameter (1 mm) of the reflective gold. However, the relative magnitude between defocus and astigmatism aberrations obtained is similar in both experiments. Moreover, the defocus Zernike term obtained from the two methods is equivalent when the values shown in Fig. 7 are scaled to the pupil size used to obtain the result in Fig. 11, following the scaling approach described in [20, Table 1].

3) Finite-Element Modeling of the VFMs: The static thermomechanical behavior of the VFM was modeled using FEM software, CoventorWare [21]. The VFM model, built from the device layout design file, consists of two materials. First is the 0.65-μm-thick gold layer that serves as the reflective part of the VFM; second is the 10-μm-thick single-crystal silicon structural layer including the micromirror plate and eight suspensions. The gold layer experiences an in-plane tensile residual stress of around 300 $\pm$15 Mpa, which was calculated by applying the Stoney equation [22] to the measurement of a gold-coated test cantilever fabricated with the same process as for the VFM. The silicon layer experiences an in-plane compressive residual stress of around -3.9 MPa [14] and through-thickness stress gradient of 2.4 MPa/μm [23]. The electrothermal actuation of the VFM was simulated by applying 11 voltage values between 0 and 10 V to two oppositely located electrical pads along the Y-axis in the CoventorWare model. Heat losses such as heat conduction from the VFM device to the substrate, heat convection, and radiation from the surfaces to the surrounding environment were included in the FEM simulation. The ambient air temperature and the convection coefficient were assumed to be 20 °C and 25 W/m^{2}K, respectively. The material properties of the structural silicon and the gold layers of the VFM used are listed in Table I.

The measured and simulated ROC variations of the VFM as a function of the electrothermal actuation power have an agreement value of 97%, as shown in Fig. 12. The simulated VFM ROC variation shows a small nonlinear trend that has not been experimentally observed. This could be due to the

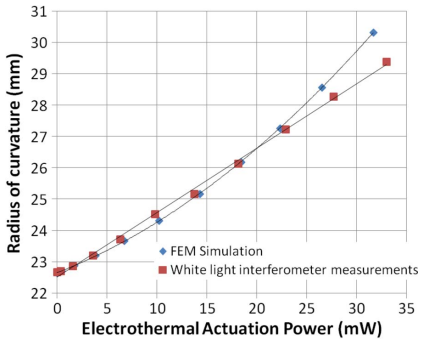

Fig. 12. FEM-simulated ROC and measured ROC from the white-light interferometer as a function of driving power.

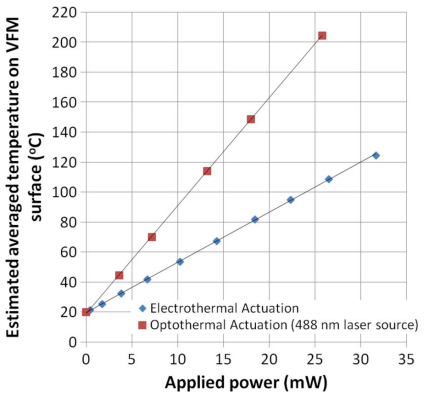

Fig. 13. Estimated average temperature of the surface of the bimorph VFM by electrothermal and optothermal actuation.

assumptions on the material properties or surface boundary conditions of heat losses and needs a deeper analysis, which is beyond the scope of this paper.

The simulated average temperature of the micromirror surface as a function of the electrothermal and optothermal actuation power is plotted in Fig. 13 and displays strong linearity. Using the FEM simulation, the average temperature rise of the mirror surface as the applied power is varied has been evaluated for both electrothermal and optothermal actuation. The simulation results, as shown in Fig. 13, show a higher average temperature rise occurring for optothermal actuation over electrothermal actuation for the same applied power. The ROC change, which depends on average temperature rise, is consequently higher.

The temperature distributions of the VFM model actuated through two opposite electrical pads [see Fig. 14(a) and (b)] and through two adjacent electrical pads [see Fig. 14(d) and (e)] were also simulated. The higher resolution temperature profiles shown in Fig. 14(b) and (e) show the local variations in the temperature profile of the micromirror surface. We examined these areas of temperature variation using the white-light interferometer but did not observe any measurable local deformation. The center of the serpentine-shape springs experiences significantly higher temperatures than the rest of the VFM.

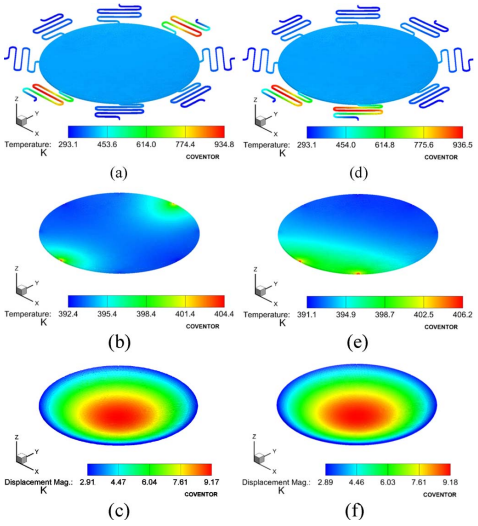

Fig. 14. (a), (b), (d), (e) Temperature distribution and (c), (f) mechanical deformation of the FEM simulation of the bimorph VFM when driven by a pair of (a)–(c) opposite and (d)–(f) adjacent electrical pads at 33 mW.

To simulate the optothermally actuated VFM, the diameters of the two actuating laser beams are required, and they were measured to be ∼0.6 mm at 488 nm, and ∼0.4 mm at 532 nm. The laser power was assumed to be absorbed through the thickness of the VFM. Therefore, a cylinder with a cross-sectional diameter equal to that of the laser beam was defined through the VFM silicon layer thickness in the FEM model. The absorbed power, determined from the experimental measurement, was taken as the heat source within this cylindrical volume. The heat dissipation mechanism was assumed to be the same as for the electrothermally actuated VFM simulations. Fig. 15 shows an agreement value of at least 92% between the measured and FEM-simulated ROC values during optothermal actuation.

B. Dynamic Response

The dynamic response of the VFM was obtained by measuring its response to a step voltage. A 1.2-Hz 50% duty cycle square-wave voltage signal operating between 0 and 10 V was applied to two opposite electrical pads of the VFM. At the same time, the vertical displacement at the center of the VFM was measured using a scanning laser Doppler vibrometer (Polytech OFC 3001). As shown in Fig. 16, the 0%–90% rise time and the 90%–0% fall time of the VFM were 130 and 121 ms, respectively. The vertical displacement at the center of the VFM

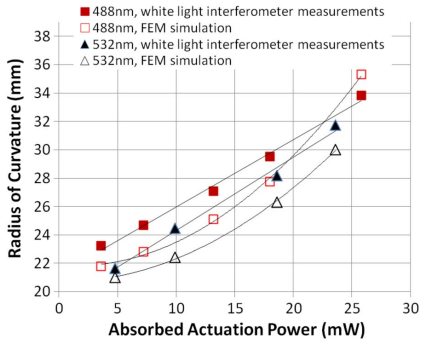

Fig. 15. FEM-simulated ROC and measured ROC as a function of absorbed 488-nm laser power.

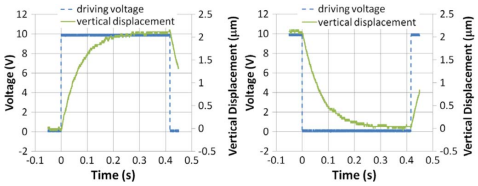

Fig. 16. Dynamic response of the vertical movement of the center point of the VFM to a 50% duty cycle square wave between 0 and 10 V.

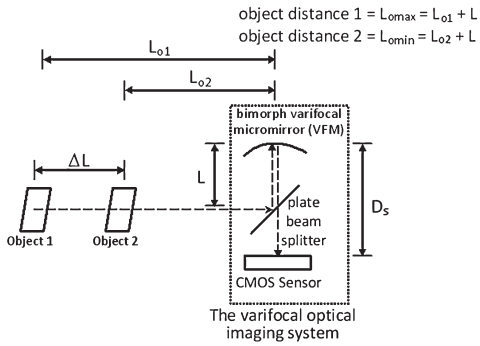

Fig. 17. Varifocal optical imaging system using the VFM.

was measured at ∼2.2 μm, which was in line with the surface profile scanner measurements displayed in Fig. 2.

IV. Optical Imaging System and Results

In order to demonstrate the performance of the VFM in an imaging application, the device was incorporated into a compact imaging system (see Fig. 17). Illuminated objects were placed along the optical axis with the object-to-VFM distance ranging from $L_{o\min}$ to $L_{o\max}$. The light from the object was directed to the VFM surface using a 50% transmission plate beam splitter and was focused onto a CMOS image sensor located at a distance D_s from the VFM.

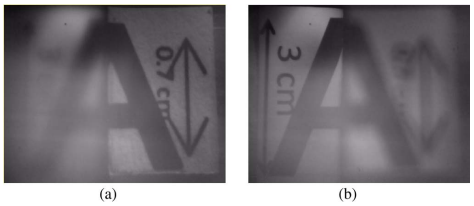

(a) (b)

Fig. 18. Images of the left half of a 30 mm × 30 mm letter A and the right half of a 7 mm × 7 mm letter A obtained by the varifocal imaging system with D_s of 15 mm, $L_{o\max}$ of 175.5 mm, and $L_{o\min}$ of 41.5 mm. In (a), the unactuated mirror focuses on the right part of letter A, whereas in (b), with 31 mW applied to the VFM, the imaging system focuses on the left part of letter A.

Using the simple mirror equation, the minimum and maximum object distances ($L_{o\min}$ and $L_{o\max}$) are related to the $\mathrm{ROC}_{\min}$ and $\mathrm{ROC}_{\max}$ of the VFM by the following equations:

$$L_{o\min} = \frac{D_s \times \mathrm{ROC}_{\min}}{2D_s - \mathrm{ROC}_{\min}} \tag{3a}$$

$$L_{o\max} = \frac{D_s \times \mathrm{ROC}_{\max}}{2D_s - \mathrm{ROC}_{\max}} \tag{3b}$$

where D_s is the distance between the CMOS image sensor and the VFM; $\mathrm{ROC}_{\min}$ and $\mathrm{ROC}_{\max}$ are the radii of curvature of the VFM at 0 mW and the maximum driving power at 10 V (i.e., 31 mW for the VFM used in the imaging system), respectively. The minimum and maximum ROC values of the present VFM were measured at 22 and 27.8 mm, respectively.

In the varifocal imaging system, two different objects were located at the smallest and the largest object distances (i.e., $L_{o\min}$ and $L_{o\max}$) to represent the imaging system tracking range. The CMOS sensor was located at a fixed distance of 15 mm from the VFM. As shown in Fig. 18(a), when no actuation power is applied, the right half of a 7 mm × 7 mm object, i.e., the letter A, placed at a distance $L_{o\min}$ of 41.5 mm was sharply imaged. The left half of a 30 mm × 30 mm letter A placed at a distance $L_{o\max}$ of 175.5 mm was sharply imaged when 31 mW was applied to the VFM. As a result, the imaging system presented an object tracking range of 134 mm with D_s fixed at 15 mm. Additionally, a blue and a red pencil were sharply imaged at $L_{o\min}$ of 30.5 mm and at $L_{o\max}$ of 66.5 mm, respectively, when D_s was fixed at 17.5 mm (see Fig. 19). The focused imaging results using the optothermally actuated VFM were also obtained when D_s was 15 mm. An example of this optothermal actuation is shown in Fig. 20 where the VFM was driven by 22.8 mW of laser output power ($\lambda = 488$ nm, 60% VFM absorption) with the red and blue pencils located at $L_{o\max}$ of 209 mm and $L_{o\min}$ of 44 mm from the CMOS sensor, respectively. With no actuation, the blue pencil was in focus whereas the red one was in focus with incident optothermal actuation of 22.8 mW.

Table II summarizes the results of the varifocal imaging experiments. As expected, the object tracking range reaches a maximum as D_s approaches the $\mathrm{ROC}_{\max}$ of the VFM. During the electrothermal actuation, less than 3% discrepancy between

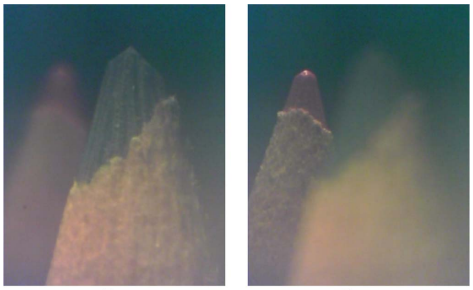

(a) (b)

Fig. 19. Images of the blue and red pencils located 30 and 66.5 mm from the VFM with D_s of 17.5 mm. In (a), the unactuated mirror focuses on the blue pencil, whereas in (b), with 31 mW applied to the VFM, the imaging system focuses on the red pencil.

(a) (b)

Fig. 20. Images of the blue and red pencils located 44 and 209 mm from the VFM with D_s of 15 mm. In (a), the unactuated mirror focuses on the blue pencil, whereas in (b), the mirror driven by using 488-nm wavelength 22.8-mW laser power focuses on the red pencil. Imaging of the scattered blue laser light leading to speckle over the target objects of the color pencils is also displayed in (b).

the measured and calculated object distances was observed in the experiments. For optothermal actuation, the last row of data in Table II for the results in Fig. 20(b) presents a 27% difference between the calculated and measured object distances for the focused image. This is due to the depth of field (DOF) of the imaging system. Using the DOF equations given in [31] and taking the diameter of the aperture as 1 mm and the estimated circle of confusion for the CMOS sensor to be $\sim$0.02 mm, the near limit of the DOF of the varifocal imaging system at the VFM optothermal actuation power of 22.8 mW was calculated to be 133 mm whereas the far limit was 217 mm. It can be seen that the measured object distance lies between these two limits, thus explaining the origin of focusing uncertainty (error), which leads to the large difference of 27%. We calculated the near limit of DOF and far limit of DOF for all the rows in Table II, and in all cases, the measured object distance lies between these limits. For a fixed aperture, the DOF increases when the VFM ROC is increased by the actuating power. Moreover, the judgment on the sharpness of the image results in Fig. 20(b) is made more difficult by the small image size of the red pencil, which is placed further away than the blue pencil and also by the speckle from the scattered actuating laser collected by the sensor.

V. Discussion

In this VFM design, a tradeoff between the aperture size for imaging applications and the thermomechanical response time had to be considered. For instance, a 2-mm-diameter VFM fabricated using the same SOIMUMPs was experimentally measured to have rise and fall times of around 150 ms, which is about 20% longer than the measured response time of the 1.2-mm-diameter VFM. Thus, using a smaller mirror will result in a faster dynamic response; however, this will restrict its implementation in imaging applications. The thickness of the silicon layer set by the SOIMUMPs limits the maximum variation to $\sim$18 dioptre when actuated by 33-mW electrothermal actuation power and $\sim$28 dioptre when actuated with 43 mW of optical power at 488-nm wavelength.

For electrothermal actuation, the eight suspensions supporting the VFM permit the use of different combinations of actuation pads. No significant difference in the ROC variation was observed when applying the electrothermal actuation power through different combinations of electrical pads (either through two opposite or two adjacent electrical pads, or through more than one pair of electrical pads). The optothermal actuation method provides a more efficient and noncontact method of control of the VFM by delivering the actuation power directly onto the micromirror.

To understand scaling issues, the simulated behavior of a larger 2-mm-diameter VFM has been also studied under the assumption of same material properties, boundary conditions, and initial stress distribution as for a 1.2-mm device. The simulation indicates that the initial ROC of the 2-mm VFM model is 40 mm, an increase of 77% over the initial ROC of a 1.2-mm VFM. The ROC change of the 2-mm-diameter VFM is simulated to be 1.7 mm, a reduction of 73% when compared with a typical 1.2-mm VFM. These comparative values apply when both the 1.2- and 2-mm VFMs experience the same 10-V actuation voltage. Although the larger VFM collects nearly three times more optical power, its ROC change is not as high under the same driving conditions.

To study the impact of the initial curvature of the VFM on the ROC variation achieved during electrothermal actuation, a lower residual stress of 210 MPa (instead of 300 MPa) was simulated in the gold layer of the same FEM model used in this paper. The simulation results, as shown in Fig. 21, indicate that a VFM with an initially flatter surface (i.e., a larger ROC value) has a higher variation range of ROC over the same range of electrothermal actuation power. The ROC variation range of the VFM surface could be also theoretically improved by increasing the thickness of the gold layer on the micromirror surface (as modeled in Fig. 22). However, this enhancement can only be achieved provided that the residual stress of this thicker gold layer does not introduce further initial curvature.

It was shown in Fig. 6 that the initial ROC of three different VFM devices differed by around 1.5 mm due to microfabrication variability; consequently, the focal length of the VFMs has a variation of $\pm$0.75 mm around the average value. Practical imaging systems will be usually designed to accommodate small variations in the performance of low-cost microoptic components. Most imaging systems rely on closed-loop

TABLE II
MATERIAL PROPERTIES OF THE VFM USED IN THE FEM SIMULATION MODEL

		Power [mW]	D_s [mm]	ROC [mm]	Calculated object distance: L_o [mm]	Measured object distance: $\bar{L}_o$ [mm]	$\lvert L_o - \bar{L}_o \rvert / L_o$ [%]	Object tracking range: ΔL [mm]
ETM	Fig. 18 (a)	0	15	22	41.3	41.5	0.6%	134
	Fig. 18(b)	31		27.6	175.7	175.5	0.1%	
	-	0	16.5	22	33	32.5	1.5%	52
	-	31		27.6	85	85	0%	
	Fig. 19 (a)	0	17.5	22	29.6	30.5	3%	36
	Fig. 19 (b)	31		27.6	65.7	66.5	1.2%	
OT	Fig. 20 (a)	0	15	22.5	45	44	2.2%	165*
	Fig. 20 (b)	22.8		27.5	165	209	27%	

ETM and OT are short for electrothermal and optothermal actuation methods respectively. The value of optothermal actuation power listed is the incident laser power with the absorption of 60%. (* this value has an error due to depth of field as described in the text.)

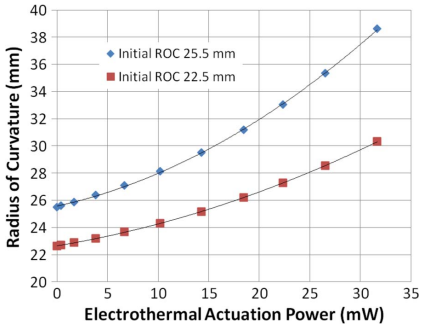

Fig. 21. Simulated VFM ROC variation and corresponding polynomial fitting as function of the actuation power with different initial ROC values.

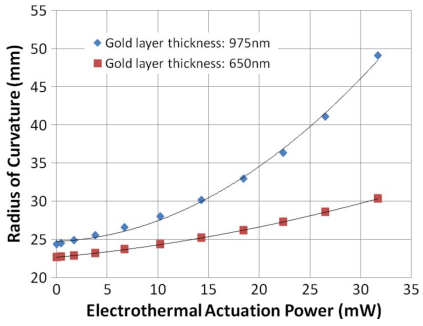

Fig. 22. Simulated VFM ROC variation and corresponding polynomial fitting as function of the actuating power when gold layers with different thicknesses but the same residual stress are deposited.

systems where an image sensor captures an image, which is then processed to evaluate the focus score after which an autofocusing algorithm will modify the characteristics of the microoptical component (i.e., position and focal properties) until the best focused image is achieved. Hence, in compact low-cost imaging systems, the microoptical component is in an active focus state enabling the inevitable small focal length differences due to manufacturing tolerances to be actively compensated.

VI. CONCLUSION

A gold-coated 1.2-mm-diameter single-crystal silicon VFM suspended by eight serpentine springs has been designed and fabricated in a 10-μm-thick structural layer using SOIMUMPs. The electrothermally actuated VFM was capable of producing a total optical power variation of $\sim$18 dioptre with 33 mW of electrical power and of $\sim$28 dioptre with 43 mW of normally incident laser optical power at 488-nm wavelength. The optothermal actuation method of the VFM enables the remote, noncontact, and nonelectrical actuation of the VFM. The ROC changes due to electrothermal and optothermal actuation were experimentally measured using a white-light interferometer. The magnitude of the ROC response to electrothermal and absorbed optothermal actuating power was measured at $\sim$0.16 mm/mW and $\sim$0.47–0.52 mm/mW, respectively. The measurements were in very good agreement with the FEM simulation. The Zernike coefficients calculated from surface profile measurements and also obtained using the Shack–Hartmann wavefront sensor indicate that the small Zernike defocus term was the main source of optical aberration in the VFM. The higher order aberrations such as astigmatism, coma, trefoil, and spherical aberrations have negligible values. Characterization of the mirror dynamic response yielded mechanical rise and fall times of $\sim$130 and 120 ms, respectively. Finally, the VFM was successfully implemented in an active compact imaging system demonstrating potential for a wide range of *in situ* microscopic/target tracking applications.

ACKNOWLEDGMENT

The authors would like to thank Dr. P. Edwards from the Department of Physics of the University of Strathclyde and Dr. C. Saunter from Durham University for their helpful discussions.

REFERENCES

[1] D. Kang, H. Yoo, P. Jillella, B. Bouma, and G. Tearney, "Comprehensive volumetric confocal microscopy with adaptive focusing," *Biomed. Opt. Exp.*, vol. 2, no. 6, pp. 1412–1422, Jun. 2011.
[2] S. T. Choi, J. Y. Lee, J. O. Kwon, S. Lee, and W. Kim, "Varifocal liquid-filled microlens operated by an electroactive polymer actuator," *Opt. Lett.*, vol. 36, no. 10, pp. 1920–1922, May 2011.
[3] A. Mermillod-Blondin, E. McLeod, and C. B. Arnold, "High-speed varifocal imaging with a tunable acoustic gradient index of refraction lens," *Opt. Lett.*, vol. 33, no. 18, pp. 2146–2148, Sep. 2008.
[4] W. Liu and J. J. Talghader, "Current-controlled curvature of coated micromirrors," *Opt. Lett.*, vol. 28, no. 11, pp. 932–934, Jun. 2003.

[5] R. Hokari and K. Hane, "A varifocal convex micromirror driven by a bending moment," *IEEE J. Sel. Topics Quantum Electron.*, vol. 15, no. 5, pp. 1310–1316, Sep./Oct. 2009.
[6] C. Knoernschild, C. Kim, B. Liu, F. P. Lu, and J. Kim, "MEMS-based optical beam steering system for quantum information processing in two-dimensional atomic systems," *Opt. Lett.*, vol. 33, no. 3, pp. 273–275, Feb. 2008.
[7] A. Ishii and J. Mitsudo, "Constant-magnification varifocal mirror and its applications to measuring three-dimensional (3-D) shape of solder bump," *IEICE Trans. Electron.*, vol. E90-C, no. 1, pp. 6–11, Jan. 2007.
[8] M. Mescher, M. Vladimer, and J. Bernstein, "A novel high-speed piezoelectric deformable varifocal mirror for optical applications," in *Proc. IEEE 15th Int. Conf. Micro Electro Mech. Syst.*, 2002, pp. 511–515.
[9] A. A. Alzaydi, J. T. Yeow, and S. L. Lee, "Hydraulic controlled polyester-based micro adaptive mirror with adjustable focal length," *Mechatronics*, vol. 18, no. 2, pp. 61–70, Mar. 2008.
[10] W. Liu and J. Talghader, "Spatial-mode analysis of micromachined optical cavities using electrothermal mirror actuation," *J. Microelectromech. Syst.*, vol. 15, no. 4, pp. 777–785, Aug. 2006.
[11] T. Sasaki and K. Hane, "Initial deflection of silicon-on-insulator thin membrane micro-mirror and fabrication of varifocal mirror," *Sens. Actuators A, Phys.*, vol. 172, no. 2, pp. 516–522, Dec. 2011.
[12] H. T. Hsieh, H.-C. Wei, M.-H. Lin, W.-Y. Hsu, Y.-C. Cheng, and G.-D. J. Su, "Thin autofocus camera module by a large-stroke micromachined deformable mirror," *Opt. Exp.*, vol. 18, no. 11, pp. 11 097–11 104, May 2010.
[13] A. Cowen, G. Hames, D. Monk, S. Wilcenski, and B. Hardy, *SOIMUMPs Design Handbook*. Durham, NC: MEMSCAP Inc., Revision 8.0 ed. [Online]. Available: http://www.memscap.com
[14] D. C. Miller, B. L. Boyce, M. T. Dugger, T. E. Buchheit, and K. Gall, "Characteristics of a commercially available silicon-on-insulator MEMS material," *Sens. Actuators A, Phys.*, vol. 138, no. 1, pp. 130–144, Jul. 2007.
[15] J. H. Jou, C. N. Liao, and K.-W. Jou, "A method for the determination of gold thin film's mechanical properties," *Thin Solid Films*, vol. 238, no. 1, pp. 70–72, Jan. 1994.
[16] Y. Okada and Y. Tokumaru, "Precise determination of lattice parameter and thermal expansion coefficient of silicon between 300 and 1500 K," *J. Appl. Phys.*, vol. 56, no. 2, pp. 314–320, Jul. 1984.
[17] D. Malacara and B. J. Thompson, Eds., *Handbook of Optical Engineering*. New York: Marcel Dekker, 2001, p. 143.
[18] M. Born and E. Wolf, *Principles of Optics*, 7th ed. Cambridge, U.K.: Cambridge Univ. Press, 1999, ch. 9.
[19] R. W. Gray and J. M. Howard, "A MATLAB function to work with Zernike polynomials over circular and non-circular pupils," in *Zernike-Calc*. Natick, MA: The MathWorks, Inc., Oct. 18, 2011. [Online]. Available: http://www.mathworks.com/matlabcentral/fileexchange/33330-zernikecalc
[20] J. Schwiegerling, "Scaling Zernike expansion coefficients to different pupil sizes," *J. Opt. Soc. Amer. A, Opt. Image Sci.*, vol. 19, no. 10, pp. 1937–1945, Oct. 2002.
[21] Coventor Inc., Cary, NC, CoventorWare Integrated Suite of Design Simulation Software. [Online]. Available: http://www.coventor.com/products/coventorware/
[22] D. C. Miller, C. F. Herrmann, H. J. Maier, S. M. George, C. R. Stoldt, and K. Gall, "Thermo-mechanical evolution of multilayer thin films: Part I. Mechanical behavior of Au/Cr/Si microcantilevers," *Thin Solid Films*, vol. 515, no. 6, pp. 3208–3223, Feb. 2007.
[23] L. Li, V. Stankovic, L. Stankovic, L. Li, S. Cheng, and D. Uttamchandani, "Single pixel optical imaging using a scanning MEMS mirror," *J. Micromech. Microeng.*, vol. 21, no. 2, p. 025022, Feb. 2011.
[24] D. R. Lide, *CRC Handbook of Chemistry and Physics*, 85th ed. Boca Raton, FL: CRC Press, 2004.
[25] T. P. Weihs, S. Hong, J. C. Bravman, and W. D. Nix, "Mechanical deflection of cantilever microbeams: A new technique for testing the mechanical properties of thin films," *J. Mater. Res.*, vol. 3, no. 5, pp. 931–942, Oct. 1988.
[26] M. A. Hopcroft, W. Nix, and T. Kenny, "What is the Young's modulus of silicon?" *J. Microelectromech. Syst.*, vol. 19, no. 2, pp. 229–238, Apr. 2010.
[27] Y. S. Yang, Y. H. Lin, Y. C. Hu, and C. H. Liu, "A large-displacement thermal actuator designed for MEMS pitch-tunable grating," *J. Micromech. Microeng.*, vol. 19, no. 1, pp. 015001-1–015001-12, Jan. 2009.
[28] P. W. Chapman, O. N. Tufte, J. D. Zook, and D. Long, "Electrical properties of heavily doped silicon," *J. Appl. Phys.*, vol. 34, no. 11, pp. 3291–3295, Nov. 1963.
[29] P. J. Timans, "Emissivity of silicon at elevated temperatures," *J. Appl. Phys.*, vol. 74, no. 10, pp. 6353–6364, Nov. 1993.
[30] L. N. Aksyutov, "Normal spectral emissivity of gold, platinum, and tungsten," *J. Eng. Phys. Thermophys.*, vol. 27, no. 2, pp. 913–917, Aug. 1974.
[31] S. Ray, *Applied Photographic Optics*, 3rd ed. Oxford, U.K.: Focal Press, 2002, ch. 22, pp. 217–221.

Li Li received the joint B.Eng. degree in electronic and electrical engineering from North China Electric Power University, Beijing, China, and the University of Strathclyde, Glasgow, U.K., in 2008, and the M.Sc. degree in control, communication, and digital signal processing from the University of Strathclyde, Glasgow, U.K., in 2009. She is currently a Ph.D. research student in the Centre for Microsystems and Photonics, Department of Electronic and Electrical Engineering, University of Strathclyde.

Her main research interests are the design, characterization, and finite-element method simulation of MEMS devices.

Ran Li received the B.Eng. degree in electrical engineering and automation from Shanghai University of Electric Power, Shanghai, China, in 2010, and the M.Sc. degree in electronic and electrical engineering from the University of Strathclyde, Glasgow, U.K., in 2011. He is currently working toward the Ph.D. degree in the Centre for Microsystems and Photonics, University of Strathclyde, where he is engaged on the development of advanced controllable Raman lasers.

Walter Lubeigt received the Engineering Diploma degree in optoelectronic systems from the Ecole Supérieure des Procédés Electroniques et Optiques, University of Orléans, Orléans, France, in 2001, and the Ph.D. degree from the University of Strathclyde, Glasgow, U.K., in 2006, for work on solid-state laser performance enhancement using intracavity adaptive optics techniques.

He subsequently worked on the development of diamond Raman lasers at the Institute of Photonics, University of Strathclyde. Since 2010, he has been with the Centre for Microsystems and Photonics, University of Strathclyde, where his research interests include the development of MEMS-controlled solid-state lasers, the use of intracavity adaptive optics to improve the performance of solid-state Raman lasers, and the development of novel laser systems for environmental remote sensing.

Deepak Uttamchandani (SM'05) received the Ph.D. degree from University College London, London, U.K., in the area of optical fiber sensors, in 1985.

He is currently the Director of the Centre for Microsystems and Photonics, University of Strathclyde, Glasgow, U.K. His early research in MEMS concentrated on optothermal microresonator sensors and in investigating techniques for general MEMS material characterization using MEMS micromechanical resonators. His recent research has concentrated on developing system applications of optical MEMS such as intracavity MEMS-based laser systems, MEMS-based photoacoustic spectroscopy for gas sensing, and MEMS-based single-pixel imaging systems. He has also published in the field of subwavelength tip-based Raman spectroscopy, which has contributed to the development of tip-enhanced Raman spectroscopy and in the area of *in situ* intraocular drug detection systems via optical spectroscopy in the living eye.